Computational studies of cell-penetrating peptides interactions with complex membranes models



Jean Hélie

Department of Biochemistry and Oriel College, Oxford

Michaelmas 2014

A thesis submitted in partial fulfilment of the requirements for the degree of Doctor of Philosophy at the University of Oxford

A copy of thesis has been deposited in the Bodleian Library, Oxford.

The *viva voce* examination was held on Monday 19th January 2015. The examiners were Dr Sylvia McLain (Department of Biochemistry, University of Oxford) and Professor Birgitt Schiøtt (Department of Chemistry, University of Aarhus).

I dedicate this thesis to my family.

Abstract

Membrane active peptides with the ability to cross the plasma membrane represent a promising class of therapeutic compounds. However, translocation efficacy and membrane toxicity of these peptides appear correlated and a better understanding of their mechanisms of action is needed to achieve the desired effect. Here, a range of coarse grain molecular dynamics simulations have been performed to systematically investigate the interactions of such cell-penetrating peptides (CPPs) with biologically relevant membranes. Challenges associated to the development of a suitable asymmetric mammalian membrane model demonstrated the importance of lipid species distribution on the bilayer mechanical properties, as well as the effect of coarse graining on its electrostatic properties. However, simulations successfully discriminated between two CPPs, penetratin and transportan, and were consistent with the experimental data available for these. The results obtained suggest that the ability of transportan peptides to aggregate into flexible, dynamic, transmembrane bundles is responsible for their relative membrane toxicity. The stability and structure of these aggregates, as well as the extent of the bilayer perturbations they induced, were shown to depend on the membrane composition and asymmetry, thus providing a molecular basis to explain how the toxicity of CPPs is modulated by membranes. In particular, bilayer destabilisation was enhanced by the presence of anionic lipids and hampered by that of cholesterol. Transportan aggregates were also observed to trigger lipid flip-flops above a certain size and a new pathway for such events, not relying on the formation of water defects, was characterised.

Acknowledgements

Quite a few people had to bear with me for this thesis to come into existence. First of all, I must thank my academic supervisor, Prof. Mark Sansom, for welcoming me into his lab and supporting me throughout the years despite his ever increasingly busy schedule. I am in particular grateful to Mark for being always present to provide guidance and advice that prevented my thesis from going off tracks, while at the same time giving me the freedom to pursue my research interests. I am also indebted to Dr Francesca Milletti, my industrial advisor from Roche, for her patience and understanding of the different paces at which academic and industrial projects sometimes operate. Thanks to Francesca I have been able to visit Roche research facilities in Nutley several times and I feel truly privileged for this unique opportunity to discover how pharmaceutical research is performed in a non-academic environment and the chance to meet many scientists involved in this complex process. Within Roche, my most sincere thanks also go to Dr Bryn Roberts for helping with my funding situation: without his support my experience as a research student would have been altogether different. I also thank Prof. Charlotte Deane for setting up the industrial collaboration within the EPSRC-funded Systems Approaches to Biomedical Science programme I was part of, and for getting me started with my research project. The time and energy Lisa Bligh dedicated to sorting out the paperwork involved with my particular situation within the Doctoral Training Centre are also warmly acknowledged. I am very grateful too for the financial assistance provided by Oriel College over the years.

Within the lab I was fortunate enough to meet Dr Mickaël Lelimousin and Dr Matthieu Chavent who, in addition to having the good grace of both being French, provided invaluable support, academic and personal alike. Their friendship helped to keep me sane and motivated throughout the thesis journey and I am very much indebted to both of them. Discussions during our numerous coffee breaks were always either scientifically useful or therapeutical, and sometimes both. I am particularly thankful to Mickaël for his supervision: his infinite patience, constant availability and scientific knowledge all contributed to the fruitful completion of this thesis. More generally, I am also grateful for the working and social environment provided by the SBCB lab as a whole: Lukas, Maria, Praf, Heidi, Chen, Jerome, Anna Duncan, Joe, Matthias, David, Phil F, Jemma, Shabs, Tyler, Sonya and Amanda all contributed to great memories either in the pub (mostly), lab, squash court, swimming pool or during runs and bike rides.

Away from the lab many people also deserve credit for helping me, directly or indirectly, to complete this degree. Lara Sibley played an important role in deciding me to quit my corporate job at L'Oréal and to undertake this endeavour. Prof. Julien Lalande, my chemistry teacher from *prépa*, has my gratitude for relentlessly arguing in favour of rigorous scientific methods and for his willingness to write countless reference letters over the years. In Oxford, it is impossible to list all the characters I met, many of whom have come and gone, and who contributed to make the last four years memorable. I am especially grateful for friends such as José, my Oriel neighbour who was great company until he moved back to Colombia, and Falk and Corinna, the friendly Germans. My housemates Hannah, Anna and Tom at 14 Fettlers House are also acknowledged for providing fun company at a time I needed it. In Essex street, Jaco is kindly thanked for not making me pay rent - and for bearing with my jokes about it. Despite the cold and often not-so-great visibility, I will also keep some fond memories of my diving and instructing with the Oxford student scuba diving club and of several of its members. Outside of Oxford, I am very lucky to have been able to rely

on such great friends as Bastien and Laurence, whose successive London apartments were all like a second home to me whenever I ventured to the capital. Likewise, I have shamelessly abused of the hospitality of Elodie in Cambridge who always cheerfully welcomed me, as well as my very muddy bike, in her flat. London friends such as Amy and Jacqueline are acknowledged too. Whenever I returned to France I am also thankful to Florian, Fabien, Gaëlle and Guillaume for always trying to work around Eurostar train schedules. Further afield, Caroline is warmly thanked for letting me invade her Hoboken flat whenever my research led me to the East Coast of the USA. Similarly, José, Kristen, Isak and Elaine were all fantastic hosts in New-York, Boston and Vermont - a special mention going to José for putting up with an inflatable mattress for two weeks in a studio. Over the years many of these friends also came visit and it was always a pleasure to welcome them as well as Pauline, Belinda, Thomas and Sina (also thanked for their hospitality in Zurich), Maïlis or Véro. A special thank you goes to Pauline for also hosting me in Cairo and providing the best "get away from it all" holidays of those last four years. I am all the more grateful to all of these people as work commitments in the last stages of the thesis meant I neglected many of them.

Finally, but without a doubt most importantly, I am incredibly fortunate for the love and understanding of my family who supported me throughout my various projects - despite still not being sure what it is exactly that I do. My parents and my sister, Claire, have shown formidable patience with me and I could not have done this thesis without them. Un énorme merci également aux grands-parents de Castres et au Papy de Biarritz pour leur soutien inconditionnel - la thèse est peut-être en Anglais mais cette partie est en Français! I am also ever so happy for having met Metta[1] and cannot thank her enough for being who she is and all that she has already done for me. I am truly lucky and grateful.

[1] Ik houd zoveel van je dat ik je je eigen voetnootje gegeven heb.

Contents

Contents **xi**

List of Figures **xvii**

List of Tables **xxi**

List of Abbreviations **xxiv**

1 Introduction **1**

1.1 Cells and membranes 1

1.1.1 Eukaryotic and prokaryotic cells 1

1.1.2 Plasma membrane transport 3

1.2 Membrane active peptides 7

1.2.1 Therapeutic potential 8

1.2.2 Cell-Penetrating Peptides 12

1.3 The case for Molecular Dynamics simulations 19

1.3.1 Limitations of experimental studies 20

1.3.2 Molecular insights from *in silico* studies 22

1.3.3 Limitations of Molecular Dynamics simulations 24

1.4 Thesis outline 25

2 Theory and methods **27**

2.1 Molecular dynamics simulations 27

2.1.1 Classical description of biomolecular systems 28

2.1.2 The force field 28

2.1.3 Algorithms and simulation techniques 31

2.2 Coarse grain simulations 42

2.2.1 Multiscale approaches: choosing the appropriate resolution 43

2.2.2 The MARTINI force field 46

2.3 Analysis of molecular dynamics simulations 53

3 Modelling of biologically relevant membranes **55**

3.1 Introduction 55

3.1.1 Lipid distribution 56

3.1.2 Transmembrane potential 59

3.1.3 *In vitro* and *in silico* membrane models 60

3.2 Initial approach 62

3.2.1 Lipid composition and distribution 62

3.2.2 Protocol 63

3.2.3 Results 66

3.2.4 Challenges 67

3.3 A working model 74

3.3.1 New composition 74

3.3.2 New protocol 75

3.3.3 Free energy barrier to cholesterol flip-flop 77

3.3.4 The question of membrane equilibrium 79

3.4 Electrostatics properties 80

3.4.1 Visualisation and significance of the electrostatic potential 80

3.4.2 Electrostatic potential profile in the AM model 84
3.5 Conclusion 86

4 Comparison of the stability of two cell-penetrating peptides in lipid bilayers 89
4.1 Introduction 89
4.2 Peptides selection and modelling 91
4.2.1 Penetratin 92
4.2.2 Transportan 95
4.2.3 Peptides models 96
4.3 Self-assembly simulations of penetratin and transportan 98
4.3.1 Simulations setup 98
4.3.2 Identification of peptide conformations 99
4.3.3 Preferential orientation and conformation of a single peptide 102
4.3.4 Interfacial depth of insertion 104
4.4 Embedded simulations of penetratin and transportan 106
4.4.1 Simulation setup 107
4.4.2 Monomers stability 109
4.4.3 Peptide collective behaviour 110
4.4.4 Peptide-membrane interactions 120
4.5 Conclusion 129

5 Aggregation of transportan peptides and associated membrane perturbations 133
5.1 Introduction 133
5.2 Transportan in biological membrane models 134
5.2.1 Composition of membranes 135
5.2.2 Simulations performed 136
5.3 Transportan orientation and conformations 139

5.3.1 Relative stability of transmembrane monomers 139
5.3.2 Kinetics of clustering and translocation 144
5.3.3 Density profiles of transportan clusters 152
5.4 Characterisation of membrane properties 156
5.4.1 Bilayer thickness and lipid tails order parameter 156
5.4.2 Recruitment of lipids 160
5.5 Conclusion 163

6 Characterisation of lipid flip-flops induced by transportan 167
6.1 Introduction 167
6.2 Flip-flopping lipids 169
6.2.1 Simulations 169
6.2.2 Identification method 170
6.2.3 Results 171
6.3 Interactions of flip-flopping lipids with transportan 174
6.3.1 Method 175
6.3.2 Influence of cluster size 176
6.3.3 Preferential sampling of basic residues 177
6.4 New insights in the mechanism of flip-flops 180
6.4.1 The role of local charge density 180
6.4.2 CG flip-flops dot not reveal water permeation of membranes 182
6.4.3 Influence of transportan on the free energy barrier of flip-flops . . . 185
6.5 Conclusion 189

7 Future directions 193
7.1 Summary of findings 193
7.2 *In silico* and *in vitro*: bridging the gap 197

7.2.1 Large scale CG simulations 197
7.2.2 Remaining challenges 199
7.3 Towards experimental validation 203

Appendix A Lipid structures **205**

Bibliography **209**

List of Figures

1.1 Eukaryotic and prokaryotic cells 2
1.2 Structure of the plasma membrane 4
1.3 Endocytosis by eukaryotic cells 6
1.4 Models of bilayer destabilisation by membrane-active peptides 9
1.5 Inverted micelle mechanism 15
1.6 Factors influencing experimental studies of CPPs 17
1.7 A continuous spectrum of membrane active peptides 19
1.8 Limited resolution of experimental techniques 20
1.9 Molecular level insights from MD simulations 23

2.1 The MD algorithm 31
2.2 Periodic boundary conditions 38
2.3 Level of details and corresponding time and length scales accessible 44
2.4 Coarse grain mapping of a phospholipid in MARTINI 47

3.1 Asymmetric distribution of lipids species in the plasma membrane 57
3.2 Difference between bacterial and mammalian membranes 58
3.3 CG representation of lipids species 63
3.4 Initial protocol for asymmetric membrane building 64
3.5 The AMv1 model 67

3.6 Importance of matching leaflets areas 69
3.7 Cholesterol flip-flops 70
3.8 Redistribution of cholesterol between leaflets 72
3.9 The AM model 76
3.10 Cholesterol free energy of flip-flop 77
3.11 Transmembrane electrostatic potential profile 82
3.12 Effective electrostatic potential profile of the AM bilayer 84

4.1 Penetratin 93
4.2 Transportan 95
4.3 Penetratin and transportan models 97
4.4 Possible conformations of the peptides 100
4.5 Automated identification of peptides conformations 101
4.6 Outcome of SA simulations 103
4.7 Transportan sinks deeper into the bilayer than penetratin 105
4.8 Final orientations in simulations of a single embedded peptide 110
4.9 Different collective behaviour of transportan and penetratin 111
4.10 Transportan aggregates are disordered 112
4.11 Aggregation patterns of transportan and penetratin 114
4.12 Transportan oligomerisation is energetically favourable 116
4.13 Translocation of penetratin and transportan 117
4.14 Desorption of penetratin from a zwitterionic membrane 119
4.15 Solvent exposure of penetratin residues at the surface of a DOPC bilayer . . 120
4.16 Calculation of bilayer's thickness 122
4.17 Peptides induced bilayer thinning 123
4.18 Transportan flexibility critical in inducing bilayer deformation 124
4.19 Calculation of lipid tails order parameter 127

4.20 Peptides induced lipid tails disorder 128

5.1 Simulations pipeline 138
5.2 Membrane asymmetry influences stability of transmembrane conformations 142
5.3 Transportan conformations and total potential energy of the system 143
5.4 Evolution of transportan biggest cluster size 145
5.5 Graphical representation of transportan aggregation 147
5.6 Aggregation of transportan peptides in zwitterionic membranes 148
5.7 Aggregation of transportan peptides in anionic membranes 149
5.8 Translocation of transportan 151
5.9 Residues density profiles in transportan aggregates 154
5.10 Transportan clusters induce local membrane thinning and disorder 158
5.11 Anionic lipids recruiting by transportan clusters 161
5.12 Charges density profiles in transportan aggregates 163

6.1 Successive stages of a phospholipid flip-flop 171
6.2 Flip-flops detected in the simulations performed 172
6.3 Flip-flopping lipids: z coordinate of the phosphate bead 173
6.4 Flip-flopping lipids preferentially interact with larger transportan clusters . 176
6.5 Flip-flopping lipids preferentially sample basic residues 178
6.6 Electrostatic interactions drive flip-flops 179
6.7 Influence of cluster size on local charge density 181
6.8 Influence of cluster shape on local charge density 182
6.9 Electrostatic pore do not involve water penetration 183
6.10 Anionic lipids flip-flops free energy profiles 186
6.11 Particles and energy vs charges density 188

7.1 Membrane perturbation by membrane active peptides: conclusions 196

7.2 Very large CG systems 198
7.3 Evolution of peptides distribution and number of flip-flops 199
7.4 Undulation and tabulation of the AMLarge system 200
7.5 Bilayer undulations depend on lipid composition 202
7.6 Conversion back to atomistic details 203

A.1 Glycerophospholipids 205
A.2 Acyl chains 206
A.3 Sphingolipids 207
A.4 Cholesterol 207

List of Tables

1.1 Diversity of CPPs sequences 13

2.1 Representation of residue side chains in the MARTINI model 50

3.1 AMv1: membrane composition 62

3.2 AM: membrane composition 75

3.3 Free energy barriers to cholesterol flip-flops 78

4.1 Self-assembly simulations of penetratin and transportan 99

4.2 Embedded simulations of penetratin and transportan 107

5.1 Composition of the membrane models used 135

5.2 Simulations of transportan in different membrane models 137

5.3 Conformations adopted by a single embedded transportan peptide 140

5.4 Average bilayer thickness 159

5.5 Average lipids tails order parameter 160

List of Abbreviations

AM	Asymmetric membrane model
AMv1	Initial asymmetric membrane model (include sphingolipids)
AMP	Antimicrobial peptide
CERA	Ceramide
CG	Coarse grain
CHOL	Cholesterol
CPP	Cell-penetrating peptide
DHPC	1,2-diheptanoyl-*sn*-phosphatidylcholine
DLPC	1,2-dilauroyl-*sn*-phosphatidylcholine
DOPC	1,2-dioleoyl-*sn*-phosphatidylcholine
DPPC	1,2-dipalmitoyl-*sn*-phosphatidylcholine
DSPC	1,2-distearoyl-*sn*-phosphatidylcholine
EL	Simulations of 9 transportan embedded in a large bilayer
ES	Simulations of a single transportan embedded in a small bilayer
GUV	Giant unilamellar vesicle
IL	Simulations of 9 transportan positioned on the surface of a large bilayer
LUV	Large unilamellar vesicle
MD	Molecular dynamics
POPC	1-palmitoyl-2-oleoyl-*sn*-phosphatidylcholine

POPE	1-palmitoyl-2-oleoyl-*sn*-phosphatidylethanolamine
POPS	1-palmitoyl-2-oleoyl-*sn*-phosphatidylserine
PPCS	Sphingomyelin
SA	Self-assembly simulations
SMa	Symmetric membrane made of the anionic leaflet of the AM model
SMz	Symmetric membrane made of the zwiterrionic leaflet of the AM model
TM	Transmembrane as well as a particular conformation of transportan
TM*	A particular transmembrane conformation of transportan

Chapter 1

Introduction

1.1 Cells and membranes

Cells represent the fundamental building blocks of life, both from a structural and a functional perspective, and all living organisms are composed of one or more cells. While a multitude of different cell types exist, with distinctive characteristics allowing them to perform various biological functions, at the most basic level all cells are membrane-enclosed entities which fall within two categories, prokaryotes and eukaryotes.

1.1.1 Eukaryotic and prokaryotic cells

The content of all cells is delimited by a biological membrane called the plasma, or cytoplasmic, membrane. The corresponding intracellular space is the cytoplasm. In eukaryotic cells, the genetic material is located in the nucleus, a distinct intracellular compartment separated from the cytoplasm by the nuclear enveloppe. In contrast, prokaryotic cells do not possess a nucleus to store their DNA and, as illustrated in Figure 1.1, such cells are relatively smaller and simpler than eukaryotic cells [1]. Prokaryotic cells account for two

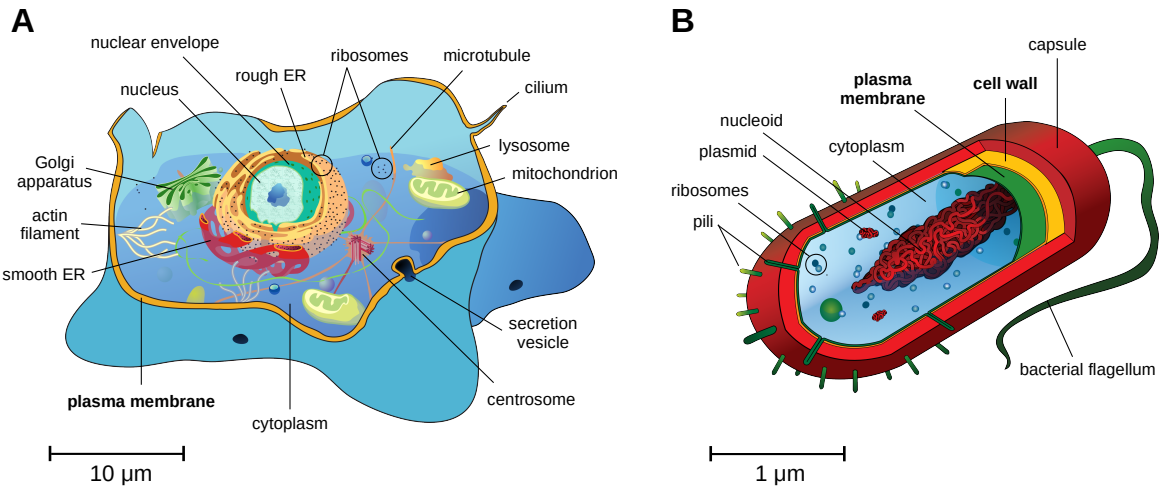

Figure 1.1 Schematic representation of the structure and content of (A) an eukaryotic mammalian cell, and (B) a prokaryotic bacterial cell. In contrast to prokaryotic cells, the cytoplasm of eukaryotic cells contains numerous membrane-bound organelles, such as the nucleus where DNA is located. They also possess a cytoskeleton consisting of microtubules as well as actin and intermediate filaments. Scale is approximate and indicated for reference only. Bacteria usually do not exceed a few micrometers in length but the shape and size of eukaryotic cells vary greatly and while most are commonly 5 to 100 µm in diameter some specialised cells such as neurons can extend as far as 1 m [1]. Images respectively adapted and reproduced from originals by Mariana Ruiz Villarreal[a,b].

[a] http://commons.wikimedia.org/wiki/File:Animal_cell_structure_en.svg
[b] http://commons.wikimedia.org/wiki/File:Average_prokaryote_cell-_en.svg

of the three domains of life, archaea and bacteria, with eukaryotes constituting the third one [2]. Archaea and bacteria are single cell microorganisms whereas eukaryotes exist as both unicellular, such as some plants and fungi, or multicellular organisms, such as animals. In particular, while most are harmless or beneficial, bacteria[1] represent a significant source of pathogens for higher organisms [4]. Although structural differences exist between, for instance, plant and animal cells, two other distinguishing features of all eukaryotic cells, further to the existence of a nucleus, are the presence of numerous specialised organelles. These correspond to membrane-bound compartments where specific metabolic activities occur, and the existence of a cytoskeleton, which is a complex network of protein filaments controlling the cells mechanical properties. On the other hand, one universal property of all

[1] There is no clear evidence that pathogenic archaea exist [3].

eukaryotic and prokaryotic cells is the ability to transport molecules in and out the cell in order to ensure their survival and/or perform their cellular functions. The mechanisms by which they achieve this are presented below.

1.1.2 Plasma membrane transport

Passive and enhanced transport

The plasma membrane is a protective barrier which maintains the physical integrity of the cell but, conversely, it must also allow for the exchange of compounds such as nutrients and wastes between the cytoplasm and the local extracellular environment. As illustrated in Figure 1.2, this biological membrane is composed of amphiphilic lipids arranged in a bilayer so that their hydrophilic heads face the cytoplasm and the extracellular space while their tails form a hydrophobic barrier. Small nonpolar molecules such as CO_2 or O_2 can readily dissolve in such a lipid environment and consequently they easily move across it by *passive diffusion*. Similarly, small polar molecules such as water or urea can also diffuse unassisted across the plasma membrane, although at a much slower rate [1].

In contrast, the lipid bilayer represents an impermeable barrier for charged molecules, such as ions, and larger compounds. However, as shown in Figure 1.2, cell membranes also contain a wide range of membrane proteins and these allow cells to receive signals and communicate between them [6] as well as to control the import and export of molecules. Such membrane proteins can be broadly categorised as integral membrane proteins, which are permanently attached to the membrane, and peripheral membrane proteins, which are only temporarily attached to the membrane (for instance via association with an integral membrane protein). Integral membrane proteins can be partly embedded in the lipid bilayer or span it entirely and often also contain both extracellular and cytoplasmic domains. The hydrophobic transmembrane (TM) domains of integral membrane proteins fall into two main structural types: α-helical, comprising either a single-pass helix or multiple helices

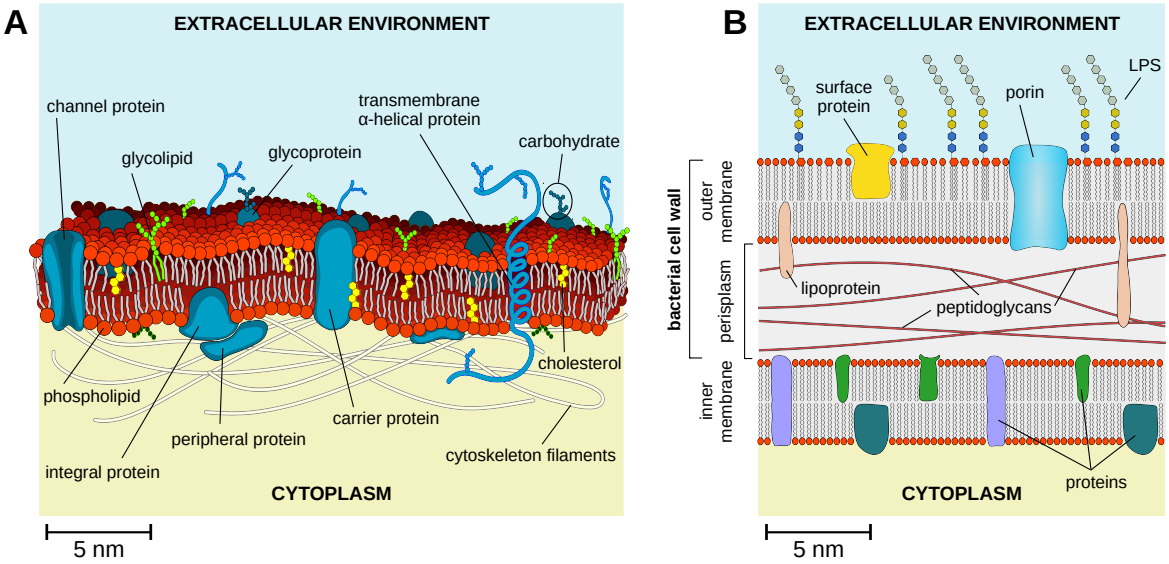

Figure 1.2 Schematic representation of the structural organisation of the plasma membrane of (A) a mammalian cell, and (B) a gram-negative bacteria. The lipid bilayer structure of the plasma membrane constitutes a protective hydrophobic barrier of the cell cytoplasm. Red spheres correspond to the lipids hydrophilic head group while their hydrophobic tails are shown in grey. Selective transport of solutes across the bilayer is mediated by proteins embedded in the membrane such as carrier or channel proteins. Unlike mammalian cells, bacteria possess an external cell wall composed of cross-linked peptidoglycans that provides structural integrity to the cell but is relatively porous [5]. The cell wall of gram-negative bacteria additionally contains an outer membrane which is connected to peptidoglycans by lipoproteins and delimits a perisplasmic space together with the plasma/inner, membrane. In contrast, the outer membrane is absent in gram-positive bacteria but the layer of peptidoglycans is many times thicker. Images adapted from originals by respectively Mariana Ruiz Villarreal[a] and Jeff Dahl[b].

[a] http://commons.wikimedia.org/wiki/File:Cell_membrane_detailed_diagram_en.svg
[b] http://commons.wikimedia.org/wiki/File:Gram_negative_cell_wall.svg.

bundles together, and β-barrels, consisting of antiparallel β-strands forming a cylindrical sheet. Interestingly, α-helical TM proteins are ubiquitous but β-barrel TM proteins such as porins are only found in bacterial and mitochondrial membranes. However, despite their biological importance, there is a paucity of structural data for membrane proteins: while they are estimated to constitute approximately 30% of the proteome of organisms [7], out of the $\simeq$ 105000 structures currently deposited in the Protein Data Bank (PDB) [8] only $\simeq$ 1500 are for membrane proteins, of which only $\simeq$ 500 correspond to unique proteins[2]. This severe

[2] http://blanco.biomol.uci.edu/mpstruc/

under-representation is a consequence of the intrinsic experimental challenges associated to the structure determination of these proteins [9, 10] which makes it difficult to understand the exact mechanisms by which they operate. Nevertheless, it is known that the transport of solutes is mediated by two major classes of integral membrane proteins, carriers and channels, which precisely regulate solutes transit in and out of the cell, thereby effectively making the plasma membrane a selectively permeable barrier. A carrier protein binds to a specific solute to form a complex that following several conformational changes can release the solute on the opposite side of the membrane. Such carriers constitute a very diverse group and can transport ions as well as charged and uncharged organic molecules [11]. In contrast, channel proteins form aqueous pores spanning the lipid bilayer that can open and close to allow the rapid passage of specific ions. The gating mechanism of these channels can be voltage-dependent [12], activated by the binding of a ligand [13] or even stretch-activated following a change of the mechanical stress within the plasma membrane [14]. Channels and passive carriers thus act as molecular gate keepers specifically facilitating the diffusion of certain solutes in response to external stimuli. However, the direction and extent of such a *facilitated diffusion* process remain driven by the concentration gradient of the solutes between the cytoplasm and the extracellular environment. In order to maintain homeostasis or compete for resources, the *active transport* of solutes across the plasma membrane is also achieved by cells. This process similarly relies on carrier proteins but also requires the use of metabolic energy, such as hydrolysis of ATP to ADP, to for instance pump ions against their concentration gradient or accumulate molecules such as sugars or amino acids.

Endocytosis

Although membrane transport proteins allow the passage of small essential molecules such as ions, sugars or amino acids across the plasma membrane they are unsuitable for larger

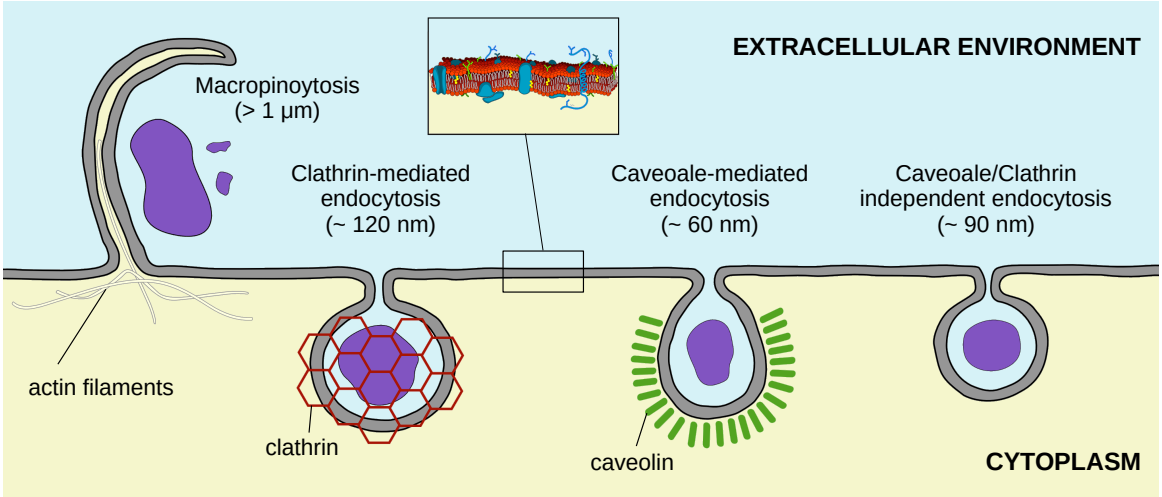

Figure 1.3 Schematic representation of plasma membrane deformation in the different types of pinocytosis and size of the corresponding vesicles formed. A detailed review of these different endocytic mechanisms can be found in [15]. In particular, clathrin proteins rearrange themselves in a cage-like structure to form clathrin coated vesicles while caveolin proteins have a hairpin structure leading to smaller, elongated vesicles. Experimentally, markers and inhibitors of specific endocytic mechanisms can be used to determine which pathway is involved in the uptake of a particular molecule. Illustration not to scale but Figure 1.2A is reproduced in the inset for reference.

macromolecules. Prokaryotic cells synthesise extracellular enzymes which break down organic macronutrients into substrates of smaller sizes that can then enter the cell [16]. Similar extracellular enzymes are present in the digestive systems of animals and play an essential role in the bioavailability of nutrients [17]. However, unlike prokaryotes, all eukaryotic cells also rely on deformation of their plasma membrane to engulf and internalise macromolecules. This process, known as endocytosis, is possible because of the absence of a rigid cell wall like in bacteria (Figure 1.2) and the existence of a complex cytoskeleton controlling the cell's shape (Figure 1.1). Endocytosis can be classified as either phagocytosis or pinocytosis, respectively meaning "cell eating" and "cell drinking" [18]. As the name implies the former involves the internalisation of larger biomolecules, such as bacteria, and is usually restricted to specialised cells such as macrophages [19]. On the other hand, pinocytosis can be performed by all eukaryotic cells and via different mechanisms usually classified as either macropinocytosis, clathrin-mediated endocytosis, caveolae-mediated endocytosis or

clathrin- and caveolae- independent endocytosis [15]. These mechanisms are all energy-dependent and involve protein-mediated invagination of the plasma membrane, with the exception of macropinocytosis where ruffled membrane extends from the cell surface before folding back on it, and formation of an intracellular vesicle, the size of which depends on the particular process considered. This is depicted schematically in Figure 1.3. The vesicle and its content are then degraded further down the endocytic pathway, and the resulting products either consumed in metabolic activities or recycled towards the plasma membrane to allow the process to repeat [20][3]. Importantly, in contrast with the membrane transport mechanisms described previously, the extracellular molecules engulfed by the deformation of the plasma membrane remain trapped into various intracellular membrane-bound vesicles such as endosomes and lysosomes as they are routed and degraded through the endocytic pathway but are not released into the cytoplasm.

1.2 Membrane active peptides

Membrane active peptides refer to a diverse group of relatively short amino acid sequences (usually less than 40 residues) that possess the ability to directly interact with the plasma membrane of cells. Given the crucial role of this protective barrier in cellular activity, such peptides are of considerable biological interest. In particular, membrane active peptides can destabilise or penetrate cell membranes and are historically distinguished based on the type of cells they act upon and the nature of their interactions with the lipid bilayer. However, such peptide-centric boundaries have been shown to be fluid as membrane active peptides exhibit a range of activity and the fundamental role of the lipid bilayer in their modulation is becoming increasingly recognised [22]. This section presents an overview of the therapeutic potential associated to such membrane active peptides before then focusing on the

[3] Eukaryotic cells are estimated to internalise and recyle the equivalent of their membrane surface 1 to 5 times an hour through this process [21].

characteristics of so-called cell-penetrating peptides.

1.2.1 Therapeutic potential

Overcoming the challenge of antibiotic resistance: antimicrobial peptides

The discovery of peptides with antimicrobial activity dates back to the 1940s when gramicidin, a peptide extracted form gram-positive bacteria, was shown to protect mice from pneumococci infection [23–25]. In the 1980s similar antimicrobial peptides (AMPs) synthesised by eukaryotic cells were isolated for insects (cecropins [26]), amphibians (magainins [27]) and humans (defensins [28]), and it was later demonstrated that AMPs form an important element of the innate immune system of all multicellular organisms to defend themselves against a broad range of gram-positive and gram-negative bacteria [29–31]. To date, more than 5000 such peptides have been identified [32] with a great diversity of sequences and uncertainties remain regarding their exact mode of action [33, 34]. However, a large group of AMPs are cationic and hydrophobic peptides with a strong propensity to form amphipathic α-helices and it is generally accepted that they induce bacterial cell death by permeabilisation of the plasma membrane leading to leakage of the cell's content. This hypothesis is supported by the fact that synthetic peptides containing only D-amino acids showed the same antimicrobial activity as the native all-L AMPs [35–38], hence suggesting that a receptor-mediated mechanism was unlikely and that, rather, the peptides directly interacted with the lipid bilayer. This is further corroborated by *in vitro* studies relying on model membranes which demonstrated that these AMPs could induce leakage of lipid vesicles [39–41].

Common mechanisms by which AMPs are thought to destabilise the plasma membrane are represented by the Shai-Matsuzaki-Huang model [42–44] and illustrated in Figure 1.4. In the barrel-stave pore model, the peptides helices aggregate in a transmembrane structure whereby their hydrophilic faces are oriented inwards and form a channel through which

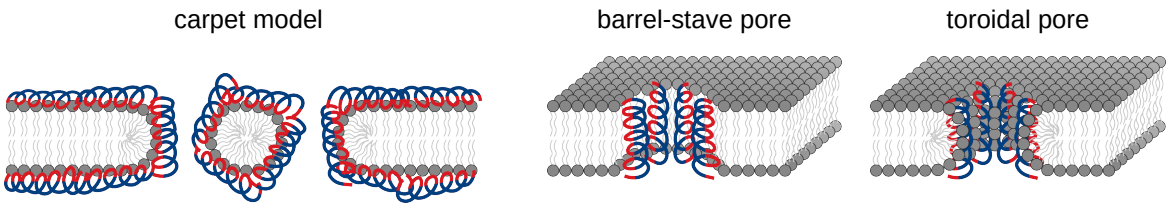

Figure 1.4 The three main models of membrane destabilisation by antimicrobial peptides. The hydrophilic face of the amphipathic α-helice formed by each AMP is coloured in blue and the hydrophobic one in red. Toroidal pores differ from barrel-stave pores as they involve a local deformation of the bilayer so that the hydrophilic head groups of the lipids line their interior. The carpet model involves a detergent like action of the peptides on the membrane, without formation of distinct aggregates. Images adapted from [33].

leakage of small molecules can occur. The toroidal pore model involves the formation of a similar transmembrane bundle but in this case the bilayer is locally deformed so that the pore formed by the AMPs is lined by the hydrophilic head groups of the lipids. In contrast, although also a cooperative mechanism, the carpet model does not require formation of membrane-spanning peptides structures but suggests that destabilisation and lysis of the membrane occur via a detergent-like action of the AMPs. Importantly, however, while well defined pores conforming to either the barrel-stave or toroidal model have been characterised for some peptides [44–46], the permeabilisation of membranes is likely to occur via intermediate and possibly transient structures representing different gradations of these idealised modes of action [39]. In this regard, a "chaotic" toroidal-like pore model [47] and a "sinking-raft" model inducing transient permeation of the bilayer [48] have also been suggested. Notably, pores formed by AMPs need not to be stable, as reviewed in [49].

Regardless of the exact nature of the defects induced by AMPs in the plasma membrane of bacteria, a generic killing mechanism based on the specific targeting and permeabilisation of this protective lipid bilayer holds promising therapeutical potential to overcome the growing problem of antibiotic resistance. Indeed, most antibiotics work by targeting enzymes specific to bacteria which are necessary to their growth and cellular function: while this is an efficient strategy to ensure specificity towards the pathogenic bacteria cells, it can be eas-

ily be defeated by a functional mutation of the antibiotic target or the activation of redundant metabolic pathways [50, 51]. For instance, β-lactam antibiotics, which represent the most common group of antibiotics, target enzymes catalysing the cross-linking of peptidoglycans forming the cell wall of prokaryotic cells (see Figure 1.1). As mammalian cells lack a cell wall these compounds are selective for bacteria but a mutation of the targeted enzyme can restore its functionality, hence rendering the bacteria resistant to such antibiotics [52]. In contrast, it is difficult for cells to significantly change the structure and composition of their plasma membrane and resistance to AMPs is thereby more difficult to achieve. However, the therapeutic use of AMPs is then conditional to their selectivity for bacterial membranes and toxicity towards mammalian cells remains a major hurdle towards the development of effective therapeutic strategies [53]. For instance, while gramicidin based compounds are used as antibiotics they remain limited to topical applications due to the haemolytic activity of this peptide. In this regard, a better understanding of the interactions between AMPs and the respective lipid bilayers constituting the plasma membrane of mammalian and bacterial cells is needed to develop clinically useful peptides [54].

Overcoming the delivery bottleneck: cell-penetrating peptides

The identification of peptides possessing the ability to cross the plasma membrane of mammalian cells occurred later than the discovery of antimicrobial peptides and was mostly serendipitous. Its origins can be traced back to the late 1980s when work on the HIV virus led to the observation by two independent research groups that the HIV protein Tat, an 86-residue long transactivation factor, was taken up by eukaryotic cells following exogenous addition to the medium [55, 56]. Remarkably, they also observed that the protein accumulated into the cell's nucleus where it retained its biological function and led to the stimulation of RNA synthesis. These results were particularly puzzling since, on the one hand, the size of the Tat protein, which also contained several basic residues, was thought to be incompat-

ible with the direct crossing of a hydrophobic lipid barrier, but, on the other, the absence of degradation of the protein and its ability to reach the nucleus were at odds with a classical endocytic internalisation process. However, shortly after, in 1991, similar observations were reported by another research group investigating homeoprotein transcription factors as a 60-residue long sequence (AntpHD) corresponding to Drosophila Antennapedia homeodomain was found to penetrate neuronal cells and to specifically target their nuclei where it bound to DNA and led to morphological changes [57]. In addition to accumulating in the nucleus, the homeoprotein was observed to be uniformly distributed in the cytoplasm and not confined to endocytic vesicles such as those represented in Figure 1.3. Furthermore, the authors were also able to retrieve the homeoprotein intact from the cells, thus demonstrating that the internalisation mechanism did not lead to its degradation. Finally, the cellular uptake of AntpHD also appeared to occur efficiently at 4°C, ie in conditions where energy-dependent metabolic processes are severely limited, thereby further arguing against a simple endocytosis based mechanism.

Collectively, these initial results thus suggested the proteins studied possessed the intrinsic property of translocating across the plasma and nuclear membranes. Shortly afterwards it was determined that the ability of Tat and AntpHD to enter cells was due to relatively short sequences of less than 20 residues [58, 59], referred to as protein transduction domains (PTDs), and that these could also be used to internalise other hydrophilic compounds, such as proteins or oligonucleotides, in many different types of cells [60–62]. By the late 1990s short chimeric and synthetic peptides with cell-penetrating properties had also been identified [63, 64]. These remarkable properties were rapidly recognised as holding formidable potential for the intracellular delivery of therapeutic compounds [65, 66] and the research field of cell-penetrating peptides (CPPs) was born [67]. Since then a considerable amount of work has been dedicated to the study of peptides which are able to translocate across biological membranes and to carry a cargo along with them [68–74]. Indeed, drug deliv-

ery represents a major bottleneck in the development of efficient therapeutic strategies as compounds with promising activity *in vitro* fail to reach their target *in vivo*. In particular, intracellular targets, either cytoplasmic or within organelles such as the nucleus, are especially challenging to address [75–77]. In this context, the ability of CPPs to cross cellular membranes is of particular interest to extend the range of pharmaceutical compounds which currently predominantly relies on small molecules able to diffuse through lipid bilayers [78]. These peptides could indeed help overcome issues such as the poor bioavailability of drugs internalised via endocytosis [79] or the crossing of the blood-brain barrier [80]. In a post-genomic era, such peptides also provide a basis to leverage on the high specificity and potency provided by protein-like molecules to implement effective therapeutic strategies unrestricted by biological barriers, allowing for instance to regulate or rescue expression of a specific gene, as demonstrated by the early Tat and AntpHD studies. This vast repertoire of possibilities was recently extensively reviewed in [81]. However, as discussed in the next section, the numerous studies conducted during the last decade have revealed a more complex picture than initially thought, and, similarly to antimicrobial peptides, harnessing the therapeutic potential of CPPs will require a more detailed understanding of the mechanisms by which these peptides interact with lipids in the cell membrane.

1.2.2 Cell-Penetrating Peptides

More than 20 years after the pioneering work on Tat and Antp, hundreds of amino acids sequences possessing some cell-penetrating properties have been identified [82]. These have been referred to as CPPs, PTDs, Membrane Translocating Sequences (MTSs) or other similar names such as membrane-translocating peptides, with this initial variety in terminology illustrating the diversity and rapid evolution of this research field and arguably some confusion regarding the types of molecules and properties referred to [83]. The standard definition of CPP now used within the research community corresponds to peptides possessing

the intrinsic property of ubiquitously crossing cell membranes [84]. However, this generic definition encompasses many different peptides discovered with a broad range of properties and distinct interactions with biological membranes, as is reviewed in this section.

Physicochemical properties and classification

In addition to peptides derived from proteins and their homologues, many synthetic peptides have been shown to be CPPs [85]. There is a great variety in the peptides discovered and there appears to be no common structural motif or conserved sequence absolutely necessary for cellular uptake. As such, CPPs constitute a loose family of peptides essentially defined by their ability to penetrate into cells. Nevertheless, some common properties can be identified.

Table 1.1 Examples of different cell-penetrating peptides. It can be noted that the charge density decreases with the peptide length while the hydrophobicity increases. Many tat-derived peptides have been synthesised, the sequence indicated is the commonly used segment corresponding to residues 48 to 60. Penetratin corresponds to residues 43-58 of the third helix of AntpHD.

Name	Sequence	Length	Charge[1]	Hydroph.[2]	Ref.
Protein derived					
tat	GRKKRRQRRRPPQ	13	+8	2.37	[59]
penetratin	RQIKIWFQNRRMKWKK	16	+7	1.52	[58]
Designed					
R8	RRRRRRRR	8	+8	2.58	[86]
MAP	KLALKLALKALKAALKLA	18	+5	0.58	[87]
transportan	GWTLNSAGYLLGKINLKALAALAKKIL	27	+4	0.56	[63]

1. Net charge of the peptide at physiological pH.

2. Mean hydrophobicity calculated using the von Heijne whole residue hydrophobicity scale [88] where more negative values reflect greater hydrophobicity, with isoleucine being the most hydrophobic residue (-0.6) and aspartic acid the least ($+3.49$).

As illustrated in Table 1.1, most CPPs are short (less than 30 residues) and positively charged. Notably, pure poly-arginines sequences are able to cross cell membranes [86]. Additionally, while the presence and distribution of hydrophobic residues vary, many CPPs appear to possess an amphipathic character. Consequently, recent classification attempts

are based on the hydrophobic and cationic properties of the peptides rather than on their origins [89, 90]. In this regard, three categories of CPPs are usually distinguished [91]:

1. **Primary amphipathic.** These CPPs contain sequentially hydrophobic and cationic domains and are usually more than 20 residues long (eg transportan).

2. **Secondary amphipathic.** The amphipathic character of these CPPs is dependent on their secondary structure and revealed when they form α-helical structures in contact with membranes. They tend to be shorter than primary amphipathic peptides (eg MAP or penetratin).

3. **Non-amphipathic.** Peptides in this category predominantly consist of cationic residues. They are also usually shorter than other CPPs (eg tat or R9).

Interestingly, this approach provides a simple biophysical basis to explain the different interactions between CPPs and lipid bilayers that have been reported in the literature.

Mechanisms of internalisation: an on-going debate

Investigations of the cellular uptake of CPPs are a long history of conflicting reports and, to date, the mechanisms by which these peptides enter cells remain a controversial issue and the subject of numerous recent reviews [91–103]. The role of endocytosis in the internalisation of CPPs has been a matter of particular debate. Initial reports that all-D and inverso peptides accessed the cell cytoplasm as efficiently than the natural all-L peptide, including at very low temperatures, argued against an energy-dependent or receptor-mediated process and in favour of one based on direct interactions with the lipid bilayer [104]. This was further supported by studies showing that CPP uptake occurred in the presence of endocytic inhibitors [63]. Accordingly, one mechanism suggested was based on the formation of a peptide-induced "inverted micelle" (see Figure 1.5) able to accommodate the CPP and its potential cargo within the bilayer before release into the cytoplasm [104, 105]. However, in

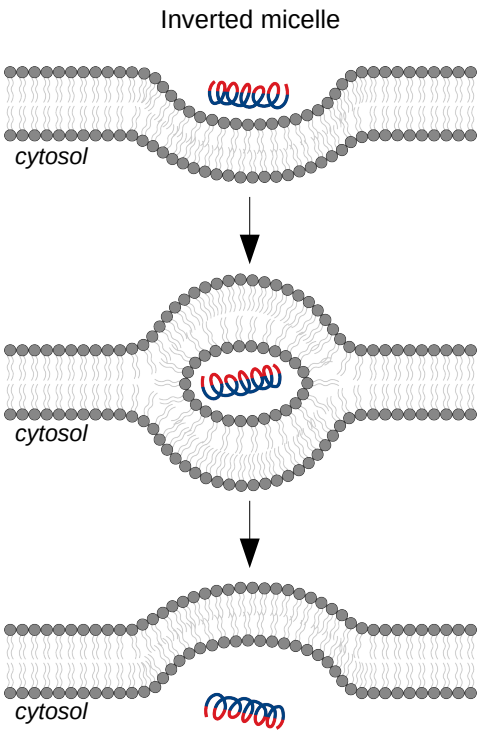

Figure 1.5 In this translocation model based on earlier studies of penetratin [104, 105] the destabilisation of the membrane by the peptides induces the formation of inverted micelles where the peptides are trapped. The opening of the inverted micelle on the cytosolic side of the membrane then allows release of the peptide into the cytoplasm. In this model the peptide essentially remains in an aqueous environment.

the early 2000s it was shown that the uniform cytoplasmic distribution or nuclear accumulation of CPPs could be an artefact caused by peptides redistribution during the fixation of cells [106, 107]. Consequently, the cellular uptake of CPPs was reexamined using updated experimental protocols and this led to a re-evaluation of the role of endocytosis, with the research community shifting its focus from direct translocation mechanisms to endocytic ones [103].

Over the years it became evident that multiple uptake routes are available to CPPs and that different internalisation mechanisms are likely to occur concomitantly [95]. In particular, the apparent incoherence between an endocytosis-based process and the absence of degradation of the peptides has been resolved by additional evidence demonstrating that CPPs were able to escape acidified endosomes early in the endocytic pathway, thereby

avoiding hydrolysation [108–111]. Although different than the direct diffusion across the cell membrane initially envisioned, such an internalisation route still requires the CPP to be able to cross the lipid bilayer delimiting the vesicle in order to gain access to the cytoplasm. However, several studies also support the direct translocation of CPPs across the plasma membrane via a non-vesicular pathway [95, 112–116]. Furthermore, *in vitro* studies using membrane models have shown that CPPs can penetrate lipid vesicles (see Figure 1.8B), thus demonstrating they can cross pure lipid bilayers in an energy independent fashion [116–122]. This ubiquitous ability of CPPs to cross biological membranes unassisted is corroborated by the fact that they enter bacterial cells, which are not capable of endocytosis (see 1.1.2) [123, 124].

Additionally, it has been shown that the uptake routes available to a given CPP *in vivo* depended not only on its intrinsic properties but also on its relative concentration with respect to cells, thus suggesting that cooperation between peptides and the peptide to lipids ratio (P:L) played an important role in the mechanisms of internalisation [94, 95, 98, 103, 125]. As illustrated in Figure 1.6, it has also become clear that the activity of CPPs was influenced by several factors such as the type of cargo [126–128] or fluorophore [129–132] used. Notably, fluorescent labelling of CPPs has been observed to promote endocytosis over direct translocation pathways [132]. Such experimental considerations are of particular relevance since historically many CPPs have been studied as delivery vectors of various therapeutic cargos rather than on their own. This approach has hampered comparison between studies and limited the understanding of the fundamental interactions at play between the peptides and the lipid bilayer. Conversely, it does provide a basis to explain the apparently inconsistent findings that continue to be reported [101, 133].

Altogether these observations illustrate that while CPPs do possess the remarkable and intriguing property of translocating across biological membranes, the simple view of a "magic bullet" able to carry hydrophilic compounds into cells does not conform to the com-

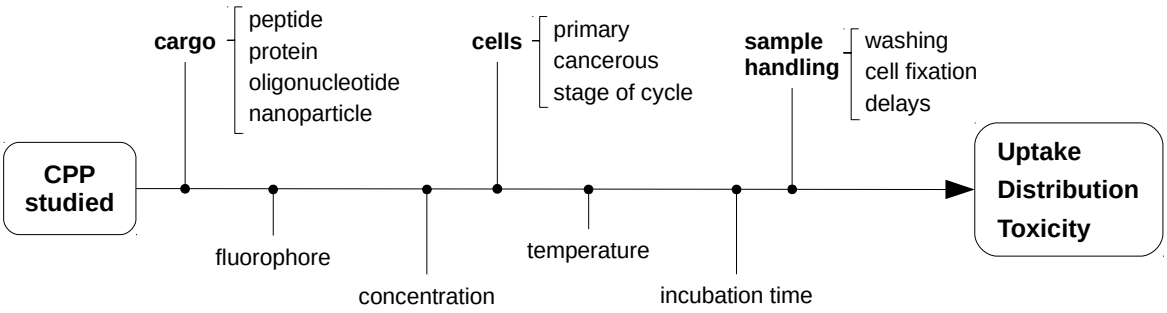

Figure 1.6 Main factors influencing the experimental study of the biological activity of CPPs. Diagram adapted from [92].

plex picture revealed by more than two decades of investigations. Notably, they highlight the necessity to focus on relatively simple systems to elucidate the mechanisms by which short sequences of basic amino acids can interact with lipid bilayers and cross the hydrophobic barrier they represent. In this regard, artificial bilayer models are increasingly considered as a valuable tool and have already allowed to demonstrate the influence of lipid composition on the internalisation of CPPs [122, 134].

Membrane translocation and membrane toxicity: two sides of the same coin

Even though the mechanisms by which CPPs penetrate cells remain speculative, it is clear that they involve some degree of perturbation of the lipid bilayer. Notably, while there is some evidence in favour of the inverted micelle model [135, 136] or related membrane deformations [137] for some peptides, numerous studies have shown that the internalisation of CPPs leads to transient permeabilisation of the membrane crossed. Although the extent of such destabilisations are a matter of debate, early *in vivo* experiments suggested that cytotoxicity may be a possible side-effect of the activity CPPs [138]. This was later confirmed by additional experiments that characterised the time, cargo and concentration dependence of cellular toxicity induced by several CPPs [128, 139–142]. In particular, while it is possible that internalised peptides can also induce cytotoxicity by binding to intracellular proteins and disturbing associated cellular functions, it has been specifically demonstrated that CPPs

could induce membrane toxicity [143]. Furthermore, the hypothesis that biological membranes are destabilised by CPPs is also supported by the observation that these peptides trigger a membrane repair response mechanism [144]. Additionally, recent studies showed that direct translocation across the plasma membrane or endosomal escape both relied on the ability of the CPPs to induce defects disrupting the structure of the bilayer [115, 145]. These observations are in agreement with *in vitro* experiments relying on fluorescence spectroscopy that revealed that CPPs induced some leakage of the contents of lipid vesicles [120, 146] or electrophysiological measurements that showed that these peptides could form pore-like structures allowing the passage of ions [147].

As a consequence, it has been suggested that the direct translocation of cell-penetrating peptides relied on mechanisms similar to those suggested for antimicrobial peptides albeit involving perturbations of lesser extent and stability (see Figure 1.4). Notably, the hypothesis that, unlike AMPs, CPPs induce transient defects in membranes can explain the graded leakage, as opposed to all-or-none, of vesicles or the stochastic nature of the ionic current detected [49, 147, 148]. In this regard, mechanisms representing toned down gradation of the carpet model have been proposed, such as the sinking raft model, wherein the sinking of small aggregates of peptides into the bilayer leads to its temporary permeabilisation but not to membrane lysis [48, 120]. Similarly, disordered pore-like structures related to the toroidal or barrel-stave pore model could account for both the translocation and transient perturbation of the bilayer. Importantly, in such models dye efflux occurs through local and transient destabilisation of the bilayer and not because of pore formation [48, 120].

As illustrated in Figure 1.7, these considerations have shown that the distinction between CPPs and AMPs is fluid and that members of these historical families represent a continuous spectrum of membrane active peptides [149, 150]. For instance, mutations in the sequence of penetratin have been shown to increase its membrane toxicity without altering its translocation efficacy [151]. Additionally, while CPPs can enter both mammalian and bacterial

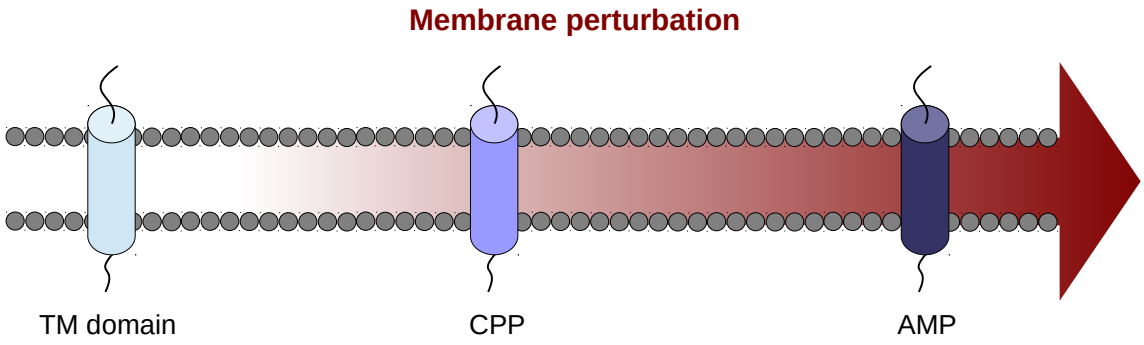

Figure 1.7 Schematic representation of the intensity of perturbations (in red) induced by membrane active peptides. The plasma membrane accommodates many integral proteins with transmembrane (TM) domains which do not destabilise the lipid bilayer. In contrast CPPs and AMPs can induce significant perturbations. Despite what these two classifications may suggest such peptides represent a continuous spectrum of membrane activity and of associated bilayer destabilisations.

cells, they have been shown to induce some destabilisation of bacterial membranes [123]. Consequently, the two AMP and CPP classifications are essentially a legacy reflecting the historical context of the discovery of such membrane active peptides. These classifications have since evolved to describe the types of membrane activity such peptides can exhibit rather than well defined intrinsic peptide properties. This evolution, a natural consequence of findings revealing that peptides could act both as AMP and CPP [149, 150], accounts for some of the confusion and diverging opinions that remain in the scientific community regarding the definition of what exactly constitute CPPs and AMPs. In this context, the lipid bilayer characteristics appear to play a fundamental role in modulating the activity of such membrane active peptides [22, 152]. Understanding the molecular interactions regulating the interplay between lipids and CPPs will thus help to rationalise their observed membrane activity and to achieve the desired effect while minimising unwanted ones [153, 154].

1.3 The case for Molecular Dynamics simulations

In biological sciences, computational approaches are increasingly recognised as a valuable tool to test models, detect possibly significant correlations between the properties of the sys-

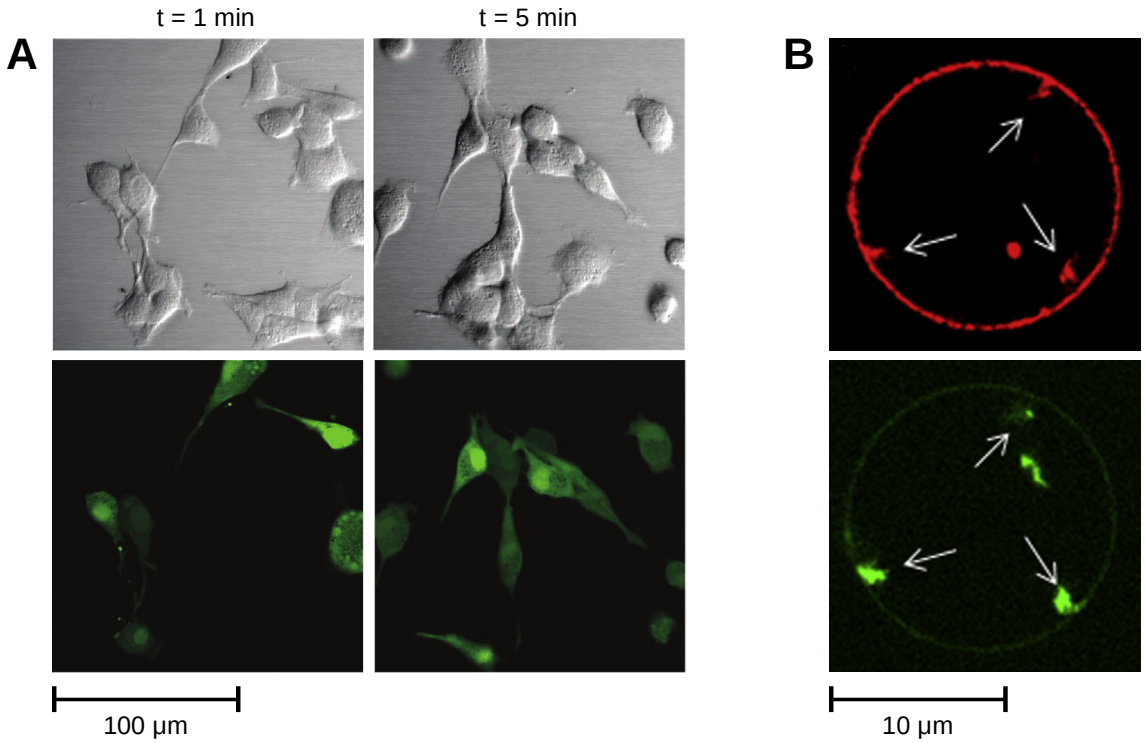

Figure 1.8 Experimental visualisation of internalisation of CPPs. (A) Live mouse fibroblasts 1 min and 5 min after addition of 100 µM FITC-labelled Tat. The top row shows images of the cells obtained by Differential Interference Contrast (DIC) while the bottom row contains corresponding confocal microscopy images illustrating the cellular uptake of Tat. Cells were rinsed before imaging to remove fluorescent peptides from the extracellular space. (B) Confocal slices of Plasma Membrane Spheres (PMS, see 3.1.3) labelled with di-4-ANEPPDHQ (red) 25 min after addition of 10 µM carboxyfluorescein-labelled penetratin (green). The PMS were induced from MDCK cells and the white arrows indicate co-localisation of lipids and peptides. Reproduced from [156] and [116].

tems studied and explore levels of details otherwise difficult to access [155]. In particular, in the case of processes involving membrane-proteins interactions, simulations of interactions between individual molecules can provide structural and dynamic insights complementing the ensemble observations and mostly static structures obtained experimentally.

1.3.1 Limitations of experimental studies

As previously described (see Figure 1.6), experimental studies of cell-penetrating peptides is influenced by many factors. Although standard protocols of study are being developed [157], these factors possibly hinder the identification of the intrinsic peptide and

membrane properties that are relevant to membrane translocation and/or perturbation. Besides, in addition to possible artefacts due to the choice of fluorophore, fluorescence-based microscopy techniques traditionally used to study the internalisation of CPPs in cells or vesicles (Figure 1.8) are well suited to qualitative observations of the activity of different peptides but dot not readily allow to make quantitative comparisons. In this regard, recent techniques based on mass spectrometry allow to overcome this limitation and to precisely quantify the amount of internalised CPPs [158, 159] but at the cost of sample degradation and convenient time-monitoring of the distribution of peptides with time.

Additionally, current experimental techniques cannot provide structural insights regarding the manner in which peptides interact with lipids within membranes. Indeed, as illustrated in Figure 1.8, although the micrometer scale resolution of imaging techniques allows to distinguish localised bilayer defects it is not suitable to the characterisation of the associated peptide-lipids structures. Similarly, evaluation of membrane toxicity by LDH or dye release assays is limited by the size of the probe used [160] and while graded or all-or-none patterns can be observed with smaller dyes, thus allowing to distinguish different types of bilayer destabilisations, this approach yields limited information on the nature of the perturbations involved. Electrophysiology measurements [147] or techniques measuring the evolution of the dielectric constant of artificial bilayers [161] allow to detect more subtle destabilisations of the model membrane but do not provide insights regarding their underlying structure. Finally, while diffraction studies have allowed to elucidate the overall shape of stable pores formed by antimicrobial peptides [44–46], they do not inform on the specific peptide-peptide or peptide-lipid interactions involved and, in any case, this strategy is not appropriate to examine the transient structures formed by translocating CPPs.

Collectively, these remarks show that while many experimental tools exist to assess the biological activity of CPPs *in vivo* or *in vitro*, these are less appropriate to the physicochemical description of the underpinning molecular mechanisms.

1.3.2 Molecular insights from *in silico* studies

Molecular Dynamics (MD) simulations provide an interesting computational tool to investigate peptide-peptide and peptide-lipids interactions with a temporal and spatial resolutions otherwise inaccessible. This is all the more relevant since the simple view of biological membranes as passive hydrophobic bilayers has given way to a recognition of the importance of the specific properties of their constituting lipids [162], and, consequently, of the necessity to access molecular details in order to interpret membrane regulated processes [163]. In this regard, modelling of the properties of lipid bilayers using MD simulations has made considerable progress in recent years [164] and is suitable to the description of local, non-planar defects [165] that cannot be tackled by simpler continuum approaches [166, 167]. Notably, MD simulations predicting the membrane partitioning of model amphipathic helices in membranes of different shape and composition, based on an analysis of lipid-packing defects, have recently been validated by *in vitro* experiments [168].

Accordingly, MD simulations have been used to complement experiments and investigate the interactions of promising therapeutic compounds with model membranes [169] and are increasingly featured in recent reviews dedicated to the internalisation mechanisms of CPPs [99, 101, 102, 122]. In particular, MD simulations have allowed to examine the role of particular residues and lipid species on the conformational behaviour of CPPs and their binding to bilayers when positioned at the water interface [170–173] or fully inserted into the membrane [174, 175]. Notably, a study of a CPP and of its analogues which combined cellular uptake assays and MD simulations of the corresponding sequences in presence of a model lipid bilayer reported a consistent correlation between higher disturbance of the membrane and greater translocation efficacy [176]. Furthermore, despite their limited timescales with respect to biological processes, MD simulations have provided molecular insights regarding how the cooperation of membrane active peptides can lead to membrane destabilisation. For instance, several studies revealed a concentration dependence of the

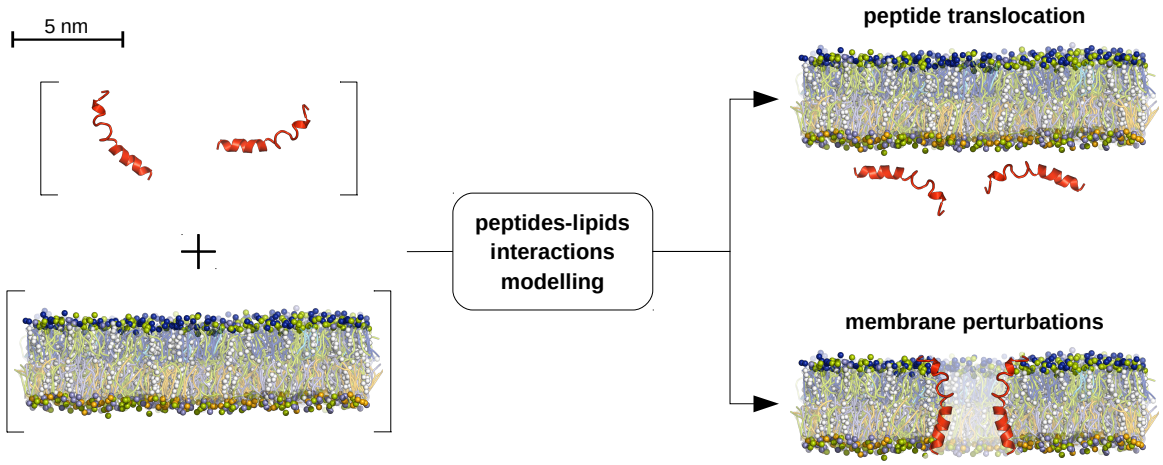

Figure 1.9 MD simulations allow to study interactions between peptides and lipids at the molecular level and within a sub-nanosecond temporal resolution. This computational approach allows to conveniently investigate factors such as the presence of particular lipids species or the number of peptides interacting with the bilayer and to identify which role they play in the ability of peptides to cross the membrane or destabilise it. Here cholesterol molecules and the phosphate head groups of phospholipids are shown as spheres and the acyl chains of phospholipids are shown as transparent. Different lipid species are indicated by different colours. Peptide translocation and membrane perturbations are represented schematically for illustration purpose.

ability of AMPs to cooperatively insert into the bilayer and showed that they induced dynamic toroidally-shaped pores with significant disorder [177, 178]. Subsequent experimental studies found that these findings provided a structural model in good agreement with the observed transient vesicle leakage associated to internalisation of CPPs [120]. Similarly, combined studies involving electrophysiology measurements and MD simulations showed that Tat and poly-arginine peptides translocated in presence of a transmembrane potential and induced water defects consistent with the ionic currents measured [179, 180].

Crucially, despite the relative simplicity of *in silico* models compared to *in vivo* environments, MD simulations allow to readily examine the influence of different parameters on the interactions between peptides and lipids at the molecular level. As schematically illustrated in Figure 1.9, similarly to *in vitro* experiments relying on simplified membrane models to help elucidate activity observed *in vivo* [122, 181], MD simulations are therefore a useful tool to perform computational experiments providing insights into the molecular origins of

the bilayer perturbations induced by membrane active peptides and to systematically examine their dependence on peptide characteristics (eg charge distribution, concentration, structure) and membrane properties (eg lipid composition). In this regard, coarse grain models have extended the time and length scales accessible by MD simulations, thus rendering more convenient the exploration of the collective dynamic behaviour of membrane active peptides in various membrane-mimetic environments [182]. While they do sacrifice some molecular details in order to achieve higher computational efficiency, such models have recently been shown to successfully discriminate between different antimicrobial peptides as they revealed the formation of peptides aggregates with different structures, corresponding to bilayer defects consistent with the respective dye efflux profiles induced by these peptides in *in vitro* experiments [183]. Altogether, these observations illustrate how our understanding of the mechanisms by which membrane active peptides interact with biological membranes can benefit from *in silico* approaches.

1.3.3 Limitations of Molecular Dynamics simulations

In light of the above mentioned advantages, Molecular Dynamics simulations are sometimes referred to as a "computational microscope" [184]. However it is important to bear in mind the limitations inherent to such simulations and to what extent they relate to and can inform on actual biological or biophysical systems. Of particular note is the fact that, due to the computational cost of MD techniques, biologically relevant temporal and/or spatial scales associated to the problem at hand may not be fully accessible. Even when simulating the behaviour of relatively small systems, such as ion channels, the question of whether MD simulations allow to adequately sample the conformational space of the structures investigated remains an important issue [185, 186]. It is also crucial to remember that, in addition to access to sufficient computational power, insights provided by MD simulations are fundamentally dependent on the quality of the physical models on which these simu-

lations are based. In this regard, the recent development of dedicated hardware facilities, allowing to reach millisecond timescales for fully atomistic simulations of proteins [187, 188], has highlighted the influence of force field parametrisation on the robustness and accuracy of the results achieved [189–191]. One should therefore keep in mind that, unlike a microscope allowing observation of the system of interest, Molecular Dynamics simulations remain a modelling tool and as such are limited by the accuracy of the underlying physical model as well as by the resources available to perform the associated calculations. Consequently, while MD simulations represent a valuable technique to investigate the role of specific molecular interactions and allow to conveniently perform "thought experiments" by modifying the simulations setup, they cannot represent a substitute for experiments but rather complement them by suggesting hypotheses to be confirmed by experimental studies.

1.4 Thesis outline

This thesis describes coarse grain (CG) MD simulations of cell-penetrating peptides interacting with different models of biological membranes. The main problem addressed is two-fold and regards the quantitative characterisation of dynamic peptides aggregates in complex membrane models as well as that of the local bilayer perturbations induced by these.

First, the theoretical basis and practical implementation of molecular dynamics simulations are reviewed in the following chapter, Chapter 2, along with a discussion of the relevance of coarse grain approaches. Important considerations regarding the analysis of such simulations are also briefly presented. Chapter 3 is then dedicated to the presentation of the strategy adopted to build biologically relevant bilayer models and discusses some of the challenges associated to their characterisation. In particular, the issue of asymmetric lipid distribution is examined . Following this, Chapter 4 addresses the question of the relevance of such complex membrane models and CG MD simulations to discriminate be-

tween different CPPs by presenting comparative simulations of penetratin, a non-membrane toxic CPP, and transportan, a CPP known to induce greater membrane destabilisation. The influence of lipid composition and distribution on the collective behaviour of transportan peptides and their destabilising effect on the membrane is then investigated in Chapter 5. The next and final results chapter, Chapter 6, subsequently builds on these results to focus on lipid flip-flops and presents a detailed characterisation of this specific type of membrane perturbation. Future perspectives to expand on the work presented, as well as remaining challenges, are then outlined in Chapter 7 along with some preliminary work building on the computational framework established in the previous chapters.

Chapter 2

Theory and methods

This chapter introduces the theoretical background to the molecular dynamics (MD) simulations performed in this thesis. In particular, an overview of important technical aspects of their implementation is given. Additionally, the strategy adopted to analyse such simulations is presented.

2.1 Molecular dynamics simulations

Molecular dynamics simulations were first used in the late 1950s to study the behaviour of atoms using a hard-sphere model [192, 193]. Following the continuous development of computational techniques, simulations have now become an established tool to study biological systems, alongside experimental techniques [194]. In this regard, the recent award of the 2013 Nobel Prize in Chemistry to Karplus, Levitt, and Warshel for "Development of Multiscale Models for Complex Chemical Systems" recognises the importance of *in silico* approaches [195]. Molecular modelling methods and their applications rely on a number of physical and mathematical principles which have been the subject of extensive reviews [196, 197]. This section focuses on the concepts most relevant to the work presented in this thesis.

2.1.1 Classical description of biomolecular systems

Biomolecular systems can be described at various scales, from detailed representations where electrons are explicitly represented to more simplified models focusing on their mesoscopic properties [198]. Historically, in MD simulations atoms are treated as particles with a point charge and connected by harmonic potentials. Interactions between particles in this "ball and spring" model are governed by molecular mechanics (MM) where forces are deterministic and derive from simple potential energy functions [199]. The dynamical behaviour of a collection of N such particles is then followed using the set of $3N$ second order coupled differential equations provided by the classical Newtonian equations of motion:

$$m_i \ddot{\mathbf{r}}_i = \mathbf{F}_i \tag{2.1}$$

where m_i refers to the mass of the ith particle, $\mathbf{r}_i$ to its position and $\mathbf{F}_i$ to the force exerted on it[1]. In particular, $\mathbf{F}_i$ is given by:

$$\mathbf{F}(\mathbf{r}_i) = -\nabla V(\mathbf{r}_i) \tag{2.2}$$

where $V(\mathbf{r}_i)$ corresponds to the value of the potential energy of the particle i at $\mathbf{r}_i$ as determined by the molecular mechanics model. The application of this approach to the study of protein dynamics was pioneered by eg McCammon and coworkers in 1977 [200] and the next section details the functional forms of the potentials describing the interactions between particles in the simulations performed here.

2.1.2 The force field

Molecular mechanics force fields consist of the set of equations and associated parameters describing the characteristics of atoms and their interactions. Over the years many force

[1] Vectors are printed in bold and dots indicate their derivative with respect to time.

fields have been developed for biomolecular simulations and a recent comparative study of the most widely used ones illustrated their ability to provide a realistic description of the molecules studied [190]. While the values of the parameters and the methods to obtain them may differ, the mathematical formalism used remains similar. In particular, the potential energy function is calculated as the sum of bonded and non-bonded interactions:

$$V = V_{bonded} + V_{non-bonded} \tag{2.3}$$

whose respective functional forms are detailed below.

Bonded interactions

Bonded interactions restrain the relative motion of covalently linked particles. As such, they are calculated using two-, three- or four-atom potentials for bond stretching, bond angle and bond torsion:

$$V_{bonded} = \sum_{i,j} V_{bond}(\mathbf{r}_i, \mathbf{r}_j) + \sum_{i,j,k} V_{angle}(\mathbf{r}_i, \mathbf{r}_j, \mathbf{r}_k) + \sum_{i,j,k,l} V_{torsion}(\mathbf{r}_i, \mathbf{r}_j, \mathbf{r}_k, \mathbf{r}_l) \tag{2.4}$$

The stretching of the bond between two atoms i and j separated by a distance $r_{ij} = |\mathbf{r}_i - \mathbf{r}_j|$ is represented by a harmonic potential:

$$V_{bond}(r_{ij}) = \frac{1}{2} k^b_{ij} (r_{ij} - b_{ij})^2 \tag{2.5}$$

where b_{ij} is the reference bond length (eg obtained from crystal structures) and k^b_{ij} its spring constant. Similarly, the bond angle vibration between a triplet of atoms is described by:

$$V_{angle}(\theta_{ijk}) = \frac{1}{2} k^\theta_{ijk} (\theta_{ij} - \theta^0_{ij})^2 \tag{2.6}$$

where θ_{ij} is the bond angle and θ^0_{ij} its reference value.

Bond torsions are described using dihedral angle potentials between four i, j, k, l atoms, whereby the dihedral angle corresponds to the angle between the normal vectors of the (ijk) and the (jkl) planes. The potential associated to proper dihedral angles, ϕ_{ijkl}, relies on a periodic function of the form:

$$V_{dihedral}(\phi_{ijkl}) = k_\phi(1+\cos(n\phi_{ijkl}-\phi_{ref})) \tag{2.7}$$

Additionally, improper dihedral angles, denoted ξ_{ijkl}, and a harmonic potential are also implemented as per the following equation:

$$V_{improper}(\xi_{ijkl}) = \frac{1}{2}k_\xi(\xi_{ijkl}-\xi_{ref})^2 \tag{2.8}$$

in order to prevent out of plane bending of planar groups such as rings as well as inversion of tetrahedral geometries.

Non-bonded interactions

Non-bonded interactions between atoms may be described by additive pairwise interactions including contributions from a Lennard-Jones potential V_{LJ} and a Coulomb potential V_C:

$$V_{non-bonded}(\mathbf{r}_i) = \sum_{j\neq i} V_{LJ}(\mathbf{r}_i,\mathbf{r}_j) + \sum_{j\neq i} V_C(\mathbf{r}_i,\mathbf{r}_j) \tag{2.9}$$

The Lennard-Jones potential corresponds to short range interactions and applies to all particles. It contains a repulsion term in $(1/r)^{12}$ and a dispersion (attractive) term in $(1/r)^6$:

$$V_{LJ}(r_{ij}) = 4\varepsilon_{ij}\left[\left(\frac{\sigma_{ij}}{r_{ij}}\right)^{12} - \left(\frac{\sigma_{ij}}{r_{ij}}\right)^{6}\right] \tag{2.10}$$

where the depth of the potential well and the distance at which the potential is zero are respectively determined by ε_{ij} and σ_{ij} for the pair of atoms considered.

Additionally, charged particles also interact via long-range electrostatic interactions given by the Coulomb potential:

$$V_C(r_{ij}) = \frac{1}{4\pi\varepsilon_0}\frac{q_i q_j}{\varepsilon_r r_{ij}} \tag{2.11}$$

where q_i and q_j represent the particles charges, ε_0 the dielectric permittivity of vacuum and ε_r the relative dielectric constant of the environment.

Importantly, the calculation of non-bonded interactions raises issues regarding which atoms should be considered as interacting with each other in order to avoid artefacts while ensuring computational efficiency. Because of their short-range nature, interactions described by the Lennard-Jones potential can be neglected beyond a certain cutoff distance, typically in the order of 1 nm. In contrast, long-range electrostatic interactions are more problematic and discussed in more details in the next section.

2.1.3 Algorithms and simulation techniques

Having presented the theoretical framework and the functional forms of the equations governing the interactions of particles, this sections focuses on how MD simulations are carried

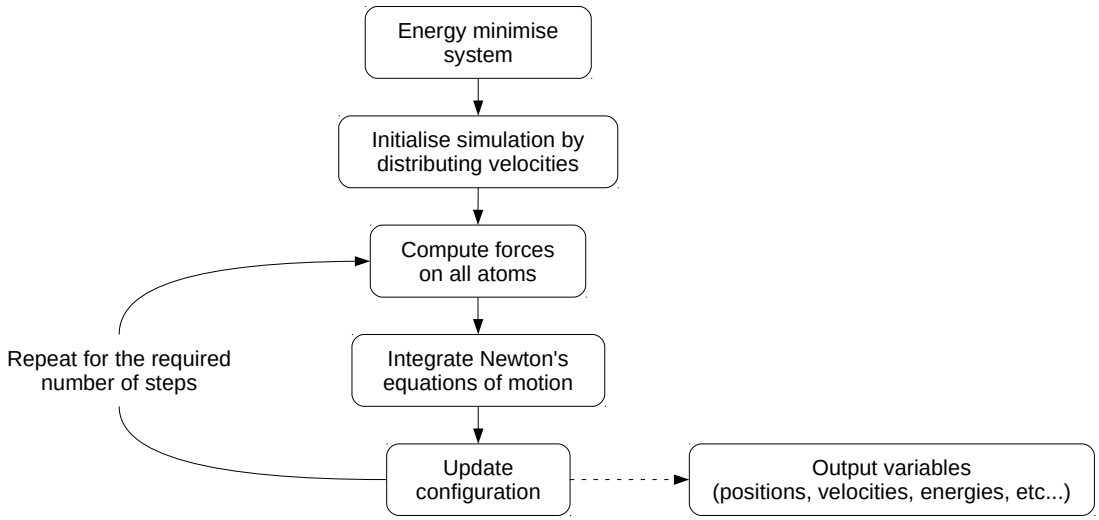

Figure 2.1 Flow chart summarising the successive operations performed in MD simulations.

out in practice. The overall algorithm is illustrated in Figure 2.1 and important practical aspects and concepts associated to its implementation are discussed below. More precisely, all the simulations performed in this thesis were executed with the Groningen Machine for Chemical Simulations (GROMACS) package [201, 202], of which an in-depth technical presentation can be found in [203].

Energy minimisation

An initial energy minimisation step is often required to optimise the starting configuration of the system to study. This is not based on a dynamic study of the system but consists of an optimisation procedure whereby the position of the atoms are slightly adjusted so as to reach a nearby local minimum in the potential energy landscape determined by the molecular mechanics force field presented above. This process allows the system to be simulated to "relax" and to avoid starting the study of its dynamics behaviour with intractably high forces due, for instance, to steric clashes.

This is particularly important when the initial configuration is obtained by artificial positioning of the molecules such as when two lipid monolayers are overlaid on each other (Chatpers 3 and 4) or a large system is created by replication of a smaller one (Chapters 5 and 6). The steepest descent algorithm, one of the most common energy minimisation techniques [196], has been used throughout this thesis.

Integrating the equations of motion

Finite difference methods to numerically solve Newton's equations of motion were developed by Verlet in the 1960s [204]. The Verlet approach relies on the forwards and backwards Taylor expansion in time of the coordinates $\mathbf{r}_i(t)$ of a particle i, respectively given by:

$$\mathbf{r}_i(t+\Delta t) = \mathbf{r}_i(t) + \dot{\mathbf{r}}_i(t)\Delta t + \ddot{\mathbf{r}}_i(t)\frac{\Delta t^2}{2} + \mathscr{O}(\Delta t^3) \tag{2.12}$$

and:

$$\mathbf{r}_i(t-\Delta t) = \mathbf{r}_i(t) - \dot{\mathbf{r}}_i(t)\Delta t + \ddot{\mathbf{r}}_i(t)\frac{\Delta t^2}{2} + \mathscr{O}(\Delta t^3) \tag{2.13}$$

Adding these two expressions and combining them with Equation 2.1 yields the Verlet position-update relation:

$$\mathbf{r}_i(t+\Delta t) = 2\mathbf{r}_i(t) - \mathbf{r}_i(t-\Delta t) + \frac{\Delta t^2}{m_i}\mathbf{F}_i(t) \tag{2.14}$$

All simulations presented in this thesis were performed using the leap-frog integrator [205], a variant of the Verlet algorithm which provides similar performances but scales more efficiently for large systems such as those presented in Chapter 7 [203]. In this approach, positions and velocities are respectively updated at integer time steps and integer-plus-a-half time steps, hence "leap-frogging" over each other.

An estimate of the velocity $\dot{\mathbf{r}}_i(t)$, based on values of the position $\mathbf{r}_i$ separated by a time interval of $2\Delta t$, can be obtained by subtracting Equation 2.13 from Equation 2.12:

$$\dot{\mathbf{r}}_i(t) = \frac{\mathbf{r}_i(t+\Delta t) - \mathbf{r}_i(t-\Delta t)}{2\Delta t} \tag{2.15}$$

It follows that velocities values at integer-minus-a-half or integer-plus-a-half time steps can be evaluated using positions at integer time steps separated by an interval Δt, and are respectively given by:

$$\dot{\mathbf{r}}_i\left(t - \frac{\Delta t}{2}\right) = \frac{\mathbf{r}_i(t) - \mathbf{r}_i(t-\Delta t)}{\Delta t} \tag{2.16}$$

and:

$$\dot{\mathbf{r}}_i\left(t + \frac{\Delta t}{2}\right) = \frac{\mathbf{r}_i(t+\Delta t) - \mathbf{r}_i(t)}{\Delta t} \tag{2.17}$$

Rearranging Equation 2.17 then yields the expression used to update positions in the leap-frog algorithm:

$$\mathbf{r}_i(t+\Delta t) = \mathbf{r}_i(t) + \dot{\mathbf{r}}_i\left(t + \frac{\Delta t}{2}\right)\Delta t \tag{2.18}$$

The relationship to update velocities is obtained by first expanding $\mathbf{r}_i(t+\Delta t)$ in Equation 2.17 using Equation 2.14, which leads to:

$$\dot{\mathbf{r}}_i\left(t+\frac{\Delta t}{2}\right)=\frac{\mathbf{r}_i(t)-\mathbf{r}_i(t-\Delta t)}{\Delta t}+\frac{\Delta t}{m_i}\mathbf{F}_i(t) \tag{2.19}$$

and then, based on Equation 2.16, to the following expression:

$$\dot{\mathbf{r}}_i\left(t+\frac{\Delta t}{2}\right)=\dot{\mathbf{r}}_i\left(t-\frac{\Delta t}{2}\right)+\frac{\Delta t}{m_i}\mathbf{F}_i(t) \tag{2.20}$$

Temperature and pressure coupling

In molecular mechanics force fields, the forces exerted on particles are conservative. Consequently, integration of the equations of motion as described above for a system of N particles whose interactions in a simulation box of volume V are governed by such a force field will lead to conservation of the system's total energy:

$$E_{tot}=E_{pot}+E_{kin} \tag{2.21}$$

where E_{pot} corresponds to the potential energy function defined in Equation 2.3 and E_{kin} to the system's total kinetic energy. Direct application of molecular dynamics under these conditions leads to an NVE ensemble (constant number of particles, constant volume, constant energy). However, it is preferable to maintain these two parameters at biologically relevant values in order to facilitate comparison with experimental conditions. Accordingly, several algorithms, such as the Nosé-Hoover thermostat [206, 207] or the Parrinello-Rahman barostat [208], have been developed to implement such NPT ensembles [209, 210].

In the simulations described in this thesis, temperature control was achieved using the Berendsen thermostat [211]. Following the equipartition theorem, the instant temperature

$T(t)$ of a system of N particles is related to its kinetic energy as follows:

$$E_{kin}(t) = \frac{1}{2}\sum_{i=1}^{N} m_i \left|\dot{\mathbf{r}}_i(t)^2\right| = \frac{3}{2}Nk_BT(t) \tag{2.22}$$

where k_B is the Boltzmann constant. The Berendsen thermostat maintains the system's temperature around the desired T_{ref} value by coupling it to an external heat bath. This involves scaling the particles velocities at each time step such that the corresponding rate of change of the system's temperature is proportional to its deviation from that of the bath:

$$\frac{dT}{dt} = \frac{T_{ref} - T(t)}{\tau} \tag{2.23}$$

where the parameter τ determines the strength of the coupling and the speed at which deviations from the reference temperature T_{ref} are allowed to relax.

Likewise, the Berendsen barostat [211] was used to control the system's pressure. It relies on the approach devised by Andersen [212]. In essence, the method is similar to that used for temperature coupling with deviations of the pressure in the system from the reference pressure controlled by a compressibility matrix β and a relaxation constant. Notably, it involves rescaling of the length of the simulation box vectors and can lead to important changes in the volume and shape of the simulation box if the system simulated deforms significantly. Importantly however, rescaling can be performed semi-isotropically so that coupling in the (x,y) plane is not correlated to that in the z direction, which ensures a zero surface tension can be achieved for planar bilayers.

Time steps

The time step Δt used in the numerical integration scheme of the equations of motion, as per Equation 2.18 and Equation 2.20, is a crucial parameter of MD simulations. While a small step is desirable for an accurate description of the dynamics of the molecules studied,

it comes at the expense of an increased computational cost which limits the timescale accessible. Conversely, a too large time step introduces greater error and may lead to instabilities and termination of the simulations. In this regard, MD simulations are commonly started with a small time step which is progressively increased to the desired value. This technique, detailed in Chapter 3, allows to avoid instabilities following the initial random attribution of velocities to particles corresponding to the temperature at which the system is simulated.

Importantly, to ensure minimum accuracy and stability, the time step should be smaller than the time constant associated to the fastest motion in the system. As such, the rapid vibration frequency of bonds involving hydrogen atoms are usually the limiting factor and constraint algorithms have been developed to overcome this problem and ensure a set of desired parameters always satisfy their equilibrium values without having to reduce the speed of the simulations [213]. Crucially however, such a limitation inherently depends on the resolution with which biomolecular systems are represented, and time steps used in MD simulations typically range from 1 fs to 40 fs. It should also be mentioned that the interpretation of the simulation time scales depends on the resolution of the model used to describe the biomolecular system simulated. In detailed atomistic representations the time scale is well defined and the simulation time can be considered to correspond to experimental time, as evidenced by properties such as water diffusion coefficients or comparison of long time scale simulations of ion channels and electrophysiology experiments [214–217]. On the other hand, as discussed further in 2.2.1, in more abstract, reduced resolution models interpretation of how the simulation time relates to actual experimental time is more complex. In this thesis a 20 fs time step was used, which is a standard value for coarse grain simulations.

Position restraints

It is possible to drastically limit the motion of some particles by defining position restraints. In GROMACS this is achieved by imposing a harmonic restraint potential around the refer-

ence position. It is especially useful when, as in Chapter 4, a molecule is manually inserted into a lipid bilayer since it allows to maintain it in the desired orientation and conformation while the neighbouring molecules adjust their position as the system equilibrates.

Periodic boundary conditions

Periodic boundary conditions (PBC) are used to better approximate physical behaviour by simulating systems containing a relatively small number of particles as if they were in a homogenous bulk phase. Here, a cubic simulation box was used for all simulations and so a particle moving outside of the box at one face re-entered it with the same velocity at the opposite face. When using PBC the distance between particles in the simulation box is determined via the minimum image convention. As illustrated in Figure 2.2, this convention can be easily conceptualised by imagining there is a copy of the simulation box along each of its face. Consequently, along a given axis the maximum possible distance separating two particles in the system studied is equal to $L/2$ where L represents the dimension of the simulation box along that axis. Accordingly, the larger the system the less its structural deformation, such as long wavelength undulations, are limited by PBC. This is a particularly relevant point for the large scale simulations presented in Chapter 7. Also of practical importance for the simulations presented in this thesis, another consequence of the minimum image convention is that determining the coordinates of the centre of geometry of several particles is not straightforward, especially when studying aggregates of multiple molecules that span the simulation box boundaries. This issue is addressed in Chapter 5.

As mentioned previously, non-bonded interactions described by the Lennard-Jones potential (Equation 2.10) are short-range and become negligible after a distance of approximately 1 nm, which is well below the size of typical simulation boxes in any dimension. Pairs of particles interacting with each other via Lennard-Jones interactions can thus easily be identified using the minimum image convention, as shown in Figure 2.2. On the other

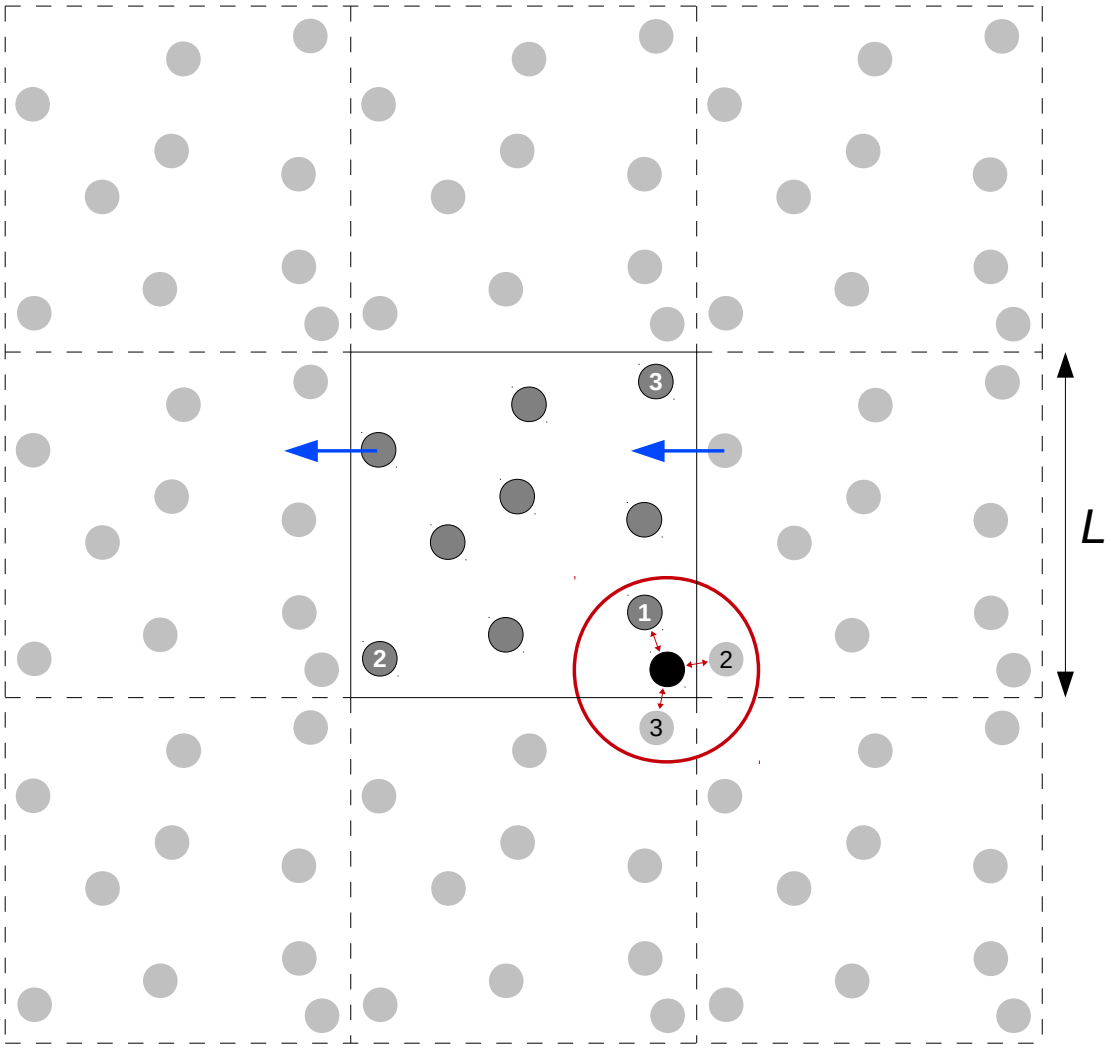

Figure 2.2 Schematic representation of periodic boundary conditions (PBC) in two dimensions. The central square represents the simulation box containing the particles studied (solid lines, dark grey), while periodic images along each face are represented by the adjacent squares and their content (dashed lines, light grey). The blue arrow indicates how a particle leaving the simulation box from one face reenters by the opposite face with the same velocity. The implementation of the minimum image convention to determine interacting pairs of particles within a cut-off distance (red circle) is illustrated by the red arrows which indicate the three particles that interact with the black one.

hand, the effect of long-range electrostatic interactions governed by the Coulomb potential (Equation 2.11) extends beyond the characteristic dimensions of the simulation box and neglecting their contribution after $L/2$ can lead to artefacts [218–220]. A common strategy used to treat these electrostatic interactions is described below.

Particle Mesh Ewald

The calculation of long-range electrostatic interactions between atoms explicitly represented in a comparatively very small simulation box constitutes an important challenge in MD simulations. Here I present the important concepts that underpin the popular Particle Mesh Ewald (PME) technique used to address this problem [221]. Interestingly, this method relies on a strategy developed by Ewald almost a century ago, well before the advent of computers, in order to calculate electrostatic energies in ionic crystals [222]. In particular, the approach devised by Ewald fundamentally relies on the periodicity of the system studied. In this case, the total Coulomb potential of a charge q_i located at the position $\mathbf{r}_i$ in the unit cell can be expressed as:

$$V_C(\mathbf{r}_i) = q_i \Phi_{tot}(\mathbf{r}_i) = \frac{q_i}{4\pi\varepsilon_0\varepsilon_r} \sum_n {\sum_j}' \frac{q_j}{|\mathbf{r}_i - n\mathbf{r}_j|} \tag{2.24}$$

where $\phi_{tot}(\mathbf{r}_i)$ is the total electrostatic potential at $\mathbf{r}_i$, with the sums over j and n respectively representing contributions from all the charged particles in the unit cell and their periodic copies. Importantly, the distance $|\mathbf{r}_i - n\mathbf{r}_j|$ represents the distance between the charge q_i and the charge q_j without taking into account the minimum image convention. Accordingly, the $'$ symbol indicates that $j \neq i$ when $n = 0$, meaning that q_i does not interact with itself. However, q_i does interact with periodic copies of itself. While, by definition, the assumption of periodicity is appropriate for crystal structures its relevance to MD simulations is less straightforward and involves considering the simulation box as a unit cell repeated infinitely in all directions. This can be envisioned as an extension of the PBC represented in Figure 2.2, leading to an infinite array of periodic images. Consequently, this approach takes into account the electrostatic interactions of each particle with periodic images of the biomolecular system simulated. Nevertheless, although all such long distance interactions are not necessarily biologically relevant, they allow a better estimation of the long range effect of electrostatic interactions than the use of cutoffs.

As a $1/r$ function, the infinite sum in Equation 2.24 converges very slowly towards the electrostatic potential ϕ_{tot}. To overcome this problem, Ewald devised an efficient summation technique based on the simple observation that for any given function f:

$$\frac{1}{r} = \frac{f(r)}{r} + \frac{1-f(r)}{r} \tag{2.25}$$

and that a judicious choice of f could then allow to split the slow converging expression in Equation 2.24 into two rapidly converging sums. This is akin to *adding* and *subtracting* a suitable charge distribution around the position $\mathbf{r}_j$ of each point charge q_j. In particular, considering a gaussian charge density $\rho_j(r) = q_j \mathrm{e}^{-(\alpha r)^2}$, solving Poisson's equation:

$$\nabla^2 \Phi_j = -\frac{\rho_j}{\varepsilon_0 \varepsilon_r} \tag{2.26}$$

leads to the corresponding electrostatic potential:

$$\Phi_j(\mathbf{r}_i) = \frac{1}{4\pi\varepsilon_0\varepsilon_r} \frac{q_j erf\left(\alpha|\mathbf{r}_i - \mathbf{r}_j|\right)}{|\mathbf{r}_i - \mathbf{r}_j|} \tag{2.27}$$

where $erf()$ indicates the error function defined by:

$$erf(x) = \frac{2}{\sqrt{\pi}} \int_0^x \mathrm{e}^{-t^2} \mathrm{d}t \tag{2.28}$$

and it follows that, taking into account the respective potential contributions due the *addition* and *subtraction* of such Gaussian charge distributions around the q_j charges, the total electrostatic potential defined in Equation 2.24 can be expressed as:

$$\Phi_{tot}(\mathbf{r}_i) = \frac{q_i}{4\pi\varepsilon_0\varepsilon_r} \sum_n {\sum_j}' \left[\frac{q_j}{|\mathbf{r}_i - n\mathbf{r}_j|} + \frac{q_j erf\left(\alpha|\mathbf{r}_i - n\mathbf{r}_j|\right)}{|\mathbf{r}_i - n\mathbf{r}_j|} - \frac{q_j erf\left(\alpha|\mathbf{r}_i - n\mathbf{r}_j|\right)}{|\mathbf{r}_i - n\mathbf{r}_j|} \right] \quad (2.29a)$$

$$= \frac{q_i}{4\pi\varepsilon_0\varepsilon_r} \sum_n {\sum_j}' \left[\frac{q_j erf\left(\alpha|\mathbf{r}_i - n\mathbf{r}_j|\right)}{|\mathbf{r}_i - n\mathbf{r}_j|} + \frac{q_j erfc\left(\alpha|\mathbf{r}_i - n\mathbf{r}_j|\right)}{|\mathbf{r}_i - n\mathbf{r}_j|} \right] \quad (2.29b)$$

where $erfc(x) = 1 - erf(x)$ is the complementary error function.

Using Ewald technique, the total electrostatic potential can thus be calculated as the sum of two potentials:

$$\Phi_{tot}(\mathbf{r}_i) = \Phi_{dir}(\mathbf{r}_i) + \Phi_{rec}(\mathbf{r}_i) \quad (2.30)$$

where Φ_{dir} and Φ_{rec} are respectively defined by:

$$\Phi_{dir}(\mathbf{r}_i) = \frac{q_i}{4\pi\varepsilon_0\varepsilon_r} \sum_n {\sum_j}' \frac{q_j erfc\left(\alpha|\mathbf{r}_i - n\mathbf{r}_j|\right)}{|\mathbf{r}_i - n\mathbf{r}_j|} \quad (2.31)$$

and:

$$\Phi_{rec}(\mathbf{r}_i) = \frac{q_i}{4\pi\varepsilon_0\varepsilon_r} \sum_n {\sum_j}' \frac{q_j erf\left(\alpha|\mathbf{r}_i - n\mathbf{r}_j|\right)}{|\mathbf{r}_i - n\mathbf{r}_j|} \quad (2.32)$$

Due to the very fast convergence of the $ercf()$ function towards 0, the Φ_{dir} potential can easily be obtained by *direct* calculation of the sum in Equation 2.31 and application of a short cutoff of approximately 1 nm. Crucially, this direct approach is possible because the influence of charges not located in the direct vicinity of q_i is now effectively negligible due to the $erfc\left(\alpha|\mathbf{r}_i - n\mathbf{r}_j|\right)$ term. In contrast, the sum in Equation 2.32 remains very slowly convergent as the $erf()$ function rapidly converges to 1 and thus the Φ_{rec} potential cannot be calculated directly. However, it can be noted that Φ_{rec} corresponds to the electrostatic potential created by the Gaussian charge distributions ρ_j that were *added* to the system, and, bearing in mind the periodic structure of the system, Ewald's technique then involves using

Fourier transforms to solve the corresponding Poisson equation (see Equation 2.26) in the reciprocal Fourier space. Details regarding the mathematical derivation of the method can be found in [223] but the expression eventually obtained is of the form:

$$\Phi_{rec}(\mathbf{r}_i) = \frac{q_i}{4\pi\varepsilon_0\varepsilon_r}\sum_k \frac{\widetilde{\rho}(k)}{|k^2|}\mathrm{e}^{i\mathbf{k}\cdot\mathbf{r}_i} \tag{2.33}$$

where the sum over k indicates a sum over reciprocal space vectors and $\widetilde{\rho}(k)$ corresponds to the Fourrier coefficient of the Gaussian charge distributions *added* to the system and can be expressed as:

$$\widetilde{\rho}(k) = S(k)\mathrm{e}^{-\left(\frac{k}{4\alpha}\right)^2} = \left(\sum_j q_j \mathrm{e}^{-i\mathbf{k}\cdot\mathbf{r}_j}\right)\mathrm{e}^{-\left(\frac{k}{4\alpha}\right)^2} \tag{2.34}$$

where $S(k)$ represents the structure factor of the system and is calculated over the charges present in the unit cell only. Crucially, thanks to the terms in $1/k^2$ and e^{-k^2}, the *reciprocal* space sum converges rapidly towards Φ_{rec}. The relative speed of convergence of the direct and reciprocal sums in Equation 2.31 and Equation 2.33 depends on the width of the Gaussian charge distributions used and is controlled via the parameter α.

Several such Ewald summation schemes have been implemented and their respective performances are reviewed in [224]. The PME technique interpolates the distribution of charges q_j in the system onto a regular grid, or mesh, which allows to use very computationally efficient fast fourier transform (FFT) algorithms to calculate the structure factor $S(k)$ [221]. This approach achieves an overall $\mathscr{O}(Nlog(N))$ efficiency, where N is the number of charged particles in the system, scaling better than simple $\mathscr{O}(N^2)$ Ewald techniques.

2.2 Coarse grain simulations

The set of equations and techniques described in the previous section represent a generic approach to simulate interactions of particles within a biomolecular system based on a "ball and spring" model. As mentioned in 2.1.1, although historically developed at an atomistic

resolution, such a model can also be used with a reduced resolution description of the system of interest. Such lower resolution approaches, where interacting particles (the "balls") represent larger groups of atoms, are referred to as coarse grain representations. While the notion of bonded and non-bonded interactions may be more abstract than in the case of atomistic representations it is important to realise that interactions between coarse grain particles can be described using the same mathematical formalism. In this section, the respective merits of using different resolution approaches are briefly reviewed before then focusing on the coarse grained model used for the simulations presented in this thesis.

2.2.1 Multiscale approaches: choosing the appropriate resolution

The molecular events underpinning biological processes occur on different scales of time, length and energy. Therefore, a suitable representation of the biomolecular system studied must be chosen in order to be able to appropriately investigate the properties of interest [225, 226]. For instance, highly detailed description where all atoms are explicitly included are useful to examine small confined systems such as the selectivity filter of ion channels and provide insights into the atomistic interactions governing the permeation of ions into such channels [227, 228]. The CHARMM36 [229] and OPLS-AA [230] force fields are two such *all-atom* force fields commonly used to study lipid and/or protein systems while the AMBERff99 [231] all-atom force field is preferred for nucleic acids. In case the ionisable nature of the molecules studied is of paramount importance, further detailed force fields taking into account polarisability have also been developed [232]. Conversely, in *united-atom* force fields, such as GROMOS53a6 [233], non-polar hydrogen atoms are not explicitly represented but rather combined into a single particle with their parent carbon atom. As a consequence, the total number of interactions to calculate in lipid systems is greatly reduced and the computational cost of MD simulations significantly decreased. In biomolecular systems where they are unlikely to be relevant to the properties investigated, the partial

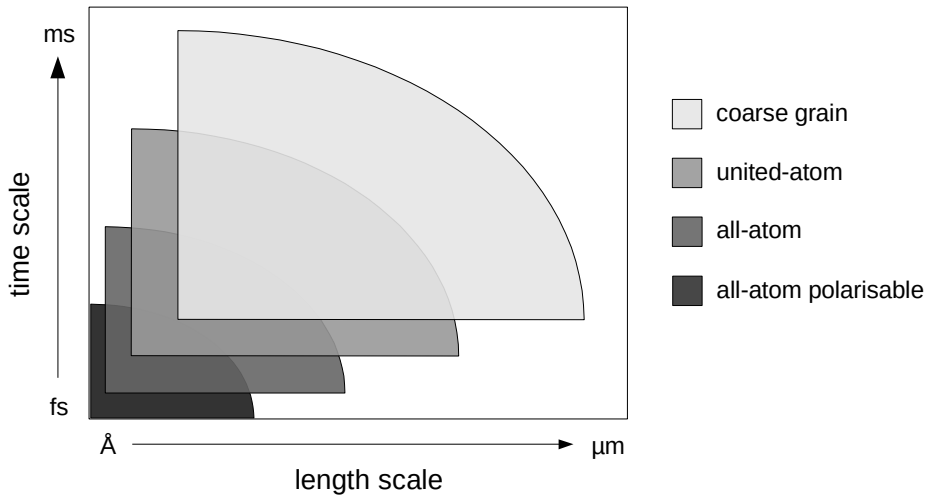

Figure 2.3 Schematic representation of temporal and spatial scales typically accessible by MD simulations.

sacrifice of such atomistic details therefore allows to simulate larger systems for longer, as illustrated in Figure 2.3.

In coarse grain (CG) approaches, representation of biomolecules is simplified by merging groups of atoms into a smaller number of CG sites. In recent years, several CG models have been developed for the study of lipid and/or protein systems with typically three to five heavy (non hydrogen) atoms being mapped to a single CG particle [234–238]. Importantly, such reduced resolution models effectively lead to smoothing of the potential energy landscape as the fastest degrees of freedom are removed from the system. As mentioned earlier in 2.1.3, this makes it possible to use a larger time step for integration of the equations of motion than in atomistic models, where it is usually limited to approximately 2 fs, and CG models remain stable with values of up to 40 ns. Together with the drastically decreased number of interactions, this allows to achieve a speed-up of 2 or 3 orders of magnitude in simulations and the enhanced dynamics of CG MD allow to efficiently sample temporal and spatial scales otherwise inaccessible (Figure 2.3). However, it is important to bear in mind that the interpretation of such CG time scales is not straightforward as it is difficult to assess how they effectively relate to atomistic time scales or actual experimental times. Indeed,

while smoothing of the energy landscape allows for its faster sampling the corresponding speed-up is unlikely to be the same for all degrees of freedom [239]. Consequently it is difficult to define the speed-up factor achieved compared to atomistic simulations and "real time" as it depends on the system studied and/or the property of interest. For instance, in the MARTINI CG force field, described in more details below, a speed-up factor of about 4 was estimated based on the lateral diffusion of lipids and transmembrane peptides [240, 241] but for other compounds it was found to be up to 17 [242] while phase separation events were observed to occur about 40 times faster than in atomistic simulations [243]. Therefore, although a multiplication factor is sometimes applied to such CG time scales to report an effective time scale [244, 245], one must remain aware that CG time scales should be interpreted with care. Nevertheless, it remains that the speeding up of the kinetics of the biomolecular system of interest achieved by CG representations allows convenient investigation of phenomenon difficultly observable in atomistic resolution. Accordingly, coarse grain models involving a higher level of abstraction, where for instance lipid molecules are only described by 3 particles, have also been developed in order to make the simulation of very large systems tractable [246–248]. However, such representations do not explicitly reproduce specific molecular interactions and are more suitable to the study of mesoscopic properties [226]. For the investigation of the interactions of cell-penetrating peptides with lipid bilayers, which is the subject of this thesis, it is desirable to not totally abstract from the chemical features of the species studied and to retain some molecular and structural details. In this regard, a few hybrid approaches mixing CG and atomistic models have been developed with the intent to improve computational efficiency of MD simulations while retaining a local detailed representation of the molecules of interest [249–251]. Although these are potentially promising techniques, their implementation for complex systems, such as multiple peptides interacting with a lipid bilayer, remains problematic [252]. In contrast, it is relatively straightforward to convert coarse-grained structures back to atomistic repre-

sentations [253–255]. This allows to adopt a serial multiscale approach where the enhanced dynamics and scales of CG MD and the atomic details provided by atomistic simulations can complement each other. The power of such a strategy is for instance demonstrated in a study by Schulten and co-workers where the serial combination of atomistic and CG representations contributed to provide insights on how the cooperative interactions of BAR domains could induce membrane bending [256].

In this thesis, simulations were performed using the CG force field initially parametrised for lipids by Marrink and co-workers in 2004 [237]. This force field was updated and renamed the MARTINI force field in 2007 [240], and later extended to include protein parameters [257]. Since then it has successfully been used in a wide range of studies of lipid and/or protein systems [242]. As described in the following section, it is a comparatively high resolution CG model and as such is well suited to perform systematic MD simulations of medium size systems that explore the molecular interactions of multiple cell-penetrating peptides with complex membrane models.

2.2.2 The MARTINI force field

Comparison with atomistic force fields

In the MARTINI force field an average 4:1 mapping of heavy atoms to CG particles is used, with the property of each CG particle depending on those of the atoms it represents. As illustrated in Figure 2.4, this mapping scheme allows to retain a certain degree of chemical details for the molecules modelled. The model is based on the building block principle ie on the assumption that carefully parametrised individual beads, via reproduction of the properties of small building block molecules, can be stringed together to appropriately describe larger molecules. The parametrisation of the MARTINI force field then relies on comparison with more detailed atomistic simulations and reproduction of experimental data [237, 240]. For instance, partitioning free energies between aqueous and organic phases of amino

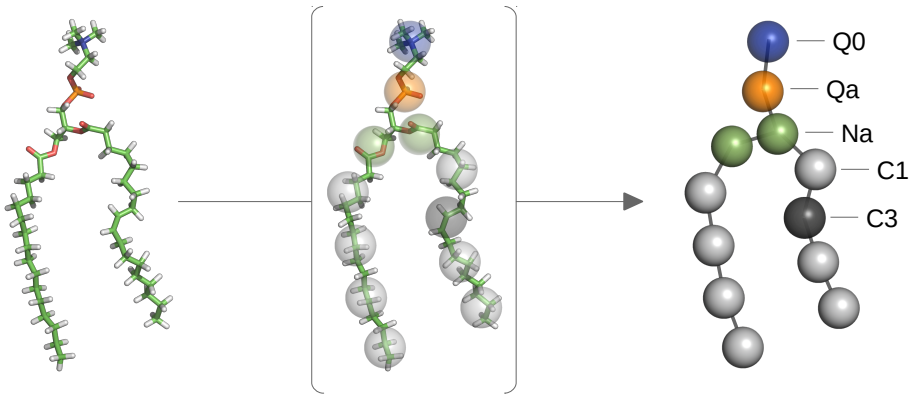

Figure 2.4 Schematic representation of the coarse graining of a phosphatidylcholine lipid with palmitoyl and oleoyl acyl tails (POPC) in the MARTINI force field. Nitrogen atoms are represented in blue, phosphorous in orange, oxygen in red, carbon in green and hydrogen in white. Similarly, CG beads are coloured according to the type attributed to the particle. In particular, while all aliphatic atoms are represented by apolar particles of type C, the unsaturation in the oleoyl chain is taken into account with a bead of higher polarity (C3). The zwitterionic nature of the phosphatidylcholine head group is also reproduced in the CG lipid model, with the choline (Q0) and phosphate (Qa) beads respectively bearing a charge of $+1$ e and -1 e. Coarse grain bonds are shown as dark grey lines.

acid side chain analogues as well as their dimerisation free energies are matched within 1-2 kT compared to atomistic profiles [258]. The area per lipid, which is of importance for lipid bilayer simulations, is typically reproduced within 0.2 nm^2 or experimental accuracy of experimental values [237, 240]. The modelling of peptides molecules, of particular interest as well for the work presented in this thesis, also compares favourably with experimental data as evidenced by several simulation studies: the relative binding free energy of a systematic series of pentapeptides to membrane interface was found to be consistent with the experimental hydrophobicity scale derived from these peptides [259], the dimerisation free energies of transmembrane helices were calculated to be within the range of experimental values derived from FRET data [260] and the structure of a glycophorin dimer satisfyingly reproduced NMR data [261]. Recently, parameters of the force field were further refined to better match structural properties derived from the Protein Data Bank (PDB) and/or obtained via atomistic MD simulations [257]. Although the focus of this thesis is on the interactions of peptides with phospholipids, it should be stressed that the MARTINI

force field can be used to model other biomolecules such as carbohydrates [262], glycolipids [263], polymers [264, 265] or nanoparticles [266, 267] and DNA fragments [268, 269], hence providing a comprehensive tool to perform CG MD simulations of biologically relevant systems. A comprehensive overview of the variety of applications of this particular coarse grain approach can be found in [242]. Interestingly, one of the initial applications of the extension of the MARTINI force field to the modelling of proteins included simple simulations of antimicrobial peptides that successfully compared to previous observations from atomistic simulations [257].

As for atomistic force fields, interactions between CG particles in the MARTINI force field are described using the formalism presented in 2.1.2. The following sections present the different types of particles involved in the model as well as the approach taken to implement efficient calculation of their interactions.

Particle types

The MARTINI model relies on four main types of CG particles in order to capture the chemical nature of the underlying atomic structure. These types are respectively labeled polar (P), apolar (C), non-polar (N) and charged (Q). Accordingly, hydrophilic groups of atoms are represented with polar particles while hydrophobic ones are modelled with apolar particles. The non-polar type represents an intermediate between polar and apolar particles and is used for mixed groups of atoms that are partly polar and partly apolar. Importantly, particles of type Q are only intended for groups bearing full, or close to full, charges such as phosphate or ammonium groups. These main particle types are further broken down into subtypes to allow for a more accurate representation of the molecules modelled. In the case of types N and Q, a letter is used to distinguish their different hydrogen-bonding abilities (d = donor, a = acceptor, da = both donor and acceptor and 0 = neither donor nor acceptor). Similarly, the degree of polarity of types P and C is indicated by a number between 1 (low

polarity) and 5 (high polarity). Figure 2.4 illustrates how these different particle types are used to model a glycerophospholipid. Additionally, a special class of ring particles based on a higher 3:1 or even 2:1 mapping was developed to preserve the geometry of cyclic groups. Particles within this modified set are indicated by a prefix "S" (eg SP1) and are useful to represent compounds such as aromatic residues or sterols.

Using this set of particle types, amino acids are described by a backbone particle and up to 4 additional particles to model their side chains. Due to their small size alanine and glycine residues are represented by a single backbone particle. The mapping used for the side chains of the remaining residues is described in Table 2.1. It should be noted that the types of backbone particles are set depending on the local secondary structure of the protein. The polar character of the backbone in disordered structures, such as coils or bends, is modelled by CG particles of type P. Conversely, the effect of interbackbone hydrogen bond networks in more ordered helical or sheet-like structures is taken into account by using significantly less polar particles of type N. Finally, four water particles are described by a single particle of type P4 and ions are represented by Q type particles which are considered to include their hydration shell. The mass of four water molecules, 72 Da, is also used to set the mass of all CG particles, with the exception of the special ring beads to which a smaller mass of 45 Da is associated in order to account for their increased resolution mapping.

Particle interactions

Bonded interactions between CG particles are modelled using harmonic potentials, as described previously in 2.1.2. In the case of proteins, the bond lengths and force constants between backbone and side chain beads or, where appropriate, between two side chain beads depend on the amino acid represented. In contrast, the bond length between backbone particles is set to 3.5 Å. However, the corresponding bond force constants and other backbone parameters such as angles and dihedrals involving only backbone beads depend

Table 2.1 Representation of residue side chains in the MARTINI force field. Ala and Gly are represented by a single backbone particle. The prefix "S" denotes a special class of particles used to model rings. Table adapted from [257].

Side chain	CG particles mapping
Leu	C1
Ile	C1
Val	C2
Pro	C2
Met	C5
Cys	C5
Ser	P1
Thr	P1
Asn	P5
Gln	P4
Asp	Qa or P3 (uncharged)
Glu	Qa or P1 (uncharged)
Arg	N0—Qd or N0—P4 (uncharged)
Lys	C3—Qd or C3—P1 (uncharged)
His	SC4—SP1—SP1
Phe	SC4—SC4—SC4
Tyr	SC4—SC4—SP1
Trp	SC4—SP1—SC4—SC4

on the secondary structure (but not on the residue type). In particular, periodic potentials (see Equation 2.7) are introduced to impose restraints on proper dihedral angles between backbone particles and maintain the protein's secondary structure. Importantly, this means that the CG approach does not allow appropriate sampling of conformational changes of protein secondary structure. Similarly, restraints can also be applied between backbones particles which are not directly connected in order to create an elastic network that prevents unfolding of the protein structure [270]. The possible impact of limited secondary structure sampling of the peptides studied is addressed in Chapter 4.

In the MARTINI force field non-bonded interactions are essentially described by a Lennard-Jones potential, as per Equation 2.10. The strength of interactions between two CG particle types i and j is indicated by the well depth of the potential, ε_{ij}, and is given

by an interaction matrix where 10 different levels are used, ranging from 2 kJ.mol^{-1} to 5.6 kJ.mol^{-1}. The same effective size $\sigma = 4.7$ Å is used for all CG beads, except again for the smaller ring particles for which 4.3 Å is used. Lennard-Jones interactions between particles are calculated within a cutoff of 12 Å and smoothly shifted to zero from 9 Å to 12 Å to avoid the generation of noise associated to the cutoff.

Additionally, charged CG particles (type Q) also interact via a Coulomb potential (Equation 2.11) which is shifted smoothly from 0 to 12 Å and where a relative dielectric constant $\varepsilon_r = 15$ is used. Here it is important to bear in mind that electrostatics interactions arising from partial charges on atoms are treated implicitly via Lennard-Jones interactions and the choice of CG particle types representing them. In this context, the explicit short-range treatment of electrostatic interactions between groups of atoms bearing an overall full charge is intended to reproduce the effect of distance dependent screening while ensuring computational efficiency. Consequences of this approach on the electrostatic properties of the biomolecules modelled are discussed in Chapter 3.

Version used and improvements

The version 2.1 of the MARTINI force field, as described in [240] and [257], was used for all the simulations performed in this thesis. It should be noted that a polarisable version of the force field has also been developed [271] in an attempt to address some of the shortcomings associated to the simplified water model and to better represent electrostatic interactions felt by charged particles in different dielectric environments. In this polarisable model, water beads are represented by a central neutral particle bound to two particles respectively carrying a positive and a negative charge. Within such a water bead the central particle is only involved in Lennard-Jones interactions while the charged particles solely interact via a Coulomb potential. This polarisable water model is able to reproduce local, environment-dependent, electrostatic screening and the global dielectric constant was re-

duced accordingly to $\varepsilon_r = 2.5$. However, it is more computationally expensive, due to the increased number of interactions calculated and the necessity to use the PME technique described earlier in order to benefit from the improved solvent description, and simulations are almost one order of magnitude slower than with the standard non-polarisable force field. This somewhat reduces the ability to take advantage of the speed-up achieved by the CG representation to perform a large number of simulations investigating different systems. Furthermore, unlike the standard MARTINI model that has been successfully used in a wide range of applications, this polarisable version has not yet been as thoroughly tested. Finally, it is also worth mentioning that updated protein parameters were recently released and are referred to as MARTINI 2.2 [272, 273]. The changes operated between MARTINI 2.2 and 2.1 essentially aimed at correcting the interactions of oppositely charged residues by introduction of an off-center charge model and at introducing polarisable beads on polar side chains, similar to the approach taken for water particles in the polarisable water model. Consequently, while the MARTINI 2.2 parametrisation corresponds to a significant improvement when using the polarisable water model to describe systems containing both negatively and positively charged residues, it should not otherwise lead to substantially different observations than those obtained with the 2.1 version for the systems presented in this thesis. Nevertheless, it is important to bear in mind differences do exist between the two force fields.

Conversely, as of the time of writing of this thesis, an implicit solvent version of the MARTINI force field was released [274]. Unlike the improvements discussed above, which aimed at addressing the shortcomings associated to coarse grain water beads compared to atomistic molecules, this represents an effort in the direction of more abstraction and, while less accurate to investigate local defects such as those of interest in this thesis, the associated computational speed-up makes this approach appropriate to study very large systems and may contribute to bridge the gap between the MARTINI force field and mesoscopic models.

2.3 Analysis of molecular dynamics simulations

The techniques described in this chapter illustrate how the dynamic properties of a biomolecular system can be simulated at the atomistic, or near atomistic, level. As such, the output of MD simulations consist of a trajectory describing the evolution with time of the coordinates of each particle represented. These can be visualised using software such as VMD [275] or Pymol [276]. While visual observation of the systems modelled is important and can provide important insights in the molecular interactions involved, it is imperative to also be able to quantitatively describe the properties of interest. Although visualisation softwares allow some degree of such analysis, they remain more suitable for qualitative exploration of the characteristics of a system. In this regard, the GROMACS package includes several tools which have been well optimised for the analysis and processing of the simulation outputs [203]. However, limiting oneself to these tools might not allow one to adequately characterise the particular properties most relevant to the biomolecular system investigated and analysis of MD simulations can benefit tremendously from the implementation of more appropriate custom approaches.

In this context, the MDAnalysis library [277] provides a valuable tool to analyse MD simulations. It allows the use of Python, a simple and powerful programming language [278], to examine and manipulate coordinates of particles in the trajectory. Rather than providing a set of ready-to-use analysis tools, this approach makes it possible to code custom metrics relevant to the system studied. In particular, this approach benefits from the performances of thoroughly tested data structures and mathematical functions, such as those provided by the NumPy package [279], that have been developed for scientific computing. Furthermore, thanks to the module based nature of Python, findings from relevant research fields, eg regarding the characterisation of geometrical features, can easily be applied to the analysis of MD simulations. Virtually all analyses presented in this thesis were performed by code

written in Python (version 2.7) and the different metrics implemented are discussed in the relevant chapters. Pymol was used to render snapshots of the molecular structures.

Chapter 3

Modelling of biologically relevant membranes

3.1 Introduction

The organisation of biological membranes as fluid lipid bilayers containing a mosaic of embedded proteins, the so-called "fluid mosaic model", was widely accepted in the early 1970s [280]. Numerous studies have since then provided further evidence that cell membranes are complex assemblies of a variety of lipids and proteins and that, far from a passive barrier with a simple compartmental role, they play an active and integral role in the regulation of many cellular processes such as signal transduction, protein aggregation or membrane trafficking [162, 281–287]. However, the ubiquitous activity of CPPs and AMPs suggests their interactions with biological membranes are not mediated by specific receptors but, rather, rely on direct interactions with the multiple lipid species present in the bilayer. The compositional differences between the inner membrane of bacteria and the plasma membrane of mammalian cells have been suggested as the origin of AMPs ability to

distinguish between prokaryotic and eukaryotic membranes and, consequently, as the reason for their *selective* disruption of bacterial membranes [43, 288–290]. Biologically relevant membrane models are therefore essential to study the interactions of CPPs with lipid bilayers. In this first results chapter I discuss the approaches taken to create such models *in silico*, after having first presented the pertinent characteristics of the plasma membrane of mammalian cells and briefly reviewed the bilayer models used experimentally and in previous MD simulations.

3.1.1 Lipid distribution

In eukaryotic cells, the membranes of most organelles exhibit an asymmetric distribution of lipid types across the bilayer [285, 291]. In particular, the highly asymmetric nature of mammalian cells membranes, or plasma membranes, has been demonstrated in 1972 by Bretscher and co-workers [292] and further characterised in numerous subsequent studies which are reviewed in [293]. However, the precise composition of such biological lipid bilayers is difficult to establish, due both to the inhomogeneous nature of plasma membranes and the limitations of the experimental techniques used [293, 294]. Consequently, uncertainties remain regarding the relative distributions of lipid species in each leaflet. These studies showed that the lipid composition of mammalian plasma membranes consists of approximately 65% glycerolipids, 10% sphingolipids and 25% sterols such as cholesterol. They also revealed that the extracellular leaflet is enriched in the choline-containing lipids, phosphatidylcholine (PC) and sphingomyelin (SM), whereas the amine-containing lipids, phosphatidylethanolamine (PE) and phosphatidylserine (PS), are almost exclusively located in the cytoplasmic leaflet (Figure 3.1). One important consequence of this lipid distribution is that the cytoplasmic leaflet of the plasma membrane is anionic in nature as the negatively charged PS lipids are exclusively found in this leaflet. It was initially proposed that asymmetrical membrane biogenesis, coupled to the fact that passive transbilayer diffusion

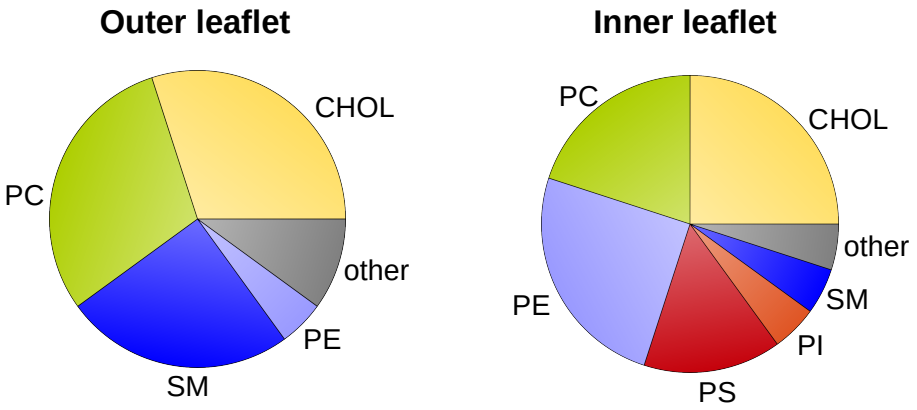

Figure 3.1 Approximate relative distribution of lipid species in the outer (extracellular) and inner (cytoplasmic) leaflets of mammalian plasma membranes. The outer leaflet is enriched in phosphatidylcholine (PC) and sphingomyelin (SM), while phosphatidylethanolamine (PE) and phosphatidylserine (PS) are preferentially located in the inner leaflet. In addition to PS, the inner leaflet also contains other minor phospholipids that are negatively charged such as phosphatidylinositol (PI). The preferential distribution of cholesterol (CHOL) remains controversial but it is abundant in both leaflets [309–311]. Other lipids in the outer leaflet include glycosphingolipids. Data aggregated from [285, 293, 296, 300, 312].

of phospholipids, or flip-flop, is a slow process with a half-time of hours to days [295–298], prevented the rapid redistribution of lipids between leaflets [299]. However, it was later revealed that the asymmetric lipid distribution is actively maintained by cells via the action of dedicated flippases [299–302]. These are enzymes which catalyse the transport of specific lipid species between leaflets. In particular, the transport of PS lipids on the external leaflet of the plasma has been shown to be involved in the early stages of apoptosis [303–305] and to be associated with various pathological conditions [306–308].

Interestingly, this asymmetric distribution of charges is in contrast with the inner membrane of Gram-negative bacteria where negatively charged lipids such as phosphatidylglycerol (PG) and cardiolipin (CL) can be found in both leaflets [313, 314]. Additionally, unlike mammalian cell membranes, bacterial membranes do not contain cholesterol [310]. These compositional differences are illustrated schematically in Figure 3.2 and have been suggested as the origin of the selective perturbation of bacterial membranes by antimicrobial peptides [43, 290]. Indeed, the haemolytic activity of AMPs was shown to be enhanced for

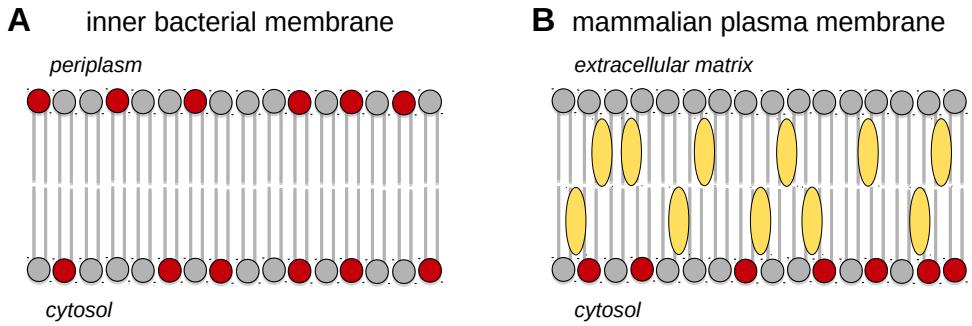

Figure 3.2 Schematic representation of the compositional differences between the lipid bilayers of (A) prokaryotic and (B) eukaryotic membranes. Cholesterol molecules are represented in yellow. The plasma membrane of mammalian cells is abundant in cholesterol (represented in yellow) and anionic phospholipids (represented in red) are exclusively found in the inner leaflet. In contrast, in inner bacterial membranes anionic lipids are distributed in both leaflets and cholesterol is generally absent. Zwitterionic lipids are represented in grey.

cholesterol-depleted erythrocytes [315], while model membranes studies involving leakage assays of liposomes in presence of AMPs demonstrated that dye release was significantly reduced in cholesterol-rich lipids mixtures [316]. This has been attributed to the "rigidifying" effect of cholesterol on lipid bilayers which render them less susceptible to peptide-induced deformations due to their increased mechanical stiffness [317, 318]. Conversely, the activity of AMPs on bacteria and some cancerous cells has been been correlated with the strong affinity of these cationic peptides for the anionic lipids exposed on the outer leaflet of the membranes of those cells [319, 320]. Epand and co-workers further showed that clustering of anionic lipids contributed to the membrane toxicity of these peptides [321]. Similarly, as discussed previously in 1.2.2, electrostatic interactions have been shown to play an important role in the activity of CPPs [91, 102] and it has been suggested that translocation could occur via an electroporation-like mechanism due to charge imbalance following the accumulation of the cationic peptides on the extracellular zwitterionic leaflet [322–324].

Altogether, these observations show that the perturbations of lipid bilayers by membrane active peptides depend on the characteristics of the target membrane in addition to that of the peptides studied. It is therefore important to use membrane models with a biologically

relevant lipid distribution in order to explore and characterise how they may be destabilised by CPPs.

3.1.2 Transmembrane potential

The lipid bilayer of the plasma membrane of eukaryotic cells also constitutes a barrier to the diffusion of ions. Ionic species are transported selectively across the hydrophobic bilayer by specialised membrane proteins and this results in a charge imbalance and a negative voltage of approximately -60 to -100 mV in the cytoplasm compared to the extracellular environment [325, 326]. This transmembrane potential is actively maintained by cells and is integral to the regulation of many cellular functions [327]. Such an electric potential gradient exerts a force towards the interior of cells on positive charges and it is therefore reasonable to imagine it may play a role in the activity of cationic membrane active peptides. This has been confirmed by several experimental studies relying on model bilayer systems which showed that the application of a transbilayer potential enhanced the translocation of CPPs into lipid vesicles [131, 328–331] or their escape from endosomes [332]. In a comparative *in vitro* and *in vivo* study involving LUVs and HeLa cells, Castanho and co-workers concluded the negative transmembrane potential across the bilayer was responsible for the internalisation of the cationic CPP studied [331]. Conversely, Wender and co-workers showed that a neutralisation of the plasma membrane potential led to a significant reduction of cellular uptake [330].

On the other hand, the application of a transmembrane voltage has also been shown to induce transient pore formation by CPPs [147], suggesting it may as well contribute to the membrane toxicity of these peptides. This is further supported by the finding of Matsuzaki and co-workers that the weak membrane potential of erythrocytes protected them from lysis by AMPs [315].

These considerations illustrate the importance of comparing membrane models with

different transbilayer electrostatic properties and how the ability to characterise the local electrostatic potential inside those lipid bilayers can be of great interest.

3.1.3 *In vitro* and *in silico* membrane models

Experimental studies involving lipids bilayers usually rely on the use of large or giant unilamellar vesicles (respectively LUVS and GUVs) as models of the cell membrane [333]. These simple systems facilitate the investigations of peptide - membrane interactions in the absence of metabolic energy and allow the study of individual parameters such as membrane curvature or lipid composition [118, 288]. In 2003 Weitz and co-workers developed a technique to engineer vesicles with an asymmetric lipid distribution, thereby mimicking cell membranes more accurately [334]. Interestingly however, *in vitro* studies of CPPs continued to rely on the use of symmetric LUVs or GUVs and although those membrane models highlighted the importance of anionic phospholipids on the behaviour of CPPs, the influence of their asymmetric distribution has been poorly investigated [98, 335, 336]. However, it is important to bear in mind that in the absence of cellular energy the passive transbilayer diffusion of phospholipids will eventually lead to asymmetry loss. The difficulty in working with asymmetric vesicles, the stability of which depends on the characteristics of the lipids head groups and the saturation of the acyl chains [337, 338], might therefore account for this observation. Nevertheless, in the last few years, progress has been made regarding asymmetric vesicles engineering that may benefit future *in vitro* investigations of membrane active peptides [339–343]. In this regard, the approach of Pooga and co-workers in a recent comparative study of several CPPs is of particular interest as they used membrane "blebbing" to obtain giant vesicles, referred to as Giant Plasma Membrane Vesicles (GPMV) or Plasma Membrane Spheres (PMS), with the same complex composition as that of the parent plasma membrane [134]. They reported an accumulation of all CPPs in the lumen of the vesicles, instead of a mere equalisation with the extravesicular peptide concentrations as ob-

served with simple LUVs and GUVs. Although further conclusions on the role of particular lipid species are rendered difficult by the complex composition of the vesicles, this study illustrates the relevance of asymmetric lipid bilayer models.

Similarly, MD simulations of membrane proteins and membrane active peptides have traditionally relied on simple, symmetric lipid bilayers [182, 227]. In a few computational investigations of membrane active peptides, multi-component systems involving both zwitterionic and anionic lipids were introduced in order to examine the preferential interactions of those peptides with different lipid species [170, 171, 344–346]. Yet, to date, only a single MD study of a CPP has been performed in the presence of an asymmetric bilayer mimicking the plasma membrane, wherein Zhen-lu and co-workers reported that the membrane asymmetry drove the translocation of poly-arginine peptides towards the inner anionic leaflet, thereby providing further evidence of the role of membrane composition on the activity of CPPs [347].

However, in recent years, in a trend somewhat similar to what has been observed regarding the development of vesicles models, several groups have published MD simulations of more sophisticated, asymmetric, plasma membrane models. In particular, full-atom representations have been used to investigate the electrostatic profiles of asymmetric bilayers with some studies using a double bilayer system to delimit two water compartments with different ionic concentrations in an effort to reproduce the transmembrane potential arising from the charge imbalance between the extracellular environment and the cell cytoplasm [348–351]. Although such approaches yielded transbilayer voltage differences in good qualitative agreement with experimental data, they remain computationally expensive and hindered by several technical issues for the correct treatment of long-range electrostatic interactions as highlighted by Gurtovenko and co-workers [351]. In contrast, coarse-grained models have recently been favoured to investigate the interplay between mechanical properties, domain formation and lipid organisation of large asymmetric bilayers [352–356]. These studies

have begun to offer molecular-level insights into the origin of the complex and dynamic properties of cellular membranes and hold the potential to provide a valuable *in silico* tool complementing high-resolution imaging techniques.

3.2 Initial approach

3.2.1 Lipid composition and distribution

In a first attempt to reproduce the main characteristics of the plasma membrane, a first asymmetric bilayer model referred to as AMv1 was built with the lipid distribution presented in Table 3.1. Notably, anionic phosphatidylserine lipids (POPS) were positioned in the inner leaflet only while sphingomyelin (PPCS) were exclusively positioned in the outer leaflet. In contrast, phosphatidylcholine (POPC) and phosphatidylethanolamine (POPE) were distributed across both leaflets, with POPE predominantly positioned in the inner leaflet.

Table 3.1 Composition of the outer and inner leaflets of the first asymmetric membrane model (AMv1). The % correspond to relative intra-leaflet distributions. Both POPC and POPE are zwitterionic lipids, while POPS has a negatively charged head group. PPCS and CERA respectively indicate sphingomyelin and ceramide.

	outer leaflet	inner leaflet
CHOL	30 %	20 %
POPC	30 %	25 %
POPE	5 %	30 %
POPS	-	25 %
PPCS	30 %	-
CERA	5 %	-

The transbilayer distribution of cholesterol (CHOL) remains a matter of debate [354, 357] and I chose to slightly increase its proportion in the outer leaflet for two reasons. First, interactions between cholesterol and sphingomyelin leading to the formation of ordered domains has been well documented [358–361]. And, second, the cytoplasmic leaflet of plasma membranes has been demonstrated to be more fluid than the extracellular one [362–

365], which has been suggested to act as a more robust outer coating [366], and it therefore seemed reasonable to attempt to reproduce this feature by including a smaller proportion of rigidifying cholesterol molecules in the inner leaflet. Finally, a few ceramide lipids (CERA) were also included in the outer leaflet as this lipid species has been shown to facilitate lateral segregation of sphingomyelin rich domains [367, 368] and to modulate the curvature of plasma membranes [369] and Brock and co-workers observed that it promoted the direct translocation of polyarginines CPPs [370]. The coarse-grained representations of these lipid species using the MARTINI force field [240] are illustrated in Figure 3.3.

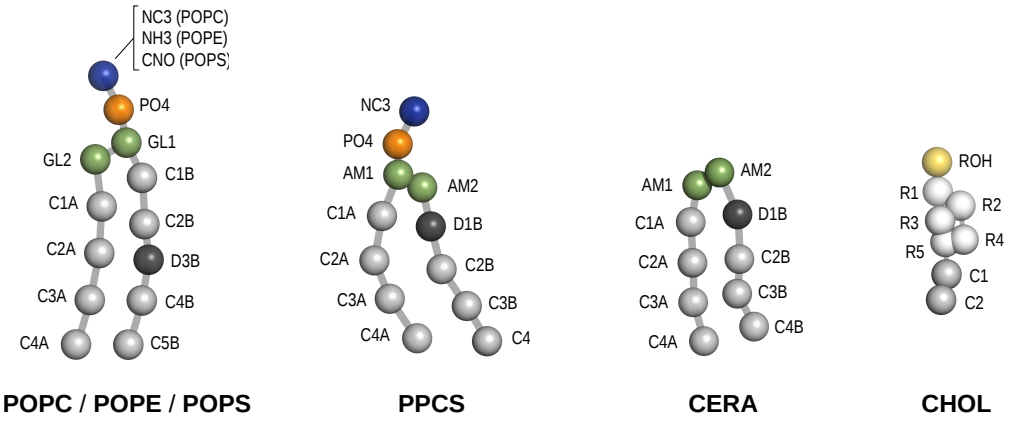

Figure 3.3 CG representations using the MARTINI model of the lipid species taken into account in the plasma membrane model used. The glycerophospholipids all have have the same Palmitoyl (saturated) and Oleoyl (one unsaturation) acyl chains with phosphatidylcholine (PC), phosphatidylethanolamine (PE) and phosphatidylserine (PS) only differing by one head group bead. The ceramide (CERA) molecule simply corresponds to sphingomyelin (PPCS) without the two head group beads. Colours highlight distinct groups of beads, in particular phosphate are shown in orange, glycerol or their sphingolipids equivalent in green and acyl chain unsaturations in black. Chemical formulas of the lipids can be found in Appendix A.

The following sections detail the simulation protocol used to set up the simulations and the results obtained as well as some of the challenges associated to the approach taken.

3.2.2 Protocol

As illustrated in Figure 3.4, the asymmetric membrane AMv1 was built by manually assembling monolayers isolated from two symmetric membranes, SMzv1 and SMav1, which

respectively had the lipid composition of the outer and inner leaflets. This approach was used previously by Berkowitz and co-workers to build a small asymmetric bilayer of 128 lipids with a united-atom model containing only cholesterol, sphingomyelin (in the outer leaflet) and phosphatidylserine (in the inner leaflet) molecules [371]. All simulations were executed using Gromacs version 4.5.4 [372] with the standard Martini 2.1 parameters [240].

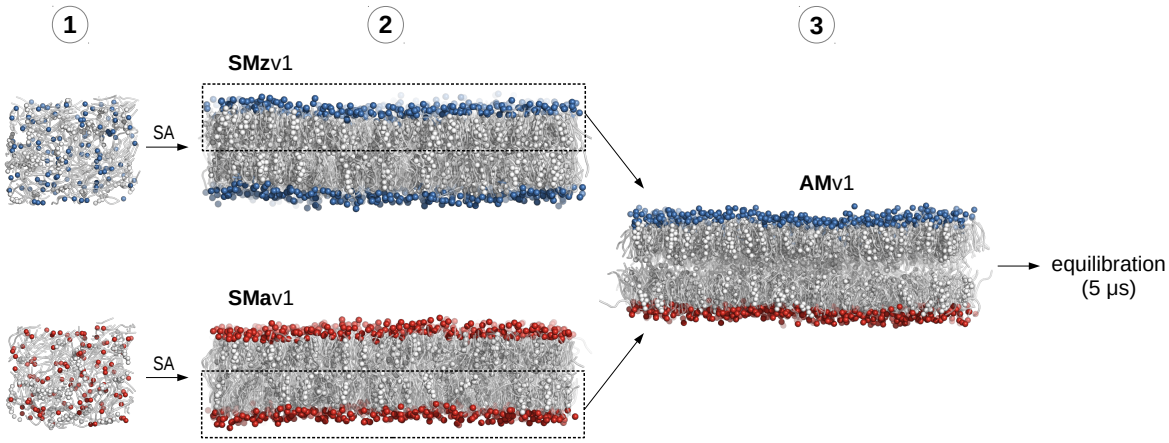

Figure 3.4 Schematic representation of the protocol followed to build the asymmetric membrane AMv1. Two symmetric bilayers, SMzv1 and SMav1, with the respective compositions of the outer (blue) and inner (red) leaflets were self-assembled separately (1). Monolayers were then extracted from these symmetric bilayers (2) and simply positioned on top of each other to build the asymmetric bilayer (3). After energy minimisation the system was run for 5 µs.

Self-assembly of symmetric membranes

The same protocol was followed for both the SMzv1 and SMav1 membrane. First, 1360 lipids were positioned into a $22 \times 22 \times 9$ nm simulation box, with the mixture of species corresponding to the composition of either the outer or inner leaflet of the plasma membrane (Table 3.1). Next, in order to ensure formation of the membrane in the x,y plane the box was extended to 14 nm in the z direction and the system was then solvated with counter ions added as appropriate to achieve a neutral total charge. Following energy minimisation the systems were equilibrated by successively running 10,000 iterations with increasing time steps (0.5 fs, 1 fs, 2 fs, 4 fs, 10 fs and 20 fs), after which a production run of 1 µs

using a 20 fs time step was performed. The temperature was kept constant at 323 K by separately coupling the lipids and solvent to a heat bath using the Berendsen algorithm [211] with a coupling constant $\tau_T = 1$ ps. The system pressure was semi-isotropically coupled in the bilayer plane x,y and along the bilayer normal z, using the Berendsen algorithm at 1 bar with a coupling constant $\tau_P = 1$ ps and a compressibility of 5×10^{-6} bar^{-1} in each direction. In both cases the lipids self-assembled within tens of nanoseconds and the length of the simulations thus ensured the bilayers were fully equilibrated. No lipid clustering was observed in either membrane.

Manual assembly of the asymmetric bilayer

Using the last frames of the SMzv1 and SMav1 simulations, two leaflets extracted from the self-assembled bilayers were manually positioned on top of each other in order to create the asymmetric AMv1 bilayer. As previously, the simulation box was extended to 14 nm and the bilayer was solvated and neutralised by adding the required number of sodium counterions. The resulting final system contained 1305 lipids, 24748 water particles (non polarisable) and 161 Na^+ ions. After energy minimisation it was progressively equilibrated following the same iterative procedure as above. A production run of 5 µs was then performed, using the same simulation parameters as detailed previously.

Here it may be worth stressing that although some of the CG simulations reported in the literature involve a 0.15 M NaCl salt concentration in an attempt to more faithfully reproduce physiological conditions (see for instance [356]), it is common practice to simply neutralise the charge of the system. This may be justified by the limitations of the modelling of electrostatics interactions in the MARTINI force field, as a cutoff of 1.2 nm is used in conjunction with a uniform screening (dielectric constant set to 15). Furthermore, Sansom and co-workers showed that salt concentration had a negligible effect on the interactions of membrane active peptides with a zwitterionic bilayer in both CG and full-atom

simulations [373]. Additionnally, given the relatively short-range or electrostatic forces in the MARTINI model, I was concerned that the use of a salt concentration would contribute to screen the anionic nature of the inner leaflet and "hide" negatively charged lipids from cationic CPPs in future simulations. Nevertheless, it remains important to correctly neutralise the system as several studies have demonstrated that a non null charge can lead to membrane-destabilising artefacts [178, 179, 374].

3.2.3 Results

The resulting asymmetric membrane is presented in Figure 3.5. Although the lipid bilayer was simulated for 5 µs (see details in next section) no domain formation was observed in either leaflet, with the distributions of lipids being similar to Figures 3.5B & C in both the initial and final frames. The absence of co-clustering between sphingomyelin and cholesterol molecules is at odds with the nano-domains observed experimentally [375, 376] and likely to reflect the limitations of the MARTINI model for these lipids. Indeed, although the sphingolipids parameters have been made available by the Marrink group for several years they are still listed as experimental (http://md.chem.rug.nl/cgmartini/images/parameters/ITP/martini_v2.0_lipids.itp) and, to date, their propensity to induce cholesterol rich domains has yet to be confirmed in a computational study, similarly to what was recently carried out for glycolipids [263]. In particular, it is possible that the hydrogen bonding pattern thought to be important in stabilising sphingomyelin and cholesterol interactions [377, 378] is not adequately reproduced by the beads types modelling sphingomyelin amide and hydroxyl groups. However, uncertainties remain on the origins of the preferential interactions of cholesterol with sphingolipids [379]. Additionally, the coarse grained representation may not be able to properly capture the minor difference between the acyl chains of sphingomyelin and that of the glycerophospholipids [371] as previous computational studies relying on the MARTINI force field showed that phase separation in the

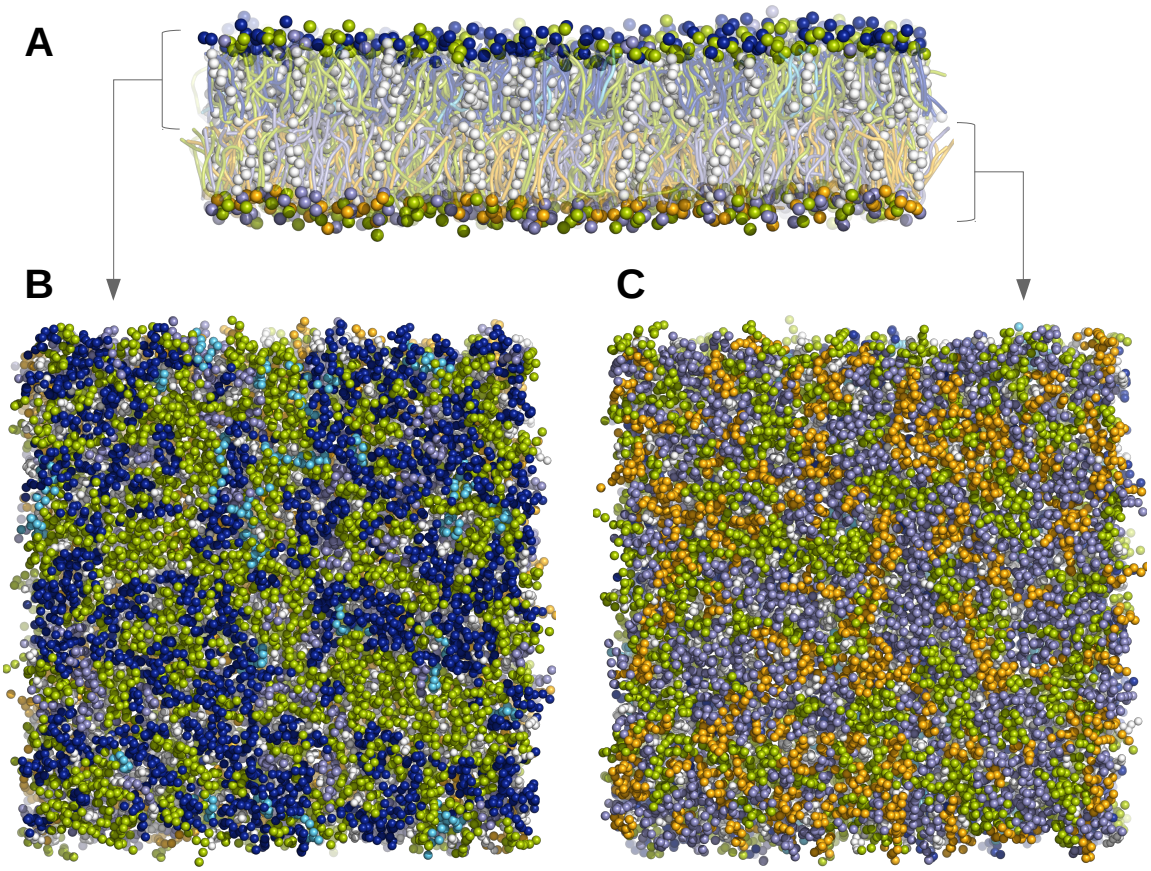

Figure 3.5 Snapshots of the asymmetric membrane AMv1. (A) Side view of the bilayer oriented with the outer (extracellular) leaflet upwards; the phosphate bead of each phospholipid is shown as a sphere, lipids tails as transparent cartoon and cholesterol as white spheres. (B) & (C) top view of the outer and inner leaflet respectively, with all lipids represented as solid spheres. Species are coloured as follows: phosphatidylcholine (POPC) in green, sphingomyelin (PPCS) in dark blue, ceramide (CERA) in cyan, phosphatidylethanolamine (POPE) in purple, phosphatidylserine (POPS) in orange and cholesterol (CHOL) in white. In (B) and (C) cholesterol molecules are predominantly hidden by the phospholipids head groups as they sit deeper in the bilayer, between the lipids acyl chains.

presence of cholesterol only occurred between lipids with both chains saturated and lipids with both chains unsaturated [353, 380–382].

3.2.4 Challenges

Despite the successful building of an asymmetric bilayer mimicking the composition of mammalian cells plasma membrane, the approach followed exposed some practical issues which are detailed below.

Area mismatch between leaflets

The area of the equilibrated SMzv1 membrane was found to be approximately 10% smaller than that of the SMav1 one (337.5 nm^2 and 371.4 nm^2 respectively). Combined with the need to avoid steric clashes between the acyl tails, this mismatch rendered adequate overlaying of the extracted zwitterionic and anionic leaflets difficult. As illustrated in Figure 3.6A, they would either drift apart or the bilayer would buckle with empty regions between the two monolayers. Interestingly, these observations are in agreement with experimental studies showing that a difference in lateral pressure between leaflets triggered by an area mismatch as low as 5% can lead to vesicle rupture and collapse [383, 384]. Here, both leaflets were extracted from bilayers containing the same total number of lipids but the zwitterionic membrane had a smaller number of phospholipids due to the higher percentage of cholesterol and hence a smaller area. To remediate this problem, the desired relative distribution of species was maintained but the total number of lipids in the anionic membrane was reduced until its area approximately matched that of the zwitterionic membrane (Figure 3.6B). This was achieved using 1224 lipids instead of 1360, so that the lower and upper leaflets of the AMv1 bilayer initially contained 620 and 685 lipids respectively. A similar method was adopted by Vachá and co-workers in a MD study using a united-atom model [350].

Evolution of lipids distribution: the challenge of cholesterol

The simulations revealed rapid transbilayer diffusion, or flip-flop, of cholesterol molecules. This interleaflet mobility is illustrated in Figure 3.7 and is consistent with experimental evidence that, unlike for phospholipids, spontaneous transmembrane diffusion of sterols and fatty acids occur rapidly in biological membranes [309, 385, 386]. Indeed, numerous *in vitro* studies using live cells and vesicles have investigated the characteristic timescale of cholesterol flip-flops and half-times in the order of milliseconds [387], seconds [388] or minutes [385, 386, 389] have been suggested. In contrast, in a recent small-angle neutron

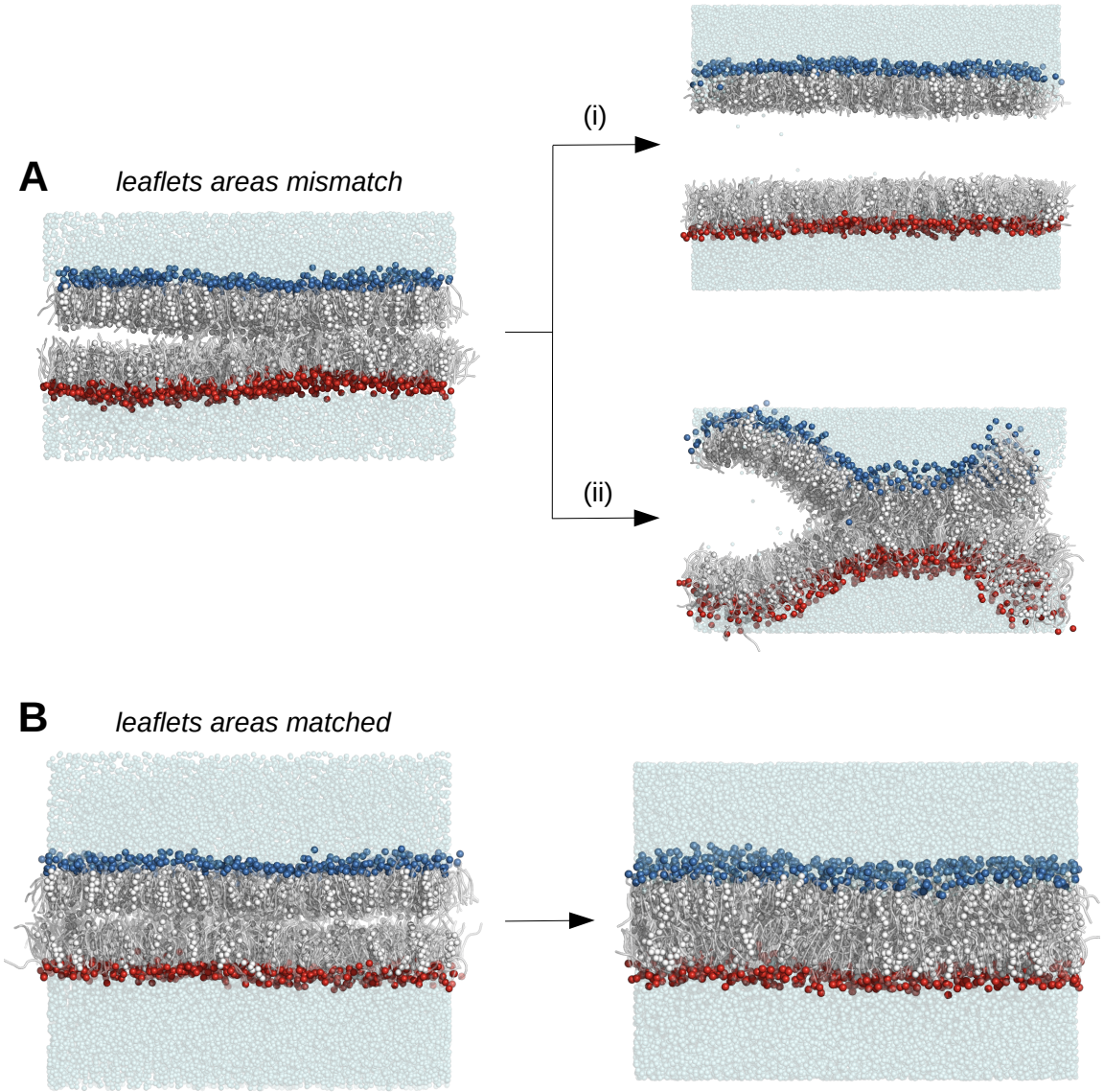

Figure 3.6 Importance of matching monolayers areas in order to build stable bilayers. (A) The smaller number of phospholipids due to the relatively higher percentage of cholesterol led to a smaller surface for the zwitterionic leaflet (blue) compared to that of the anionic one (red) and prevented formation of a stable membrane. The monolayers either drifted apart (i) or only partially joined to form a bilayer where buckled regions of the membrane where separated by vacuum (ii). (B) A stable bilayer rapidly formed after manual overlaying of two leaflets with matching surfaces. Phospholipid tails are shown as cartoons in transparent grey while cholesterol molecules are represented by solid white spheres. Water particles are shown as small transparent spheres in light cyan.

scattering (SANS) study Garg and co-workers deducted a half-time of several hours [390] but their methodology has been disputed and it is now generally agreed that unfacilitated cholesterol flip-flop occurs on a sub-second timescale [391, 392]. This is supported by several computational studies relying on CG MD [354, 393–395], atomistic MD [394, 396–398] or implicit model simulations [399] which all estimate cholesterol residence time to be in the order of micro to milliseconds. On the other hand, no phospholipid flip-flops were observed, in agreement with previous simulations of lipid bilayers [400] and their slower (hours to days) passive transbilayer diffusion observed experimentally [297, 298]. Ceramide lipids were not observed to flip-flop either which is also consistent with both experimentally derived residence time of tens of minutes [401] and MD simulations showing their flip-flop rate was 2 or 3 orders of magnitude slower than that of cholesterol [395, 397].

As illustrated in Figure 3.8A, this inter-leaflet mobility led to a redistribution of cholesterol molecules between the outer and inner leaflets of the AMv1 membrane. This led to two issues. First, a direct consequence was that the initial percentages of cholesterol in each leaflet (respectively 30% and 20%) could not be maintained. Indeed, the relative enrichment of the outer leaflet decreased within the first couple of hundred nanoseconds of

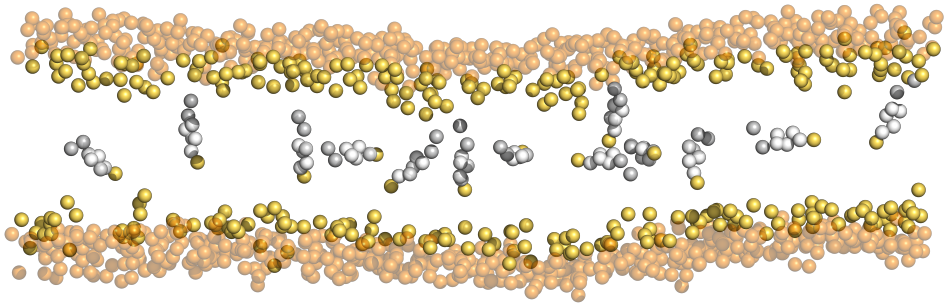

Figure 3.7 Side view snapshot of the AMv1 membrane illustrating the transbilayer mobility of cholesterol. Phosphate groups are shown as transparent orange spheres while the hydroxyl group of cholesterol is shown as solid yellow. For clarity solvent and phospholipids tails are omitted and only the cholesterol molecules present in the core of the bilayer are represented in full (as white and grey spheres). Cholesterol sits between the phospholipids acyl chains and is able to flip-flop between leaflets. Although it can be transiently stabilised when in a horizontal orientation in the inter-leaflet plane, flip-flop events were fast and completed within tens of nanoseconds at most.

the simulation as a net diffusion of cholesterol molecules towards the inner leaflet was observed (dashed rectangle in Figure 3.8A). This is in agreement with atomistic simulations performed by Choubey and co-workers wherein an initial imbalance in cholesterol concentration between the two leaflets was compensated by subsequent flip-flops [398]. After this initial redistribution, cholesterol concentrations in the outer and inner leaflets of the AMv1 membrane oscillate around approximately 28% and 22.5% respectively. While these numbers are close to the desired compositions, the difference nonetheless highlights the difficulty of controlling cholesterol composition in a membrane model. This leads to the second issue, namely the question of knowing whether the final cholesterol distribution in the AMv1 bilayer corresponds to a meaningful equilibrium state. Indeed, while it is possible that preferential interactions of cholesterol molecules with specific lipid species drive the partial asymmetry maintained, the redistribution of cholesterol is also limited by the creation of an area mismatch between the leaflets. Interestingly, in [398] equipartition of the number of cholesterol molecules was not observed either. However, the authors found that the redistribution of cholesterol led to an equalisation of the lateral pressure profiles and bending free energies of the two leaflets. Consequently, they concluded that cholesterol flip-flops allowed to relieve mechanical stress in the lipid bilayer. This hypothesis is further supported by the experimental work of Bruckner and co-workers who showed that rapid interleaflet diffusion of cholesterol mediated stress relaxation in lipid vesicles [387]. Besides this mechanically driven nature of cholesterol flip-flops, lipid-lipid interactions have also been demonstrated to play a role in cholesterol distribution. In particular, experimental studies showed that, in addition to its strong affinity for sphingomyelin [375, 376], cholesterol had a strong preference for lipids with saturated acyl chains as polyunsaturated chains prevented its stable orientation between the lipids tails [402]. Cholesterol distribution in biological membranes therefore appears to be the result of a complex balance between its preferential interactions with the lipid species present in each leaflet and mechanical constraints.

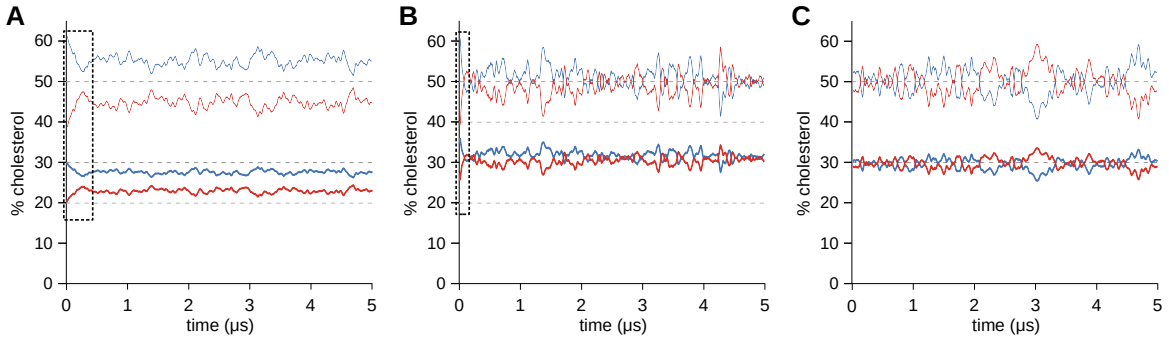

Figure 3.8 Evolution of cholesterol distribution in (A) the AMv1 membrane, (B) a POPC bilayer initially containing twice as much cholesterol in the upper leaflet than in the lower one, and (C) an asymmetric bilayer initially containing 30% of cholesterol in each leaflet with an equal mixture of POPC and PPCS in the upper leaflet and an equal mixture of POPC, POPE and POPS in the lower one. Cholesterol concentrations in the upper and lower leaflets are represented by blue and red lines respectively, with intra-leaflet ratios shown as thick lines and inter-leaflet ratios as thin lines. Dashed lines indicate initial intra-leaflet percentages and the 50% inter-leaflet ratio. Ratios were calculated by performing a rolling average on successive frames over 40 ns. The greater fluctuations in (B) and (C) are due to the smaller number of lipids ($\sim$200) in those systems compared to (A) ($\sim$1300). The dashed rectangles in (A) and (B) highlight the rapid initial redistribution of cholesterol molecules.

Although the destabilising effect of chain unsaturation has been satisfyingly reproduced in both atomistic and CG MD simulations, with flip-flop rates increasing by a couple orders of magnitude in bilayers with two polyunsaturated chains [354, 393, 394], it is unlikely to be of influence in the AMv1 membrane where all glycerophospholipids share the same palmitoyl and oleoyl chains. However, in a CG MD study by Yesylevskyy and co-workers using a simple asymmetric bilayer model with the MARTINI force field, cholesterol was also observed to preferentially distribute in the anionic leaflet [354]. This is at odds with the final distribution observed in Figure 3.8A and suggests other factors prevented full re-distribution of the cholesterol molecules in the AMv1 model. Using united-atom MD simulations, Bennett and co-workers showed that the flip-flop rate of cholesterol was dramatically reduced in the presence of a raft-like bilayer containing sphingomyelin lipids, with residence half-times increasing from microseconds to minutes [397]. It is thus tempting to hypothesise that, despite the absence of domain formation, preferential interactions with sphingomyelin were responsible for the final asymmetric distribution of cholesterol in the CG AMv1 bilayer.

In order to separately investigate the influence of mechanical stress and membrane composition on cholesterol distribution, I built two smaller (∼200 lipids) control systems using the same protocol as described in Figure 3.4. First, a simple POPC bilayer containing an equal number of phospholipids in each leaflet but twice as many cholesterol molecules in the outer one (∼40%) than in the inner one (∼20%) was assembled to study the effect of imbalance between leaflets lateral pressure. Second, the relative affinity of cholesterol for anionic lipids and sphingomyelin was investigated by assembling a bilayer containing the same number of cholesterol (∼30%) and phospholipids molecules in each leaflet, with an equal mixture of POPC and PPCS in the outer leaflet and an equal mixture of POPC, POPE and POPS in the lower leaflet. Both bilayers were simulated for 5 µs with the same parameters as detailed in 3.2.2 and the evolution of cholesterol distribution in each system is represented in Figure 3.8B & C respectively. In both cases equidistribution of cholesterol was observed. In particular, the initial concentration imbalance in the POPC bilayer disappeared within approximately the first 100 ns of the simulation and neither leaflet of the more complex bilayer was enriched in cholesterol. Although it might be argued that the effect of sphingomyelin and negatively charged lipids exactly counter-balanced each other this is unlikely. Rather, these results highlight the limitations of CG representations and suggest that, unlike atomistic models, the MARTINI force field does not appropriately reproduce the preferential interactions of sphingomyelin with cholesterol.

The final asymmetric distribution of cholesterol in the AMv1 membrane therefore appears as a consequence of mechanical constraints preventing complete redistribution of the molecules. It is difficult to assess to what extent this is an artefact due to the bilayer composition or assembly protocol used but it raises questions regarding the significance of the mechanical properties of the membrane obtained. This is a particularly relevant problem if, as is the case in this thesis, membrane destabilisation and perturbations induced by CPPs are later to be examined.

The need for simplicity

The ceramide lipids included in the model did not facilitate the formation of sphingomyelin rich domains, unlike what is observed experimentally [367, 368]. The AMv1 bilayer obtained therefore consists of a single fluid phase. In this context, its composition complexity may hinder the investigations of the role of specific lipid species in the presence of CPPs. Indeed, due to the very small concentrations of POPE and CERA in the outer leaflet (5%, see Table 3.1), only approximately 30 lipids of each of these species are present and their sampling probability by the peptides would be low. As for the inner leaflet, although all phospholipid species are well represented, their different concentrations (respectively 20%, 25% and 30%) would render it difficult to identify preferential peptide-lipid interactions from diffusional sampling of the lipids population. A lipid bilayer with a simpler composition, focused on reproducing the asymmetric distribution of anionic lipids in the plasma membrane of mammalian cells, may therefore be more informative and suitable to the systematic investigation of the role of each lipid species. Similarly, the influence of cholesterol rich ordered domains on the behaviour of membrane-active peptides could be more appropriately investigated using simple phase separating systems [357, 381, 382].

3.3 A working model

In order to mitigate the issues mentioned in the previous section, a simpler asymmetric bilayer model of the plasma membrane was developed using a different assembly technique. Thereafter this new model will simply be referred to as the AM model.

3.3.1 New composition

A simplified lipid composition was chosen and is presented in Table 3.2. Unlike in the AMv1 model, cholesterol molecules were initially equally distributed in each leaflet. Ad-

ditionally, sphingomyelin and ceramide lipids were removed altogether from the model as their presence did not lead to domains formation. Instead, the concentration of phosphatidylethanolamine lipids (POPE) was increased in the outer leaflet, in order to address the sampling issues mentioned previously, and a simple 1:4 ratio was chosen with respect to phosphatidylcholine lipids (POPC). Finally, in the inner leaflet, those two lipids species were distributed in a simple 1:1:1 mixture with the anionic phosphatidylserine lipids (POPS) so that the three phospholipid types were present in equal concentration.

Table 3.2 Initial lipid composition of the outer and inner leaflets of the second asymmetric membrane model (AM). The % correspond to relative intra-leaflet distributions. Both POPC (phosphatidylcholine) and POPE (phosphatidylethanolamine) are zwitterionic lipids, while POPS (phosphatidylserine) has a negatively charged head group.

	outer leaflet	inner leaflet
POPC	60 %	25 %
POPE	15 %	25 %
POPS	-	25 %
CHOL	25 %	25 %

3.3.2 New protocol

To avoid the issues associated with manual assembly of two monolayers, a method was developed to easily create a membrane with the desired lipid composition in each leaflet from a simple pure POPC bilayer. In this approach, detailed in [403], a POPC bilayer with the desired number of lipids is first self-assembled as described previously and randomly chosen POPC lipids are then replaced by the different lipid species in order to achieve the desired composition in each leaflet. The process is illustrated in Figure 3.9 along with the resulting distribution of lipids in the outer and inner leaflets of the AM model. This new bilayer contained 1116 lipids and, as before, was solvated using water and counterions only in a simulation box measuring approximately 14 nm in the z direction. After energy minimisation, the asymmetric membrane thus obtained was progressively equilibrated following the

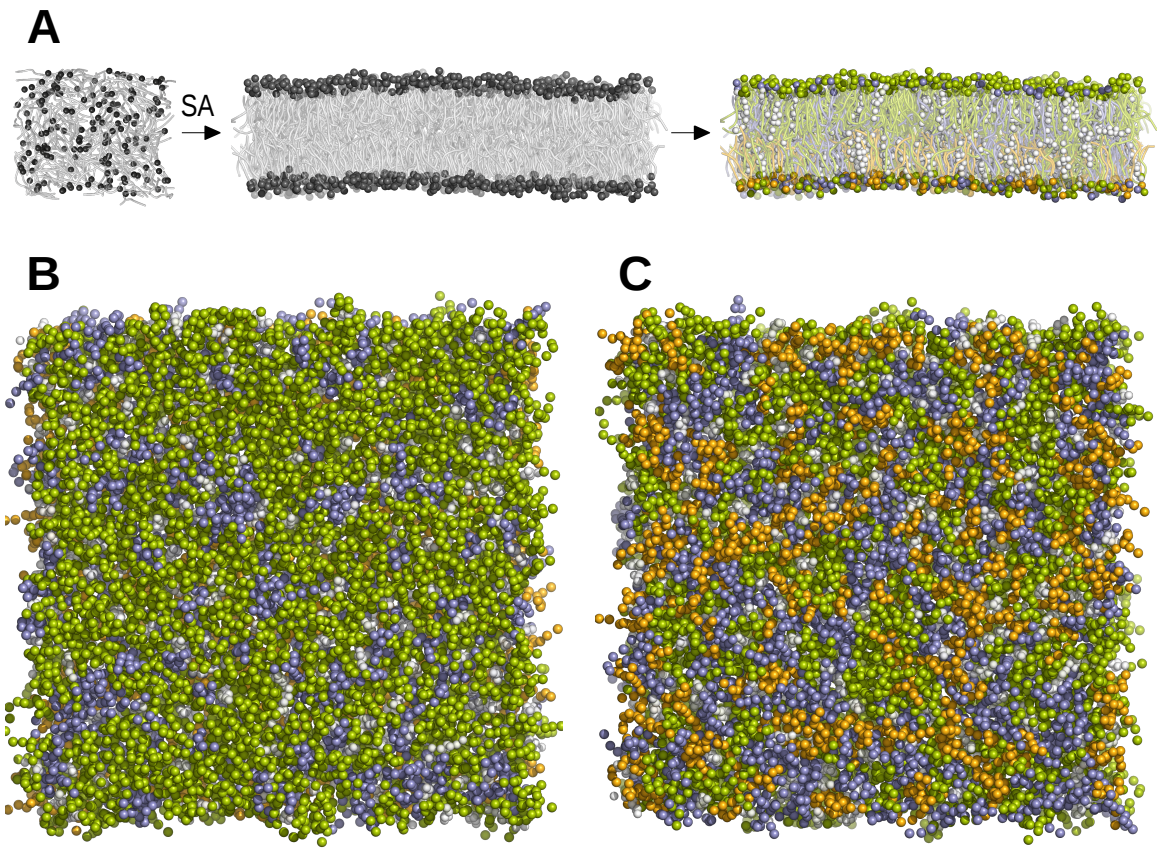

Figure 3.9 Protocol followed to create the AM model and resulting lipids distribution. (A) A pure POPC bilayer containing 1116 lipids is self-assembled. POPC lipids are then randomly replaced by other lipid species, according to the method detailed in [403], in order to achieve the desired composition. Phosphate beads are shown as spheres, lipids tails as transparent cartoon and cholesterol as white spheres. (B) & (C) top view of the outer and inner leaflets of the AM bilayer, with all lipids represented as solid spheres. Species are coloured as follows: phosphatidylcholine (POPC) in green, phosphatidylethanolamine (POPE) in purple, phosphatidylserine (POPS) in orange and cholesterol (CHOL) in white. In (B) and (C) cholesterol molecules are predominantly hidden by the phospholipids head groups as they sit deeper in the bilayer, between the lipids acyl chains. For clarity the pure POPC bilayer is represented in grey in (A).

iterative procedure previously described and a production run of 15 µs was then performed, using the same simulation parameters as detailed in 3.2.2. Recently, similar approaches have been developed and made available to build complex lipid bilayer for both all-atom [404] and united-atom [405] representations. In 2014, the Marrink group also released such a tool for the CG MARTINI force field[1].

[1] http://md.chem.rug.nl/cgmartini/index.php/insane

3.3.3 Free energy barrier to cholesterol flip-flop

The evolution of the distribution of cholesterol was again examined and is presented in Figure 3.10A. Overall, cholesterol molecules were found to remain essentially equidistributed for the duration of the simulation performed, with flip-flops in one direction counter-balanced by those occurring in the other. A marginal redistribution towards the inner leaflet was observed (red lines in Figure 3.10A) but it is difficult to assess whether it corresponds to preferential interactions with anionic lipids or to lateral pressure relaxation. This is somewhat at odds with the strong preference of cholesterol for anionic lipids reported by Yesylevskyy and co-workers [354]. However, their findings relied on a different methodology involving an asymmetric bilayer exclusively containing anionic lipids in the inner leaflet and thus may

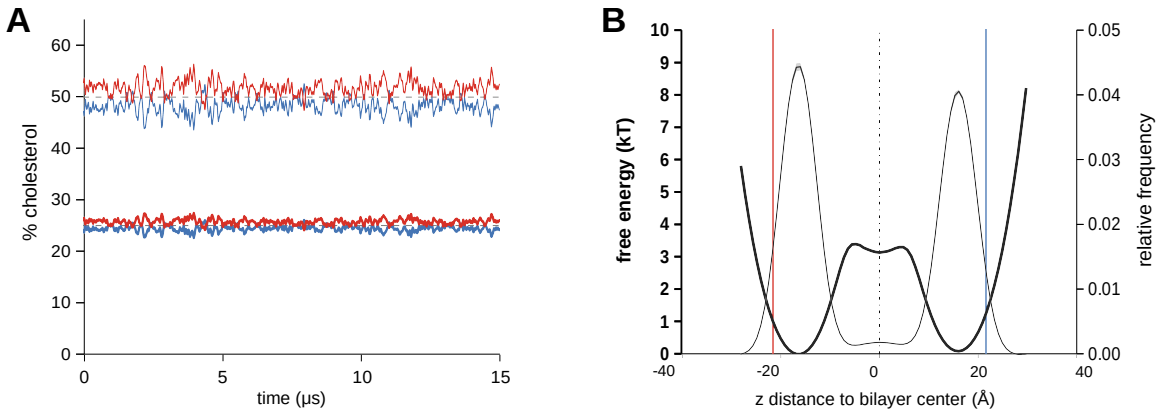

Figure 3.10 (A) Evolution of cholesterol distribution in the AM bilayer and (B) corresponding density (thin line) and free energy (bold line) profiles. In (A) cholesterol concentrations in the upper and lower leaflets are represented by blue and red lines respectively, with intra-leaflet ratios shown as thick lines and inter-leaflet ratios as thin lines. Dashed lines indicate the initial intra-leaflet ratio (∼25%) and the 50% inter-leaflet ratio. Ratios were calculated by performing a rolling average on successive frames over 40 ns. In (B) cholesterol free energy profile along the normal to the bilayer is represented in bold black, with the the average position of phosphate groups in the anionic and zwitterionic leaflet indicated by red and blue lines respectively. The average cholesterol hydroxyl bead density was calculated over 3 windows of 5 µs each (0-5 µs, 5-10 µs and 10-15 µs). The free energy profile was then obtained by averaging the free energy profile obtained by Boltzmann inversion for each window. Standard deviation is shown as a grey area but is marginal and essentially hidden by the lines thickness. The slight asymmetry of the free energy profile corresponds to the marginal preference of cholesterol for the anionic leaflet.

not be directly comparable to the system presented here. Besides, they found that the extent of cholesterol enrichment in the inner leaflet depended heavily on the saturation of the acyl chains of the lipids used, which were all different than those included in the AM model.

Table 3.3 Free energy barrier to cholesterol flip-flop in various lipid environments. UA and AA respectively correspond to united-atom and all-atom representations. The umbrella sampling method is described in [406] and the diffusion map method, which is based on Boltzmnan inversion, in [407].

Bilayer	$\Delta G_{barrier}$ *(kT)*	Model	Technique	Ref.
AM[1]	3.3	CG	Boltzmann inversion	this thesis
POPC	4.8	CG	umbrella sampling (1D)	[394]
POPC	8.6	CG	umbrella sampling (1D)	[397]
POPC	11.6	AA	umbrella sampling (2D)	[396]
POPC + CHOL (10%)	4.4	CG	Boltzmann inversion	[393]
DPPC	6.0	CG	umbrella sampling (1D)	[394]
DPPC	8.9	CG	umbrella sampling (1D)	[394]
DPPC	10.3	AA	umbrella sampling (2D)	[396]
DPPC + CHOL (20%)	11.5	UA	umbrella sampling (1D)	[394]
DPPC + CHOL (30%)	8.0	UA	diffusion map	[398]
DPPC + CHOL (40%)	15.3	UA	umbrella sampling (1D)	[394]
DPPC + CHOL (40%)	9.3	CG	umbrella sampling (1D)	[394]

1. see Table 3.2 for composition

The free energy profile associated to cholesterol was also determined and compared with previous computational studies. The Gromacs utility *g_density* was used to obtain the density distribution of cholesterol hydroxyl group and the corresponding free energy profile was then calculated by Boltzmann inversion (Figure 3.10B). This led to an estimation of the free energy barrier to cholesterol flip-flop of approximately 3.3 kT, which is in good agreement with previous CG MD simulations (Table 3.3). It should be noted that umbrella sampling methods [406] are likely to result in higher estimates of the free energy barrier associated to cholesterol flip-flop as restraining of the molecule may not allow to adequately sample the conformations which actually occur along the flip-flop path [408, 409]. However, different bilayer compositions may also account for the variations observed as these studies also demonstrated the influence of phospholipids type as well as of cholesterol concentration

on the free energy barrier associated to flip-flops. Finally, atomistic MD simulations led to higher free energy barriers, thereby suggesting that the CG representation in the MARTINI force field resulted in an under-estimation of free energies. However, in a 2009 study Bennett and co-workers performed a systematic comparison of cholesterol flip-flops in various lipids bilayers using CG and united-atom models and found that the MARTINI force field satisfyingly reproduced the evolution of the free energy barrier of cholesterol flip-flop in the different membranes studied [394]. Since the results obtained with the AM bilayer are consistent with such previous CG MD calculations, it suggests that this membrane model and the Boltzmann inversion method can be used to obtain reasonable free energy estimates.

3.3.4 The question of membrane equilibrium

Although the new lipid composition and assembly method of the AM model address the main issues detailed in the previous section, it is important to bear in mind that the mechanical properties of complex asymmetric lipid bilayers remains a challenging issue. Indeed, even putting aside the question of cholesterol distribution and that of acyl chains saturation, simple differences between phospholipids head groups can lead to different bilayer properties. For instance, X-ray data obtained from vesicles show that the smaller head group of POPE lipids lead to an area per lipid of approximately 60 $Å^2$ at physiological temperatures [410] compared to 68 $Å^2$ for POPC lipids [411]. This is likely to be of importance as the influence of the monolayers respective areas on the shape adopted by lipid bilayers models has been well documented *in vitro* [412, 413]. Additionally, Heerklotz showed that asymmetric stress resulting from area imbalance between leaflets could also lead to membrane permeation [414]. Furthermore, and of particular relevance to this thesis, Huang and co-workers found that membrane insertion of membrane active peptides as well as subsequent pore formation were controlled by the area expansion of the outer leaflet following peptides accumulation on the external layer of the vesicles [415].

Altogether these observations demonstrate the relevance of leaflets stress profiles to the study of bilayer destabilisation. In this regard, it is encouraging that packing differences between lipid species can be reproduced by the MARTINI force field, as I obtained area per lipids of 64 $Å^2$ and 68 $Å^2$ respectively when performing simple control simulations of pure POPE and POPC symmetric bilayers containing 1116 lipids each. On the other hand it also introduces additional complexity as it is likely that even relatively simple asymmetric lipid mixtures, such as those used in the AM bilayer, will lead to asymmetric stress profiles. Also, Marrink and co-workers showed that unrealistic bilayer models with highly asymmetrical lateral pressures could be kinetically trapped in a metastable state, in both atomistic and CG representations [416]. Therefore, the future development of biologically relevant membrane models might benefit from investigating and quantifying such stress imbalances in order to assess the mechanical equilibrium of the bilayer.

3.4 Electrostatics properties

As discussed in the first chapter (see 1.2.2), CPPs are positively charged peptides and electrostatic forces play an important role in their interactions with biological membranes. It is therefore important to characterise the electrostatic properties of the bilayer model developed in order to better assess its relevance and understand its limitations. In this last section I thus present the methodology developed to calculate the effective electrostatic potential in coarse grain systems before then discussing the potential profile of the AM plasma membrane model.

3.4.1 Visualisation and significance of the electrostatic potential

In the MARTINI model electrostatic interactions are limited to groups of atoms bearing a full, or close to full, net charge and are cut off at 12 Å and gradually shifted to zero so

that they vanish at this cutoff distance in order to avoid discontinuities [240]. This means that the potential created by a charged bead will only affect neighbouring charges located within a sphere of a 12 Å radius. It follows that traditional calculation techniques of the electrostatic potential based on double integration of the charge density are inappropriate to characterise the effective potential of a CG system. Instead, I implemented the following direct approach:

1. The simulation box is mapped to a regular tridimensional grid, using a spacing of 1 Å along each axis.

2. The total charge of each grid cell is calculated by binning charged beads into the closest grid cell. If several frames are processed the average charge of each cell is obtained by dividing the total charge by the number of frames processed.

3. For each cell of the grid, the effective electrostatic potential is then obtained by summing the contributions of all charges present in neighbouring cells within the 12 Å cutoff distance. Charges contributions are calculated using the shifted electrostatic potential implemented in the MARTINI force field (see 2.2.2).

4. The tridimensional map of the system's effective electrostatic potential thus obtained can then be averaged along one or two dimensions in order to represent the evolution of the potential in an average membrane slice or along the normal of the bilayer.

The method was validated on a simple DPPC bilayer obtained by self-assembly and containing 48 lipids. This system was simulated at 323 K using the MARTINI 2.1 force field and the same parameters as described in 3.2.2. Results were compared to the explicit electrostatic potential obtained using the VMD PMEPot plugin [417] which relies on an implementation of the PME method [221] for atomistic systems. To this end, simulations of a DPPC bilayer using both united-atom and all-atom representations were also performed. The GROMOS 53a6 force field [233] was used for the united-atom simulation, with the

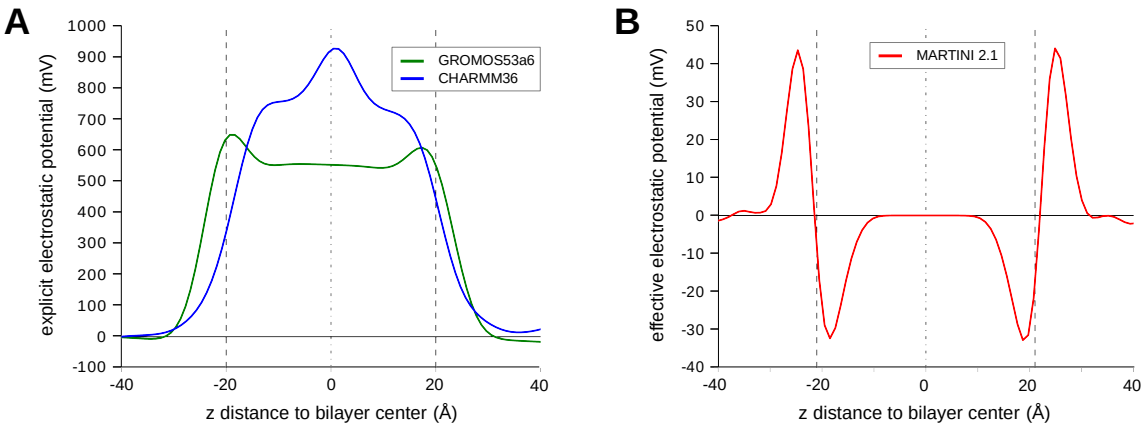

Figure 3.11 Comparison of the explicit electrostatic potential across a DPPC bilayer when using atomistic representations with the effective electrostatic potential obtained with a CG model. (A) Explicit electrostatic potential obtained with a united-atom force field (GROMOS 53a6, green) and an all-atom force field (CHARMM36, blue). (B) Effective electrostatic potential calculated when using the CG MARTINI 2.1 force field. All systems were simulated for 100 ns with a NaCl salt concentration of 0.5 M. The vertical dashed lines indicate the approximate average position of the leaflets surface, defined by phosphate beads (CG) or phosphorous atoms (atomistic).

DPPC bilayer obtained by mapping the CG MARTINI representation back to atomistic details using a method previously developed [254]. The all-atom simulation was performed using CHARMM36 force field [229] and a pre-equilibrated DPPC bilayer containing 72 lipids was downloaded from the Klauda group[2]. All simulations were executed for 100 ns using the Gromacs package version 4.5 [372]. The electrostatic potential was averaged in the x and y directions for all systems and the corresponding profiles are presented in Figure 3.11.

The results demonstrate the weak and localised nature of explicit Coulombic interactions in the MARTINI model. Using this CG representation the membrane effective electrostatic potential is confined to the solvent-lipid interface, with choline and phosphate beads creating local positive and negative electrostatic potentials respectively. This is not an unexpected result as these two beads are the only charged lipid particles in this CG model. In addition to the absence of charges on the water beads, the short 12 Å cutoff also limits the extent of the electrostatic contribution of the NaCl salt and altogether the solvent in the

[2]http://terpconnect.umd.edu/~jbklauda/research/download/dppc72-c36npt.pdb

MARTINI model is not able to influence the electrostatic properties of the bilayer interior. In contrast, atomistic representations lead to a stronger electrostatic potential throughout the lipid bilayer. However, it is important to bear in mind that these profiles correspond to different scales of modelling. In the MARTINI model, as described in 2.2.2, interactions between atoms, including electrostatic ones between partially charged atoms, are treated implicitly via Lennard-Jones interactions between the beads they have been assigned to. The explicit formulation of Coulombic interactions is limited to those collective groups of atoms that bear a full net charge while the short range treatment is both a way to mimic distant-dependent screening and to ensure computational efficiency. In the united-atom force field GROMOS 53a6, although long range electrostatic interactions are calculated via the PME method, aliphatic hydrocarbons are represented by a single particle and therefore no partial charges are present in the lipids acyl chains. As a consequence, this description also leads to a very simple potential profile in the membrane core with which the CG model is in relatively good qualitative agreement. On the other hand, in the CHARMM36 force field all atoms are explicitly represented, with a partial charge associated to each hydrogen and carbon atom in the acyl chains, and thus this model reproduces the evolution of the membrane potential more faithfully [418]. These different treatments of electrostatic interactions correspond to different trade-offs between the effects captured by the models and their required computational power [198].

Therefore, although the results presented in Figure 3.11 illustrate the limitations of the CG MARTINI force field in tackling problems where long-range electrostatic forces are paramount, it must be remembered that in this model most interactions are treated implicitly, and that the explicit short range electrostatic interactions allow to effectively qualitatively reproduce the effect of the lipids charged head groups on the electrostatic potential at the solvent-membrane interface.

3.4.2 Electrostatic potential profile in the AM model

The electrostatic potential in the AM model previously described was characterised using the above method. As a control, the electrostatic profile of a simple POPC bilayer was also determined. In addition, the influence of salt concentration on the bilayer electrostatic properties was investigated by performing a simulation of the AM bilayer in a solvent containing NaCl salt at a 0.5 M concentration. The electrostatic potential profiles obtained are presented in Figure 3.12.

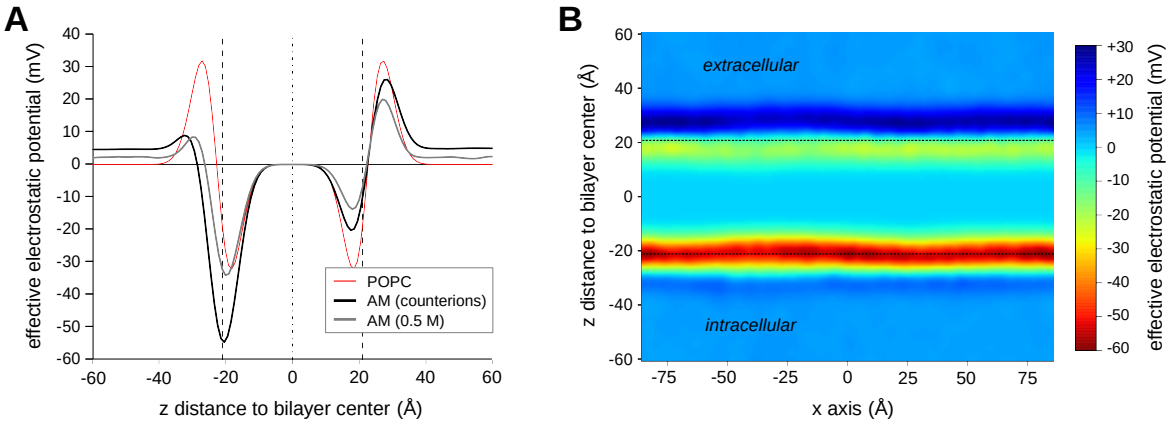

Figure 3.12 (A) Evolution of the electrostatic potential across the AM model (solid black line) and comparison with a symmetric POPC bilayer (thin red) and an AM bilayer in presence of 0.5 M NaCl (dashed, black). (B) Side view map of the electrostatic potential in the AM simulation box, averaged along the *y* axis and over 200 ns. The slightly positive potential in the solvent in the AM model is due to the presence of cationic counterions. Adding a NaCl salt concentration does not modify this as an excess of Na^+ must be maintained to neutralise the system.

Unlike what is observed for the POPC bilayer, the AM model is characterised by a strongly asymmetric potential profile due to the asymmetric distribution of anionic lipids. In particular, in the inner leaflet, because of the presence of negatively charged lipids, the positive potential created by choline and ethanolamine head groups is offset by the effect of the more numerous negatively charged beads, thus resulting in an overall mostly negative electrostatic potential. In contrast, in the outer leaflet, the electrostatic potential reflects the zwitterionic nature of all the lipids species present. Therefore, despite the limitations associ-

ated to the representation of electrostatic interactions in the MARTINI force field discussed previously, the AM model correctly reproduces the different electrostatic properties of the inner and outer leaflets of the plasma membrane of mammalian cells. This is an important point as several experimental studies demonstrated the interactions of CPPs with lipid bilayers were strongly influenced by electrostatic forces and that several CPPs exhibited different affinities for anionic and zwitterionic membranes [91, 335]. The AM model developed thus allows to study *in silico* the interactions of CPPs with a lipid bilayer containing both an anionic and a zwitterionic monolayer assembled in a manner that qualitatively mimicks the electrostatic properties of the plasma membrane of mammalian cells.

However, because of the short-range treatment of electrostatic interactions in the MARTINI model, it is important to bear in mind that a charge located within the surface of one leaflet of the AM bilayer is not influenced by the effective electrostatic potential associated to the opposite leaflet. As illustrated in Figure 3.12 the effective electrostatic potential remains null towards the centre of the lipid bilayer. Here it may be pointed out that the narrower zone of null potential compared to that observed in the DPPC bilayer in Figure 3.11 is merely a consequence of the undulations of the larger AM bilayer. As a consequence, the CG AM model is not suitable to directly investigate experimentally based suggestions that the membrane charge asymmetry provides a driving force for CPPs translocation [331] or that charge imbalance following CPPs accumulation on the extracellular leaflet of the plasma membrane can lead to electroporation of the bilayer [322–324]. The additional application of an external electric field oriented towards the intracellular side of the membrane could be used to overcome this limitation as well as to reproduce the effect of the negative transmembrane potential arising from different ionic concentrations across biological membranes [419]. However, this adds further complexity to the model and is primarily relevant to the initial stages of membrane insertion by the CPPs. Indeed, a peptide positioned inside a lipid bilayer in a transmembrane orientation with particles located within the cutoff

distance of each leaflet will "see" their different electrostatic properties and be subjected to the corresponding forces. As a first approach, it is thus reasonable to individually assess to what extent the different lipid species present in each leaflet affect the CPPs behaviour. This can then be used as a starting point for more complex models taking into account the effect of transmembrane potential on peptide-membrane interactions.

Finally, it is worth mentioning that the presence of a salt concentration does not lead to more realistic electrostatic potential profiles (Figure 3.12A). As mentioned previously, this is a consequence of the short 12 Å cutoff which prevents the ionic concentration from impacting the effective electrostatic potential in the bilayer interior. Nonetheless, a small screening of charges is observed at the solvent-membrane interface which sightly attenuates the effective electrostatic potential created by the lipids and the asymmetry of the profile. This observation justifies adding only counterions in the CG AM model in order to avoid hiding the respective electrostatic properties of the membrane leaflets from positively charged CPPs.

3.5 Conclusion

The activity of membrane active peptides depends as much on the properties of the target membrane as on those of the peptides. In particular, the selective destabilisation of bacterial membranes by AMPs is likely to be a consequence of their different lipid composition compared to the plasma membrane of mammalian cells. Investigation of the behaviour of membrane active peptides such as CPPs therefore requires models that on the one hand appropriately reproduce the complexity of biological membranes, but on the other are simple enough to remain informative. To date, although more sophisticated *in vitro* techniques have recently been developed, the vast majority of experimental studies available rely on simple symmetric lipid bilayers which do not mimic key features of the plasma membrane such as the asymmetric distribution of anionic lipids in the intracellular leaflet.

In this context, *in silico* approaches such as molecular dynamics simulations appear to provide a convenient tool to investigate peptide-membrane interactions at the molecular level using lipid bilayers possessing the desired characteristics. However, I have shown here that while such MD models can be created relatively simply, assessing their validity and biological relevance is not a straightforward task. In particular, the question of membrane equilibrium is important if membrane destabilisation and perturbations induced by CPPs are later to be examined. In this chapter, I have thus described the methodology used to develop a simple asymmetric membrane (AM) model of the plasma membrane of mammalian cells, following the issues associated to a more complex initial model (AMv1). Importantly, in addition to reproducing the respective zwitterionic and anionic nature of the outer and inner leaflets, the relative concentrations of the different phospholipids species in the AM model will allow for easy comparison of their respective sampling by CPPs. Additionally, I presented a technique to calculate the effective electrostatic potential in CG systems and discussed the limitations of the representation of electrostatic interactions in the MARTINI force field. It was shown that in spite of those shortcomings, the AM model qualitatively reproduced the different electrostatic potential of the outer and inner leaflet of the plasma membrane. This model represents a suitable first approach to characterise the interactions of CPPs with a lipid bilayer involving a biologically relevant lipids distribution and provides an important basis before developing more complex membrane models.

Chapter 4

Comparison of the stability of two cell-penetrating peptides in lipid bilayers

4.1 Introduction

Having described the approaches taken to model biologically relevant membranes in the previous chapter, this chapter shifts the focus to peptides, and addresses the question of the ability of coarse grain MD to discriminate between membrane toxic and non-membrane toxic CPPs. The relevance of asymmetric membranes models to study such peptides is also investigated. These represent necessary validation steps of the approach taken in this thesis for two reasons.

First, the membrane toxicity of CPPs has hitherto not been studied computationally as investigations of membrane perturbations caused by membrane active peptides have largely focused on antimicrobial peptides (AMPs) and the mechanism by which they destabilised bacterial membranes models [177, 178, 182, 183, 344, 346, 373, 420–422]. Interestingly, this is despite the fact that the distinction between AMPs and CPPs has been shown to be

fluid [149, 150] (see 1.2.2). There also exist several experimental studies characterising the toxicity profiles of CPPs [139, 143] or attempting to enhance their cellular internalisation while minimising their cytotoxicity [140, 141, 423]. While it is important to remember that cytotoxicity can have origins other than membrane destabilisation, the ability of some CPPs to disrupt the bilayer integrity correlate with their biological toxicity and makes them difficult to distinguish from AMPs [91, 99]. It is therefore important to check whether MD simulations can capture membrane perturbations induced by CPPs and also whether the various degrees of bilayer disruption reported experimentally for different CPPs lead to different observations *in silico*. Furthermore, consistent with the bias towards the study of AMPs, existing computational studies of membrane active peptides only involve symmetric membranes models and it is thus necessary to assess whether the introduction of an asymmetric lipid distribution, presented in the previous chapter, has any influence on the behaviour of the peptides modelled.

Second, a major limitation of the coarse grain MARTINI approach is that it does not readily allow for change of the secondary structure of proteins or peptides. Although predominantly unstructured when in solutions [135, 136, 424], CPPs have been shown to adopt a wide range of secondary structures in a lipid environment [425–430] with different studies reporting different outcomes for the same peptide [431, 432]. The nature of the correlation between CPPs secondary structure and their biological activity remains unclear [86, 433–435] but several studies produced evidence that their flexible and polymorphic nature is of importance [430, 436–438]. To date, all the molecular dynamics studies of CPPs reported made use of atomistic descriptions [170–176, 179, 180, 374, 439], and in at least 4 studies a partial change in the peptide secondary structure was reported on the simulations timescale [173, 174, 176]. However it should be noted that the study of peptides folding as they bind to lipid bilayers remains a challenging problem as the simulations timescales are too short to properly sample an equilibrium distribution of conformational states. As a

result, simulations are biased by the choice of the initial peptide structure, even when atomistic descriptions are used as McCammon and co-workers demonstrated in a recent study that compared the interactions of an antimicrobial peptide with lipid bilayers when starting with an α-helical conformation and a random-coil one [345]. When using a coarse grain approach to study the interactions of cell-penetrating peptides with model bilayers, it therefore appears all the more necessary to assess how the reduced conformational sampling can impact the simulations outcome.

4.2 Peptides selection and modelling

Since the discovery of the first CPPs in the mid 1990s [58, 59], many more sequences have been identified and CPPs now represent a broad and inhomogeneous family of peptides [89, 90, 96]. The two peptides that I studied in this thesis were selected amongst the available sequences based on the following criteria:

1. **Evidence of direct translocation.** After years of controversy it is now generally accepted that a variety of uptake mechanisms, including endocytosis and direct translocation, are involved in the cellular internalisation of CPPs (see 1.2.2). Since the focus of my work was on the membrane destabilisation induced by translocating CPPs, I selected peptides for which evidence of energy independent crossing of lipids bilayer was available.

2. **Different toxicity profiles.** In order to compare the various extent to which cell membranes can be perturbed by CPPs, both a peptide known to induce strong membrane destabilisation and one associated to lower toxicity were chosen.

3. **Different physicochemical properties.** Although point mutations have been shown to modify the cellular uptake and cytotoxic properties of CPPs [151, 440–442], the ability of the reduced resolution of the coarse grain representation to reproduce *in*

silico the different behaviours of CPPs should first be validated using unrelated sequences before attempting to tackle more subtle differences. Furthermore, despite the diversity of peptides classified as CPPs, they usually belong to one of three main categories depending on their origin (derived from protein-transuctions domains, chimeric or synthetic [89, 90]) and can also be classified into three sub-families based on their primary sequence (primary amphipathic peptides, secondary amphipathic peptides and non-amphipathic peptides [68]) which have been shown to involve different peptide-membrane interactions [91, 99] (see 1.2.2). Therefore, I chose to compare peptides representative of two different CPPs classes.

4. **Well studied.** More than a hundred sequences have been reported [90] but few CPPs have actually been studied in detail. However, the comparison of MD simulations to experimental data is important to validate the outcomes observed and interpret experimental results at the molecular level. If available, it is also informative to check the consistency of the results obtained using a coarse grain approach with those previously reported in atomistic simulations.

In the light of the above points, I chose to run comparative simulations of penetratin and transportan. The characteristics of those two peptides are first described below before then presenting the corresponding models used in the simulations.

4.2.1 Penetratin

Penetratin is a peptide which has 16 amino acids corresponding to residues 43 to 58 of the third helix of the Antennapedia homeodomain [57, 58]. Its identification followed the discovery of the existence of so called Protein-Transduction Domains (PTDs) allowing proteins to enter cells [55, 56, 66] and was a landmark breakthrough which, together with the identification of the Tat peptide a few years later [59], gave birth to the field of CPPs research [62]. Penetratin is still the most well-known member of the family of PTD-derived CPPs and is

Penetratin

- Origin: Protein Transduction Domain
- Classification: secondary amphipathic
- Length: 16 residues
- Sequence: **R**QI**K**IWFQN**RR**M**K**W**KK**
- Net charge: +7
- Cellular uptake: good
- Membrane toxicity: weak

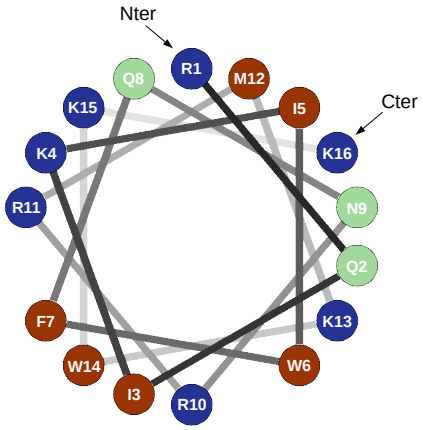

Figure 4.1 Properties and helical wheel projection of the penetratin peptide. The wheel projection was adapted from http://rzlab.ucr.edu/scripts/wheel/wheel.cgi with positively charged residues shown in dark blue, polar and hydrophilic ones in light green and hydrophobic ones in dark red.

arguably the most studied of all CPPs to date. Although penetratin contains seven positively charged residues at physiological pH, it differs from other short poly-cationic CPPs such as Tat or poly-Arginines by the presence of hydrophobic residues that have been shown to be important for its translocation [434], and exhibits different cellular uptake than those peptides [94]. Consequently, penetratin is usually classified as a secondary amphipathic peptide, even though it does not adopt a perfect amphipathic helix (Figure 4.1). This is supported by several studies that showed that, while unstructured in solution [135, 136, 438, 443], penetratin undergoes a conformational change at the surface of lipid bilayers whereas non-amphipathic arginine rich CPPs remain disordered [428, 429, 438]. The adoption of a partially α-helicoidal structure has been widely reported in circular dichroism (CD) and NMR studies [135, 443–445], and the formation of anti-parrallel β-sheet structures has also been suggested at high peptide concentrations [443, 446, 447]. Experimental studies have also highlighted the influence of lipid composition on the secondary structure adopted by penetratin [424, 448] and its ability to cross model membranes [328]. In particular, a stronger affinity of penetratin for membranes containing anionic lipids has been characterised by several groups [136, 322, 328, 447, 449, 450].

A great number of studies have been published on the cellular internalisation pathways of penetratin, with many conflicting results reported and successive predominant views on the mechanisms involved, as reviewed by Brock [103]. In short, the considerable interest initially generated by penetratin (and other CPPs) was due to reports of non-endocytic but energy and receptor independent translocation of biological membranes [104]. However, in 2003 this view was challenged by Richard and co-workers who suggested these observations were due to experimental artefacts [107] and the role of endocytosis in penetratin cellular uptake was consequently reevaluated and found to be predominant [126, 451, 452]. Nevertheless, the ability of penetratin to translocate across lipid bilayers in an energy independent fashion has since then been confirmed in several studies involving model lipid bilayers [117, 118, 322, 328, 453] and most notably in two recent ones involving plasma membrane vesicles [116, 134]. Those studies suggested that parameters such as membrane curvature [118], transmembrane potential [328] or charge imbalance [322] influence translocation efficiency but the actual mechanisms involved remain elusive. It is now the accepted view that both endocytosis and direct translocation are involved in the uptake of penetratin, with their respective contribution being possibly concentration dependent [94, 454], and some studies have suggested that direct translocation could account for the endosomal escape of penetratin into the cytosol [332, 455].

In contrast, the non cytotoxic character of penetratin and its weak perturbation of lipid bilayers have been confirmed by several studies. In live cells experiments penetratin was found to have no haemolytic nor cytotoxic activity even at concentrations as high as 100 μM [128, 143, 434, 456]. Similarly, in model systems comparative vesicle leakage assays showed that, unlike membrane toxic secondary amphipathic peptides, penetratin did not induce any perturbation of the lipid bilayer integrity [117, 136, 137, 328]. Finally, the interactions involved in the surface binding of penetratin to various lipid bilayers have been investigated in a few all-atom MD simulations studies [170–173, 374].

4.2.2 Transportan

Unlike penetratin, transportan is not directly derived from a naturally occurring protein but is a chimeric peptide: its 27 amino acid long sequence was obtained by linking via a lysine the first 12 residues of the neuropeptide galanin to mastoparan, a wasp toxin with antimicrobial properties [63]. It was one of the first members of the chimeric CPP family [89, 457]. As can be seen in Figure 4.2 it is essentially hydrophobic and because of the inhomogeneous distribution of its only four positively charged residues transportan is classified as a primary amphipathic CPP. Structural studies using CD and NMR showed that while transportan is not totally disordered in water, the degree of helicity is markedly increased in the presence of a membrane-like environment with the mastoparan domain folding into a α-helix while the galanin domain remains more unstructured [425, 426]. However, in contrast to penetratin, the secondary structure adopted by transportan was not found to be influenced by the peptide to lipid ratio nor the lipids charge [450, 458], and transportan binds with similar affinities to both zwitterionic and anionic lipid bilayers [443]. This is consistent with what has been observed with other primary amphipathic peptides [459] and has been attributed to predom-

Transportan

- Origin: chimeric
- Classification: primary amphipathic
- Length: 27 residues
- Sequence: GWTLNSAGYLLG**K**INL**K**ALAALA**KK**IL
- Net charge: +4
- Cellular uptake: good
- Membrane toxicity: strong

galanin *mastoparan*

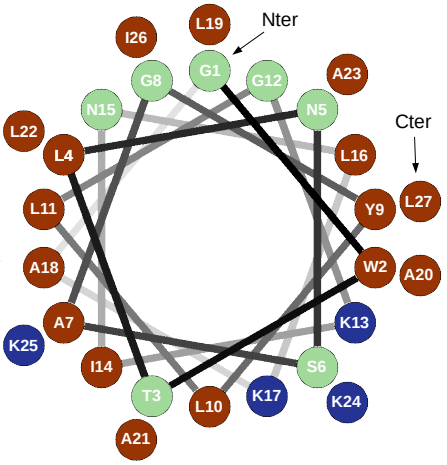

Figure 4.2 Properties and helical wheel projection of the transportan peptide. The wheel projection was adapted from http://rzlab.ucr.edu/scripts/wheel/wheel.cgi with positively charged residues shown in dark blue, polar and hydrophilic ones in light green and hydrophobic ones in dark red. The lysine linking the galanin derived domain and the mastoparan domain is underlined.

inantly hydrophobic interactions with membranes. Transportan and variants of it have been demonstrated to efficiently penetrate into cells [460–462] even when conjugated to a variety of cargos [462–464]. However, similarly to the case of penetratin, the energy and receptor independent internalisation pathway initially proposed by Pooga and co-workers [63] was later reassessed in favour of an endocytic uptake followed by endosomal escape [464, 465]. Nonetheless, it was suggested that direct translocation also contributed to internalisation and recent studies confirmed the ability of both transportan and its shorter variant (tp10) [460] to translocate across model membranes [120, 134].

These experimental studies also all revealed that peptides from the transportan family caused important bilayer perturbations even at low micro molar concentrations [128, 143, 146, 456, 462, 466], in agreement with the observation that most primary amphipathic CPPs possess a membrane lytic activity similar, albeit less pronounced, to that of antimicrobial peptides [123, 143, 147, 467]. Interestingly, the shorter tp10 variant of transportan has been found to be less membrane toxic than the original sequence and has therefore been the subject of most recent studies [468]. However, for the purpose of the work presented here, the ability of transportan to perturb bilayer integrity is a desired property and the reason I chose to focus on this peptide. In particular, comparative studies have demonstrated the much higher membrane toxicity of transportan with respect to that of penetratin [128, 456].

To date only one MD study of transportan has been reported [175], although two studies on tp10 have been conducted [174, 176], all using atomistic representations.

4.2.3 Peptides models

Solution NMR structures obtained in membrane mimetic environments were used as a starting conformation for both peptides. The penetratin structure, solved in a 9:1 tetrafluoroethylene:water mixture [469], reveals a partially α-helical structure with very little variations between the conformers ((a) in Figure 4.3A). This structure (PDB code: 1KZ0) was also

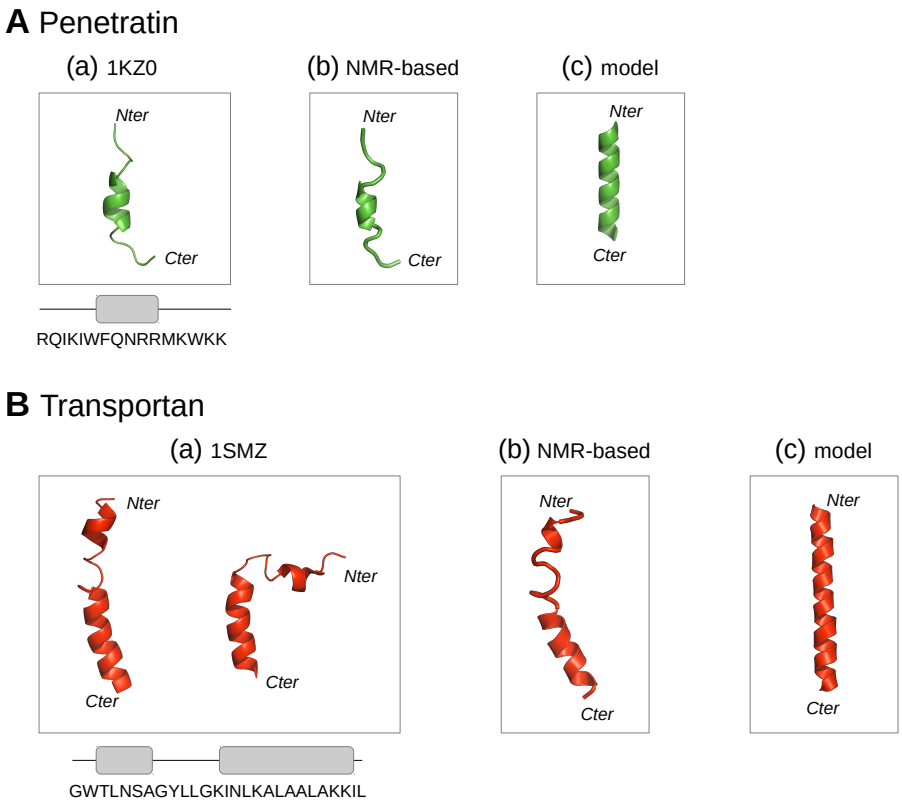

Figure 4.3 Cartoon representation of the (A) penetratin and (B) transportan peptides. (a) Conformers from the NMR solution structures and corresponding secondary structures, (b) initial CG conformation based on the NMR structures and (c) initial CG conformation of the purely α-helical models.

used in two MD studies of penetratin [171, 172] and it is interesting to note that in another MD study relying on a fully α-helical initial conformation the authors observed unfolding of the termini regions leading to a similar partially helical state [374]. The transportan structure was determined by NMR in zwitterionic phospholipid bicelles [426] and the conformers identified revealed a great flexibility around the lysine residue linking the α-helical mastoparan C terminus domain and the less structured galanin derived N terminus domain ((a) in Figure 4.3B). The same structure (PDB code: 1SMZ) was used in the only reported MD study of transportan [175]. A representative conformer of each NMR structure was converted to CG representation suitable for the MARTINI force field (v2.1) [257] ((b) in Figures 4.3A and B). The secondary structure of the peptides was maintained via dihedral angle restraints in order to allow for a degree of flexibility and conformational sampling.

Additionally, purely α-helical models of the peptides were created to assess to what extent the peptides secondary structure influenced the outcome of the CG MD simulations. Atomistic representations of these structures were built in PyMol [276] and then coarse-grained similarly to the NMR-based structures ((c) in Figures 4.3A and B).

4.3 Self-assembly simulations of penetratin and transportan

The previously reported MD studies of the CPPs [171, 172, 175] focused on the investigation in atomistic detail of the initial stages of membrane binding. However, the reduced computational costs of CG simulations allows for the self-assembly (SA) of lipids into bilayers to be performed and this is of particular interest to study the preferred, ie most stable, conformation and orientation of a protein or peptide in a membrane-mimicking environment. I therefore performed comparative SA simulations of penetratin and transportan with a variety of lipids in order to investigate the influence of lipids tail length (DHPC, DLPC, DPPC, DSPC), tail saturation (DOPC, POPC) and head group charge (presence of POPS at different concentrations) on the peptide stability.

4.3.1 Simulations setup

The simulations performed are summarised in Table 4.1. The peptide structure was initially positioned in the centre of a $8.5 \times 8.5 \times 7$ nm simulation box into which 128 lipids were then randomly added. To ensure formation of the bilayer in the x, y plane the box was extended to 9 nm in the z direction and the system was then solvated with counter ions added as appropriate to achieve a neutral total charge. Simulations were then executed as described previously in 3.2.2, using the Gromacs simulation package version 4.5.5 [372] with the standard Martini 2.1 parameters [240]. Repeat runs were performed using a different initial distribution of velocities.

Table 4.1 Self-assembly simulations of penetratin and transportan. Simulations were performed for both the NMR-based structures and the α-helical models of the peptides. P:L corresponds to the peptide to lipids ratio. The chemical formulas of the lipids can be found in Appendix A.

Lipid composition	P:L*	Duration (*ns*)	Repeats
DHPC	1:128	500	5
DLPC	1:128	500	5
DSPC	1:128	500	5
DOPC	1:128	500	5
DPPC	1:128	500	5
POPC	1:128	500	5
POPC(85%):POPS(15%)	1:128	500	5
POPC(70%):POPS(30%)	1:128	500	5

4.3.2 Identification of peptide conformations

Visual observation of the simulations showed that penetratin and transportan could both adopt either an interfacial or a transmembrane orientation. However, unlike penetratin, the NMR-based structure of transportan revealed that this peptide could adopt different conformations when it was transmembrane (Figure 4.4). In particular, two conformations, referenced to as TM and TM* (respectively (c) and (d) in Figure 4.4B), were identified. In the TM conformation the helix of the mastoparan domain spans the bilayer, with the lysine residues at its extremities in contact with opposite leaflets, whereas the disordered galanin derived domain resides closer to the interface. The situation is reversed in the TM* conformation and in this case the positive charges of the mastoparan domain are all in contact with the same interface. Interestingly, while transportan C terminus sits deeper inside the membrane in the TM conformation, its N terminus remains close to the lipids phosphate groups in both conformations which is an agreement with the interfacial anchoring of tryptophan residues observed experimentally [470]. A third transmembrane conformation, whereby transportan adopts a U-shape conformation, was observed in DHPC bilayers ((e) in Figure 4.4B). In this case the bilayer is thin enough for this conformation to accommo-

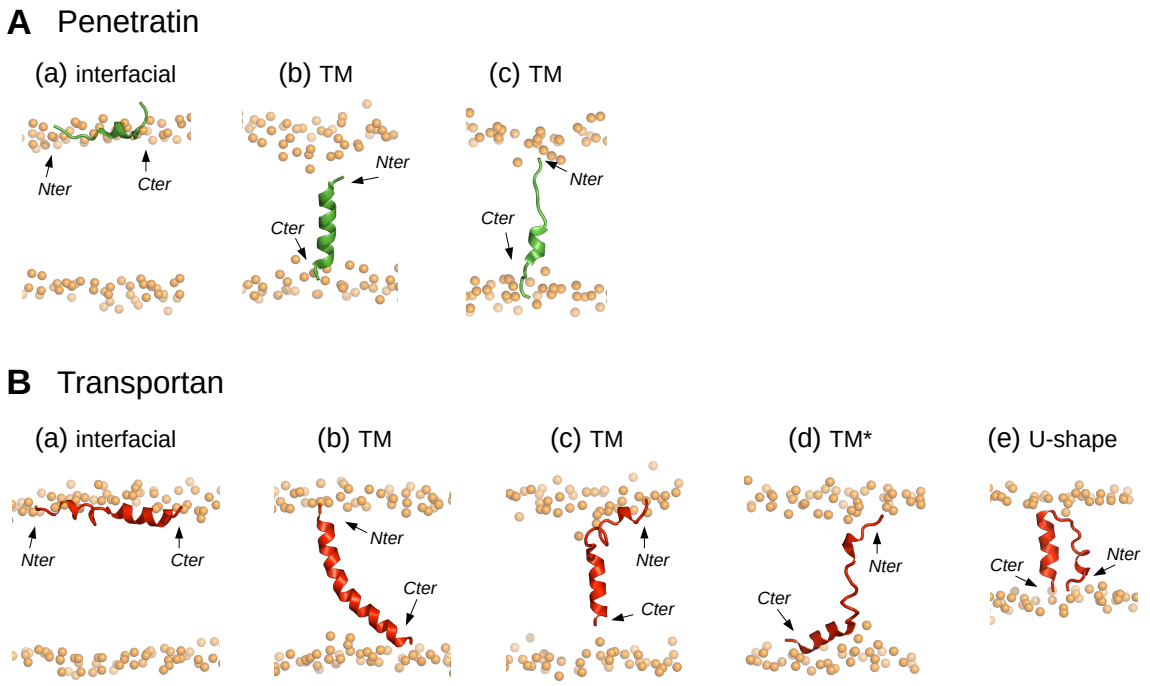

Figure 4.4 Representative conformations observed for (A) penetratin and (B) transportan in SA simulations. Phosphate beads are shown as orange spheres. All snapshots were taken in lipids with PO tails except for (e) which corresponds to the shorter DHPC lipids.

date a transmembrane orientation for both the mastoparan and the galanin domains while maintaining the interfacial anchoring of tryptophan and lysine residues. These simple structural observations suggest the relative distribution of hydrophobic and basic residues plays an important role in the interactions of transportan with lipid bilayers. Altogether these conformations also demonstrate the peptide flexibility and show that good conformational sampling is achieved despite the CG representation. This is further evidenced by the bending of the α-helical model in (b) (Figure 4.4B) which brings the central lysines (K13 and K17) closer to the phosphate groups of the lipids.

To investigate whether the lipid characteristics influenced the orientation and conformation adopted by penetratin and transportan, the final frame of each simulation was systematically examined. In order to avoid bias this was performed automatically by comparison of the relative z position of specific backbone beads with respect to that of the bilayer centre. Penetratin structures and the α-helical of model of transportan were deemed interfacial if

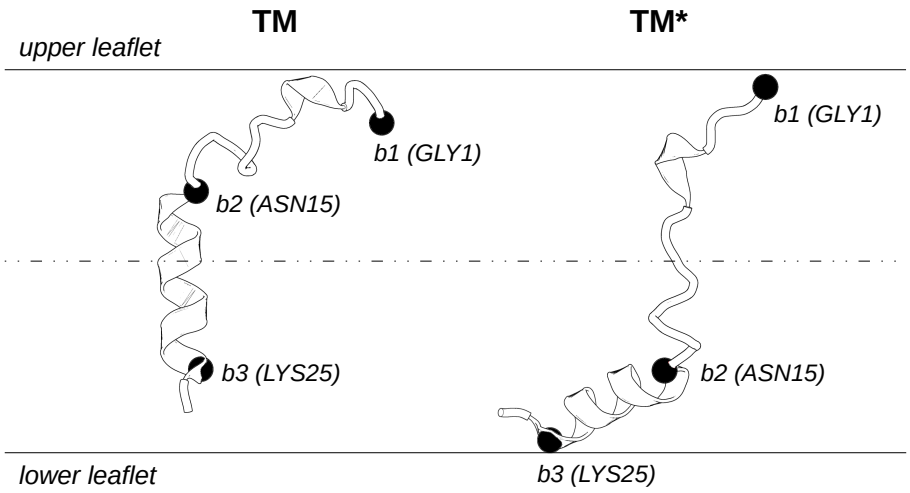

Figure 4.5 Comparison of the positioning of transportan with respect to the lipid bilayer when in TM (left) and TM* (right) conformations. The dashed and dotted line corresponds to the centre of the bilayer (delimited by the solid horizontal lines). The backbone beads b1, b2 and b3 used to determine transportan orientation and conformation are shown as black spheres and labelled with the residue they belong to.

both termini were on the same side of the bilayer centre and transmembrane otherwise. The case of the NMR-based structure of transportan was less straightforward due to the different transmembrane conformations described above. The following definitions, relying on three backbone beads (see Figure 4.5), were implemented:

- Interfacial: b1, b2 and b3 all belong to the same leaflet
- TM: b3 belongs to a different leaflet than b1 and b2
- TM*: b1 belongs to a different leaflet than b2 and b3
- U-shape: b2 belongs to a different leaflet than b1 and b3

At this point it should be mentioned that while lipids self-assembled into bilayers within a few tens of seconds, the peptides did not necessarily adopt their final orientation or conformation immediately afterwards and intermediate metastable states following bilayer formation were observed. In particular, penetratin and transportan were seen to reach an interfacial

orientation after first adopting an unstable transmembrane conformation. Interestingly, the reverse evolution was never observed. However, running the simulations for 500 ns allowed the systems to relax and ensured the orientation and conformation identified in the final frames corresponded to equilibrium states rather than transient artefacts. The relative stability of transmembrane and interfacial orientations will be examined later in the thesis, as well as that of the transmembrane conformations of transportan.

4.3.3 Preferential orientation and conformation of a single peptide

Figure 4.6 summarises the distribution of orientations and conformations identified. It reveals a significantly different patterns between penetratin and transportan with respect to the relative stability of their interfacial and transmembrane orientations. In the case of penetratin, only marginal evidence of a transmembrane orientation is observed, suggesting that the interfacial state is more favourable regardless of the lipid environment. In contrast, transportan can adopt a transmembrane orientation in all environments and this is found to be the predominant orientation in most systems.

Interestingly, the data suggest that the shorter length of penetratin does not account for its preferential interfacial orientation. Indeed, thinner bilayers (DHPC and DLPC) do not appear to favour this orientation whereas it is encountered in two DSPC simulations, thereby demonstrating that it is able to span even the largest of the bilayers studied. Furthermore, the α-helical model of penetratin is observed in a transmembrane orientation more frequently than the more disordered NMR-based structure even though it is more compact and cannot be stretched in a similar fashion (see (b) and (c) in Figure 4.4A). Rather, the difference between the two peptides likely reflects their distinct composition. The high density of positively charged residues and partially secondary amphipathic nature of penetratin (Figure 4.1) are best accommodated at the lipid-solvent interface instead of within the hydrophobic bilayer core (here it should be stressed that penetratin was never detected to reside

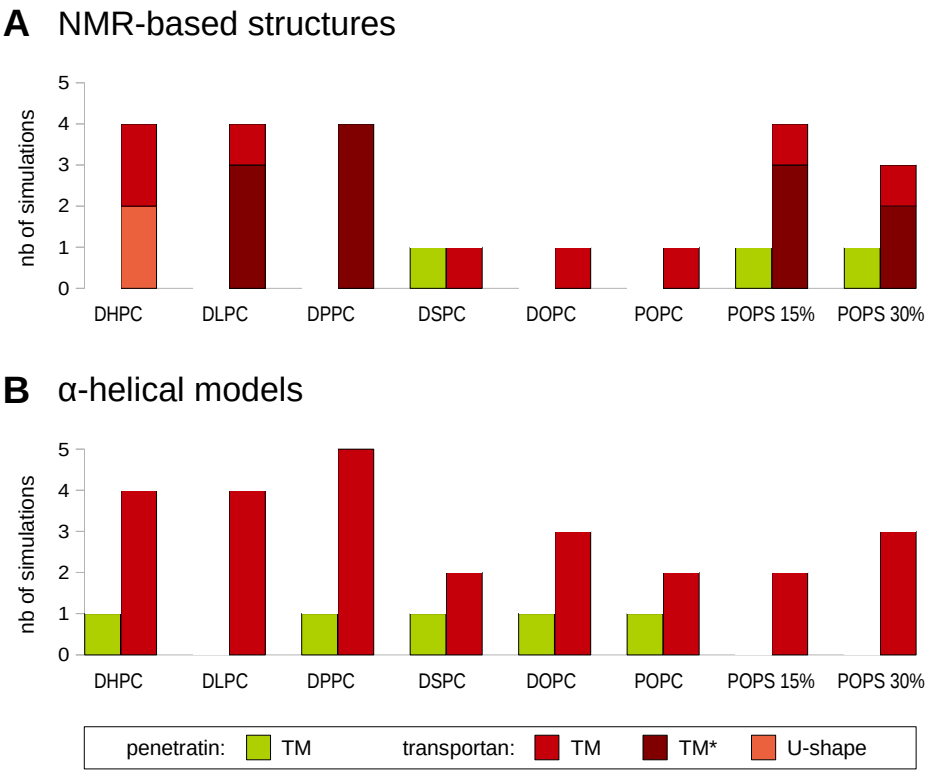

Figure 4.6 Distribution of orientations and conformations in the last frame of the SA simulations of transportan and penetratin in different lipid environments. For the sake of clarity the number of simulations in which the peptides adopted an interfacial orientation are not specifically represented but when the peptides did not adopt a transmembrane orientation they were always observed to be interfacial.

in the solvent but was always associated to the lipid bilayer). On the other hand, transportan predominantly hydrophobic nature (Figure 4.2) is consistent with the more favourable transmembrane orientation observed.

Apart from the above considerations, the possible influence of the different lipids is difficult to assess based on the limited number of simulations. High-throughput MD [471] may allow the detection of statistically meaningful patterns but would require significantly more computational time. It may simply be pointed out that the U-shape conformation is only observed in the DHPC bilayer, thereby illustrating the influence of the bilayer thickness on transportan possible transmembrane conformations. The secondary structure of transportan does not seem to fundamentally affect the relative stability of either the transmembrane or

interfacial orientation, and although in the case of the NMR-based structure comparatively fewer simulations lead to a transmembrane state in DPSC, DOPC and POPC bilayers, the statistical significance of this observation remains to be demonstrated. The relative distributions of the TM and TM* conformations does not yield a clear picture either: in the lipid environments where both are observed TM* appears predominantly sampled, however the TM conformation is more often detected overall. This suggests that these two conformations are similarly energetically favourable.

4.3.4 Interfacial depth of insertion

The residues distribution in the interfacial states of penetratin and transportan were examined in order to assess whether further differences between the two peptides could be detected in the simulations (Figure 4.7). The analysis revealed that, regardless of the secondary structure and presence of anionic lipids, transportan inserted more deeply into the bilayer than penetratin. Indeed, penetratin sits within the plane of the phosphate head groups whereas transportan center of mass appears to sink approximately 3 to 5 Å below. In addition to being again consistent with the hydrophobic nature of transportan compared to the poly-cationic one of penetratin, this is also in very good agreement with independent atomistic MD studies which found that penetratin and transportan approximate depths of insertion in a DPPC bilayer were, respectively, 1 Å and 4 Å below the nitrogen atoms present in the lipid head groups [173, 175].

The residue distribution did not appear to be particularly influenced by the secondary structure of the peptides as very similar profiles were obtained for both the α-helical models and the NMR-based structures. On the other hand, a slightly narrower distribution was observed for penetratin in the presence of anionic lipids as the arginine and lysine residues were dragged closer to the interface by the negatively charged serine head groups, thereby becoming less exposed to the solvent. Although this is a subtle effect, similarly shifted

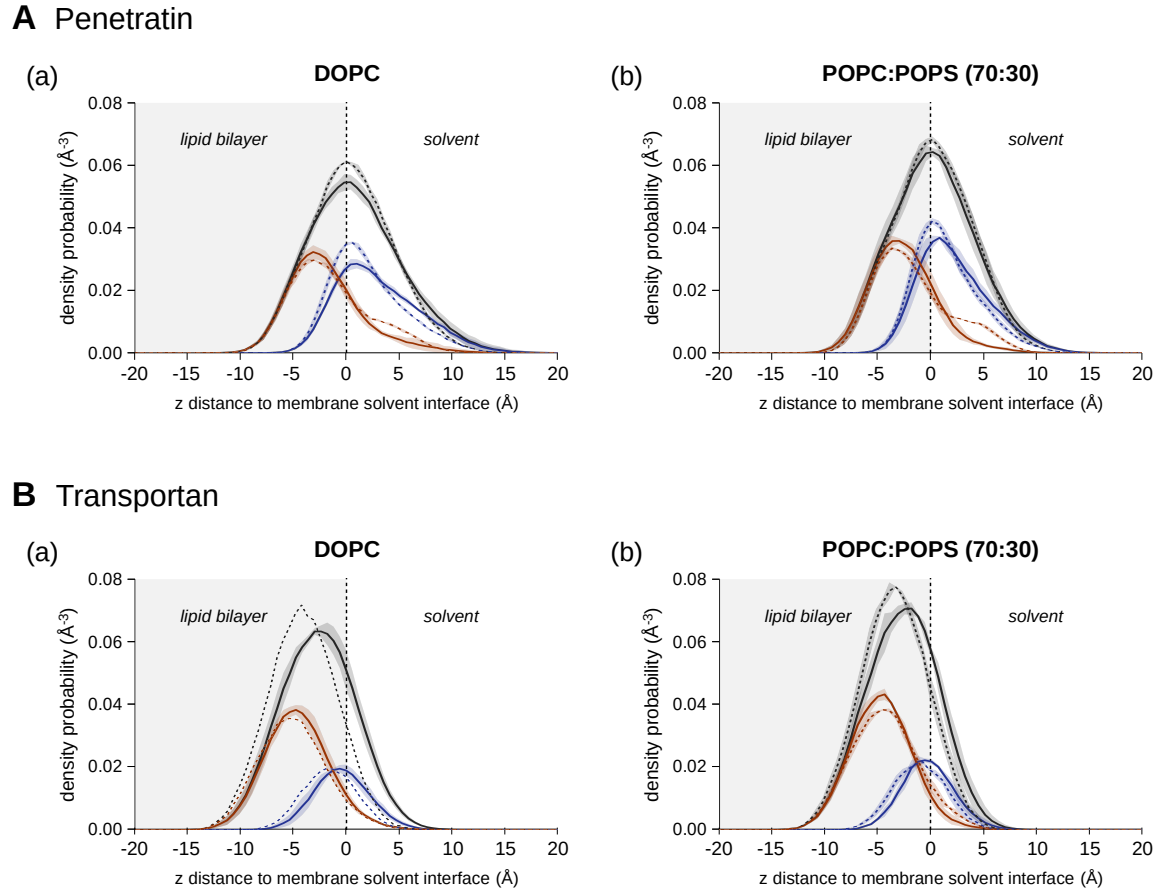

Figure 4.7 Distribution of residues in the interfacial orientation of (A) penetratin and (B) transportan. Hydrophobic residues are shown in dark red, positively charged ones in dark blue and the overall peptide density in black. The solid lines correspond to the NMR-based structures and the dotted ones to the α-helical models. The density profiles were obtained using the Gromacs utility *g_density* once the bilayer had self-assembled and the peptide reached an interfacial orientation. The average profile for each lipid environment was calculated by averaging the profiles obtained for each repeat weighted by the respective number of frames they represented (0 if the peptide never reached an interfacial orientation). The corresponding standard deviation is shown as a shaded area.

profiles were detected by Lensink and co-workers in a previous atomistic MD study [170]. These results are thus evidence that electrostatic interactions play a crucial role in the interactions of penetratin with lipid bilayers and they are in good agreement with its stronger affinity for anionic membranes compared to zwitterionic ones that have been observed experimentally [136, 322, 328, 447, 449, 450] and in previous all-atom simulations [170, 171]. In contrast, no such effect was observed for transportan which is in agreement with

experimental evidence of strong binding to both anionic and zwitterionic membranes predominantly dominated by hydrophobic interactions [443].

4.4 Embedded simulations of penetratin and transportan

Numerous experimental studies have shown that the lipid bilayer destabilisation caused by membrane active peptides is concentration dependent and more pronounced at higher peptide-to-lipids ratios (P:L) [472–477]. Accordingly, the mechanisms suggested for the formation of peptides-induced transmembrane pores as well as the commonly accepted Shai-Matsuzaki-Huang (SMH) model of membrane destabilisation by antimicrobial peptides (AMPs) all rely on the involvement of several peptides [42–44, 478] (see 1.2.1). This is further supported by several MD simulations of AMPs which revealed the necessity for these peptides to form aggregates in order to penetrate the membrane and induce perturbations [177, 178, 373, 421, 479]. A computational investigation of the membrane toxicity of CPPs must therefore involve the study of their collective behaviour. To this end, I performed simulations of systems where several penetratin and transportan peptides were initially embedded in a monomeric state in pre-formed bilayers. Although it might be argued that such a set-up does not appropriately reflect the mechanism by which CPPs enter the membrane (especially so if it involves cooperation between the peptides), it is important to remember that experiments showed the kinetics of CPPs translocation is on the order of minutes [93, 99] and therefore remains beyond the timescales accessible by MD simulations. Consequently, in contrast to AMPs, spontaneous insertion of CPPs in the lipid bilayer has never been observed in MD simulations bar one controversial study where the system simulated was not electrically neutral [179, 374]. Embedding the peptides into the membrane is thus a reasonable approach to study the peptide-peptide and peptide-lipids interactions within the lipid bilayer that may contribute to its destabilisation and has been employed in a number of previous MD studies of CPPs [174–176]. In order to assess the influence of lipids

distribution on the peptides behaviour, penetratin and transportan were embedded in both an asymmetric membrane model and a symmetric one and, as previously, both the NMR-based structures and the α-helical models of the peptides were investigated. Additionally, control simulations of zwitterionic and anionic membranes involving a single embedded peptide were also performed. These also provided a complementary approach to the self-assembly simulations discussed previously and allowed to further characterise the stability of the transmembrane orientation for transportan and penetratin.

4.4.1 Simulation setup

The simulations performed are summarised in Table 4.2. A single peptide was embedded in zwitterionic (DOPC) and anionic bilayers (POPC:POPS mixtures) containing 512 lipids in order to assess the influence of anionic lipids on its stability. Simulations of 8 peptides embedded in the same 512-lipid zwitterionic bilayer were also performed to study the effect of cooperation on peptides stability and peptide-membrane interactions. Similarly, 8 peptides were inserted into the 1300-lipid asymmetric membrane model AMv1 presented in the

Table 4.2 Embedded simulations of transportan and penetratin performed. The initial peptide-to-lipid ratio is indicated by the P:L column but the exact ratios varied for each simulation due to the insertion technique which required removing a few lipids to make room for each peptide (see text for details). For transportan NMR-based structure the TM conformation was used. In asymmetric membranes the outer leaflet corresponds to the zwitterionic one.

Lipid composition	P:L	Orientation	Duration (μs)	Repeats
Single peptide simulations				
DOPC	1:512	-	1	5
POPC(85%):POPS(15%)	1:512	-	1	5
POPC(70%):POPS(30%)	1:512	-	1	5
Multiple peptides simulations				
DOPC	8:512	-	5	5
AMv1	8:1300	Nter outwards	5	5
AMv1	8:1300	Cter outwards	5	5

previous chapter (see 3.2.1): this allowed to investigate whether a smaller P:L ratio and the lipids asymmetric distribution influenced the outcome of the simulations. The number of peptides to embed and the sizes of the bilayer patches were chosen so that the corresponding P:L ratios in the DOPC and AMv1 multiple peptides simulations (respectively 1:64 and approximately 1:160) were within the range of those used in experimental studies of membrane actives with lipids vesicles where bilayer perturbations were reported [472, 474–476, 480]. However, it is important to bear in mind that the P:L ratios in macroscopic systems represent an average value that cannot be translated into a corresponding number of peptides at the molecular scale due to local fluctuations in peptides concentrations.

The *g_membed* utility developed by Wolf and co-workers [481] was used to insert the peptides into the bilayer. In short, their approach follows a four-step process: first the protein to insert is overlaid in the desired position onto the pre-formed bilayer; second, its width is dramatically decreased in the x,y plane; third, lipids and water molecules overlapping with the compressed protein are removed, and finally, the protein is grown back to its full size in a short MD simulations. Compared to methods relying on the removal of a membrane patch, this technique attenuates the perturbations of the equilibrated bilayer as a minimum number of lipids has to be removed (typically around 6 in the case of the peptides studied) while those in the vicinity of the protein are slowly pushed away in order to gradually accommodate its presence as the protein is grown back to its original size. The main advantage of using *g_membed* is the ability to set up proteins in a transmembrane orientation in environments where this orientation cannot otherwise be obtained via SA simulations, either because of the nature of the peptide (e.g. penetratin preferential interfacial orientation in various bilayers, as illustrated in Figure 4.6) or that of the model membrane (e.g. asymmetric lipid distribution). However, it should be noted that the protocol presented in the previous chapter to control the lipid composition of pre-formed bilayers (see 3.3.2) later provided another way to achieve the same result from any transmembrane conforma-

tion obtained via SA. Simulations relying on this alternative approach will be presented in the next chapter but here transportan and penetratin structures were simply embedded with the *g_membed* tool so that they best spanned the lipid bilayers. In systems involving several peptides these were positioned randomly without being in contact with each other. The peptides were all inserted with the same relative orientation to the bilayer. The simulations were then run using the same settings as described in 4.3.1, with the 8-peptide systems run for longer (5 μs) than the single peptide ones (1 μs) in order to allow time for the peptides to interact.

4.4.2 Monomers stability

The final orientation and conformation of penetratin and transportan in single peptide simulations was determined in the same way as described previously (4.3.2) and the results revealed a very different pattern for the two peptides (Figure 4.8). Indeed, whereas transportan remained in the initial transmembrane orientation in all simulations, penetratin predominantly adopted an interfacial orientation. This is in agreement with the findings obtained from the SA simulations and confirms that the transmembrane orientation is more stable for transportan than penetratin. Interestingly, this orientation also appeared marginally more stable for the α-helical model of penetratin than the NMR-based structure. This is again consistent with the outcome of the SA simulations (see Figure 4.6): in addition to supporting the hypothesis that the peptide length does not play a determinant role in the preferential membrane orientation of penetratin, it also provides some evidence that its α-helical secondary structure does influence its affinity for the hydrophobic membrane environment.

Altogether, the simulations performed suggest that while it is possible for penetratin to adopt both a transmembrane and an interfacial orientation, the interfacial state is more energetically favourable as the transmembrane orientation is unstable on the timescale of the simulations. It is interesting to note that penetratin almost exclusively reached the leaflet

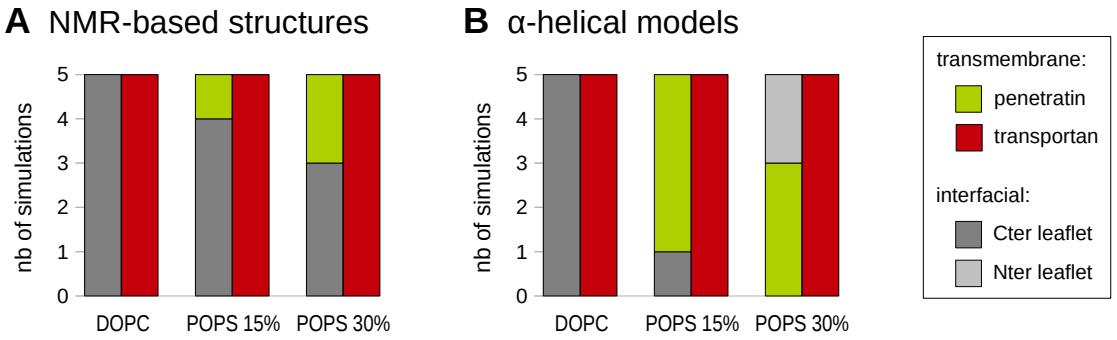

Figure 4.8 Orientation of transportan and penetratin in the last frame of the embedded simulations involving a single peptide. In the repeats where the peptide adopted an interfacial orientation the leaflet reached is referred to with respect to the initial peptide position.

closer to its C terminus. This may be explained by the predominant role of electrostatic interactions and the higher density of positively charged residues in this part of the sequence dragging the peptide towards the lipid-solvent interface. The minor stabilisation of the transmembrane orientation by the presence of anionic lipids supports this hypothesis, and so does the fact that the only two simulations in which penetratin reached the Nter leaflet (see Figure 4.8B) occurred in the most anionic bilayer, since both observations suggest stronger interactions between penetratin and the Nter leaflet.

On the other hand, transportan transmembrane and interfacial orientations appear similarly favourable. Although the transient partially-inserted states observed in some SA simulations before the peptide reached the bilayer surface (see 4.3.2) suggest the interfacial state may be more energetically favourable, the transmembrane orientation is stable enough to prevent a single peptide from leaving the lipid bilayer to reach an interfacial orientation.

4.4.3 Peptide collective behaviour

Representative snapshots of the evolution of the systems containing 8 peptides are presented in Figure 4.9. They show that, in contrast to penetratin, transportan peptides can aggregate into oligomers. These different behaviours, as well as the influence of the peptides secondary structure and the lipids distribution on the peptides stability, are discussed below.

Aggregation

In the case of penetratin, the peptides were observed to adopt an interfacial conformation within a few hundreds nanoseconds in all simulations (see (b) in Figure 4.9A) which is in agreement with the previous single peptide simulations. Transient interactions are observed between a few peptides when in a transmembrane orientation (see snapshot at 0.1 µs) but

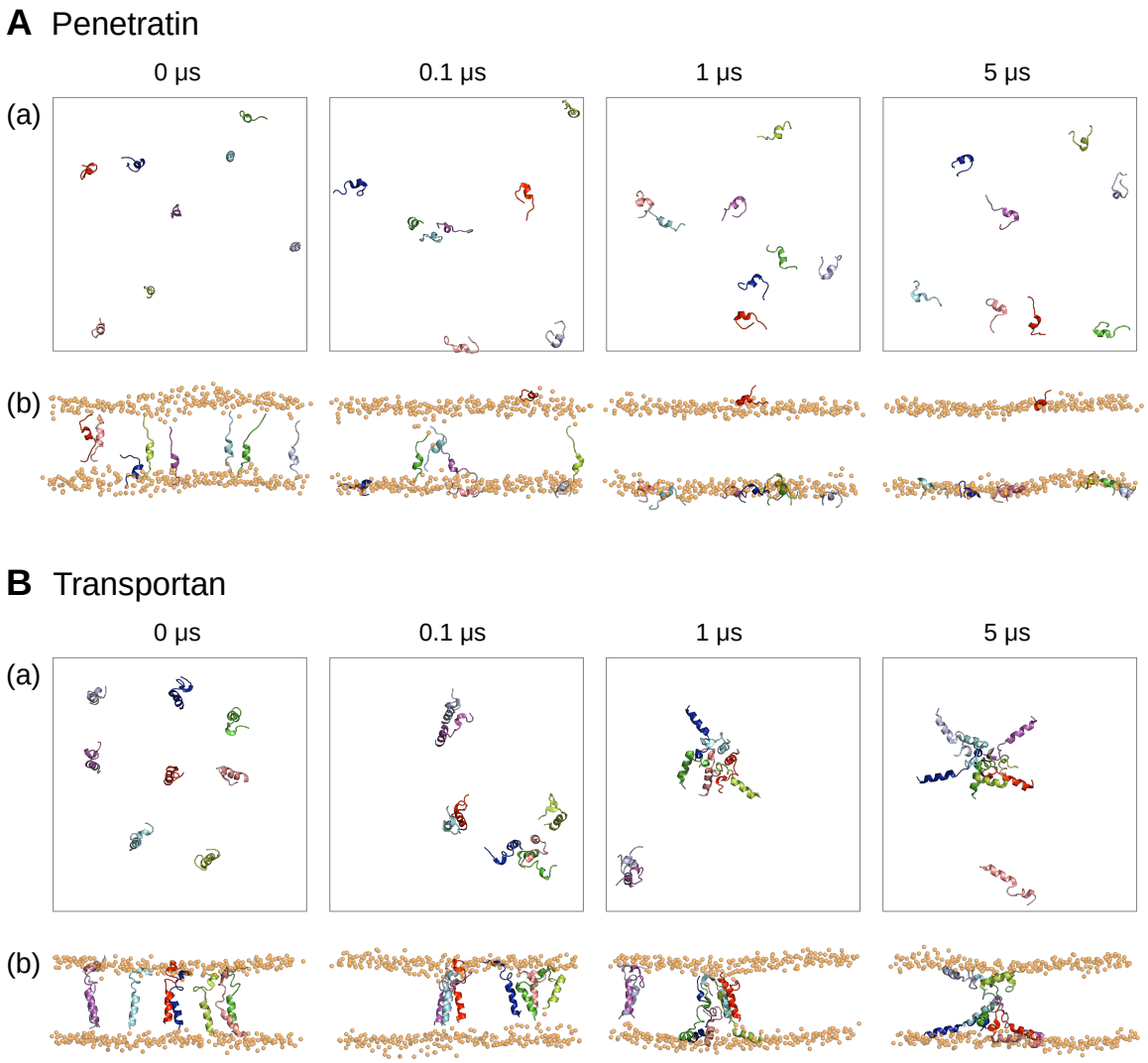

Figure 4.9 Comparison of the evolution with time of a system containing 8 (A) penetratin and (B) transportan peptides. The top row is a top view of the system, with the simulation box sown in black, and the corresponding side view is shown in the bottom row. Peptides are shown as cartoon and for clarity only the phosphate beads of the lipids are shown, as orange spheres.

once interfacial the peptides diffuse independently at the bilayer surface, without aggregating, for the rest of the simulations (see snapshots at 1 µs and 5 µs). Although these results differ from those of a previous full-atom MD study where aggregates of 8 penetratin peptides formed at the lipid-solvent interface and led to invagination of the lipid bilayer [374], they are in agreement with another atomistic study which showed no tendency for aggregation [170]. They are also further supported by an experimental study where the authors did not detect oligomerisation of membrane-bound penetratin peptides [446], in contrast to other poly-cationic peptides [156]. Conversely, in transportan simulations, the peptides remained in their transmembrane orientation and as they diffused through the lipid bilayer they progressively clustered into larger and larger aggregates (Figure 4.9A), which is consistent with the self-association of primary amphipathic CPPs observed experimentally [482–484]. Visual observations of the clusters formed by transportan revealed that they did not adopt a stable, well defined structure but, rather, were highly dynamic as illustrated in Figure 4.10.



Figure 4.10 The flexibility of NMR-based structures (A and B) results in more disordered aggregates than those involving α-helical models (C). Horizontal lines indicate approximate bilayer boundaries. The red peptide in (A) illustrates how a peptide within a cluster can be entirely located in one leaflet.

In particular, the flexibility of the NMR-based structures appeared crucial in leading to more disordered aggregates as they involved peptides in different conformations, including some close to an interfacial state (eg red peptide in Figure 4.10A). Nonetheless, different clusters shape could be identified and these will be discussed in details in the next chapter. In order to quantitatively describe the aggregation of peptides and assess whether it was influenced by their secondary structure of the lipid distribution, I tracked the evolution with

time of the size of the biggest transmembrane cluster. This first required correctly identifying transmembrane clusters, which proved more complex than anticipated. Indeed, the criteria used earlier to determine the orientation and conformation of a single peptide (see 4.3.2) would fail to detect some peptides involved in clusters as being transmembrane (see Figure 4.10A). The approach eventually chosen relied on a two-step process:

1. **Detection of clusters.** Peptides clusters were detected, regardless of the peptides orientation, using the NetworkX Python module [485]. In short, this algorithm works by connecting together points which are within a specified distance of each other. In each frame of the simulations, the distance between each peptides was calculated, using the minimum distance between their particles, and the resulting distance matrix was processed with NetworkX. A cutoff of 8 Å was chosen to define contacts between peptides. Although contact between two CG beads is usually considered to occur at a distance of 6 Å, a slightly less stringent criteria was favoured in order to minimise high frequency noise. In practice this means that, for a given frame, a peptide was considered to be part of a cluster with other peptides if *any* one of its particles was within 8 Å of a particle belonging to one of the other peptides. Another cluster detection technique relying on a density-based approach was also tested [486], but the NetworkX connectivity-based method provided the best match between the clusters identified automatically and visual observations[1].

2. **Test of their transmembrane status.** In each frame the closest phosphate bead to each peptide particle within a cluster was determined. The whole cluster was then considered to be transmembrane if these phosphate beads belonged to different leaflets. This approach was also used to determine the orientation of peptides in a monomeric form (clusters of size one).

[1] This is an example of how the analysis of dynamic systems in MD simulations can greatly benefit from research in other fields and how the modular Python-based approach makes this convenient.

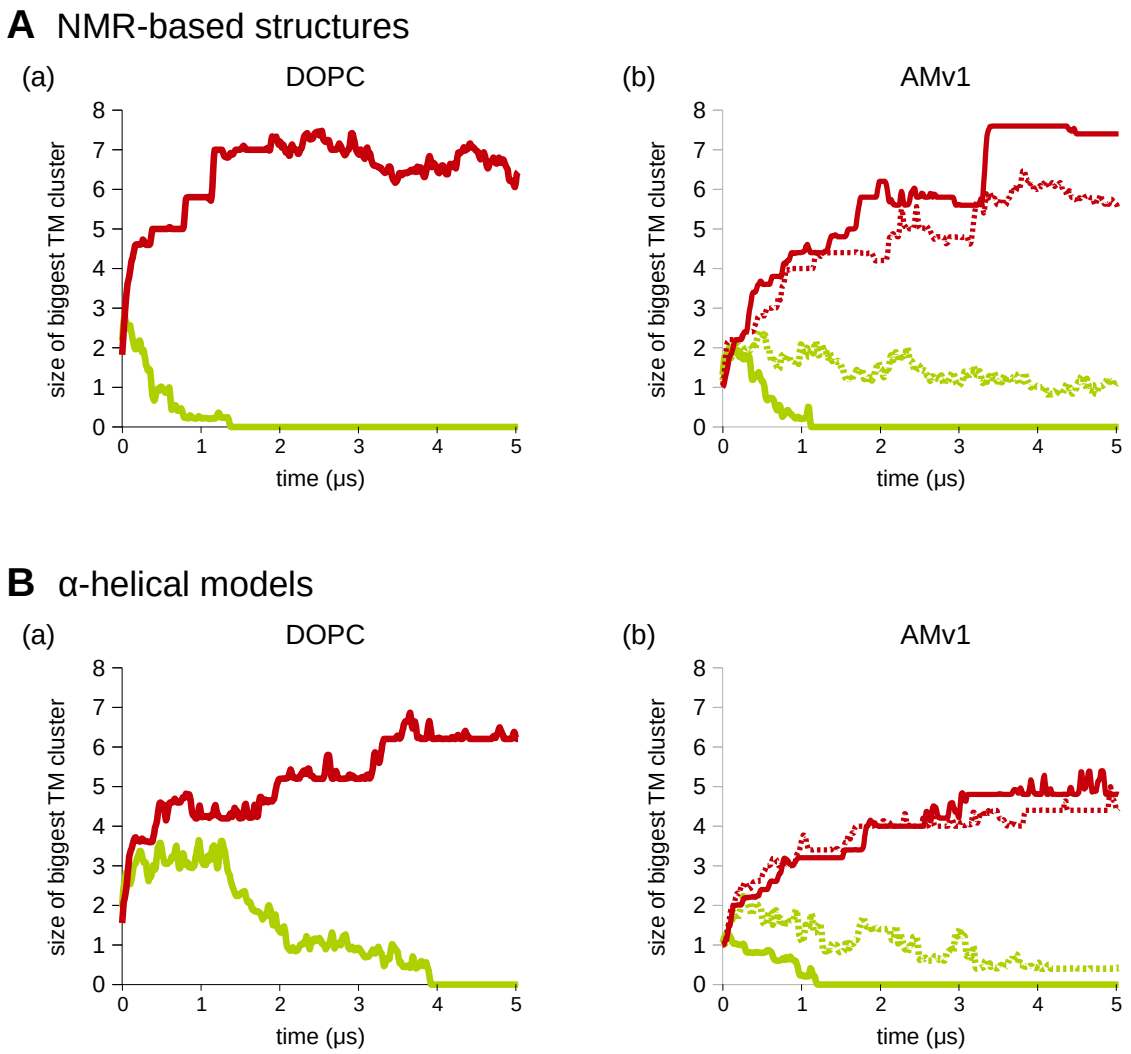

Figure 4.11 Evolution of the size of the biggest transmembrane clusters. The red and green lines correspond to transportan and penetratin clusters respectively. In asymmetric membranes, the solid lines correspond to simulations where the N terminus of the peptides was oriented outwards (in the zwitterionic leaflet) while the dotted lines correspond to the opposite orientation (C terminus outwards). Individual profiles were calculated for each repeat and the plots shown correspond to the average profile for each lipid environment, thus explaining why non integer cluster sizes are represented.

The transmembrane aggregation profiles obtained are presented in Figure 4.11. Comparison of the red and green lines provides quantitative evidence of the distinct behaviours of penetratin and transportan observed in Figure 4.9. In DOPC membranes, the data also reveal the influence of the secondary structure on the kinetics of aggregation and the stability of the peptides clusters. In the case of transportan, the aggregation of α-helical peptides appeared slowed down compared to that of the NMR-based structured ((a) in Figure 4.11A and B). This suggests that transportan flexibility is an important parameter in the aggregation process and the formation of stable peptide-peptide interactions. The structures presented in Figure 4.10 also illustrate how a polymorphic structure may be better accommodated within a cluster. On the other hand, in the case of penetratin, the α-helical models led to larger transmembrane clusters over longer periods of time. Although this is in apparent contradiction with the transportan results, it can be explained by the greater transmembrane stability of the fully α-helical structure observed previously for this peptide which allowed more time for penetratin peptides to meet and interact while in a transmembrane orientation. However, the clusters formed by α-helical penetratin remained small (trimers) and short-lived with the peptides eventually adopting an interfacial orientation after a few microseconds.

Additionally, the simulations performed in the AMv1 model plasma membrane demonstrated that the behaviour of the peptides was also affected by an asymmetric lipid distribution, particularly so when using the NMR-based structures. Indeed, the transmembrane stability of penetratin and the size of transportan aggregates appeared to be significantly influenced by the peptides initial orientation ((b) in Figure 4.11A). When positioned with their C terminus in the zwitterionic leaflet, a few penetratin peptides were found to remain in a monomeric transmembrane state throughout the simulations. This further supports the involvement of electrostatic interactions suggested previously (see 4.4.2) and can be explained by the relative positioning of penetratin asymmetric distribution of positive charges with respect to the anionic leaflet. When penetratin is positioned with its N terminus outwards, the

destabilising effect of the higher density of positive charges at its C terminus, which drag the peptide towards the interface, is enhanced by their interactions with negatively charged phospholipids present in the inner leaflet; on the other hand, in the opposite orientation, the C terminus charges provide an anchor in the zwitterionic leaflet that counter-acts the interactions between the anionic leaflet and the N terminus charges. The inability of the α-helical model to stretch to the same extent as the NMR-based structure may explain why the effect is less pronounced in these simulations. In the case of transportan, smaller aggregates formed when the NMR-based structures were oriented with their C terminus outwards. It will be demonstrated in the next section that this is also due to the influence of membrane asymmetry on the stability of the transmembrane orientation for transportan peptides.

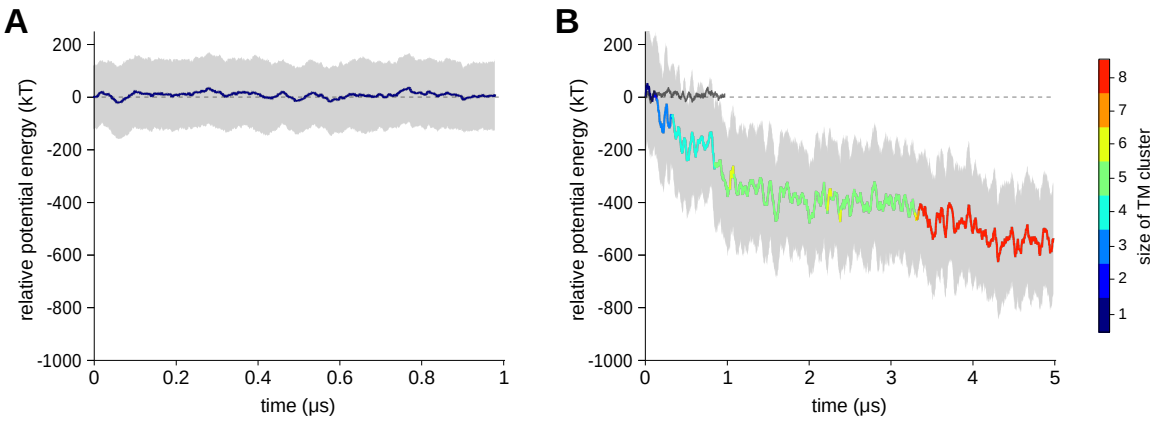

Figure 4.12 Evolution of the potential energy of (A) a POPC:POPS (85:15) system containing a single transmembrane transportan, and (B) a AMv1 system containing 8 transmembrane transportan. The energy of the whole systems were obtained using the Gromacs *g_energy* utility and the profiles coloured based on the size of the biggest transmembrane cluster. The average energy in (A) is reproduced in (B) as a grey line. The profiles allow for qualitative comparison only as the systems were of different sizes. In both cases the zero was set to the initial potential energy.

The comparison of transportan aggregation in the AMv1 and DOPC membranes also showed the influence of peptides concentration as the smaller DOPC membrane allowed peptide-peptide interactions to occur on a shorter timescale. However, the aggregation process appeared equally favourable in both environments. The stabilising effect of oligomerisation was further supported by the evolution of the systems potential energy (Figure 4.12).

Translocation

The number of peptides involved in transmembrane clusters and in an interfacial orientation in the last frame of each simulation is shown in Figure 4.13. As expected, the distribution of penetratin peptides confirms that very few retained their initial transmembrane orientation. It also shows an asymmetric distribution of interfacial peptides between the two leaflets in agreement with the role of electrostatic interactions described above. Indeed, the data show that penetratin preferentially reached the leaflet closer to its C terminus but that the presence of anionic lipids in the opposite leaflet counter-balanced this pattern to some extent.

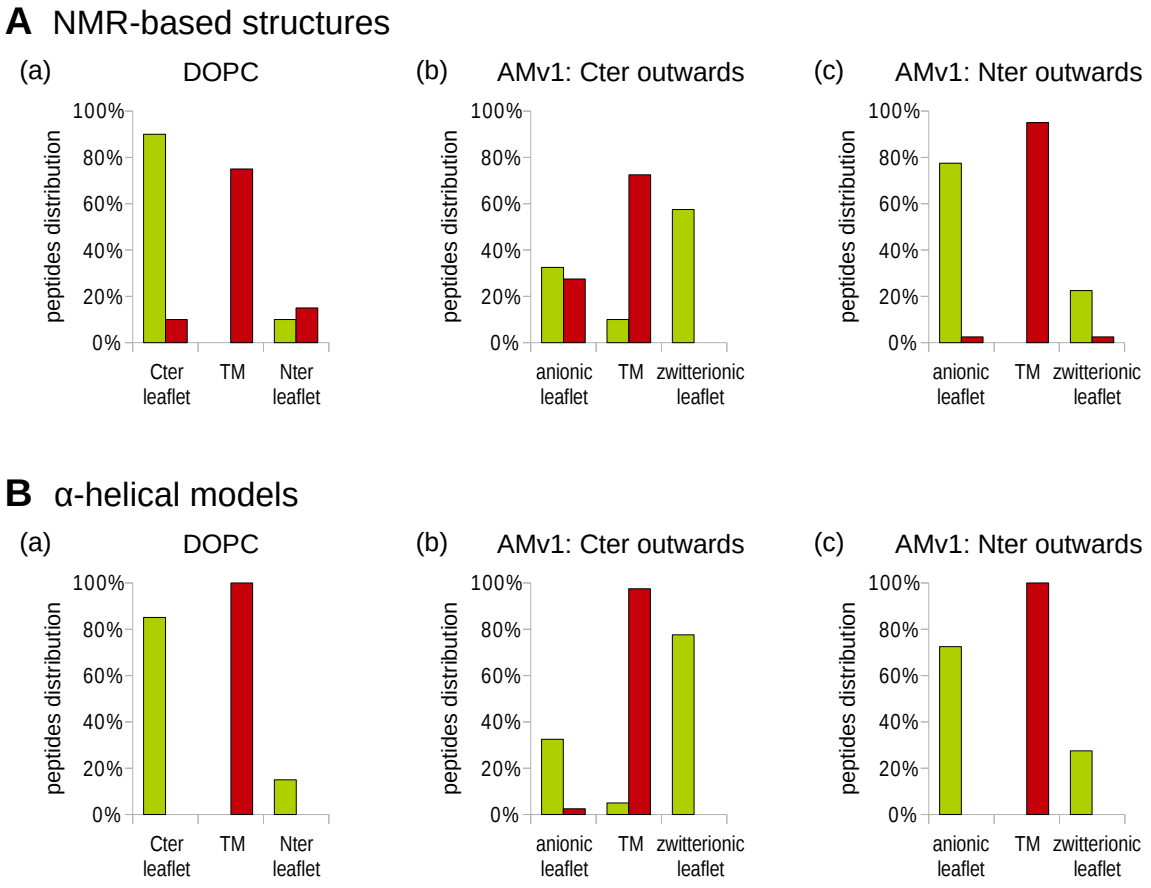

Figure 4.13 Orientation of transportan (red bars) and penetratin (green bars) in the last frame of the simulations involving 8 embedded peptides. The results of the different repeats were added together and in each plot thus represents the distribution of 40 penetratin and 40 transportan peptides. In DOPC simulations the leaflets are referred to with respect to the initial peptide position.

Interestingly, a few transportan peptides were also found to be in a final interfacial orientation. Here, it may be important to stress again that these do not take into account peptides which may be lying parallel to the bilayer surface but were still in contact with a transmembrane cluster. Combined to the earlier observations that monomeric transportan could not switch from a transmembrane to an interfacial orientation (see Figure 4.8), those results therefore indicate that the peptides detected as interfacial adopted this orientation within a transmembrane cluster from which they were then able to separate. This suggests that the aggregates formed by transportan may be a meta-stable intermediate state allowing the peptide to "translocate" and reach the more stable interfacial orientation. The fact that in simulations involving the α-helical models the peptides remained in a transmembrane orientation is evidence that conformational flexibility plays an important role in the ability of the peptide to reach the bilayer surface. Also, in asymmetric membranes, not only was translocation significantly enhanced when transportan was inserted with its C terminus outwards, but the peptides also all translocated towards the anionic leaflet. This indicates that the stability of transportan clusters is dependent on their lipid environment and explains the different aggregation profiles observed in Figure 4.11A(b). This will be examined in more details in the next chapter.

Altogether, these results suggest that the asymmetric distribution of negatively charged lipids, located in the inner leaflet of the plasma membrane only, may provide a driving force for the translocation of CPPs and they highlight the need to use biologically relevant membrane models to study their collective behaviour.

Desorption

Finally, it should be mentioned that in all but one of the DOPC simulations involving penetratin NMR-based structures, several peptides were observed to leave the lipid-solvent interface for the bulk solvent phase. In all cases, desorption required the cooperation of two

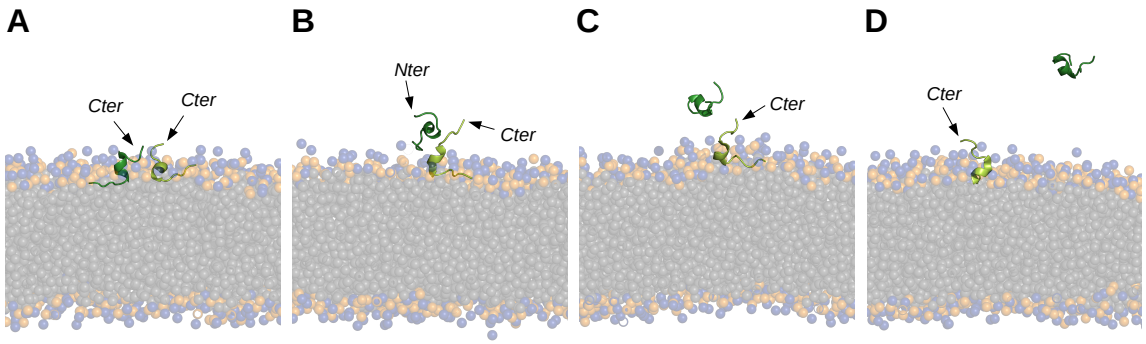

Figure 4.14 Desoprtion of an interfacial penetratin peptide from a DOPC membrane. The lipids are shown as transparent spheres, with the phosphate bead in orange, the choline bead in blue and the other beads in grey. After independenty diffusing at the bilayer surface, two penetratin peptides in an interfacial orientation interacted eventually leading to desorption of one. The process typically occurred over a few tens of nanoseconds.

peptides and snapshots illustrating the process are presented in Figure 4.14. interestingly, once they had left the lipid bilayer the peptides eventually bound back to it after randomly diffusing through the solvent and sometimes crossing the boundaries of the simulation box (in this case the leaflet they had first reached when switching from a transmembrane to an interfacial orientation was taken into account in Figure 4.13).

This is in good agreement with the weak binding of penetratin to zwitterionic membranes that has been reported experimentally [136, 322, 328, 447, 449, 450]. Furthermore, the fact that α-helical models remained bound to the lipid bilayer is consistent with experimental studies showing this conformation is more stable than a disordered one when penetratin resides at the lipid-solvent interface [135, 443–445, 487] and supported by *in vitro* experiments which demonstrated that the binding of secondary amphipathic peptides to zwitterionic bilayers, in contrast to anionic ones, was dependent on their α-helical structure [488]. The need for two peptides to cooperate as well as their relative orientation suggest that peptide flexibility plays an important role in allowing escape from the bilayer. Indeed, as can be seen in Figures 4.14B and C, the desorption occurs through peptide-peptide interactions along the solvent exposed C terminus of the peptide remaining bound to the membrane. I therefore calculated the solvent exposure of penetratin residues when in an interfacial ori-

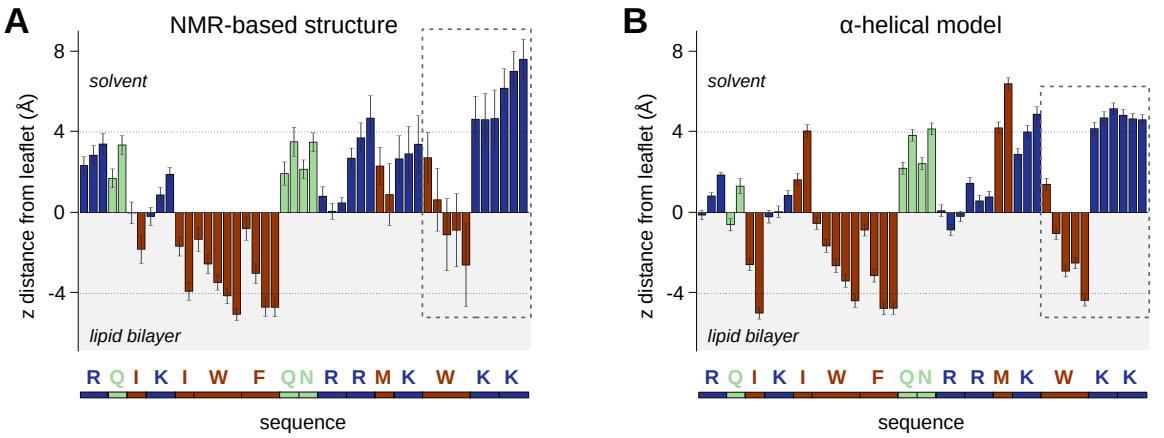

Figure 4.15 Solvent exposure of penetratin residues when in an interfacial orientation in a DOPC bilayer. Positively charged residues are shown in dark blue, polar and hydrophilic ones in light green and hydrophobic ones in dark red. In each repeat, the average distance along the z axis between the residues beads and the phosphate beads plane was calculated. The plots shown correspond to the average between repeats and the error bars indicate the standard deviation. The dashed rectangles highlight the different mobility of the C terminus residues.

entation for both the α-helical model and the NMR-based structure (Figure 4.15). I found that the difference between the two conformations is mainly located towards the C terminus, with the WKK motif more exposed to solvent and much more flexible as indicated by the large error bars. Given that the interfacial depth of insertion was found to be very similar for the two conformations (see Figure 4.7), this may actually account for the inability of the α-helical models to form interactions leading to their desorption, and, similarly to what was observed regarding aggregation of transportan peptides, it again highlights the importance of secondary structure in peptide-peptide interactions.

4.4.4 Peptide-membrane interactions

In addition to comparing the collective behaviour of penetratin and transportan, their respective influence on the lipid bilayer was also investigated and the impact of their presence on the bilayer thickness and acyl chains order parameters was studied. Indeed, visual inspections of the simulations revealed that the peptides appeared to induce some degree of local disorder in the membrane, and one would expect these two bilayer parameters to capture

this effect. However, the local calculation of these properties raises technical difficulties and several publications have been dedicated to this issue [489, 490]. Yet, the methods proposed in the literature all require averaging of the data over tens of nanoseconds (80 ns in [490]) and although this is a valid approach to characterise pure bilayers or the effect of a single protein on which the systems can be centred, it is not suitable to the description of simulations involving several highly mobile peptides that can form dynamic aggregates. I therefore implemented a custom approach allowing to estimate those parameters on a shorter and more local scale in order to characterise bilayer perturbations induced by the CPPs.

Bilayer thickness

The lipid bilayer thickness is traditionally measured as the distance along the z axis between opposite phosphorous atoms (all-atom simulations) or phosphate beads (CG representations). For a global characterisation of the system the peak-to-peak distance between the density profiles of the reference particles in the upper and lower leaflets is used. In contrast, a local calculation of the bilayer thickness involves processing each reference particle in each leaflet and assigning it a thickness value. As described in [489], this is achieved by finding the nearest neighbour of a reference particle in the opposite leaflet and subtracting their z coordinates. However, because only the x and y directions are taken into account to pair particles in opposite leaflets, this method only works in small, planar bilayers and leads to artefact in membranes with locally curved areas. It can be argued that the natural fluctuations and undulations observed in larger bilayers are smoothed out when performing time averages but the dynamic behaviour of the peptides occurred on too short timescales to allow such smoothing as the peptides would have diffused significantly during the averaging window. In any case, the fact remains that the planar approximation is not an accurate way to measure bilayer thickness in very large lipid bilayers with significant, non-transient, curvature as will be presented at the end of this thesis. Additionally, with a technique relying on

a single nearest neighbour, the results can be strongly perturbed by the position of a single phospholipid, which might not be an accurate representation of the local thickness. Again, time averaging allows to mitigate this issue to some extent. In order to overcome those problems, the nearest neighbours of a reference particle were identified using the euclidian distance between particles and the local bilayer thickness was determined by calculating the average distance of each reference particle to its five nearest neighbours, as illustrated in Figure 4.16.

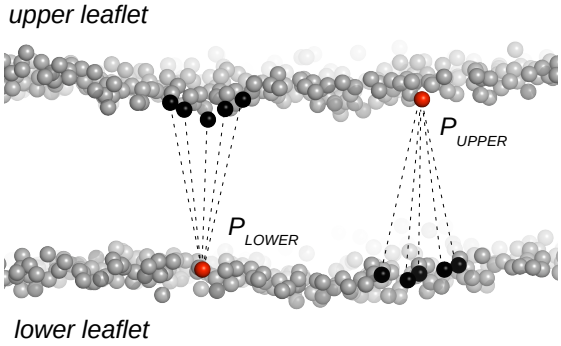

Figure 4.16 Calculation of local bilayer thickness. The phosphate beads of the lipids are shown as spheres. The coloured beads represent reference points (red) and their five nearest neighbours in the opposite leaflet (black). The thickness associated to each reference point is the average distance between red and black beads. This method does not require the bilayer to be in the x, y plane.

For visual representation, a 2D thickness matrix was built by binning the phosphate beads in a 40×40 grid based on their x, y coordinates. The AMv1 membranes containing 1300 lipids measured approximately 18×18 nm and each grid cell thus had an approximate area of 20 Å^2. This is about 3 times smaller than the area per lipid of POPC [491] and while it provides a good resolution it also means that the grid was sparsely populated by the lipids. To improve grid sampling the data of 10 consecutive frames were binned together, which corresponded to a reasonably short averaging window of 2 ns. For each grid cell containing at least a particle, a thickness value was then calculated by averaging the thickness associated to the phosphate beads present within the cell. The thickness value of empty grid cells was iteratively calculated by averaging the values of the 8 neighbouring cells, taking

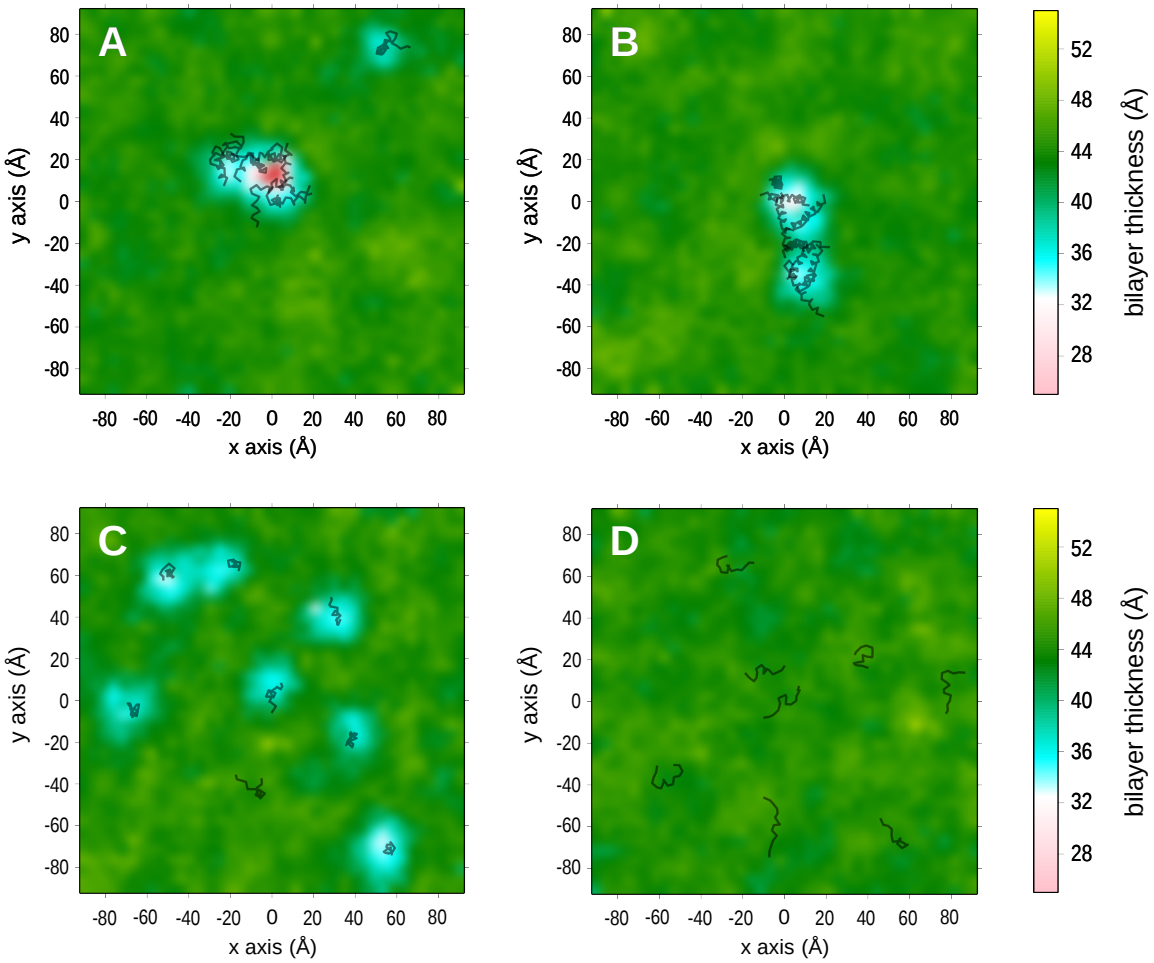

Figure 4.17 Snapshots of the thickness of the asymmetric AMv1 bilayer in the presence of (A) 8 transportan peptides using the NMR-based structures, (B) 8 transportan peptides using the α-helical structures and (C-D) 8 penetratin peptides using the NMR-based structures. In (C) all the penetratin peptides but one are still in a transmembrane orientation whereas in (D) they have all reached the bilayer surface. Bilayer thickness in the presence of α-helical models of penetratin is not shown but was similar to that observed with the NMR-based structures. The snapshots were obtained by averaging the data over 10 consecutive frame, corresponding to an averaging window of 2 ns. Thickness values below 25 Å are coloured in red. Peptides are represented in black by their Cα backbone.

periodic boundary conditions into account. The thickness matrix was then plotted using matplotlib [492] and a bicubic interpolation between grid points.

Using this custom approach, the evolution of the bilayer thickness was examined in the simulations performed and snapshots representative of the findings are presented in Figure 4.17. The analysis revealed that, unlike penetratin, transportan peptides were able to induce significant local thinning of the lipid bilayer. This effect appeared most pronounced when the peptides aggregated, as evidenced by the comparatively unperturbed bilayer around the monomeric peptide in Figure 4.17A. In addition, bilayer thinning was also enhanced around transportan NMR-based structures compared to α-helical models. These observations suggest that peptides cooperation and structure flexibility play a crucial in the interactions of transportan with lipid bilayers. The comparison of the aggregates formed by transportan, presented in Figure 4.18, further support this hypothesis. Indeed, the snapshots reveal that bilayer thinning is induced via the formation of flexible clusters able to "pinch" the bilayer by dragging the lipid head groups into the membrane core. The influence of the size of transportan aggregates, as well as that of the membrane composition and asymmetry, on the extent of the membrane thinning will be examined in detail in the following chapter.

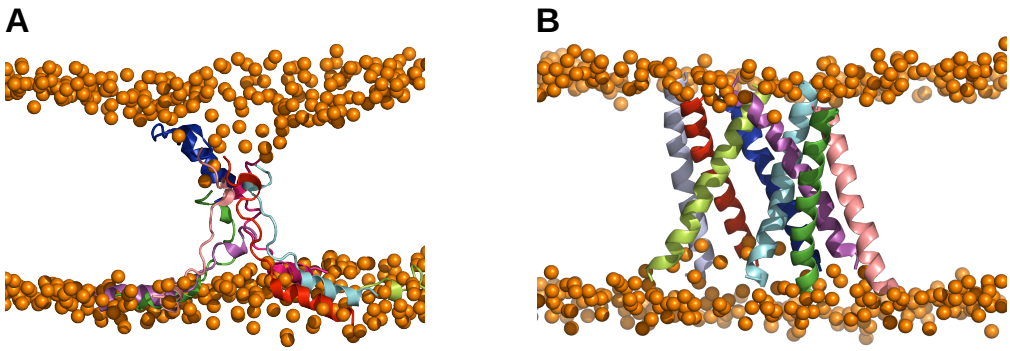

Figure 4.18 Bilayer thinning induced by transportan clusters in simulations using (A) NMR-based structures and (B) α-helical models. The orange spheres represent the lipids phosphate beads. In (A) the compact and flexible cluster shape drags the lipids head group inside the membrane core by forming a funnel-like invagination. In (B), although lipids in the lower leaflet are attracted by the loose arrangement of the more rigid α-helical structures, they do not penetrate the membrane as deeply as in (A).

In the case of penetratin, regardless of the secondary structure, transient bilayer thinning was observed when the peptides were in a transmembrane orientation (Figure 4.17C), but the peptides appeared to have no effect on the membrane thickness once they reached the bilayer surface. It is interesting to note that, when in a monomeric transmembrane state, penetratin peptides induced more thinning than transportan peptides (by a few Å). This is consistent with penetratin higher charge density and the strong interactions between its cationic residues and the bilayer surface that have been described in the previous section. The hypothesis that electrostatic interactions play a critical role in the perturbation of the bilayer may also explain why the bilayer thinning is enhanced by the aggregation of transportan peptides since clustering of the peptides leads to an increase in the local charge density. Conversely, the inability of penetratin to aggregate within the membrane due to the instability of the transmembrane orientation prevents further thinning of the bilayer.

It should be noted that the different extent to which penetratin and transportan disturb their local lipid environment is in qualitative agreement with the greater membrane destabilisation reported experimentally for transportan (see 4.2.2). However, it should be stressed that neither pore formation nor water permeation were observed in any of the transportan simulations performed, in contrast to what has been reported in previous CG simulations of antimicrobial peptides [178, 182, 422]. This is an important point as it shows that, despite its primary amphipathic nature, CG representations can distinguish between the membrane destabilisation induced by this CPP and the membrane lytic activity of AMPs.

Acyl chain order parameters

A standard way to measure the fluctuations of the orientation of lipid molecules in a bilayer around a reference axis is to calculate the second rank order parameter presented in [493]:

$$S_{ij} = \frac{1}{2}\left(3\langle\cos^2\theta_{ij}\rangle - 1\right) \tag{4.1}$$

where θ_{ij} represents the angle of the bond between the atoms i and j with the reference axis and the angular brackets denote an ensemble average. Order parameters can be determined accurately in lipids bilayer by solid-state ^{2}H NMR experiments [494] and, despite comparatively limited time and population sampling, atomistic molecular dynamics simulations have been shown to satisfyingly reproduce the S_{CD} and corresponding S_{CC} values [495]. In CG simulations, an equivalent definition relying on the vector between consecutive lipid beads has been used [237] and shown to be in good agreement with data obtained using full-atom representations [496].

It is important to understand that order parameters correspond to an ensemble average over time and as such depend on both the system disorder and its orientation. For example, an S_{CC} order parameter close to zero can correspond to a very disordered system or to a well ordered system where the lipids chains are all oriented so that $\theta \approx 55^\circ$. In order to provide a simple metric describing the orientation of each lipid in each frame of the simulations performed, equation 4.1 was adapted to calculate an average order parameter value, P_2, for the acyl chains of a given lipid:

$$P_2 = \frac{1}{2}\frac{\sum_{i=1}^{n_A}\left(3\cos^2\theta_i - 1\right) + \sum_{i=1}^{n_B}\left(3\cos^2\theta_i - 1\right)}{n_A + n_B} \tag{4.2}$$

where n_A and n_B represent the number of bonds taken into account in the acyl chain of each lipid tail. The θ_i angles were measured with respect to the z axis and the P_2 value is thus a simple measure of the overall orientation of the lipid tails relatively to the bilayer normal, as illustrated in Figure 4.19. Here it is important to stress that due to the flexibility of the two acyl chains, P_2 is a fairly crude metric of a lipid orientation with different conformations possibly leading to the same average value. Furthermore, the method assumes that the bilayer is contained within the x,y plane with its local normal parallel to the z axis and it therefore suffers from the same limitations as those discussed in the previous section on bilayer thickness. However, unlike the simple approach implemented to measure the local

bilayer thickness, the definition of a local normal to the lipid bilayer is a complex problem that yet remains to be solved.

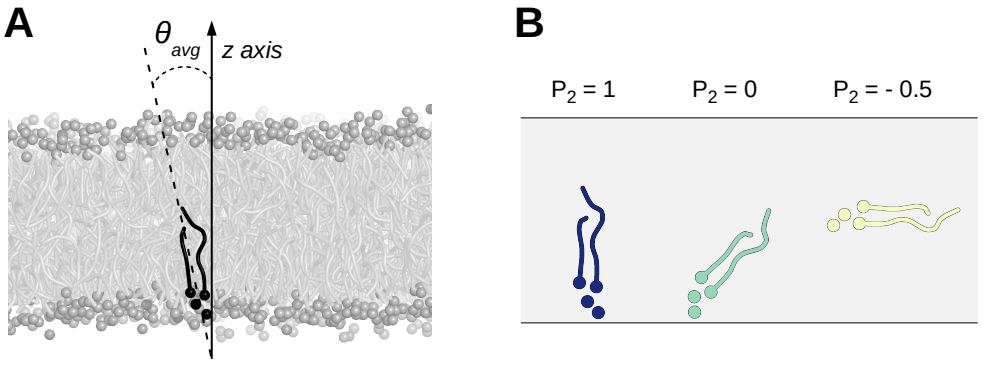

Figure 4.19 (A) Approximate overall angle between a lipid acyl chains and the bilayer normal, represented by the z axis. (B) Schematic representations of the acyl chain orientations corresponding to different P_2 values. It is important to bear in mind that the acyl chains are flexible and can adopt independent orientations and that therefore different lipids conformations can lead to the same average P_2 value.

In spite of these shortcomings, the comparative analysis of the simulations performed proved informative, as can be seen in Figure 4.20. Transportan clusters appeared to influence the orientation of the lipids in their vicinity, and Figure 4.20A again illustrates the crucial role of aggregation in the peptides ability to disrupt the lipids organisation as the orientation of the lipids around the monomeric peptide is not modified. Similarly to what was observed regarding the bilayer thickness, transportan NMR-based structures also induced stronger local membrane perturbations than the α-helical models, although the difference appeared less pronounced than for their respective thinning effect. The decrease of the P_2 value induced by transportan aggregates on neighbouring lipids show that those lipids tend to adopt a parallel orientation to the bilayer (see Figure 4.19) and is consistent with the pinching of the membrane described previously (Figure 4.18). Conversely, previous MD simulations have shown that an increase in the acyl chains order parameters led to a thickening of the lipid bilayer [353, 497]. While these results may be in agreement with the structure of a disordered toroidal pore as observed in CG MD studies of AMPs [177, 178, 422], it is important to

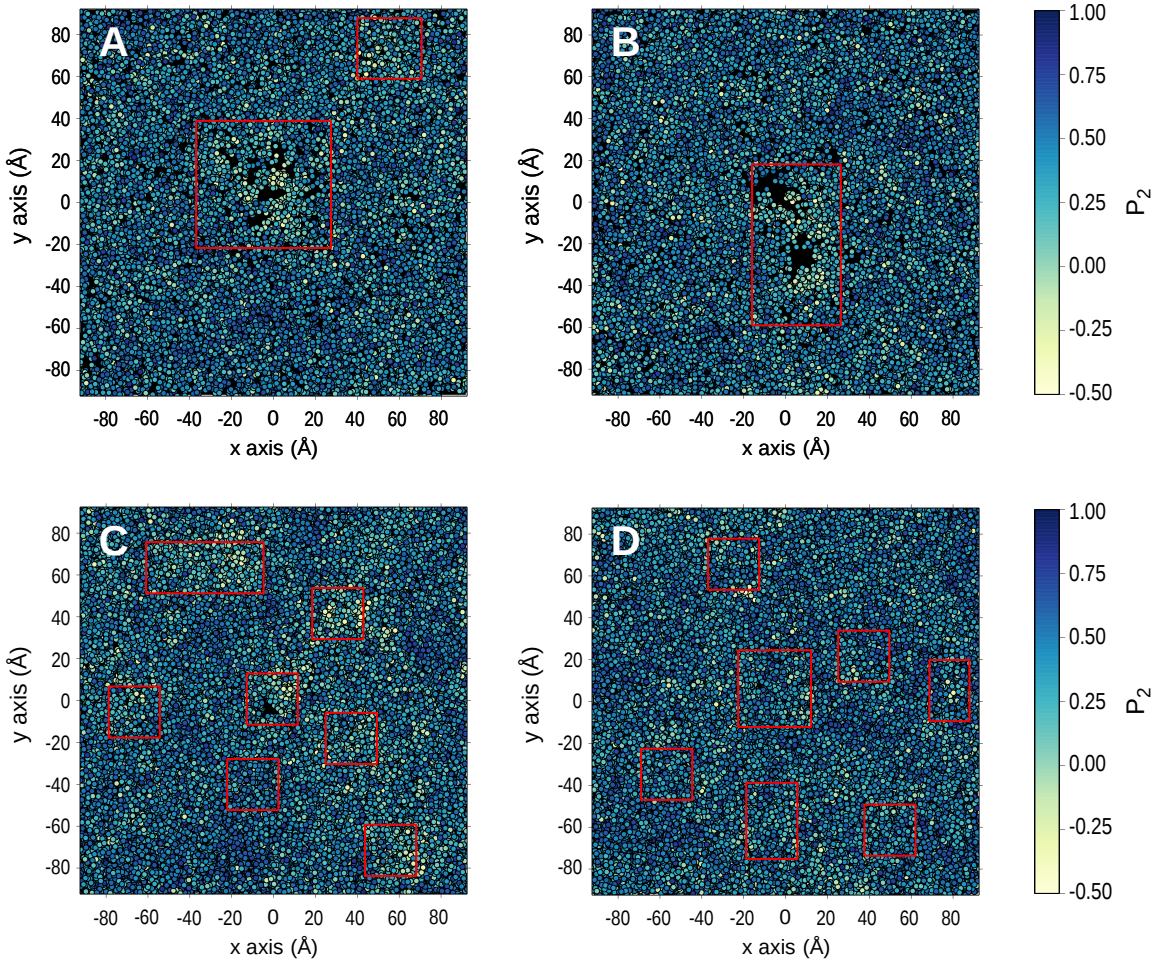

Figure 4.20 Snapshots of the lipids average order parameter P_2 in an asymmetric AMv1 bilayer in the presence of (A) 8 transportan peptides using the NMR-based structures, (B) 8 transportan peptides using the α-helical structures and (C-D) 8 penetratin peptides using the NMR-based structures. The systems are the same as those presented in Figure 4.17, the peptides have been omitted for clarity but their position is delimited by red rectangles. The lipids are represented by their phosphate beads only, shown as spheres coloured based on the P_2 value associated to the lipid. Each plot contains the data of 25 consecutive frames (corresponding to 5 ns) in order to increase spatial sampling.

bear in mind their limited extent and that the bilayer integrity was maintained in all simulations with no signs of pore formation. Interestingly, although penetratin also induced some local disorder of the acyl chains when in a transmembrane orientation, the effect appeared to vary greatly between peptides (see Figure 4.20C), somewhat in contrast to what had been observed for the bilayer thickness. On the other hand, none of the interfacial penetratin peptides had any influence on the orientation of the lipid bilayer (Figure 4.20D).

Altogether these results provide additional evidence of the different destabilising effect that penetratin and transportan on lipid bilayers.

4.5 Conclusion

In this chapter I presented comparative simulations of transportan, a chimeric primary amphipathic peptide, and penetratin, a secondary amphipathic peptide derived. Transportan has been shown to be more membrane toxic than penetratin. The CG simulations performed revealed that the peptides adopted different preferential orientation in presence of a membrane mimicking environment and that, in contrast with transportan and its more hydrophobic nature, the transmembrane orientation of poly-cationic penetratin was highly unstable. Despite the reduced resolution of the CG representation, the results obtained were consistent with previous full-atom MD studies of these peptides when residing at the lipid-solvent interface.

In agreement with experimental studies, penetratin was also found to exhibit weaker binding to zwitterionic membranes when using a disordered structure model, with the cooperation of several peptides leading to temporary desorption of the membrane surface. Interestingly, simulations of penetratin peptides embedded in an asymmetric membrane also showed that, driven by electrostatic interactions, they preferentially translocated towards the inner anionic leaflet, which is consistent with their cellular internalisation of CPPs. It should be pointed that this effect would be further enhanced by the presence of a transmembrane potential. On the other hand, transportan peptides aggregated into large disordered

transmembrane clusters over the course of the simulations. Transportan behaviour was also influenced by its secondary structure, with the slower rate of aggregation observed for α-helical models showing that peptides flexibility is an important parameter in the formation of stable peptide-peptide interactions. The importance of cooperation between peptides was illustrated further by the ability of some transportan peptides to reach the bilayer surface and leave the transmembrane cluster they were involved in whereas monomeric peptides remained in a transmembrane orientation. This suggests that transportan aggregates represent a metastable state allowing the peptide to translocate. The stability of transportan clusters was influenced by the asymmetry of the membrane and, again, peptides were observed to preferentially translocate towards the anionic leaflet. Altogether these findings thus highlight the importance of using biologically relevant membrane models for the *in silico* study of CPPs.

Finally, I also presented the implementation of methods allowing to characterise local membrane perturbations induced by the peptides on a short timescale compatible with their dynamic behaviour. The use of these methods showed that transportan aggregates led to significant thinning of the lipid bilayer and disorder of the lipids acyl chains. This is consistent with recent dynamic light scattering and solid-state NMR studies which showed that the ability of antimicrobial peptides to form oligomeric aggregates in the cell membrane enhance their potency [498–500]. However, unlike what was reported in previous simulations of antimicrobial peptides [177, 178, 422], no pore formation was observed and the bilayer integrity was maintained in all simulations. In contrast, penetratin unstable transmembrane orientation only induced minor and transient perturbations of the membranes. These results are in good agreement with the respective membrane toxicity of transportan and peptides reported experimentally and provide a framework to study CPP-induced membrane perturbations via CG MD simulations. They also showed that the flexibility of the peptides, allowing transportan to adopt different transmembrane conformations, appeared to play an

important role in their ability to aggregate into membrane destabilising structures. In the rest of the thesis I will therefore focus on NMR-based structures of transportan to characterise in more details the perturbations this CPP can induce in plasma membrane models.

Chapter 5

Aggregation of transportan peptides and associated membrane perturbations

5.1 Introduction

In the previous chapter, comparative simulations of the collective behaviour of transportan and penetratin, two well studied CPPs, revealed that only transportan molecules could form transmembrane aggregates that appeared to correlate with local perturbations of the lipid bilayer. This is in good agreement with the greater membrane toxicity reported for transportan experimentally [128, 143, 146, 456, 462, 466] and makes this peptide a suitable candidate to explore *in silico* the destabilisation of lipid bilayers induced by the activity of a CPP. In this chapter I will therefore focus on the characterisation of the aggregates formed by transportan molecules and on how they influence the local properties of their lipid environment. In particular, the aim of this chapter is to take advantage of CG MD simulations to address limitations associated with experimental techniques that hinder the elucidation of the mechanisms by which CPPs interact with lipid bilayers. Indeed, although several *in*

vitro studies have shown that the destabilisation of lipid bilayers by membrane active peptides is concentration dependent [472, 474–477] and suggested that such molecules are only active as aggregates [498–500], it remains difficult to obtain experimental evidence for the exact numbers of peptides involved in *transient* clusters [44, 501]. Similarly, dye-leakage assays [502] or electrophysiological measurements [180] usually performed to assess the extent of membrane destabilisation induced by CPPs do not readily inform on the peptide-lipids structures at the origin of bilayer perturbation. Additionally, while X-ray based techniques such as small-angle X-ray scattering (SAXS) [101, 503] or lamellar X-ray diffraction (LXD) [504] allow to monitor the evolution of bilayer properties such as thickness in the presence of CPPs, they correspond to ensemble measures which do not give access to the extent of local perturbations. Likewise, although the use of symmetric vesicles with different lipid mixtures has demonstrated the importance of composition on the interaction of membrane active peptides with lipid bilayers, highlighting for instance the role of anionic lipids (eg [505]), MD simulations present an opportunity to investigate such preferential interactions at the molecular level in model membranes where the distribution of lipid species is precisely controlled in each leaflet. This chapter thus expands on the results shown in the two previous ones in order to present an in-depth study of the evolution of the size and structural characteristics of transportan aggregates and of the local membrane perturbations induced by these in biologically relevant lipid environments. In this regard, a systematic investigation of the influence of lipid species distribution on transportan transmembrane stability and its destabilisation of the membrane model is performed, notably to assess the effect of asymmetry in the plasma membrane of mammalian cells on the behaviour of CPPs.

5.2 Transportan in biological membrane models

All the results presented in this chapter rely on simulations involving the NMR-based structure of transportan as described in 4.2.3. Unlike the α-helical model presented previously

(see 4.2.3), this structure corresponds to an actual experimental structure determined in a membrane mimetic environment [426] and its flexibility around the central kink linking the galanin and mastoparan domains appeared to play a crucial role in transportan ability to form transmembrane oligomers and disturb the lipid bilayer (see 4.4.3). This first section details the choice and method of the simulations executed in order to perform a systematic study of the behaviour of this transportan structure in biologically relevant systems.

5.2.1 Composition of membranes

The AM model described in Chapter 3 was selected as a model of a mammalian cell plasma membrane since, as explained earlier, it allows a simple comparison of the respective influence of the lipid species in each leaflet. In order to assess the role played by membrane asymmetry, transportan was also studied in presence of symmetric membrane models that had the lipid composition of the zwitterionic leaflet (SMz) or that of the anionic leaflet (SMa). Finally, as a control, I also performed simulations of transportan in presence of a simple POPC bilayer. Table 5.1 summarises the composition of the different bilayers used.

Table 5.1 Lipids composition of the membrane models used in this chapter. The SMz and SMa models are symmetric membrane models with the respective compositions of the outer and inner leaflets of the asymmetric membrane model (AM). The pure POPC bilayer acts as a cholesterol free zwitterionic control. Both POPC and POPE are zwitterionic lipids, while POPS has a negatively charged head group. Structures of the lipids are detailed in Appendix A.

				AM	
	POPC	**SMz**	**SMa**	outer	inner
POPC %	100	60	25	60	25
POPE %	-	15	25	15	25
POPS %	-	-	25	-	25
CHOL %	-	25	25	25	25

These membrane models allowed me to study transportan in presence of a biologically relevant environment (AM), as well as to separately assess the role of properties thought to be involved in the activity of CPPs such as the presence of anionic lipids, cholesterol and

curvature inducing lipids as well as membrane asymmetry.

5.2.2 Simulations performed

In most of the simulations performed transportan was initially embedded in the lipid bilayer but a few simulations were also performed starting with transportan in an interfacial orientation to check whether spontaneous insertion into the lipid bilayer could be observed. All the simulations referred to in this chapter are summarised in Table 5.2 and the two sections below provide details on why and how these were set-up.

Embedded simulations

As mentioned in the previous chapter, the use of the Gromacs *g_membed* utility raises issues regarding the stability of the systems created as well as their reproducibility. To remediate this problem, the embedded simulations performed in this chapter relied on a different approach: a frame was selected from self-assembly (SA) simulations to provide an equilibrated structure of transportan embedded in a lipid bilayer and then the in-house script described in section 3.3.2 was used to achieve the desired lipid composition. The system obtained in this way can then be replicated along the *x* and *y* directions in order to create larger membrane patches containing several embedded peptides, as represented in Figure 5.1.

This protocol allowed me to assess the stability in each membrane model of the two possible transmembrane conformations identified in Chapter 4 (TM and TM*, see Figure 4.5) by performing small single peptide simulations over an extended timescale (5 µs). The impact of multiple transportan peptides on the different lipid bilayers were then studied by performing larger simulations involving 9 peptides. For the sake of simplicity, all the peptides were positioned with the same initial orientation in systems involving the AM model, and simulations were performed for both possible initial orientations, either starting with the N terminus positioned in the zwitterionic leaflet ("Nter outwards") or with the C terminus.

Table 5.2 Simulations of transportan in different membrane models. TM and TM* indicate the starting conformation of transportan when initially positioned in a transmembrane orientation; this specifies the position of the kink in transportan structure and whether the galanin or mastoparan domain is closer to the membrane surface (see Figure 4.5 in previous chapter). In asymmetric membranes, the orientation of transportan peptides is indicated by specifying which terminus was closer to the outer (zwitterionic) leaflet for transmembrane conformations or, in the case of an interfacial orientation, by simply indicating in which leaflet the peptides resided. P:L indicates the respective number of peptides and lipids in the simulations.

Lipid composition	**P:L**	**Initial conformation**	**Initial orientation**	**Duration** (μs)	**Repeats**
Embedded simulations: small membrane (ES)					
POPC	1:124	TM	-	5	3
SMz	1:124	TM	-	5	3
SMa	1:124	TM	-	5	3
AM	1:124	TM	Nter outwards	5	3
AM	1:124	TM	Cter outwards	5	3
POPC	1:124	TM*	-	5	3
SMz	1:124	TM*	-	5	3
SMa	1:124	TM*	-	5	3
AM	1:124	TM*	Nter outwards	5	3
AM	1:124	TM*	Cter outwards	5	3
Embedded simulations: large membrane (EL)					
POPC	9:1116	TM	-	15	3
AM	9:1116	TM	Nter outwards	15	3
AM	9:1116	TM	Cter outwards	15	3
SMz	9:1116	TM*	-	15	3
SMa	9:1116	TM*	-	15	3
Interfacial simulations: large membrane (IL)					
POPC	9:1116	interfacial	-	15	1
AM	9:1116	interfacial	outer leaflet	15	1

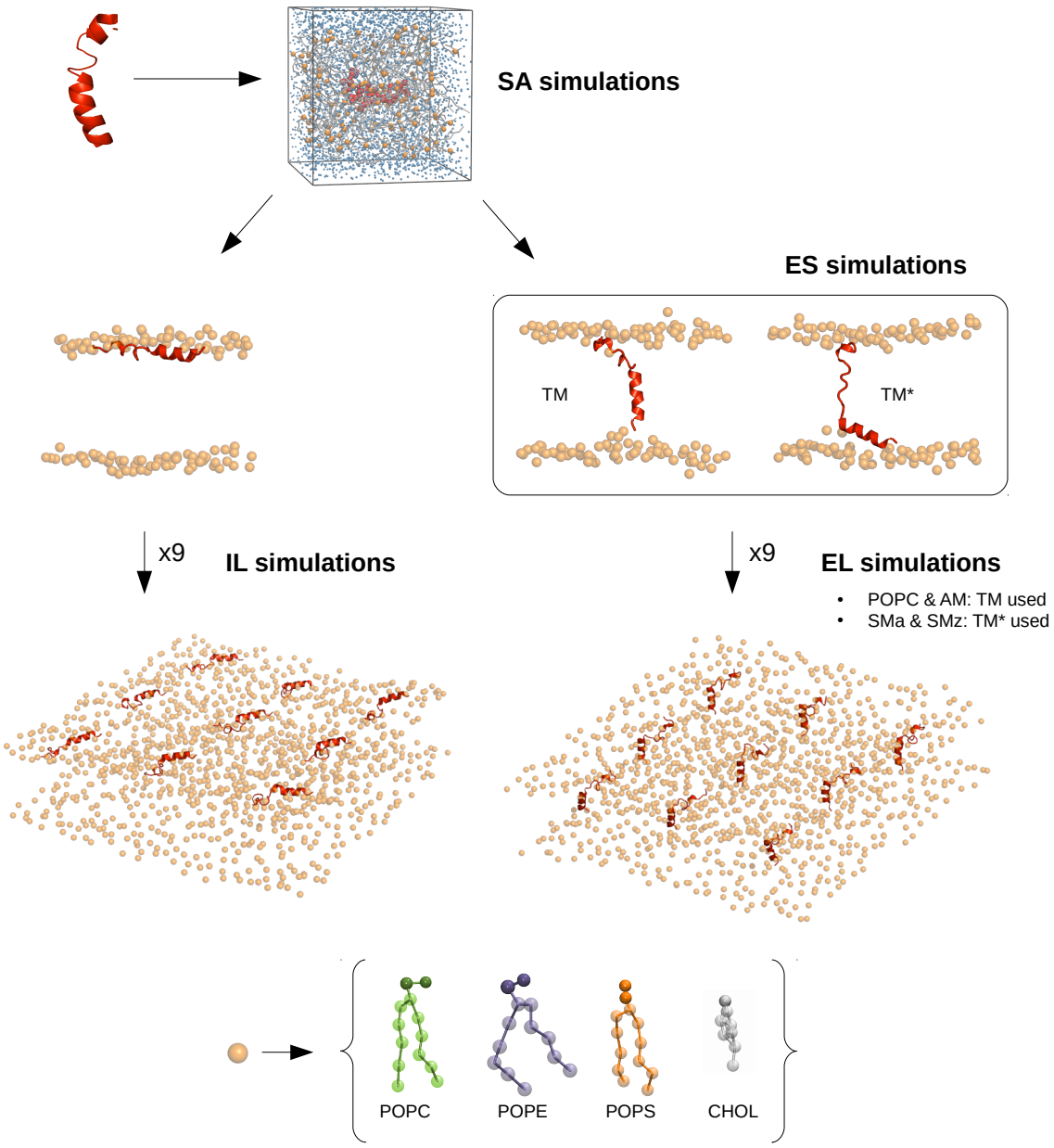

Figure 5.1 Flow chart illustrating how the simulation systems were built. Transportan peptides are represented in red as cartoon, the lipids phosphate beads as orange spheres and water particles in blue as small spheres. The lipid composition was controlled using an in-house script [403] and the relative % of the POPC, POPE, POPS and CHOL species in each system is summarised in Table 5.1. See Table 5.2 for details on the ES, IL and EL simulations.

Interfacial simulations

As illustrated in Figure 5.1 a similar approach to that described above was used to build systems were transportan was initially in an interfacial conformation. The goal of these simulations was to check whether several transportan peptides could cooperate to penetrate the lipid bilayer as had been reported for other membrane active peptides in previous computational studies [177, 178, 183, 346, 421, 422].

5.3 Transportan orientation and conformations

This section first discusses the influence of the lipid environment on the stability of transportan orientation and conformation.

5.3.1 Relative stability of transmembrane monomers

The relative stability of transportan TM and TM* conformations was examined by comparing the outcome of the simulations containing a single peptide in different lipid bilayers. The conformation adopted by transportan at the end of these ES simulations is summarised in Table 5.3. As can be observed in this table, transportan preferentially adopts a TM conformation when transmembrane, thereby indicating that the TM* state is less energetically favourable. However, the AM and SMa simulations also highlight the importance of the distribution of anionic lipids on the stability of transmembrane conformations. Indeed, the fact that transportan remained in a TM* conformation in two AM simulations (when oriented with its N terminus outwards) and in one SMa simulation may suggest at first that negatively charged lipids can have a stabilising effect on this cationic peptide. Yet, the opposite is observed in AM simulations where transportan was oriented with its C terminus outwards: not only did the TM* conformation never remain stable but in two repeats transportan reached an interfacial orientation on the anionic leaflet from a TM conforma-

Table 5.3 Final conformation adopted by transportan in the ES simulations. The lipid composition of the different membrane models can be found in Table 5.1. TM and TM* indicate the different transmembrane conformations, they differ by the position of the kink in transportan structure and whether the galanin or mastoparan domain is closer to the membrane surface (see Figure 4.5).

Lipid composition	**Transportan orientation**	**Conformation** $t = 0\mu s$	$t = 5\mu s$
POPC			
POPC #1	-	TM*	TM
POPC #2	-	TM*	TM
POPC #3	-	TM*	TM
POPC #4	-	TM	TM
POPC #5	-	TM	TM
POPC #6	-	TM	TM
AM			
AM #1	Nter outwards	TM*	TM
AM #2	Nter outwards	TM*	TM*
AM #3	Nter outwards	TM*	TM*
AM #4	Cter outwards	TM*	interfacial (inner leaflet)[1]
AM #5	Cter outwards	TM*	TM
AM #6	Cter outwards	TM*	TM
AM #7	Nter outwards	TM	TM
AM #8	Nter outwards	TM	TM
AM #9	Nter outwards	TM	TM
AM #10	Cter outwards	TM	interfacial (inner leaflet)
AM #11	Cter outwards	TM	TM
AM #12	Cter outwards	TM	TM
SMa			
SMa #1	-	TM*	TM
SMa #2	-	TM*	TM*
SMa #3	-	TM*	TM
SMa #4	-	TM	TM
SMa #5	-	TM	TM
SMa #6	-	TM	TM
SMz			
SMz #1	-	TM*	TM
SMz #2	-	TM*	TM
SMz #3	-	TM*	TM
SMz #4	-	TM	TM
SMz #5	-	TM	TM
SMz #6	-	TM	TM

1. Transportan adopted a TM conformation before reaching the inner leaflet.

tion. Interestingly, transportan did not reach an interfacial orientation in any other of the simulations performed (Table 5.3). Here it should also be noted that the transition from one conformation to another was irreversible and transportan was not observed to alternatively sample different conformations or orientation in any of the simulations performed. This implies that in an asymmetric membrane anionic lipids can actually either stabilise or destabilise transportan transmembrane conformation depending on the peptide orientation.

As summarised schematically in Figure 5.2, altogether these observations support the idea that the TM* conformation is less energetically favourable than the TM one but also, and perhaps more importantly, that both these transmembrane conformations are metastable and that their stability can be influenced by the lipid environment. Additionally, the results suggest that the transmembrane states remain less favourable than an interfacial orientation, although the ability of a single transportan molecule to reach the bilayer surface appears limited and dependent on the destabilisation induced by its orientation in an asymmetric membrane. In order to investigate this hypothesis further, I examined the evolution of the systems total potential energy. This is a fairly crude metric as it does not discriminate between the specific contributions of, for instance, peptide-lipids or peptide-water interactions. However, given the simplicity and small size of the systems in the ES simulations, it is a convenient tool to monitor whether a change in transportan conformations correlates with a change on the potential energy of the system. As illustrated in Figure 5.3, the adoption by transportan of a TM conformation from an initial TM* one did not impact the potential energy of the system. This was in sharp contrast with what was observed when transportan reached an interfacial orientation from a transmembrane one. It implies that the relatively close TM and TM* conformations also correspond to energetically similar states, thereby allowing transportan to transition from one to the other on the timescale of the simulations performed. This is consistent with the outcome of the self-assembly simulations performed in the previous chapter that led to an approximately equal proportion of TM and TM* con-

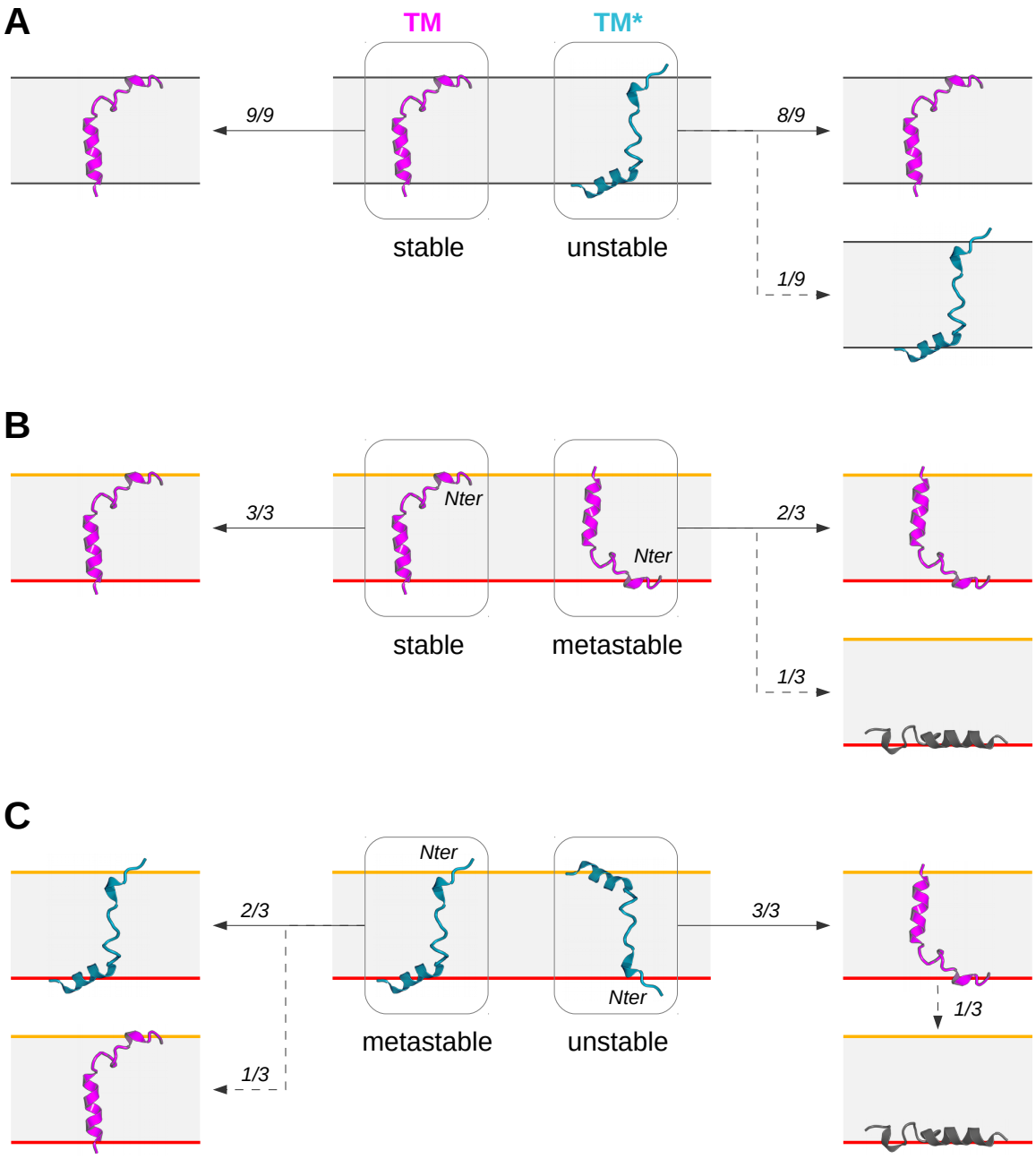

Figure 5.2 Schematic representation of the relative stability of transportan transmembrane conformations in different membrane environments. The TM and TM* conformations are represented in pink and cyan respectively while the zwitterionic and anionic leaflets of asymmetric bilayers are represented in yellow and red. The numbered arrows refer to the outcome of the 5 µs ES simulations summarised in Table 5.3. (A) Symmetric membranes simulations (POPC, SMa or SMz) show that the TM conformation is more stable than the TM* one. (B) and (C) show that in asymmetric membrane models both transmembrane conformations are destabilised when transportan N terminus is oriented "inwards" ie in the anionic leaflet, while the TM* conformation appears stabilised when the N terminus is positioned in the zwitterionic leaflet.

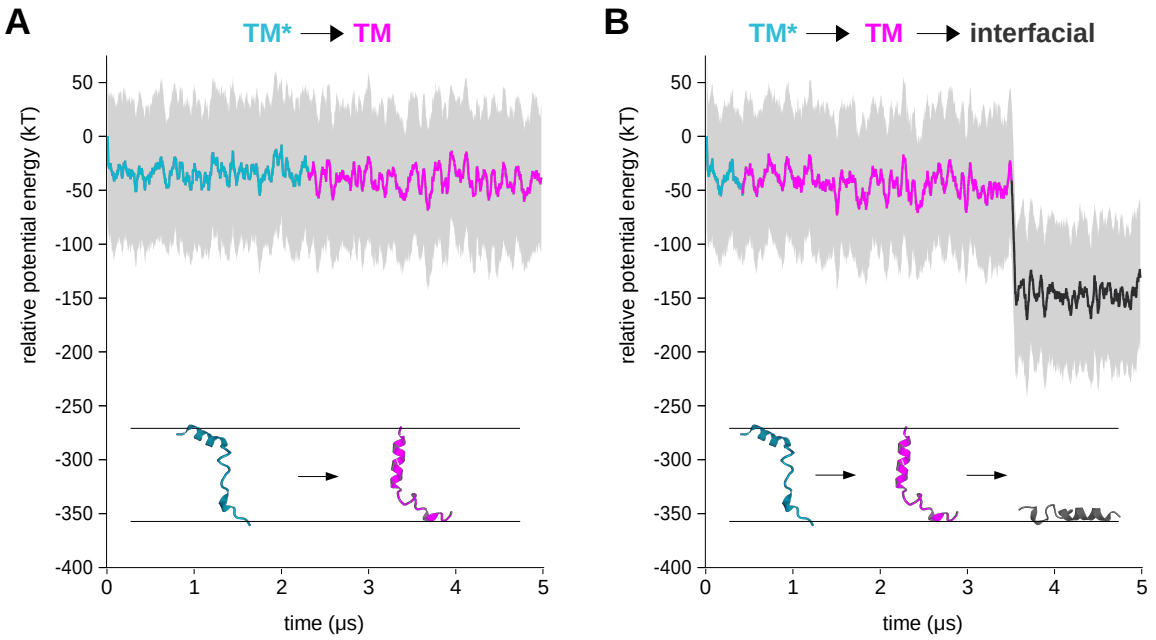

Figure 5.3 Impact of transportan conformation and orientation change on the system's total potential energy. (A) corresponds to simulation SMz #1 and (B) to AM #4. The evolution of the system's total potential energy was obtained using the *g_energy* utility and the value at t = 0 ns was used as reference. The average potential energy was calculated over 200 consecutive data points, corresponding to a time window of 40 ns, and were then coloured depending on the information and orientation status of the transportan peptide. Transportan orientation and conformation was determined for each frame using the relative position of three beads with respect to the center of the bilayer, as detailed in the previous chapter (4.3.2).

formations (see 4.3.3). On the other hand, the interfacial orientation of transportan appears to correspond to a much more energetically favourable state for the system. However, it involves a significant re-arrangement of transportan interactions with neighbouring molecules and it is thus reasonable to assume that the observation of such a transition is hindered by its associated energetic cost. In this context, it is particularly interesting that the distribution of anionic lipids in the different model membranes used influenced the ability of transportan to reach an interfacial orientation. Most notably, neither symmetric membrane models presented here nor in the previous chapter allowed a single transportan molecule to translocate and reach the bilayer surface. Figure 5.3 also illustrates that once transportan adopted a new conformation or orientation it did not sample the previous one again.

In agreement with the observations presented in the previous chapter, the ES simulations therefore indicate that a balance between electrostatic and hydrophobic interactions with the lipid bilayer account for the conformations adopted by transportan. Interestingly, they further demonstrate that, in addition to the relative distribution of basic and hydrophobic residues within the peptide sequence, the distribution of anionic lipids within the membrane plays an essential role in the relative importance of these interactions. Although there is little structural evidence to compare them to, such results are thus encouraging as they highlight the importance of membrane asymmetry which is an important feature of the biological membranes of interest but is difficult to reproduce in experimental membrane models and, hitherto, had not been studied computationally either.

5.3.2 Kinetics of clustering and translocation

Interfacial simulations

When initially positioned in an interfacial conformation (IL simulations) the transportan molecules randomly diffused on the bilayer surface during the course of the simulations: no collective behaviour was observed and no peptide entered the lipid bilayer, regardless of the lipid composition. Although this is consistent with previous computational studies of transportan and its peptide analogues [174, 175] these were performed in symmetric lipid bilayers and involved a maximum of two peptides. The results presented here thus show that, within the CG model used, cooperation between multiple peptides does not allow transportan to insert into the lipid bilayer. Interestingly, this is in contrast with simulations of AMPs but consistent with the relatively less membrane disrupting nature of transportan compared to these [177, 178, 183, 346, 421, 422].

Additionally, the AM simulations demonstrate that the introduction of an asymmetric distribution of anionic lipids does not influence the ability of transportan molecules to enter the lipid bilayer. This is somewhat unsurprising since, as explained in Chapter 3, a molecule

sitting on the surface of the membrane is not influenced by the electrostatic properties of the opposite leaflet as a result of the limitations of the treatment of electrostatic interactions in the CG model (see 3.4.2). Indeed, although it can always be argued that the simulations were not performed on a sufficiently long scale, *in vivo* experimental studies have demonstrated that passive internalisation of several CPPs was enhanced by the presence of a transmembrane potential [131, 328–331]. In order to specifically study the internalisation process of transportan molecules it may therefore be interesting to repeat the IL simulations after incorporating an electrical gradient in my membrane model in order to be able to compare these computational findings with experimental data.

Embedded simulations

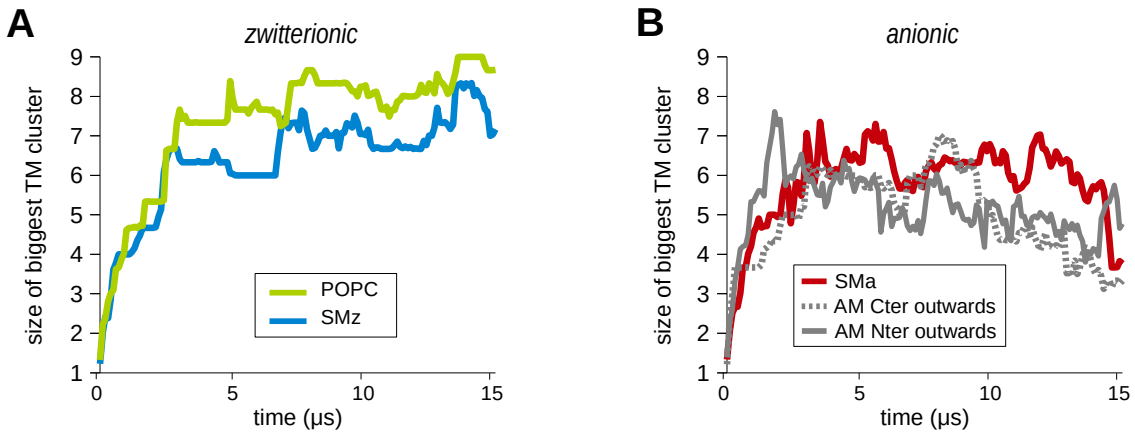

Figure 5.4 Evolution of the size of the biggest TM transportan cluster in membranes containing (A) zwitterionic lipids only and (B) zwitterionic and anionic lipids. The profiles corresponding to the three repeats were averaged for each membrane model.

In agreement with what was observed in the previous chapter, (see 4.4.3), transportan peptides were found to aggregate when initially embedded in the lipid bilayer. Transmembrane aggregates were detected using the same connectivity based approach and cutoff (8 Å) as described in 4.4.3, and the evolution with time of the size of the biggest cluster was followed in each simulation (Figure 5.4). The longer simulations presented here as well as

the diverse membrane models revealed insights on the characteristics and stability of the clusters formed. Notably, the stability of transportan TM aggregates was found to depend on the lipid environment and membrane models could be clearly separated into 2 groups based on the presence or absence of anionic lipids. In the case of lipid bilayers containing zwitterionic lipids only, transportan formed large aggregates eventually involving almost all of the peptides (Figure 5.4A). On the contrary, in membranes containing anionic lipids the clusters were less stable which prevented the aggregation of peptides into very large clusters: as shown in Figure 5.4B a smaller maximum cluster size was reached and afterwards the number of peptides involved in the largest cluster decreased continuously.

The difference in clustering kinetics between membranes containing anionic lipids and those containing only zwitterionic lipids is further apparent when tracking peptides individually throughout simulation. The approach chosen to graphically represent such multidimensional data for each simulation is detailed in Figure 5.5, and the comparison of the respective patterns obtained in Figure 5.6 and Figure 5.7 then illustrates the influence of the presence of anionic lipids on transportan clustering. In Figure 5.6 it can be seen that the octamers and nonamers formed are stable on the scale of several microseconds. In contrast, Figure 5.7 presents a very different pattern where although peptides aggregated rapidly into oligomers most were short-lived. However, Figures 5.6 and 5.7 also show that in both zwitterionic and anionic membranes the instability of transportan clusters was due to peptides leaving the clusters as they reached the bilayer surface and adopted an interfacial conformation (dark and light grey bands) rather than to the clusters separating into smaller transmembrane units. These results thus suggest that transmembrane clusters represent a transition state allowing transportan molecules to reach an energetically more favourable interfacial orientation. These findings are consistent with recent atomistic simulations of melitin, an antimicrobial peptide, which showed that the energy barrier for transition from a surfacic to a transmembrane state was significantly decreased when a melitin molecule was already

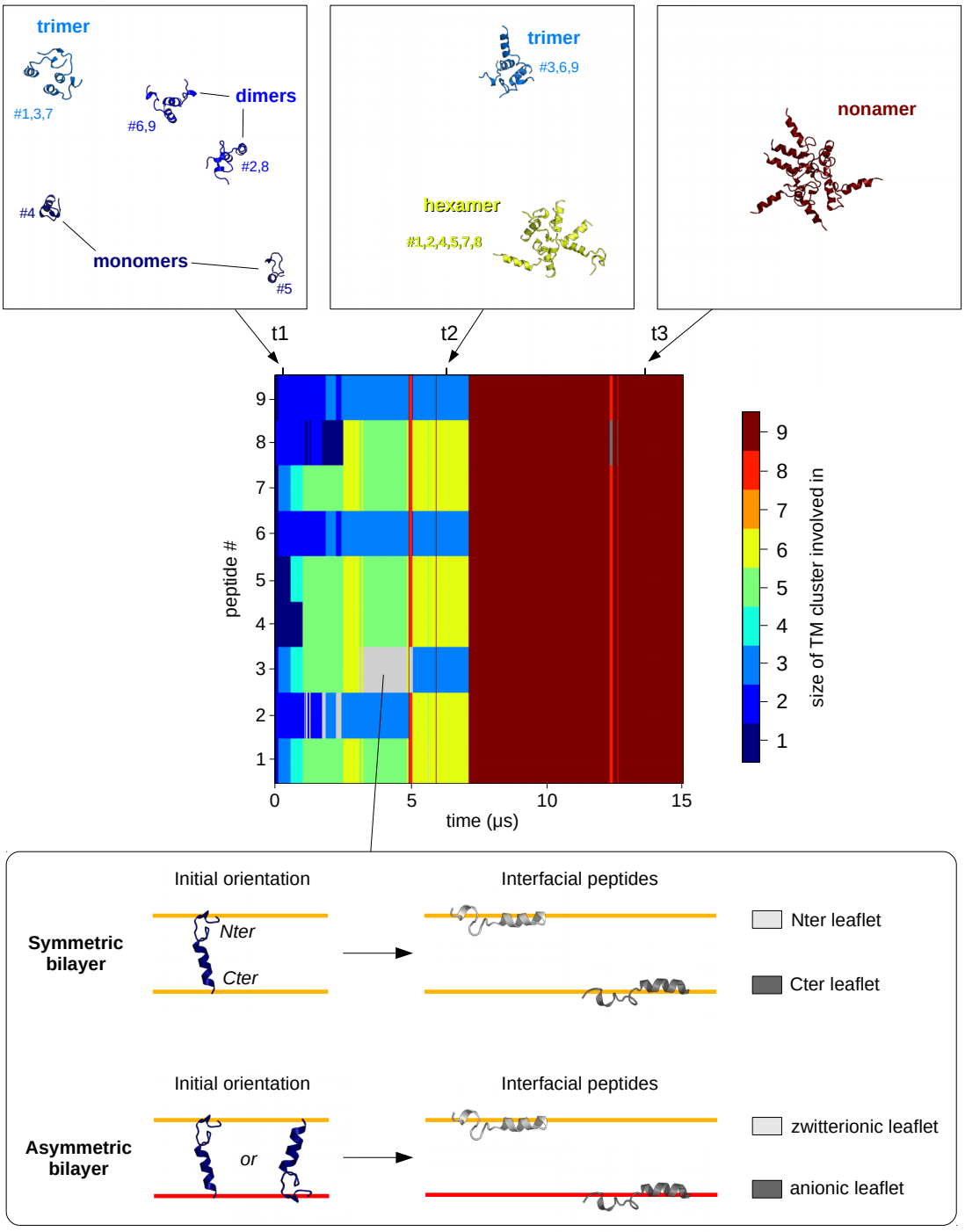

Figure 5.5 Graphical summary of the evolution of clustering in EL simulations (9 peptides). The size of the transmembrane cluster each transportan molecule is involved in is followed throughout the simulation and represented by a colour coded horizontal band. Snapshots corresponding to three different times and cluster distribution are shown in the top row. The bottom diagram illustrates how when a peptide is determined to be an interfacial orientation rather than within a transmembrane cluster, a grey colour code is used to indicate which leaflet it sits on. The algorithm presented in 4.4.3 is used to determine the peptides orientation and explains why molecules loosely involved in disordered transmembrane clusters can be detected as interfacial.

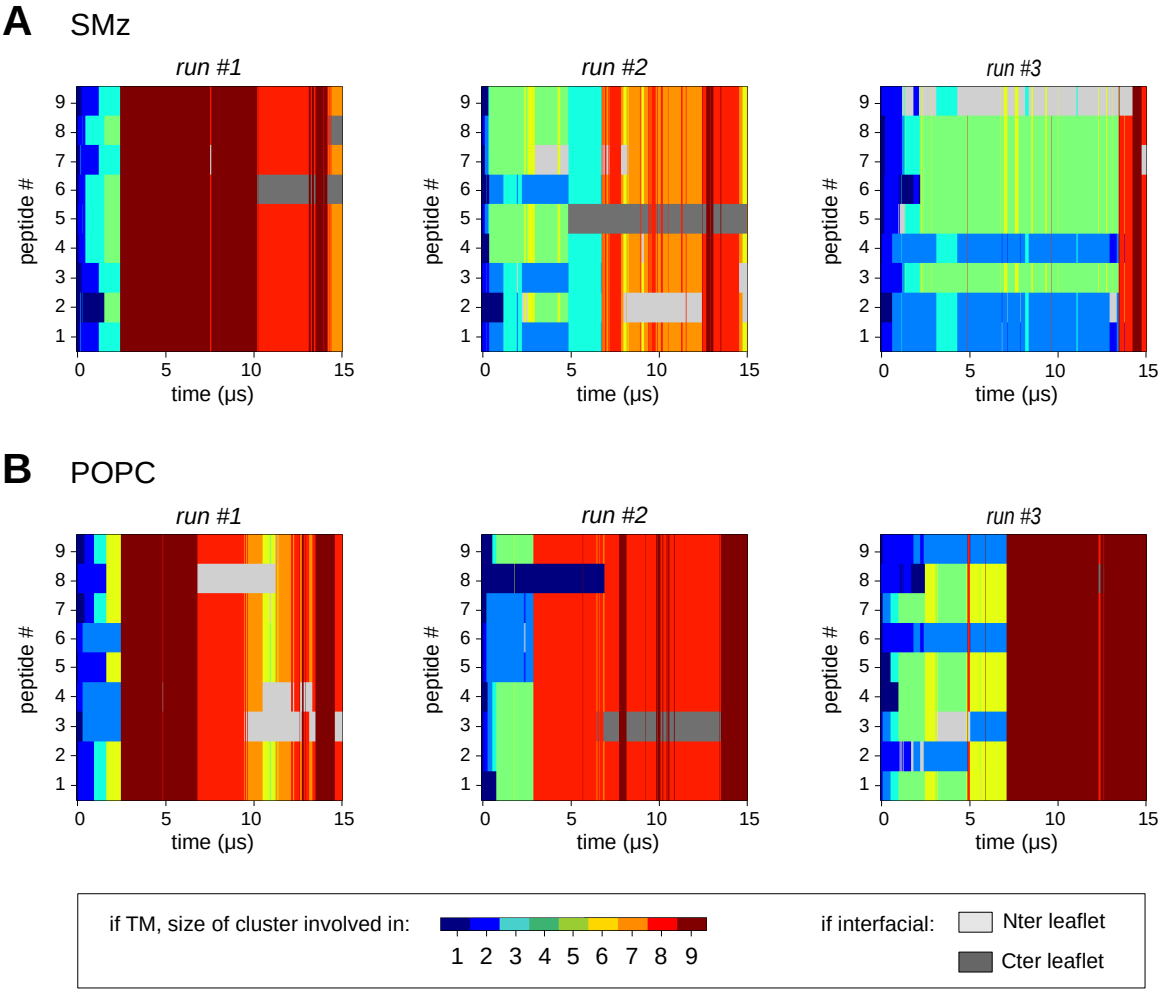

Figure 5.6 Aggregation and translocation of transportan peptides in membranes containing zwitterionic lipids only. Transmembrane peptides are coloured based on the size of the cluster they belong to. The leaflet reached by peptides that translocated to an interfacial state is coloured based on its position relative to the initial orientation of the peptides.

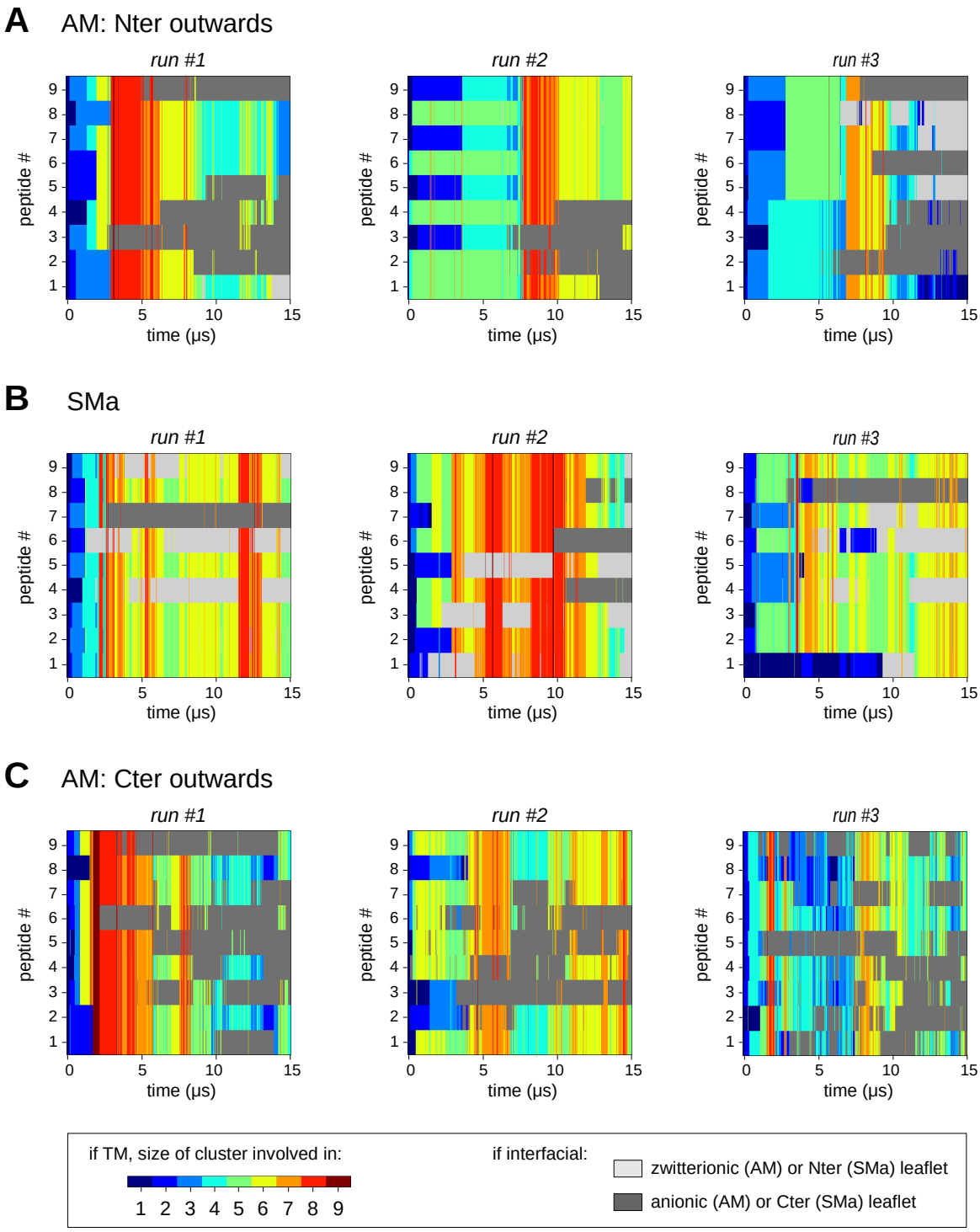

Figure 5.7 Aggregation and translocation of transportan peptides in membranes containing zwitterionic and anionic lipids. Transmembrane peptides are coloured based on the size of the cluster they belong to. Leaflets towards which peptides translocated are indicated either by their anionic or zwitterionic nature (AM simulations) or by their position relative to the initial orientation of the peptides (SMa simulations).

embedded in the bilayer due too cooperation between peptides [506]. Additionally, they also indicate that while the aggregation of transmembrane transportan peptides is favourable in all membrane models, the presence of anionic lipids destabilises the aggregates formed and facilitates the translocation of transportan. Control simulations performed with the force field MARTINI 2.2 (see 2.2.2, with and without polarisable water, led to similar aggregation patterns. These observations complement the findings regarding the transmembrane stability of a single transportan molecule reported earlier (see 5.3.1) and demonstrate the importance of cooperation between peptides on peptide-membrane interactions. In particular, they are consistent with both previous computational studies [177, 178, 183, 346, 347, 421, 422] and experimental evidence [498–500] suggesting that membrane active peptides are only active as aggregates.

Furthermore, the simulations performed also suggest a pattern regarding the leaflet towards which the transportan peptides translocated (Figure 5.8). The most striking result was observed with the AM membrane when transportan was oriented with its C terminus outwards as all the translocations observed in those simulations occurred towards the inner, anionic leaflet. Similarly, when transportan was initially oriented with its N terminus outwards a few peptides translocated towards the outer, zwitterionic leaflet but the majority also translocated towards the anionic leaflet (Figure 5.8B). In SMa simulations the distribution of translocated peptides was also very asymmetric as the leaflet in which transportan N terminus was initially positioned was reached by twice as many peptides than the C terminus leaflet (Figure 5.8D). A similar trend, although based on a few translocations and less pronounced, was observed with the SMz membrane (Figure 5.8C). The longer simulations discussed in this chapter thus expand on those presented in the previous chapter and confirms that the distribution of charged lipids can drive the translocation of peptides as evoked in 4.4.3. They also highlight the importance of being able to sample longer time scales: although the simulations performed in Chapter 4 suggested that the clusters formed by trans-

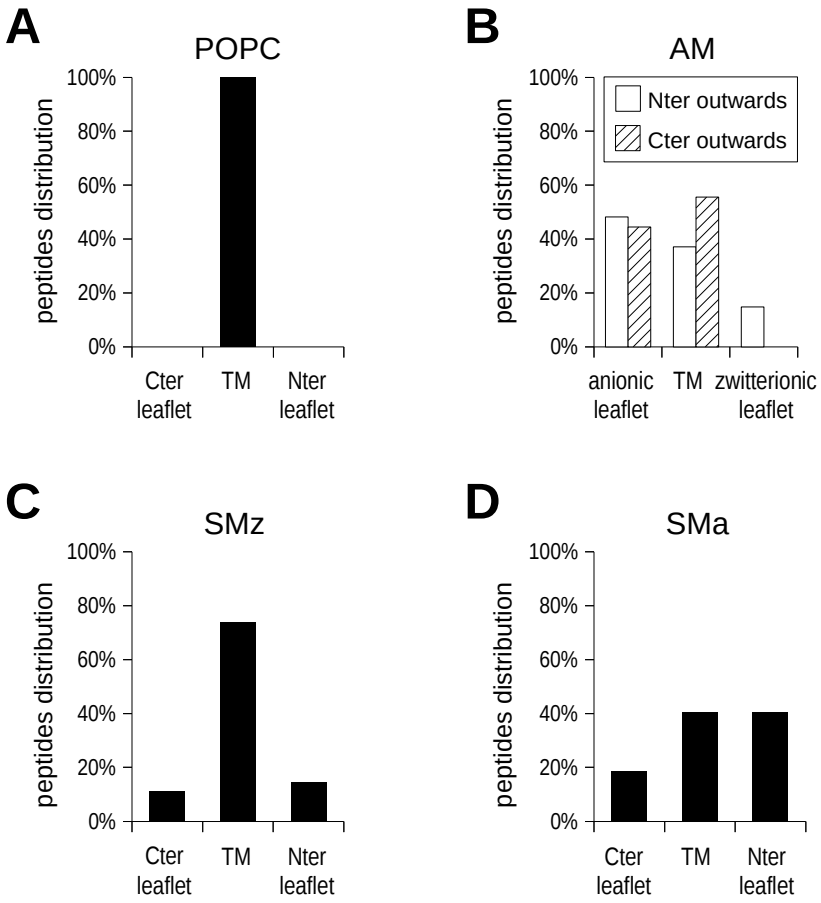

Figure 5.8 Relative distribution of interfacial and TM conformations in the final frames of EL simulations. For each membrane model the percentages were calculated after aggregating the data from all three repeats.

portan peptides did not correspond to stable structures these were were not long enough to appropriately investigate their metastable properties. In this regard it is worth noting that the translocations were all irreversible on the timescale of the simulations performed: although they occasionally regained contact which the extremities of transmembrane clusters, none of the peptides that had reached an interfacial conformation were observed to re-enter the lipid bilayer. This is consistent with the results from the IL simulations discussed in the previous section and further shows that interfacial transportan are stable even in the presence of TM aggregates.

Altogether these results stress two interesting points. First, they highlight the impor-

tance of membrane asymmetry and suggest that transportan will preferentially translocate towards the anionic leaflet regardless of its orientation in the lipid bilayer. This is particularly encouraging as anionic lipids are predominantly found in the inner leaflet of the plasma membrane and the model presented here is therefore consistent with the peptide internalisation into cells. And second, the fact that the model used could also capture a preferential translocation towards the N terminus leaflet shows the influence of residue distribution on peptide - membrane interactions and highlights how such coarse-grain models can contribute to provide insights into the mechanisms of action of membrane active peptides. These observations are in good agreement with in vitro experiments [131] suggesting that the translocation of CPPs is a physical process governed by electrostatic interactions, the efficacy of which can be modified by altering the charge of the peptides. The interplay between the distribution of residues and that of lipids is developed in more detail in the next section.

5.3.3 Density profiles of transportan clusters

Visual inspections of the simulations revealed, as suggested by Figures 5.6 and 5.7, that the transmembrane clusters formed by transportan were highly dynamic. As a consequence, it was not possible to identify well defined nor representative structures to characterise the different shapes and conformations of such flexible, out of equilibrium, oligomers and a statistical approach relying on density distribution was privileged. This is a standard approach and the Gromacs utility *g_density* is commonly used to perform this task, however it was not suitable for the problem investigated here as it cannot discriminate peptides based on their clustering status. In the following sections I therefore briefly present the method implemented to calculate density profiles for each of the cluster size dynamically identified during a simulation before then discussing the results obtained.

Method

For each frame in a trajectory the following algorithm was used:

1. Transmembrane clusters were identified as described in section 4.4.3 and their respective center of geometry was calculated. The algorithm described in [507][1] was implemented in order to deal with clusters spanning periodic boundary conditions.

2. For each cluster, a cylinder parallel to the z axis and centered on the cluster centre of geometry was defined and only the particles within it were considered. This was done in order to focus on transmembrane residues and prevent nearby interfacial peptides from biasing the distribution profiles. The cylinder radius was set to 30 Å for all clusters (evidence supporting this distance is presented in section 5.4) and the cylinder boundaries along the z axis were set at respectively 40 Å above and below the upper and lower bilayer leaflet.

3. The z coordinates of the particles selected were then stored in a different data structure for each cluster size.

Once all the frames were processed a relative distribution density was obtained by binning the coordinates into slices 0.5 Å thick and normalising the histogram by the overall number of particles selected (residues and water particles were treated independently to obtain their respective distribution profiles). This procedure thus allowed to obtain quantitative and normalised profiles for each simulation while still taking into account the dynamic nature of the clusters formed.

[1] This is another concrete example of how technical hurdles in the analysis of MD simulations can be overcome thanks to progress in other disciplines.

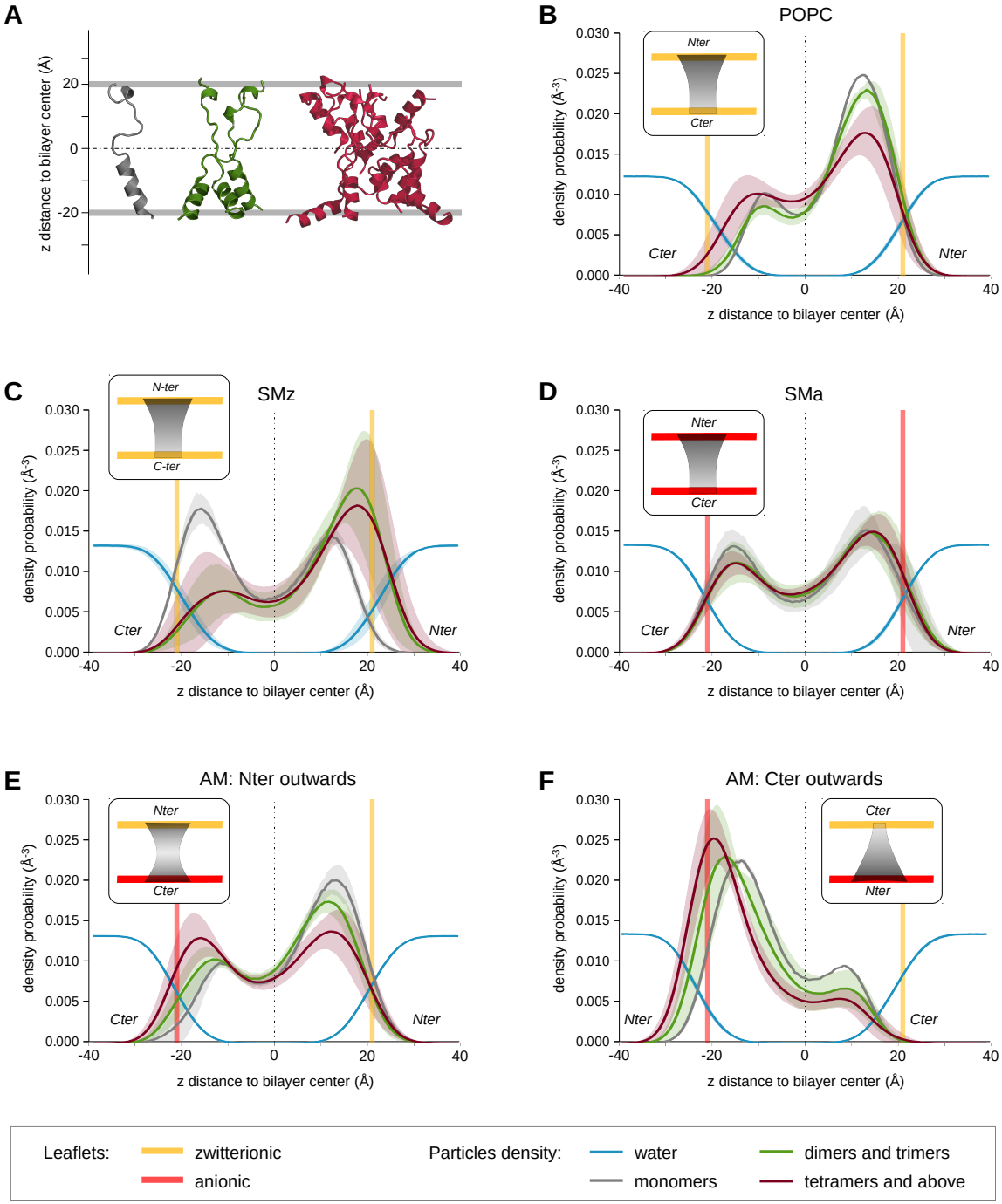

Figure 5.9 Influence of the lipid environment and cluster size on transmembrane peptides density distribution profiles. (A) Schematic representation of transmembrane cluster of different sizes: the density profiles are then obtained by projecting the number of particles on the z axis. The density profiles obtained for each size cluster size group are shown in (B-D) for symmetric membranes and (E-F) for asymmetric membranes. The cartoons represent the three different schematic residues distribution identified for the largest clusters (tetramers and above).

Results

Despite the very dynamic structures of the clusters formed, clear patterns emerged from the density profiles obtained (Figure 5.9) and provided evidence that both membrane composition and cluster size influenced the transmembrane residues distribution. In symmetric membranes the peptides aggregated into an asymmetrical hourglass shape with the residues distribution shifted towards the N terminus (dark red lines in Figure 5.9B,D and E). Although the asymmetry of the larger clusters was most pronounced in the zwitterionic membranes, the redistribution of the residues within the membrane with increasing cluster size can be observed in all cluster sizes. Furthermore, the comparison of the SMz and POPC profiles suggest that larger transportan clusters adopt the same shape, regardless of the initial transmembrane conformation of transportan (TM* for SMz and TM for POPC, see Table 5.2). Following those observations, the results obtained with the AM model then illustrate how membrane asymmetry can re-arrange the residues distribution by shifting the density profile towards the anionic leaflet. The slight asymmetry observed in the SMa membrane became indeed much more pronounced when transportan was positioned in the AM membrane model with its C terminus outwards (Figure 5.9C). In contrast, when transportan was positioned with its N terminus outwards, a "symmetrysation" of the residues distribution could be observed (Figure 5.9A). In addition, the influence of increasing cluster size on residues distribution can again clearly be seen.

Altogether, these observations confirm those made previously (see 5.3.2 and 4.4.2) regarding the asymmetric distribution of translocated peptides as the preferred leaflets correlate with the density profiles observed in the different lipid environment. The hypothesis of a preferential translocation towards the N terminus leaflet in symmetric membranes is indeed supported by the asymmetric residues distribution observed in these environment. Similarly, the different redistributions of residues observed when lipid asymmetry is introduced are consistent with the translocation patterns observed in the AM model.

5.4 Characterisation of membrane properties

This sections now focuses on the influence of the different transportan aggregates described previously on the properties of their lipid environment. In particular, the effect of membrane composition and cluster size are discussed.

5.4.1 Bilayer thickness and lipid tails order parameter

A similar approach to that described above (see 5.3.3) was implemented to calculate average perturbation profiles based on the methods described in section 4.4.4. As can be seen in Figure 5.10 this analysis revealed that two factors contributed to membrane perturbation: transportan aggregation and the presence of anionic lipids. The influence of cluster size on membrane thinning of the SMa membrane model is illustrated in Figure 5.10D and the simulations snapshots presented in Figures 5.10A-C provide further structural evidence. Transportan peptides appear to drag neighbouring lipids head group into the bilayer core and therefore the aggregation of several peptides lead to a more pronounced effect: as more lipids are pulled into the membrane the range of the perturbation increases and the disordered cluster environment allows for the stabilisation of lipids deeper into the membrane. It is also interesting to note that lipids appear to be interacting mainly with the N terminus of transportan: this is consistent with the density profiles observed previously and suggests the involvement of electrostatic interactions between transportan central lysines (K13 and K17) and the lipids negatively charged phosphate groups. This hypothesis is further supported by the clear correlation observed in Figures 5.10F-H between increased thinning and the abundance of anionic lipids, with the SMa and SMz membrane models being respectively the most and least perturbed. In addition, these three figures demonstrate that the increase of membrane thinning with cluster size is observed in all membrane models and in particular they show that the perturbation induced by a transportan monomer is the same regardless

of the lipid environment which further stresses the importance of peptide cooperativity regarding peptide - membrane interactions. At this point it should be mentioned that similar perturbation profiles are observed with the AM membrane model regardless of transportan orientation. While it is interesting to note that very different clusters shape (see Figure 5.9) can lead to similar membrane thinning it should be noted that, first, the POPS concentration is the same in both cases; second, a significant standard deviation in the immediate vicinity of the clusters is associated to the profile obtained when transportan is oriented with its N terminus outwards (Figure 5.10H); and finally, the statistical approach used does not readily inform on which structures are involved in the perturbation of the bilayer.

Another result worth commenting on is the difference observed between the SMz and POPC membranes as both are zwitterionic and accommodate peptide clusters with similar density profiles (Figure 5.9). One might imagine that the presence of POPE, known to induce spontaneous membrane curvature, would enhance bilayer deformation, however, membrane thinning occurs via pinching of the lipids leaflets which corresponds to somewhat positive membrane curvature (Figure 5.10A) whereas POPE induce negative membrane curvature given the smaller size of its head group. In contrast, the results are consistent with the presence of cholesterol in the SMz membrane as it is known to straighten the lipids acyl chains and to rigidify lipid bilayers [317, 318]. The increased membrane thinning observed in the POPC membrane is therefore a consequence of its greater deformability. Although the exact cholesterol content of the plasma membrane is the subject of much debate (see 3.2.1), these results highlight the importance of the lipid composition used in computational studies as well as the relevance of the latter to investigate the role played by lipid phases on the activity of CPP suggested by some experimental studies [91]. The membrane thickening effect of cholesterol is quantified in Table 5.4. These values also illustrate again the local nature of the membrane thinning induced by transportan, as the presence of peptides led to only a marginal decrease in membrane thickness, and are consistent with solid-state

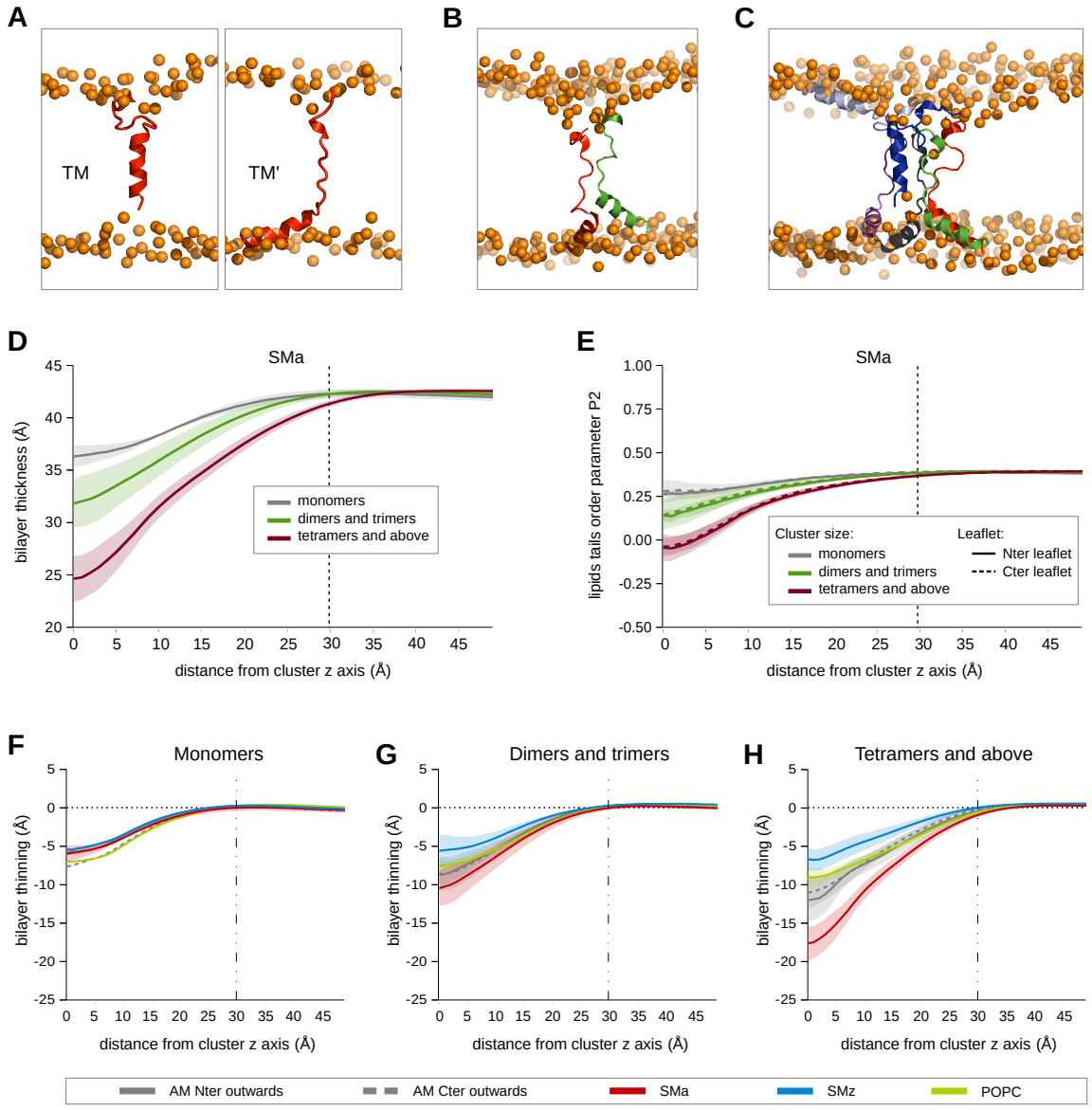

Figure 5.10 Influence of lipid environment and cluster size on transportan induced perturbations. (A-C) Phosphate head groups pulled into the membrane core by (A) a transportan monomer, (B) a trimer and (C) a hexamer. (D,E) Influence of cluster size on local (D) bilayer thickness and (E) lipid tails order parameter in SMa membranes. The vertical dashed lines indicate the 30 Å radius limit used for calculating charge and density profiles. (F-H) Influence of size and membrane compositions on membrane thinning. In all plots the solid lines represent the averages between simulations and the shaded area the corresponding standard deviations.

NMR experiments which demonstrated that the thinning of phospholipid bilayers induced by antimicrobial peptides was much more modest than the ordering and thickening effect of cholesterol [505].

Table 5.4 Influence of lipid composition and peptides presence on membrane thickness. For each simulation the thickness was calculated as an average over all lipids and over the entire length of the simulation (see 4.4.4). The fluctuation represents the corresponding standard deviation and the numbers between parenthesis correspond to the standard deviation between repeats.

Lipid composition	**P:L**	**Initial conformation**	**Transportan orientation**	**Thickness (Å)** *average*	*fluctuation*
Without cholesterol					
POPC	0:1116	-	-	40.69	±2.20
POPC	9:1116	TM	-	40.42 (0.01)	±2.50 (0.02)
With cholesterol					
AM	0:1116	-	-	42.57	±2.20
SMa	0:1116	-	-	42.64	±1.96
SMz	0:1116	-	-	42.56	±2.04
AM	9:1116	TM	Nter outwards	42.05 (0.10)	±2.63 (0.18)
AM	9:1116	TM	Cter outwards	42.11 (0.02)	±2.53 (0.03)
SMa	9:1116	TM*	-	41.93 (0.15)	±3.05 (0.19)
SMz	9:1116	TM*	-	42.19 (0.04)	±2.30 (0.01)

In addition to membrane thinning, Figure 5.10E shows that transportan clusters also perturbed the tail orientation of neighbouring lipids, the effect being again more pronounced as the clusters are larger. The decrease in the tails order parameter indicate that lipids in the vicinity of the peptides are on average at a greater angle with the local bilayer normal (assumed to be along the z axis). This is an interesting result which complement the thickness data to provide a more comprehensive picture of the membrane deformations. In particular it might be tempting to interpret the pinching of the bilayer by transportan clusters (Figure 5.10A) in terms of the mechanisms that have been suggested for membrane perturbation by antimicrobial peptides [42–44] (see 1.2.1) and argue that the results presented here are consistent with a structure similar to that of a disordered toroidal-shaped pore [47]. However, it is important to stress that no pore formation was observed in any simulations: the

membrane integrity was maintained with no permeation by water particles (as evidenced by the density profiles presented in Figure 5.9). In this regard, the large fluctuations of the lipid tails order parameter reported in Table 5.5 illustrate the higher mobility of lipids and emphasise that the statistical nature of the properties characterised cannot easily be simplified into a well defined structure. The decrease of the average tail order parameter in the absence of cholesterol is nevertheless significant and provide another metric demonstrating its rigidifying effect on the lipid bilayer, in agreement with *in vitro* measurements [505].

Table 5.5 Influence of lipid composition and peptides presence on lipids tails order parameter. For each simulation the order parameter was calculated as an average over all lipids and over the entire length of the simulation (see section 4.4.4). The fluctuation represents the corresponding standard deviation and the numbers between parenthesis correspond to the standard deviation between repeats.

Lipid composition	**P:L**	**Initial conformation**	**Transportan orientation**	**P2** *average*	*fluctuation*
Without cholesterol					
POPC	0:1116	-	-	0.28	±0.21
POPC	9:1116	TM	-	0.28 (0.00)	±0.21 (0.00)
With cholesterol					
AM	0:1116	-	-	0.38	±0.21
SMa	0:1116	-	-	0.40	±0.21
SMz	0:1116	-	-	0.37	±0.21
AM	9:1116	TM	Nter outwards	0.37 (0.00)	±0.21 (0.00)
AM	9:1116	TM	Cter outwards	0.37 (0.00)	±0.22 (0.00)
SMa	9:1116	TM*	-	0.38 (0.00)	±0.22 (0.00)
SMz	9:1116	TM*	-	0.37 (0.00)	±0.21 (0.00)

5.4.2 Recruitment of lipids

The results presented in the previous sections repeatedly suggest anionic lipids play a particular role in the interactions of transportan with lipid bilayers. The distribution of lipids species around transportan peptides was therefore investigated to further characterise possible preferential interactions. To this end the lipids whose phosphate head group were within

50 Å of the cluster axis defined in 5.3.3 were selected and binned into 1 Å wide circular bands; once all the frames were processed the relative % of each lipid species was then calculated for each band. The lipid distribution profiles thus obtained demonstrated that transportan indeed strongly clustered anionic lipids (Figures 5.11).

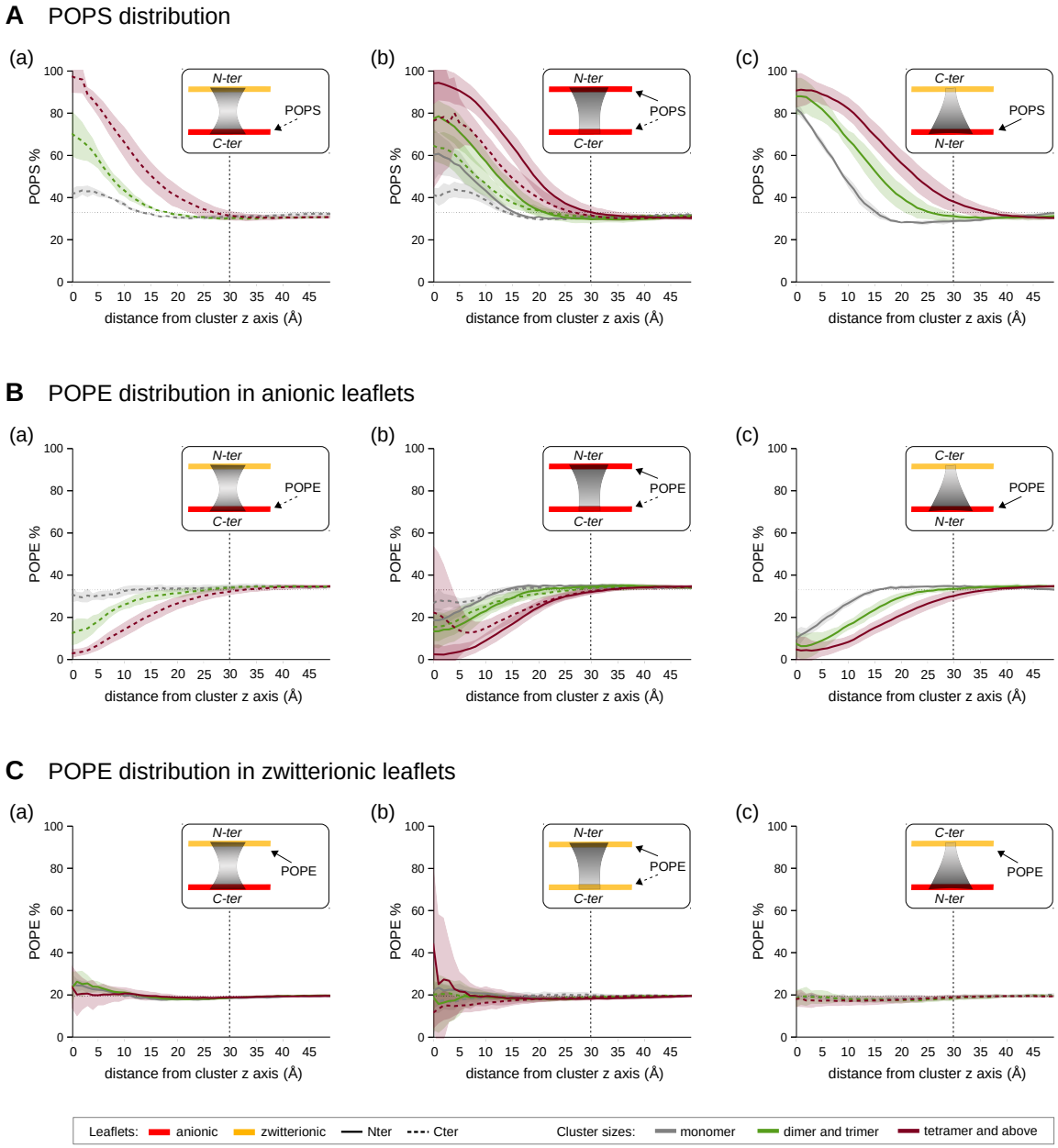

Figure 5.11 Influence of cluster size on local lipid distribution. Solid lines represent averages between simulations and the shaded areas the corresponding standard deviations. The POPC data in anionic leaflets was found to be similar to that of POPE.

This result is consistent with previous observations and is strongly supported by experimental evidence [321, 508–510]. Furthermore, the data confirmed the size dependence of the clustering effect, with larger transportan aggregates able to recruit more anionic lipids, and, perhaps more surprisingly, also revealed a strong influence of transportan orientation, with the C terminus inducing less clustering, particularly so for smaller peptides cluster sizes (Figure 5.11A). Interestingly, the distribution of transportan charges in the various models used was found to provide a plausible explanation to both of these observations. Indeed, in the AM model the charge distribution in transportan monomers is slightly asymmetric and shifted towards the N terminus (Figures 5.12A and C), which is consistent with the overall residues distributions seen in Figure 5.9. This suggests that, as proposed by the authors of several experimental studies [321, 335], clustering of anionic lipids is a function of the cationic charge density and not a straightforward consequence of a net positive charge. As the cluster size increases, the correlation between the evolution of charge distribution and the higher recruitment of anionic lipids further supports this hypothesis. When transportan is oriented with its N terminus outwards the asymmetry of the distribution is shifted towards the C terminus for large clusters (5.12A), thus explaining why the difference in POPS clustering observed between (a) and (c) in Figure 5.11A becomes less pronounced. Although the results obtained with the SMa model are less striking, the correlation between charge density and POPS recruiting is similar (Figures 5.12B and (b) in 5.11A).

As anionic lipids are recruited by transportan clusters, the distribution of zwitterionic lipids is modified accordingly (Figure 5.11B). In particular, it is interesting to note that the smaller head group of POPE does not lead to its enrichment in the vicinity of transportan clusters, and that no discrimination between POPE and POPC is observed (Figure 5.11C), which is in contrast to what has been suggested experimentally [511]. The large standard deviations reported for symmetric membranes which might suggest otherwise are actually the consequence of a single lipid getting "stuck" in poorly sampled areas and do not reflect

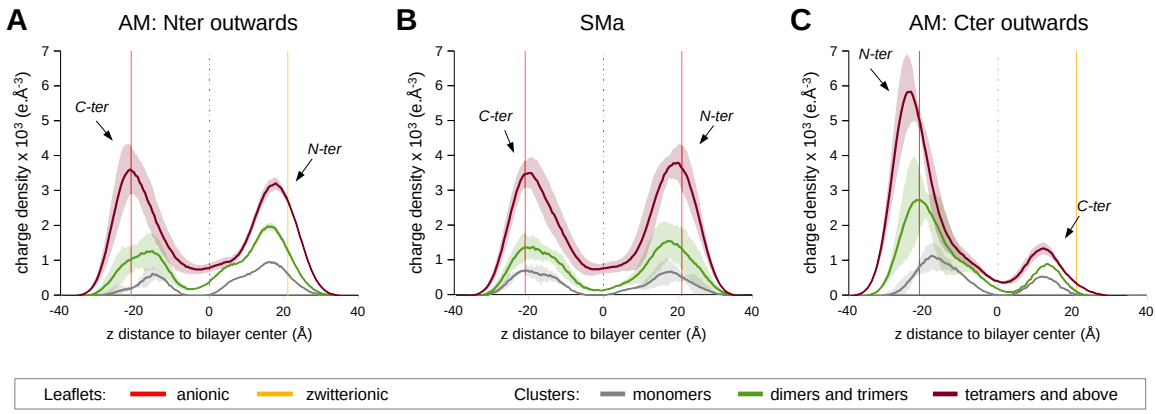

Figure 5.12 Influence of lipid environment and cluster size on transportan charge distribution. Solid lines represent averages between simulations and the shaded areas the corresponding standard deviations.

a consistent pattern (they do, however, highlight the importance of sampling and repeats). Nevertheless, combined to aggregation results presented in the previous section, the data shown in Figure 5.11 may help to explain the somewhat paradoxical higher perturbations of zwitterionic membranes compared to anionic ones that has been reported in some studies [146]. Indeed, although less pronounced, significant perturbation of the zwitterionic membrane models was also observed and could be enhanced by the greater stability of transportan clusters in these lipid environments (see section 5.3.2). Finally, cholesterol distribution was also investigated but found not to be perturbed by the presence of the peptides.

5.5 Conclusion

The results presented in this chapter show that transmembrane transportan can disrupt biologically relevant membrane models by forming metastable aggregates and provide insights regarding the driving forces at play. The study of transportan monomers highlighted the importance of the primary amphipathic nature of the peptide and showed that a balance between electrostatic and hydrophobic interactions with the lipid bilayer accounted for the transmembrane conformations identified. In the simulations involving several transportan

peptides it was difficult to associate a defined transmembrane state to peptides involved in the disordered and dynamic clusters observed, but a statistical approach unambiguously revealed a shift of the distribution of residues towards the N terminus consistent with a TM orientation that best accommodated the hydrophobicity of transportan main helix. However, the asymmetric introduction of anionic lipids also highlighted the crucial role of electrostatic interactions. These lipids were found to decrease the stability of transmembrane clusters by promoting the translocation of transportan peptides towards the anionic leaflet, which corresponds to the cytosolic leaflet. In addition to justifying the relevance of using asymmetric bilayer models these remarks provide a basis for explaining how membrane asymmetry can impact peptide-membrane interactions: in one orientation (C terminus outwards) the effects of hydrophobic and electrostatic forces are conjugated leading to a heavily asymmetrical distribution of residues within the bilayer and translocation towards the inner leaflet only, whereas in the other (N terminus outwards) the two forces are conflicting resulting in a more balanced distribution of residues that can explain why a few peptides were observed to translocate towards the outer leaflet.

The simulations performed also revealed that these aggregates induce thinning of the membrane, disordering of the lipid tails and disruption of the lipid distributions. While the defects observed remain local (within a 30 Å range) they are consistent with the membrane toxicity of transportan observed experimentally [128, 143, 146, 456, 462, 466] and are in good agreement with the experimental evidence available regarding the origins of such destabilisation. Indeed, the importance of membrane active peptides concentration and cooperativity reported in the literature [472–477] correlates with the aggravating influence of the cluster size on the extent of the defects observed. Similarly, the preferential interactions of transportan with anionic lipids is in agreement with studies showing that cationic AMPs and CPPs induce clustering of anionic lipids [508–510] and the simulations performed further supported the experimental hypothesis of the role of cationic charge density [321]. Im-

portantly, the extent of the perturbations also depended strongly on the lipid composition: they were significantly enhanced by the presence of anionic lipids, while that of cholesterol appeared to hamper them. This is in accordance with the antimicrobial activity of transportan [123, 143, 147, 467] and the suggestion that membrane asymmetry provides a basis for the selective toxicity of membrane active peptides (see 3.1.1).

Finally, the transient and disordered nature of transportan clusters, which did not involve membrane permeation and required a statistical approach for their study, differs from previous computational studies of membrane active peptides leading to poration of the lipid bilayer [182]. Bearing in mind the ambivalent nature of transportan, which exhibits both AMP and CPP characteristics, the cooperative translocation and bilayer destabilisation observed are consistent with both the cellular internalisation of transportan and its moderate membrane toxicity. They demonstrate the membrane models and the analysis approach presented here are both relevant and suitable to the study of the origins of the membrane toxicity of CPPs and provide a computational framework for further investigations of the peptide-membrane interactions involved. In this regard, the following chapter will focus on the characterisation of an additional type of membrane perturbation, namely the ability of transportan clusters to induce trans-bilayer diffusion of lipids.

Chapter 6

Characterisation of lipid flip-flops induced by transportan

6.1 Introduction

In addition to the membrane perturbations described in the previous chapter, the simulations performed also revealed the occurrence of phospholipid transbilayer movement, or flip-flops. This is an interesting observation since the hydrophilic head group of phospholipids makes their crossing of the hydrophobic bilayer core particularly unfavourable. Indeed, as discussed in Chapter 3, experimental studies showed that unassisted transmembrane diffusion of lipids in bilayers was a slow process occuring over the range of hours to days [295–298, 512] (see 3.1.1). Accordingly, the ability of biological membranes to maintain their lipid composition relies on flippase enzymes to actively transport specific lipid species between leaflets [299–302]. The disruption of the plasma membrane inter-leaflet lipid asymmetry, in particular the exposure of phosphatidylserines to the extracellular leaflet, has been shown to be involved in cell recognition by macrophages and the onset of apopto-

sis [303–305] as well as various pathologies [306–308]. In this context, the ability of some CPPs to disrupt the compositional asymmetry of the plasma membrane of mammalian cells could contribute to their membrane toxicity in a similar fashion to what has been been suggested for some proapoptotic proteins [513]. Additionally, the transmembrane diffusion of phospholipids could also indicate local permeation of the membrane and possible leakage of the cell content. This is supported by several *in vitro* studies that showed that membrane destabilisation by antimicrobial peptides also corresponded to an increase of the rate of phospholipid flip-flops by several orders of magnitude [40, 514, 515].

Numerous molecular dynamics studies have focused on the characterisation of phospholipid flip-flops [400, 516–522]. However, due to their slow nature, flip-flops do not occur spontaneously in simple lipid bilayers on the timescale of MD simulations as these remains limited to the order of hundreds of microseconds even for the less computationally expensive coarse-grained models. Consequently, the aforementioned studies relied on various approaches to investigate flip-flop events. In particular, the potential of mean force (PMF) for phospholipid flip-flops was determined using umbrella sampling methods [406], whereby the phospholipid of interest is restrained at various depths inside the lipid bilayer [400, 516, 521, 522]. Somewhat unsurprisingly, the free energy barrier was found to increase with the bilayer thickness and the degree of unsaturation of the lipids acyl chains, thereby confirming the importance of membrane properties on the energetic cost associated to flip-flops. Using atomistic representations, this barrier was calculated to be approximately 30 kT in a dipalmitoylphosphatidylcholine (DPPC) bilayer, twice as high than in a thinner dimyristoylphosphatidylcholine (DMPC) bilayer where the acyl tails are two hydrocarbons shorter in length [522]. Remarkably, this is in excellent agreement with the experimentally derived activation energy of approximately 32 kT for flip-flops in DPPC vesicles reported several decades ago by McConnell and co-workers [295]. In other simulations, application of a transmembrane electrostatic potential, created either by electrical pulses [517,

518] or an explicit ionic charge imbalance [519], as well as chemical destabilisation of the lipid bilayer [520] have been used to trigger flip-flops and investigate their molecular mechanisms. Despite the different approaches used, these studies suggest that flip-flops were pore-mediated. They yielded conflicting results regarding the respective importance of electrostatic and hydrophobic interactions but consistently agreed that the creation of water defects in membranes constituted the rate-limiting step of the flip-flop process, with the diffusion of phospholipids along the pore walls then occurring within tens of nanoseconds.

Additionally, all-atom simulations performed to investigate the influence of model transmembrane helices on the PMF of flip-flops concluded that the presence of a hydrophobic peptide only led to a marginal decrease of the free energy barrier [523]. These findings were confirmed by a recent experimental study [524]. However, in the same study, the authors also demonstrated that the promotion of flip-flops could be achieved in large unilamellar vesicles by substituting a hydrophobic residue with a charged one in the peptide transmembrane region. To date, spontaneous flip-flops in the presence of cationic membrane active peptides have only been reported in two MD studies of AMPs, which both involved permeation of the membrane by water particles, and the flip-flop events were not analysed further by the authors [177, 346]. In contrast, in the simulations performed here, multiple flip-flops were observed to occur in the presence of transportan peptides and without pore formation. This chapter presents an in-depth study of these events as well as a discussion of how they relate to experimental observations and previous computational findings.

6.2 Flip-flopping lipids

6.2.1 Simulations

All the results presented in this chapter are based on the set of simulations presented in the previous one. These simulations correspond to systems where either one or nine copies

of transportan NMR-based structure were embedded in the asymmetric plasma membrane model AM presented in Chapter 3 as well as in symmetric bilayers with the composition of its zwitterionic (SMZ) and anionic (SMa) leaflet respectively and in a simple POPC membrane. Details about these simulations were previously summarised in Tables 5.1 and 5.2.

It should be mentioned that similar phospholipids flip-flops to those discussed in this chapter were also observed in the simulations performed in Chapter 4 which involved eight copies of the NMR-based structure of transportan in the AMv1 bilayer (see 4.4.3) but these were not taken into account in the systematic analysis presented here. It is also worth stressing again that while cholesterol molecules rapidly diffused between leaflets (see 3.2.4), no phospholipids flip-flops were observed in any of the pure lipid bilayers, regardless of asymmetry. This is consistent with previous CG MD simulations of lipid bilayers [400] and the slower passive transbilayer diffusion of phospholipids due to their higher energy cost.

6.2.2 Identification method

Snapshots illustrating the successive stages observed during a phospholipid flip-flop event are presented in Figure 6.1. As can be seen, the flip-flopping process involves an intermediate orientation in which the acyl chains of the flip-flopping lipids reside roughly parallel to the local membrane plane. Although such an event can be identified by visual observation of the MD trajectory, this subjective and tedious approach is prone to error and does not scale to the analysis of several systems containing more than a thousand lipids each (see Table 5.2). However, the implementation of an automated approach presents some difficulties. First, the membrane thinning induced by transportan clusters and the associated dragging of lipids head groups into the bilayer core can render the leaflet detection algorithm [485] inefficient by the "bridging" effect of those central lipids (see 4.4.3). And second, once leaflets are identified a criteria must be defined to tell flip-flopping lipids apart from those lipids merely pulled into the bilayer. To address those issues associated with "on-the-fly"

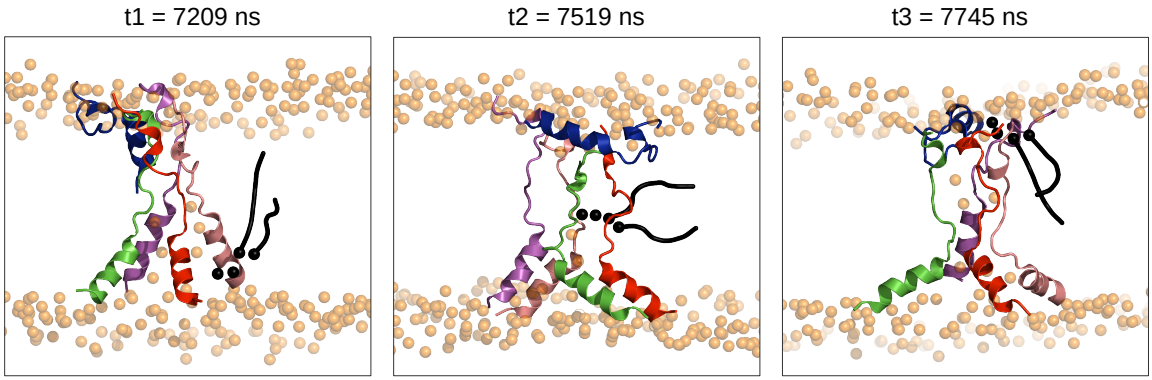

Figure 6.1 Successive stages undergone by a flip-flopping lipid (show in black) in presence of a transportan cluster. The orange spheres represent the phosphate beads of non flip-flopping phospholipids (tails are omitted for clarity) and their presence deep into the bilayer illustrate the difficulty of automated, on-the-fly detection of flip-flops.

detection of flip-flops, I simply relied on the comparison of the leaflets composition between the first and final frames of the simulations. It is important to note that while this approach is robust and practical, lipids undergoing an even number of successive flip-flops cannot be detected. However, the results discussed below suggest that, unlike cholesterol (see 3.3.3), phospholipids only flip-flopped once on the timescale of the simulations performed.

6.2.3 Results

The flip-flopping events detected are summarised in Figure 6.2. Overall, a total of 64 flip-flops were detected. As can be seen, the vast majority (89%) involved anionic lipids which is in agreement with experimental reports [514, 515, 525] and further supports the role of electrostatic interactions. Interestingly, while POPS lipids from the N terminus leaflet and the C terminus leaflet were observed to flip-flop in equal proportion in the SMa model, a different pattern was observed in asymmetric membranes. Indeed, while a similar number of POPS flip-flopped when transportan was positioned with its N terminus outwards, half as many did when it was positioned with its C terminus outwards. As for zwitterionic membranes, although very few flip-flops were observed it should be noted that most of

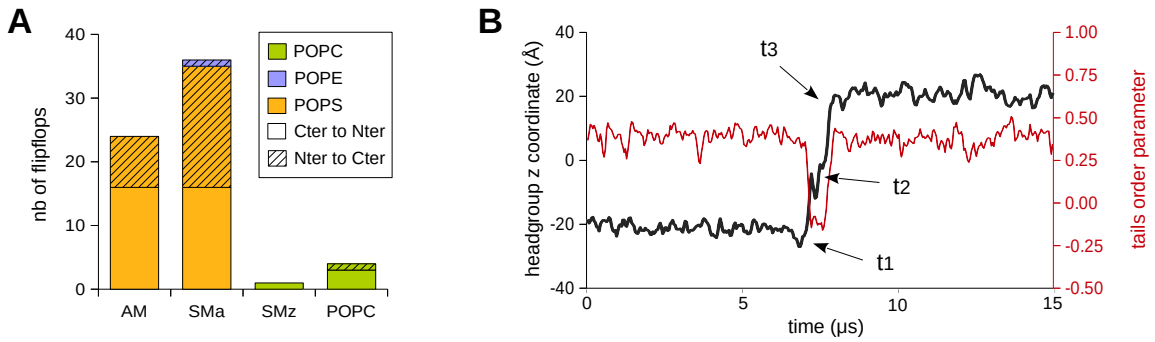

Figure 6.2 (A) Total number of flip-flops observed in each membrane model. The flip-flop direction relative to the peptides is determined based on the flip-flopping starting leaflet. (B) Evolution of the z coordinate of a flip-flopping lipid phosphate group (black line) and of the its tails order parameter (red line). The times indicated correspond to the snapshots presented in Figure 6.1.

them occurred in the POPC bilayer which is consistent with its greater deformability due to the absence of cholesterol as discussed in the previous chapter (see 5.4).

The comparison of the evolution of the z coordinate of the phosphate head group of the flip-flopping lipids identified with that of their tails order parameter (example provided in Figure 6.2B) showed they were consistent with the structures observed in Figure 6.1 thereby validating the detection algorithm implemented. Indeed, the penetration of the lipid into the bilayer correlated with a change in its orientation and indicated that the flip-flopping process involved a transient orientation orthogonal to the bilayer normal as the lipid was in the inter-leaflet area. Satisfyingly, a similar correlation was reported by Gurtovenko and co-workers in a previous united-atom study of flip-flops, thereby demonstrating that despite their lower resolution CG representations can provide valuable insights in the molecular mechanism of flip-flops [519]. Such a transmembrane orientation makes sense as it allows the flip-flopping lipid to minimise the repulsive interactions between its charged head groups and its hydrophobic environment as well as the steric clashes between its tails and the acyl chains of the neighbouring lipids. As a side note it should be mentioned that such an analysis assumes the local bilayer normal is parallel to the z axis, which may not hold true if the membrane deforms too severely.

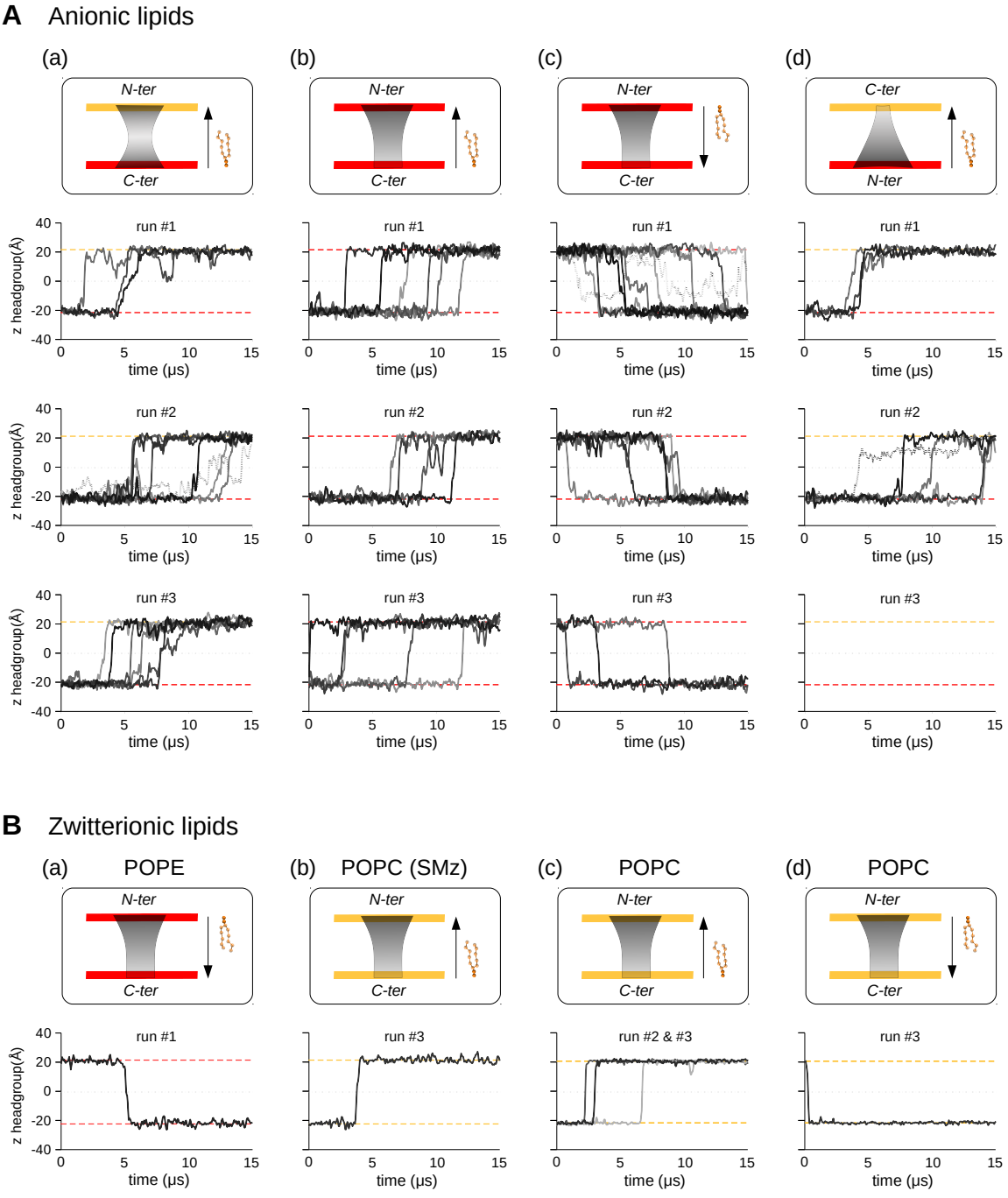

Figure 6.3 Evolution of the z coordinate of the phosphate group of flip-flopping lipids in each simulation. Lipids for which the flip-flopping process took over 1 µs are indicated by a dotted line. In (B) the species of the flip-flopping lipid is specified on each graph and in (c) the lightest shade of grey correspond to run #2. Anionic and zwitterionic leaflets are represtend by red and yellow lines respectively. The direction of flip-flops with respect to transportan peptides and the membrane is indicated on the cartoon representation of the cluster shape.

Additionally, Figure 6.2B also suggests that peptide-induced flip-flops are rapid events. I investigated this further by tracking the evolution of the z coordinate of the phosphate bead of each flip-flopping lipid detected. The results, presented in Figure 6.3, show that bar a few lipids which appeared to become trapped in the membrane core, all flip-flops occurred on a timescale of hundreds of nano seconds. Interestingly, previous atomistic MD simulations of defect-induced flip-flops reported somewhat faster translocation times, in the order of tens of nanoseconds[519, 520]. Although small, these differences may be characteristic of the different mechanisms involved, as in those simulations flip-flops were mediated by water pores. As also illustrated by Figure 6.3 the majority of flip-flops happen at different points in time evenly distributed during the simulations: this is consistent with the absence of stable pore channels and in agreement with the experimental work of Almeida and co-workers who proposed that for such membrane active peptides "dye efflux and lipid flip-flop occur concomitantly with the transient peptide-induced perturbation of the membrane" [120, 148]. However, the correlation between peptide translocation and lipid flip-flops that has been suggested by other authors [346, 525] is less clear: while visual observations does show that transportan peptides are able to drag some phospholipids along as they translocate, the results obtained also provide abundant evidence that flip-flops occur independently of such translocations as illustrated by Figure 6.1. In particular, it is interesting to note that no flip-flops were observed in one AM simulation (run #3 in Figure 6.3D) despite the translocation of most transportan peptides (see Figure 5.7C).

6.3 Interactions of flip-flopping lipids with transportan

The fact that no flip-flops were detected in the ES simulations suggest that the cooperation of several peptides is needed to induce such events. The influence of the size of transportan clusters and how flip-flopping lipids interact with such aggregates was therefore investigated and the results are presented below.

6.3.1 Method

For each flip-flopping lipid, the number of peptide particles in contact with the phosphate head group was recorded using a 6 Å cutoff along with the size of the cluster the corresponding transportan molecule was involved in. The distribution of the total number of lipid-peptide contacts with respect to cluster size was then calculated after having separated the lipids into two groups based on the flip-flop direction relative to the peptides. In order to check that flip-flops were indeed triggered by the transportan clusters and not pollute the results with random interactions due to the diffusion of lipids, a further distinction was made between contacts occurring during the flip-flopping event and those that happened either before of after. This required establishing a criteria defining the start and the end of each flip-flop, which, for reasons similar to those described previously regarding the identification of flip-flops (see 6.2.2), can be problematic. This was achieved using the following protocol:

1. In each leaflet, the 5 non flip-flopping lipids closest to the flip-flopping lipid of interest were identified based on inter phosphate groups distances and their centre of geometry (respectively G_{lower} and G_{upper}) was calculated.

2. The distances separating the flip-flopping lipid phosphate group from G_{lower} and G_{upper} (respectively d_{lower} and d_{upper}) were then calculated as well as the distance between G_{lower} and G_{upper} (d_{l-u}).

3. For a lipid reaching the upper leaflet from the lower one, the flip-flop was considered to start the first time $d_{lower} > 0.1d_{l-u}$ and to be over as soon as $d_{upper} < 0.1d_{l-u}$. The corresponding rule was used for flip-flops occurring in the opposite direction.

This approach has the advantage of taking local membrane deformations into account and, importantly, it also works regardless of the local orientation of the membrane as there is no need to assume that the bilayer is in the (x,y) plane.

6.3.2 Influence of cluster size

The overall distribution of contacts flip-flopping POPS lipids formed with the different sizes of transportan clusters is presented in Figure 6.4. As can be seen, these results demonstrate that, regardless of direction, flip-flopping lipids were interacting with larger transportan clusters as they crossed the membrane. In particular, it can be seen that clusters smaller than tetramers were virtually never involved during flip-flops and merely sampled outside the event window through random diffusion of the lipids. On the other hand, the fact that larger clusters (tetramers and above) account for most contacts both outside and during flip-

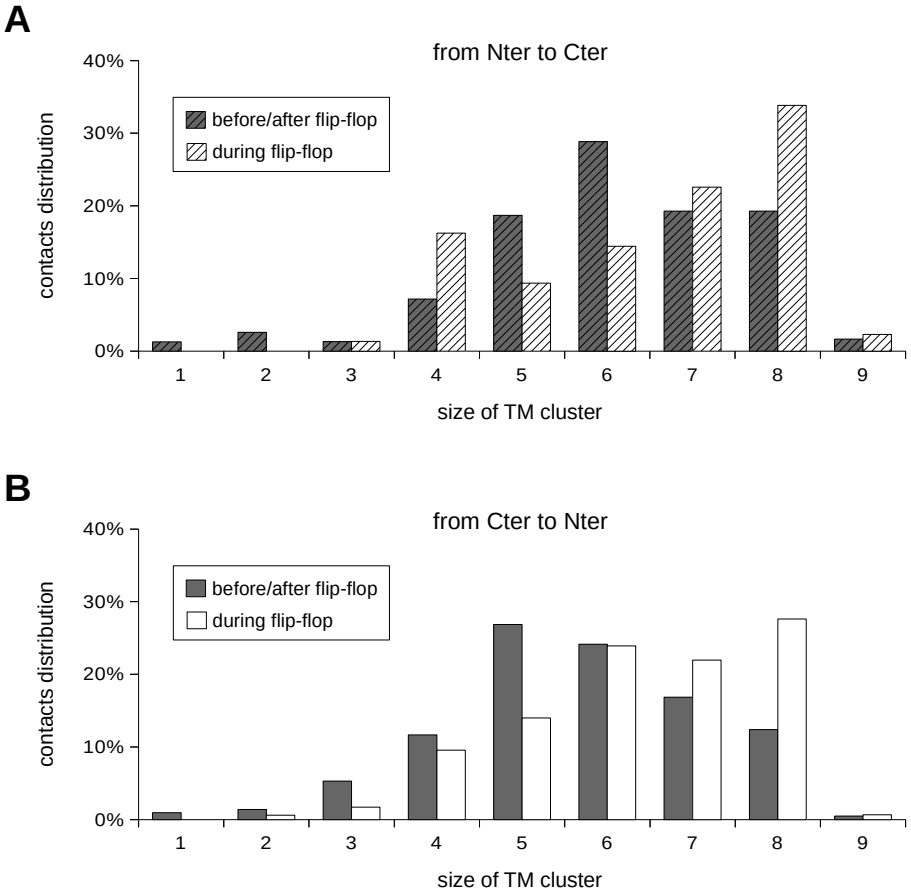

Figure 6.4 Relative distribution of contacts between flip-flopping POPS and the different sizes of transportan clusters. Data was aggregated for all POPS flip-flops as variations in the sampling of each cluster size between the different systems prevented averaging and comparison between different simulations.

flops suggest that these aggregates allowed lipids in their vicinity to overcome the energy barrier associated with the crossing of the hydrophobic bilayer. It is consistent with the snapshots presented in Figure 6.1 where, according to the criteria presented above, only the second stage t2 is detected as *during* the flip-flop. It should also be noted that, despite the variations in clustering patterns observed between simulations (see Figure 5.7), the contacts occurring outside the flip-flopping window adopt a somewhat gaussian distribution centered on hexamers (Figure 6.4A) or pentamers (Figure 6.4B), whereas the distribution of those occurring during flip-flops tend to increase with cluster size. Altogether, these observations suggests that concentration of transportan peptides plays a key role in their ability to induce flip-flops and that tetramers represent the oligomerisation threshold triggering such events.

6.3.3 Preferential sampling of basic residues

Following the previous observations, the nature of the contacts engaged by flip-flopping lipids with transportan clusters was further investigated by comparing the residues sampled with their occurrence in transportan sequence. The results presented in Figure 6.5 clearly demonstrate an enhanced sampling of basic and polar residues at the detriment of hydrophobic ones. This is unsurprising given the hydrophilic nature of the lipids phosphate head group and it complements the structures observed in Figure 6.4A to suggest that it is the aggregation of transportan peptides, rather than their translocation, that allows lipids to flip-flop by providing a favourable "hydrophilic path" within the membrane hydrophobic environment.

This analysis also revealed that with the AM model sampling of basic residues was further enhanced when transportan was positioned with its C terminus outwards (Figure 6.5D), whereas the opposite orientation led to a similar pattern to that obtained with SMa (see Figures 6.5C and A-B respectively). Similarly to what has been observed in previous sections regarding clustering of anionic lipids and the number of flip-flops, this is reminiscent of the

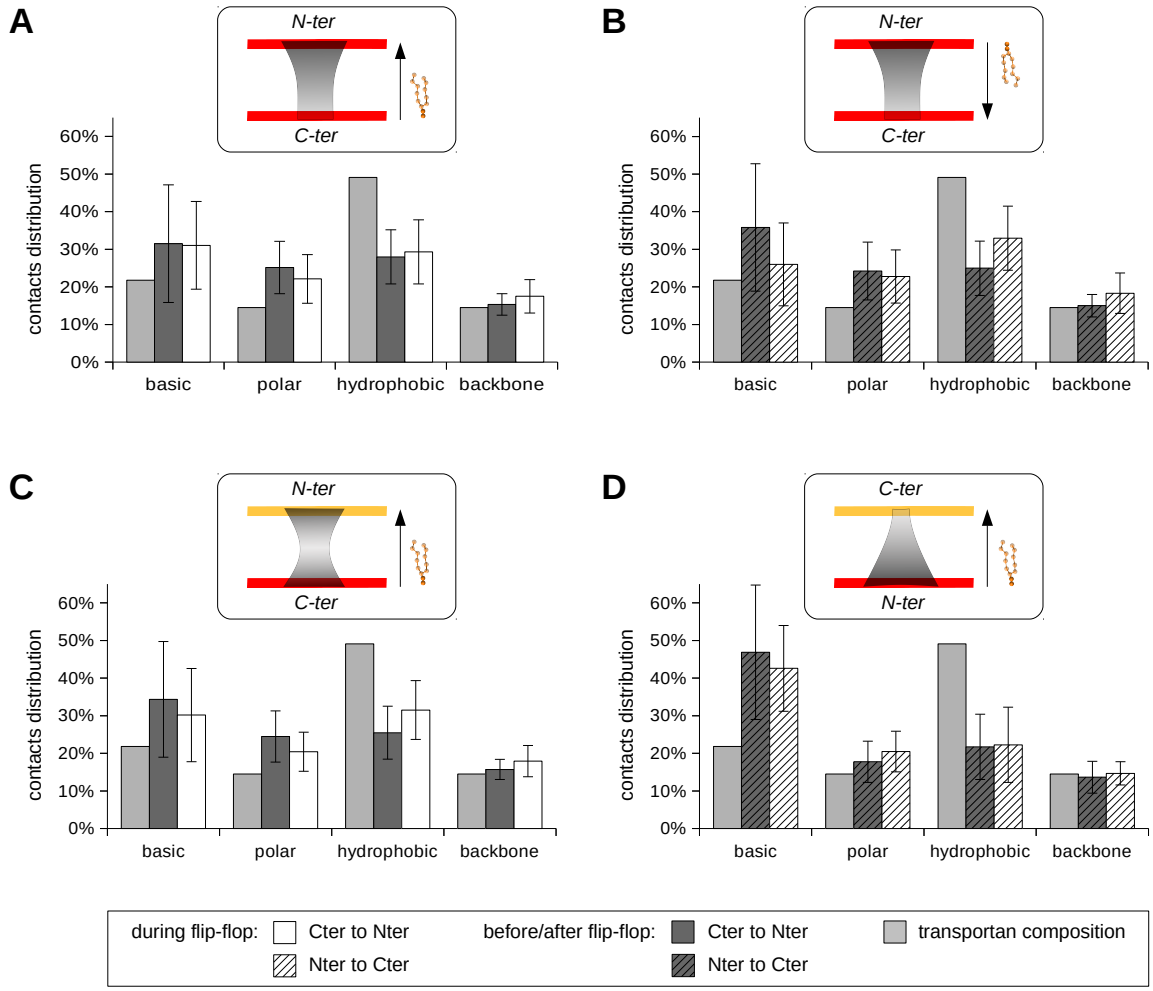

Figure 6.5 Distribution over residue types of contacts between flip-flopping POPS and transportan clusters. Residues were classified as follow: basic = ARG, LYS; polar = SER, THR, ASN, GLN, HIS; hydrophobic = VAL, ILE, LEU, MET, PHE, PRO, CYS, TYR, TRP. The "backbone" category contains ALA and GLY as in the CG Martini representation they are represented by a single bead. Distribution profiles were calculated for each flip-flopping lipid: the bar plots represent the average calculated for each membrane model and direction and the error bars the corresponding standard deviation.

influence of asymmetry and peptide orientation on residues distribution (see section 5.3.3). The density profiles of basic and hydrophobic residues were then calculated in each membrane environment in order to assess how their distribution correlated with their sampling by flip-flopping lipids and the results are presented in Figure 6.6. This revealed that basic residues were selectively sampled by the lipids even in an environment where hydrophobic residues were highly predominant. Figures 6.6D and E show that the hydrophobic to basic

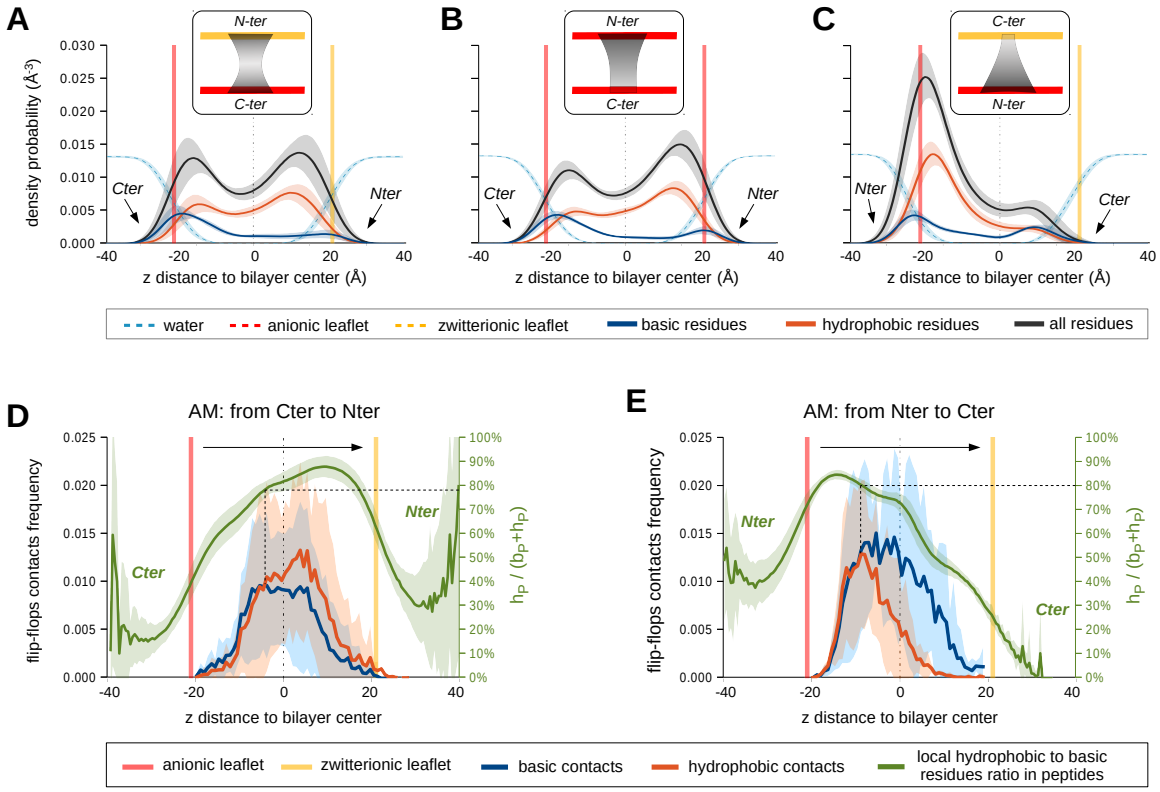

Figure 6.6 (A-C) Influence of lipid environment on residues distribution in transportan clusters involving four or more peptides. (D-E) Preferential sampling of basic residues by lipids during flip-flops: contact profiles with basic and hydrophobic were calculated for each flip-flopping lipid and then averaged (solid blue and red lines, with corresponding standard deviations shown as shaded areas) while the relative distribution within clusters of particles belonging to basic and hydrophobic (respectively b_p and h_p) was averaged between simulations (data shown in green). The black arrows in (D) and (E) indicate the direction of the flip-flops, from the anionic leaflet to the zwitterionic one.

residues ratio indeed needs to be in excess of 4 to 1 for the number of hydrophobic contacts to be greater than that of basic ones. In the light of these results, the influence of peptide orientation observed in Figures 6.5 can be explained by the different shapes of transportan aggregates.

However, it is interesting to note that the contact profiles in Figure 6.6 may appear at odds with the relative number of flip-flops observed for each orientation (see Figure 6.2A). Indeed one might imagine that flip-flops would be more facilitated by clusters providing a path that involves fewer unfavourable hydrophobic interactions than favourable basic ones, but the data show otherwise. This suggests that other factors are at play and that the relative

distribution of hydrophobic and basic residues cannot directly account for the enhanced mobility of the flip-flopping lipids.

6.4 New insights in the mechanism of flip-flops

6.4.1 The role of local charge density

Together with the correlation between positive charge density and the clustering of anionic lipids identified in 5.4.2, the above observations prompted me to investigate the role played by the distribution of charges in lipid flip-flops. To this end, I calculated the average charge density profiles around transportan clusters within a 30 Å radius, following the method presented in the previous chapter (see 5.3.3). For the sake of simplicity, only the negative charge of POPS lipids, corresponding to their phosphate bead, was taken into account in order to calculate the lipids contribution and the zwitterionic species POPC and POPE were ignored. The results are presented in Figure 6.7. As can be seen, transportan aggregates involving four or more peptides led to a continuously positive total charge density in the core of the lipid bilayer whereas smaller clusters did not. This suggests that the critical size effect observed in Figure 6.4 corresponds to the ability of larger clusters to provide a continuous positive charge distribution throughout the membrane. Furthermore, it provides a basis to explain the importance of peptides concentration and cooperation reported experimentally. Indeed, while it is difficult for the basic residues of a single transportan molecule to span the bilayer, it can be hypothesised that the aggregation of several transportan provides a scaffolding structure allowing their redistribution. However, as discussed previously, it is important to bear in mind that the disordered and dynamic nature of these clusters do not correspond to defined and stable structures. In this regard, in addition to the need for peptide aggregation, Figure 6.7 also provides evidence that the shape of the clusters formed strongly influences the charge density throughout the lipid bilayer. In particular, the AM

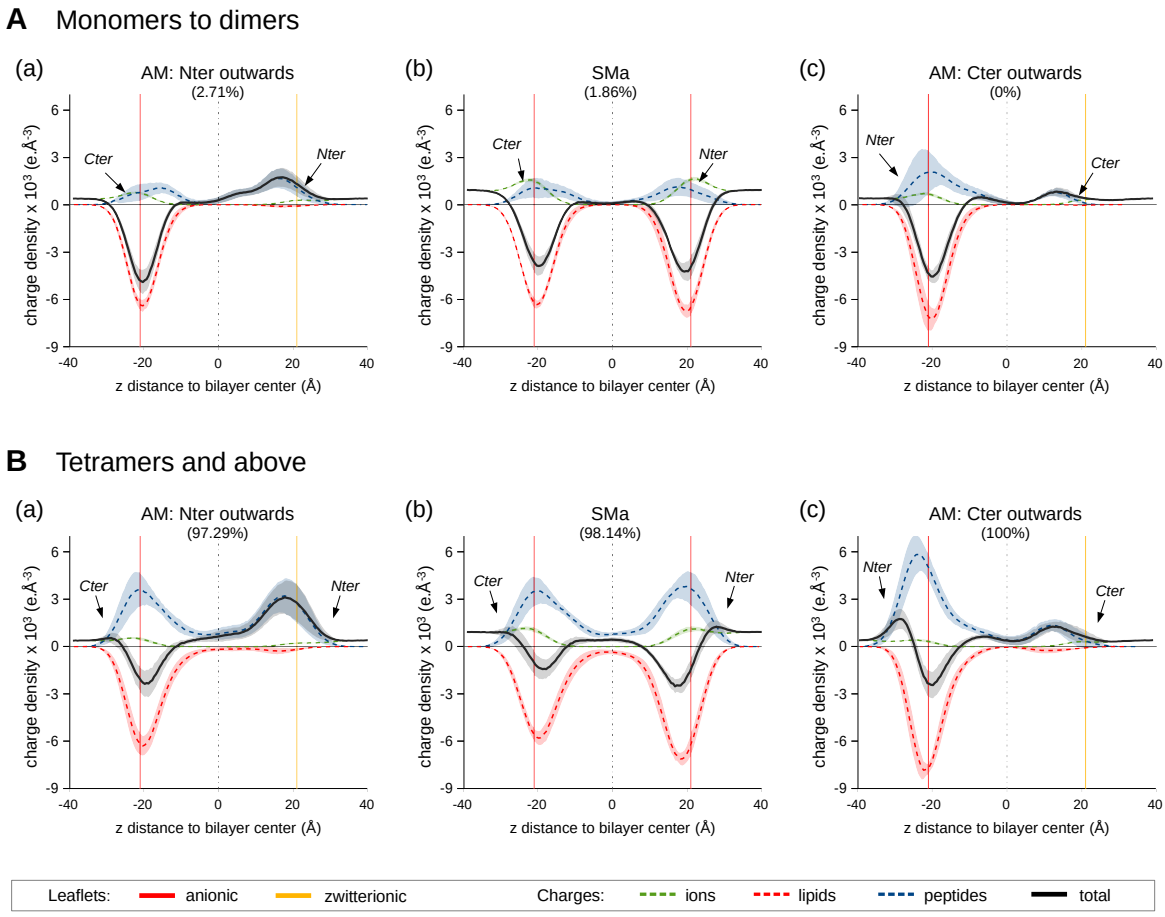

Figure 6.7 Influence of lipid environment and cluster size on local charge density. The distribution profiles were averaged between repeats and the standard deviation shown as transparent areas. The percentages indicate the proportion of the contacts (during flip-flop) between flip-flopping lipids and transportan peptides that are accounted for by clusters within the size range represented. For the sake of simplicity only POPS lipids were taken into account to determine the lipids contribution.

simulations where transportan was positioned with its C terminus outwards led to the least favourable charge density profile, featuring a pronounced dip in the centre of the bilayer (in Figure 6.7B), due to the highly asymmetric distribution of the cationic charges. Interestingly, detailed analysis of each of these simulations, presented in Figure 6.8, revealed that the number of flip-flops observed correlated with the charge density in the bilayer centre. Most notably, the absence of flip-flops corresponded to the simulation (repeat #3) where the charge density dropped to virtually zero.

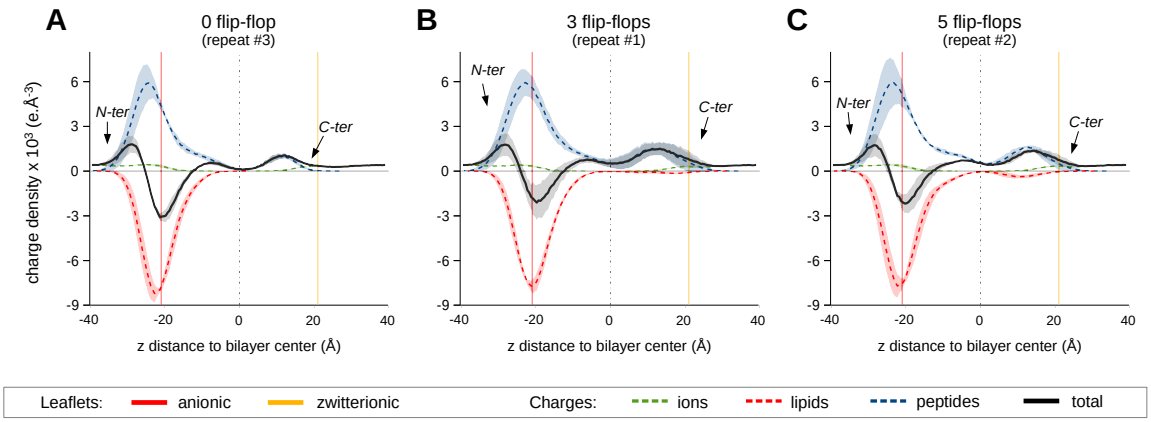

Figure 6.8 Influence of cluster shape on local charge density: individual charge density profiles for AM simulations where transportan peptides were positioned with their C terminus outwards. In each simulation the average profiles were calculated for all cluster sizes involving four or more peptides with the standard deviations thus corresponding to intra-simulation fluctuations for this size range. For the sake of simplicity only POPS lipids were taken into account to determine the lipids contribution. The number of flip-flops observed during each repeat is indicated on each plot.

6.4.2 CG flip-flops dot not reveal water permeation of membranes

Altogether these observations suggest that transportan clusters need to provide a continuous "hydrophilic path" within the membrane in order to trigger flip-flops. This is in accordance with a recent experimental study by Kaihara and co-workers who found that a hydrophobic membrane spanning peptide could enhance flip-flops following the introduction of charged residues in the transmembrane region [524]. Indeed, the results presented here lend molecular level support to the hypothesis that a locally polar region within the lipid bilayer is instrumental to the ability of phospholipid to flip-flop. Similarly, previous MD simulations found that more or less transient water pores provided hydrophilic defects that allowed flip-flopping lipids to cross the hydrophobic membrane barrier [400, 516–522].

In contrast with these studies, which described a pore-mediated flip-flop mechanism akin to what is observed during electroporation of lipid bilayers [526, 527], the integrity of the membrane was not compromised during any of the simulations performed here. This is illustrated in Figure 6.9 where the effective electrostatic potential maps and water den-

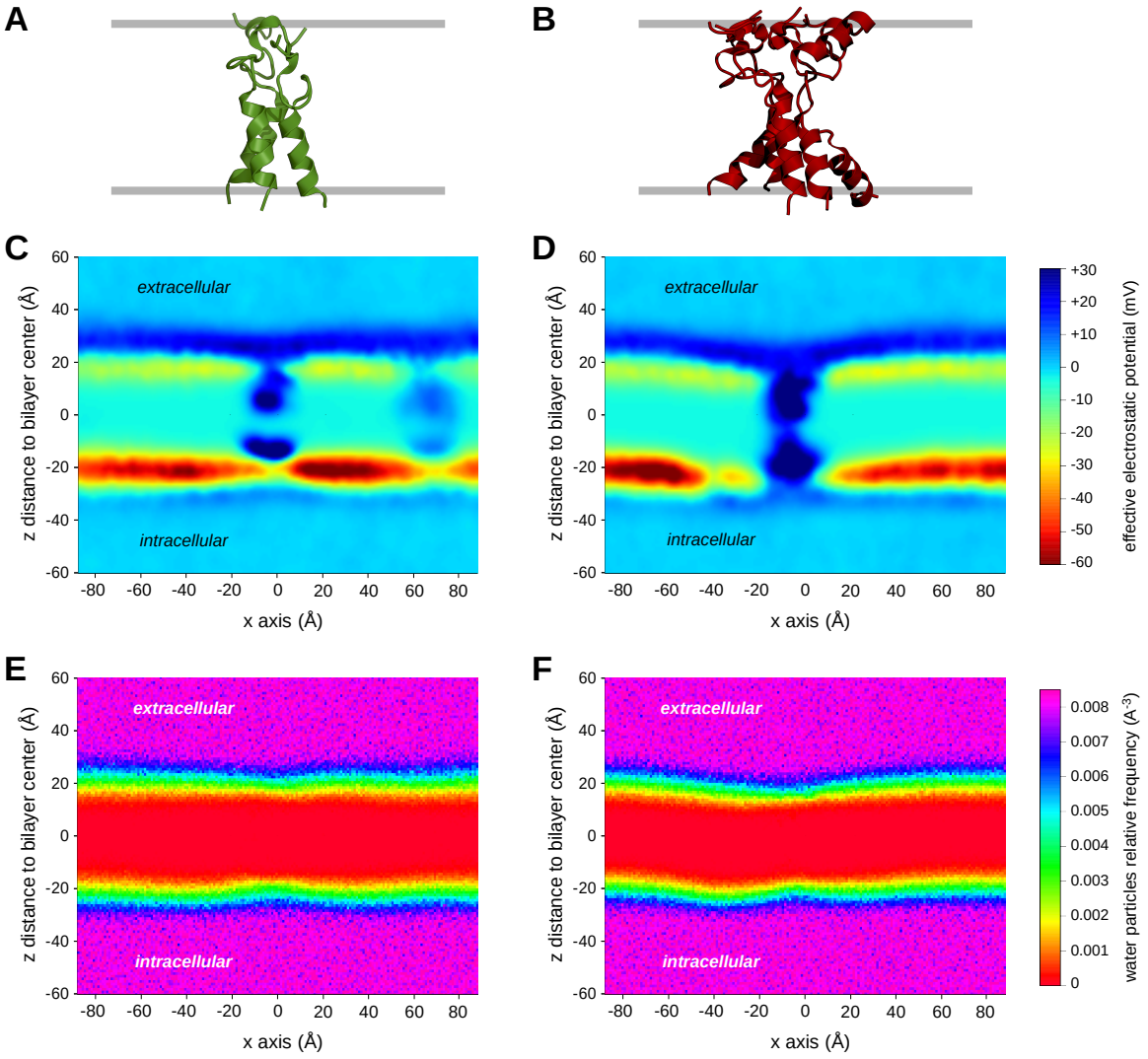

Figure 6.9 Influence of cluster size on the effective electrostatic potential (C-D) and corresponding water density (E-F). In (C) and (E) a transmembrane trimer is present in the centre of the AM bilayer and represented in (A). In (D) and (F) it is a hexamer, as shown in (B). The effective electrostatic potential was calculated as described in 3.4.1 using a spacing of 1 Å along each axis and an averaging window of 100 ns. Importantly, in (D) and (F) the averaging window was centred on a flip-flop event. The relative distribution of water particles was calculated using similar parameters by simply binning the water particles into the tridimensional grid. The 2D maps were then obtained by averaging the data over an x, z slice centred on the transportan cluster and with a thickness corresponding to half the length of the simulation box along the y axis. In (C) the positive potential inside the bilayer observed for $x \simeq 70$ Å corresponds to a secondary cluster partially present in the averaging slice.

sity profiles associated to transportan clusters which respectively did (hexamer) and did not (trimer) induce flip-flops are compared. It can be seen that water particles did not penetrate the lipid bilayer regardless of the cluster size, even though the hexamer plots were obtained during a flip-flop event. On the other hand, the effective electrostatic potential maps reveal that the larger transportan cluster leads to a continuous positive effective potential across the membrane. In contrast, in the case of the cluster involving only three transportan molecules, the extent of the positive effective electrostatic potential created by the peptides basic residues was limited to the vicinity of the leaflet surfaces and did not "bridge" the bilayer core. These observations further illustrate the influence of cluster size and residues distribution on the electrostatic properties of the bilayer core presented in Figure 6.7. Importantly, they also provide molecular insight regarding how transportan clusters can impact the local properties of their membrane environment and induce lipid flip-flops. Indeed, the results presented here suggest that flip-flops are triggered by *electrostatic pores* resulting from the aggregation of four or more transportan molecules. Crucially, although these events correspond to a significant perturbation of the properties of the membrane model, flip-flops relying on such peptide-induced defects do not require membrane permeation, unlike the water pore-mediated mechanism reported previously.

However, it is important to bear in mind that the absence of membrane permeation by water particles may be due to limitations of the CG MARTINI model used. Indeed, the coarse description of water particles may prevent the observation of small water defects such as single file water structures. In a previous combined CG and atomistic study of aggregates formed by the AMP alamethicin, atomistic simulations revealed the formation of water pores whereas only a few water beads were found inside the lipid bilayer in CG simulations [528]. Interestingly, atomistic simulations performed by Tieleman and co-workers where water ingress in the lipid bilayer was still observed when 4 water molecules were tethered together [400] suggest that the coarse size of CG water particles is not the main factor

preventing the formation of such water pores. Rather, it is likely that the simple description of water electrostatic properties, as discussed in 3.4.1, plays a preponderant role in the absence of formation of local water defects. Therefore, while it is very interesting that, unlike what was observed for previous CG MD studies of AMPs [178, 182, 422], transportan aggregates were not observed to permeabilise the lipid bilayer despite triggering lipid flip-fops, it is not possible to conclude, on the sole basis of the CG simulations presented here, that transportan peptides cannot lead to the formation of water defects inside the membrane.

6.4.3 Influence of transportan on the free energy barrier of flip-flops

In order to estimate the effect of transportan clusters on the energetic cost associated to lipid flip-flops, free energy profiles were calculated by Boltzmann inversion of the anionic lipid densities and compared to that obtained in membranes which did not contain any peptides. The results are presented in Figure 6.10 and show that, as expected, the energy barrier essentially corresponded to the crossing of the bilayer hydrophobic core. Importantly, this analysis allowed to quantify to what extent the presence of transportan molecules and their clustering lowered this free energy barrier. Indeed, in the presence of the larger transportan clusters (tetramers and above) the free energy barrier of flip-flops was estimated to be around 3 kT in the SMa model, while in the AM model it was around 4 kT when transportan was positioned with its N terminus outwards and 5 kT otherwise. Those numbers were approximately 4 kT higher in the presence of the smaller clusters. In the control simulations which did not contain any peptides no flip-flops were observed. However, unlike what the blue lines in Figure 6.10 might suggest, this of course does not mean that the free energy barrier is infinitely high but merely too high to allow sampling during the simulations performed.

The free energy barrier values obtained (or absence thereof) are in very good agreement with the extensive computational work carried by Tieleman an co-workers to characterise the PMF of flip-flops. Their findings [516, 522] indicate that flip-flops occurring on a mi-

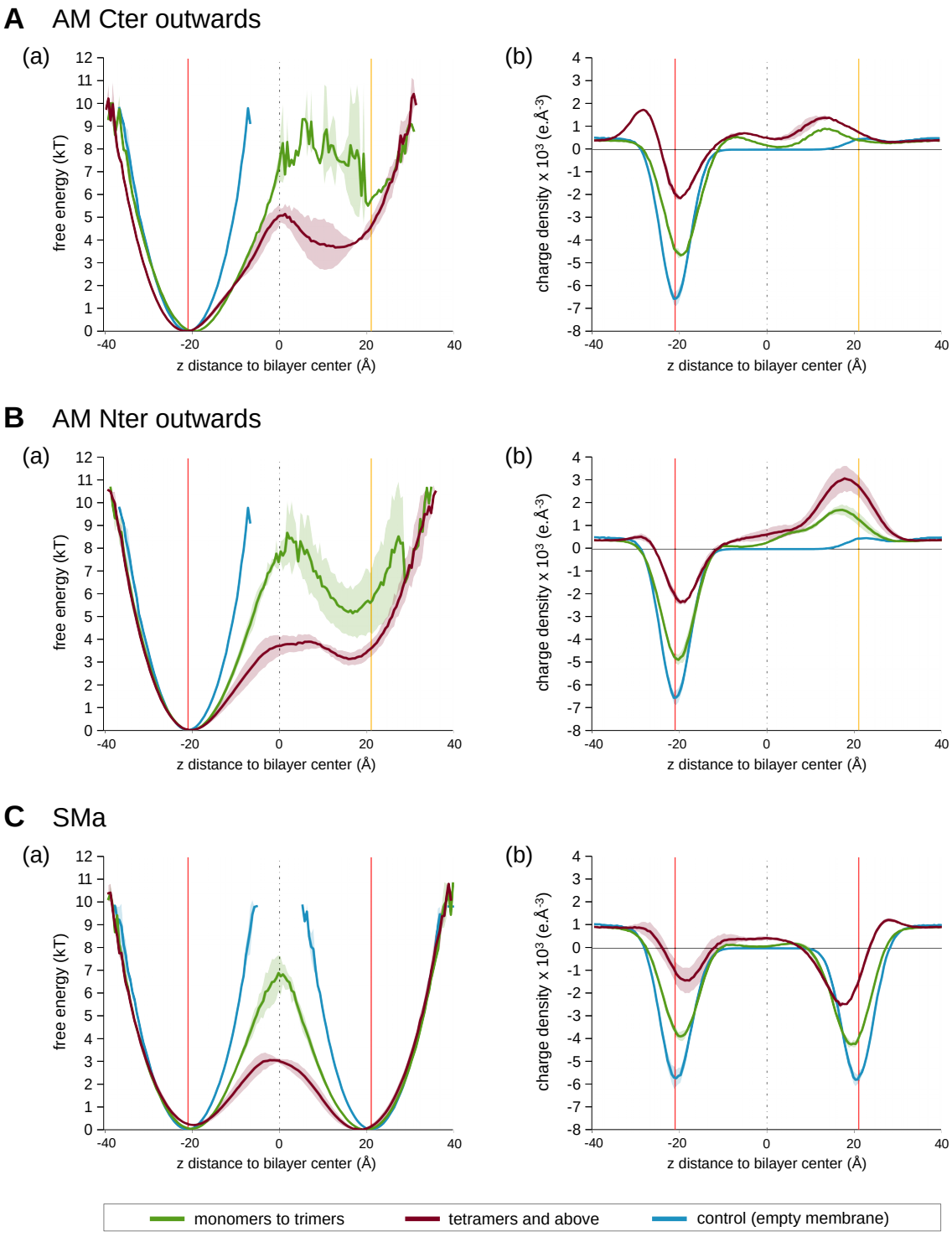

Figure 6.10 Influence of lipid environment and transportan TM clusters on total charge distribution and the free energy profiles of phopsholipids flip-flops. The free energy was calculated by Boltzmann inversion of POPS lipids density and the profiles presented were then obtained by averaging either between repeats (EL simulations) or 3 successive 5 µs windows (control simulations). In (A) the data of the simulation for which no flip-flops were observed was excluded.

crosecond timescale had to overcome a free energy barrier of approximately 6,4 kT and they estimated the energetic cost of unassisted POPC flip-flop to be 35,6 kT which corresponds to a flip-flop rate on a timescale of hours to days in accordance with experimental reports. While their values were obtained using the united-atom Berger force field [529], Tieleman's group also published a later study where the Martini model was shown to satisfyingly reproduce the atomistic energy profiles in the absence of pore formation [400]. In this context, the free energy barrier estimates of 3-5 kT obtained here in the presence of the larger transportan clusters are consistent with their lifespan of several microseconds as evidenced earlier in Figures 5.7 and 5.4. Furthermore, the fact that both the greatest reduction of the free energy barrier and the most significant bilayer thinning were obtained with the same membrane model (SMa) is consistent with the detrimental role of membrane thickness on the energetic cost of flip-flops that is demonstrated in reference [522].

In light of the above considerations, the decrease of the free energy barrier of flip-flops measured is in good agreement with the order of magnitude of the acceleration of the flip-flops rate that Fattal and Matsuzaki reported experimentally in the presence of antimicrobial peptides [514, 515]. However it is important to stress that unlike the peptides they studied, transportan clusters did not lead to pore formation thereby suggesting that membrane permeabilisation is not necessary for flip-flops to occur. In this regard, the results obtained are in very good agreement with the experimental observations of Zhang and co-workers who found that some AMPs induced flip-flops at lower concentrations than those causing vesicle leakage [40]. In particular, the simulations performed provide molecular level support to the authors hypothesis that such flip-flop events were mediated by disordered transmembrane aggregates of peptides, the collapse of which also possiby providing a pathway for peptides translocation.

Finally, the data presented in Figure 6.10 also illustrate the clear correlation between the decrease of the free energy barrier to flip-flops and the increase of the charge density

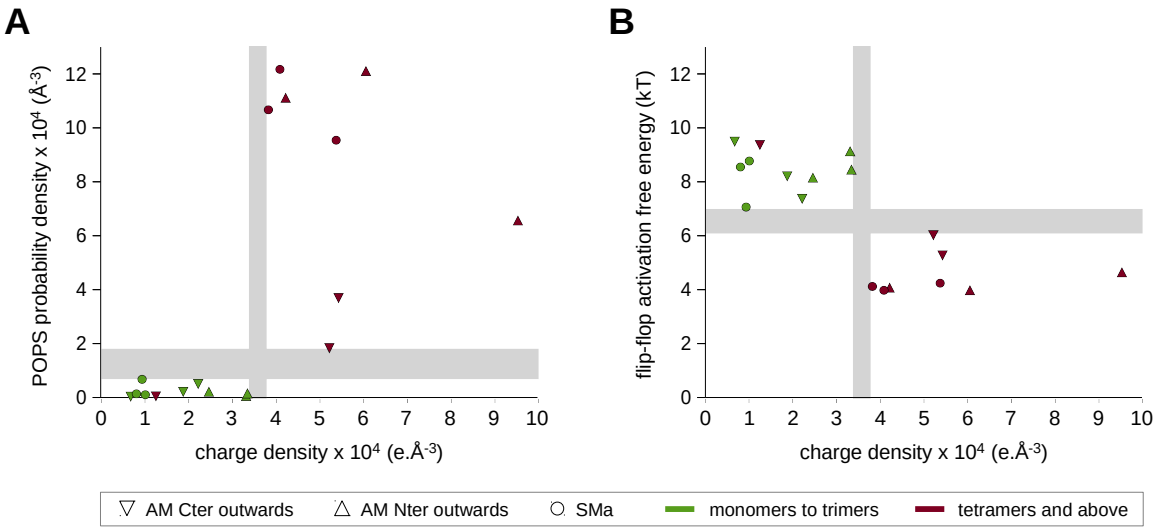

Figure 6.11 Charge density in the middle of the lipid bilayer discriminates between flip-flopping and non flip-flop inducing transportan clusters. For each simulation the (A) POPS density at $z = 0$ and (B) the corresponding relative free energy, assumed to be the free energy barrier to flip-flop, were plotted against the total charge density at $z = 0$.

throughout the lipid bilayer for all three sets of simulations. The analysis performed is therefore in agreement with the hypothesis of Kaihara and co-workers presented earlier according to which the introduction of a local polar region in hydrophobic membrane-spanning peptides enhance flip-flops by reducing their activation energy [524]. Importantly, it further complements their experimental work by providing a quantification of the free energy barrier reduction due to peptides aggregation. Interestingly though, and rather surprisingly, the comparison of the profiles associated to the larger clusters reveal that a greater positive charge density does not appear to lead to a lower free energy barrier. This is further illustrated by plotting the anionic lipids density, or free energy, against the charge density at $z = 0$ for all simulations individually, as presented in Figure 6.11. Such scatter plots successfully separate all the clusters that trigger flip-flops from those that do not (in particular they deal correctly with the case of the AM simulation for which no flip-flops were observed despite the presence of a large transportan aggregate), which confirms the relevance of the charge density in the membrane core as a metric to assess the ability of transportan clusters to enhance flip-flops. Although a cutoff value of approximately 3.5 10^4 $e.\text{Å}^{-3}$ can be

identified, it is not clear how the free energy barrier then relates to the charge density beyond this threshold. It is likely that the transient structures adopted by transportan clusters during the flip-flops are of importance and further analysis of the flip-flops would require defining some relevant structural criteria. At this point, it is worth mentioning that the critical charge density can also be achieved in zwitterionic membranes due to the similar shape of transportan clusters to that observed in the SMa model (see Figure 5.9). The marginal number of flip-flop observed in these membranes is then consistent with the hypothesis that electrostatic interactions are the driving force of the peptide-mediated flip-flops: negatively charged phospholipids are able to take advantage of the "cationic path" created by transportan clusters whereas in zwitterionic this is counter-balanced by the additional presence of a positive charge. In particular, this is in good agreement with previous experimental findings where the flip-flop rates of different lipid species were observed to correlate with the total number of charges present in the phospholipids head group [530].

6.5 Conclusion

The simulations performed showed that aggregates formed by transportan molecules triggered the transbilayer movement of phospholipids. These flip-flops were found to present four main characteristics: first, they were fast and occurred on a timescale of a couple hundreds nanoseconds; second, they occurred in the presence of transmembrane transportan clusters involving at least four molecules; third, they involved preferential contacts with basic residues; and fourth, they almost exclusively implicated anionic lipids.

The analysis presented in this chapter demonstrated that these observations support the hypothesis that flip-flops were driven by electrostatics interactions following the modification by transportan clusters of the charge density profile within the membrane. In particular, the assumption that transportan molecules need to provide a continuous "cationic path" through the lipid bilayer to trigger flip-flops can account for the importance of pep-

tides cooperation and the influence of cluster shape and residues distribution on the number of flip-flop events observed. Importantly, in contrast with the water pore-mediated mechanism observed in previous computational studies [400, 516–522], flip-flops were found to be peptide-mediated and to occur through an *electrostatic pore* which maintained membrane integrity and did not involve water penetration. Furthermore, the calculation of the flip-flop free energy profiles allowed to quantify the reduction of the energy cost associated to crossing of the hydrophobic bilayer during flip-flops in presence of transportan peptides. In spite of the different mechanism involved, the free energy barrier estimates of 3-5 kT obtained and the short sub-microsecond timescale of the flip-flopping events were in good agreement with previous MD investigations of the PMF of flip-flops [516, 522]. They were also consistent with the enhancement of the rate of flip-flops reported in lipid vesicles in presence of AMPs [514, 515].

The results obtained agree well with *in vitro* studies which demonstrated that flip-flops could be promoted by peptide-induced modifications of the local electrostatic properties of the bilayer interior [524]. Similarly, the simulations performed are consistent with experimental evidence that membrane active peptides aggregates can mediate flip-flops without causing membrane leakage [40] and provide molecular insights in the mechanism involved. In this regard, the findings presented here are again consistent with the ambivalent nature of transportan and its moderate membrane toxicity as a CPP. Indeed, in contrast to what has been reported in previous CG simulations of AMPs [178, 182, 422], the metastable aggregates formed by transportan molecules did not lead to permeation of the lipid bilayer. Nevertheless, they did induce significant destabilisation of the membrane and, notably, led to the externalisation of POPS lipids in the plasma membrane model which could contribute to their cytotoxic activity. Additionally, the absence of formation of stable channels and the stochastic nature of the successive flip-flopping events observed are consistent with the suggestion that the graded efflux of vesicles content induced by some membrane active is

due to transient peptide-mediated membrane defects [120, 148].

Altogether, these results further confirm the relevance of a CG approach to investigate peptide-induced membrane perturbations. Most notably the smoothing of the energy landscape allowed the spontaneous sampling of events otherwise inaccessible by atomistic simulations. However, this comes at the price of the structural accuracy of such reduced resolution models [400, 531] and further investigations of the mechanisms involved in the membrane defects induced by CPPs and their possible ability to trigger transient leakage will require more detailed representations, similarly to what has been done to study the membrane poration mechanism of AMPs [422, 528].

Chapter 7

Future directions

Having spent the previous four chapters presenting the different simulations and analysis performed to explore the origins of membrane destabilisation induced by cell-penetrating peptides, I briefly review the main findings in this final chapter before presenting possible directions to further investigate and validate the results obtained.

7.1 Summary of findings

An asymmetric lipid bilayer was developed to model the plasma membrane of mammalian cells and study the influence of lipids distribution on the interactions of CPPs with biologically relevant membranes. In 2011, at the time this effort began, nearly all MD simulations of bilayers reported in the literature were performed using symmetric bilayers. Although several computational tools have recently simplified the building of complex membrane models with different lipid mixtures in each leaflet, the simulations performed in this thesis shed lights on the possible concerns associated to the use of such bilayers. In particular, it was shown that the relative distribution of lipids, and notably that of cholesterol molecules, should remain simple enough in order to avoid unwarranted mechanical stress on the bilayer

and to detect the preferential interactions of CPPs with different species.

The ability of transportan, a membrane toxic CPP related to antimicrobial properties, to destabilise such a biologically relevant lipid bilayer was then systematically investigated using a series of simulations with different control membranes. The suitability of coarse-grained representations to discriminate between CPPs perturbing cell membranes to different extent was first demonstrated by performing a comparative study of penetratin, a CPP with no haemolytic nor cytoxotic activity, and transportan. In good agreement with experimental data, the stronger affinity of penetratin for the surface of anionic lealfets was reproduced while transportan molecules formed metastable transmembrane aggregates that correlated with local defects of the bilayer. Additionally, these simulations also highlighted the importance of the relative distribution of hydrophobic and basic residues in the orientation and conformation adopted by transportan peptides. Following these preliminary observations, an in-depth study of the interactions of transportan clusters with their local lipid environment provided further insights on the mechanisms by which membrane active peptides can perturb bilayers. Although the transient and disordered nature of the clusters required the implementation of a statistical description of their structural properties, the stability and shape of transportan oligomers were clearly shown to depend on the lipid composition of each leaflet and, in the case of and asymmetric membranes, on the initial orientation of the peptide. This, in turn, led to perturbations of different extent in different lipid bilayers, thereby confirming the importance of membrane asymmetry on the activity of CPPs and the need to use biologically relevant membrane models. In particular, local thinning of the bilayer and disordering of the lipids acyl chains induced by transportan clusters were promoted by anionic species and hindered by the presence of cholesterol molecules, in agreement with the hypothesis that compositional differences between bacterial membranes and the plasma membrane of mammalian cells contribute to the selective disruption of the former by AMPs. The size of transportan clusters was also found to be an aggravating fac-

tor on the extent of the perturbations induced, in accordance with the cooperative activity of membrane active peptides observed experimentally. Most notably, aggregates involving four or more molecules were found to trigger the flip-flop of anionic lipids. Crucially, the simulations performed revealed a new pathway for such events that was peptide-mediated and did not involve water penetration in the membrane, in contrast to previous computational investigations of flip-flops. Indeed, flip-flops occurred through a transient *electrostatic pore* which was formed by the distribution of basic residues within transportan clusters. Such structures provided a continuous cationic path that significantly lowered the free energy barrier associated to the crossing of the bilayer hydrophobic core by the phospholipids head groups. Remarkably, this mechanism is in good agreement with experimental findings that membrane active peptides can induce local bilayer perturbations and phospholipid flip-flops without causing membrane leakage. Overall, the simulations and analysis performed support the hypothesis that cellular internalisation of transportan occur via the formation of metastable and unstructured aggregates simultaneously inducing transient local membrane defects.

These conclusions are schematically represented on Figure 7.1. While the limitations of the CG model used should be borne in mind, it is of particular interest that, unlike what has been reported in previous CG MD studies of membrane active peptides, the collective behaviour of transportan did not involve poration of the bilayer and was dependent on the asymmetry of the membrane model. The simulations performed thus extend on existing computational studies, mostly involving simple symmetric bilayers and AMPs, to demonstrate that moving along the spectrum of membrane perturbation induced by a given membrane active can be achieved by changing the type of target membrane. As for the ability of membrane active peptides to enter cells in an energy independent fashion, the computational study presented here strongly suggests that it is driven by the asymmetry of the plasma membrane and electrostatic interactions with the anionic cytoplasmic leaflet. Having established

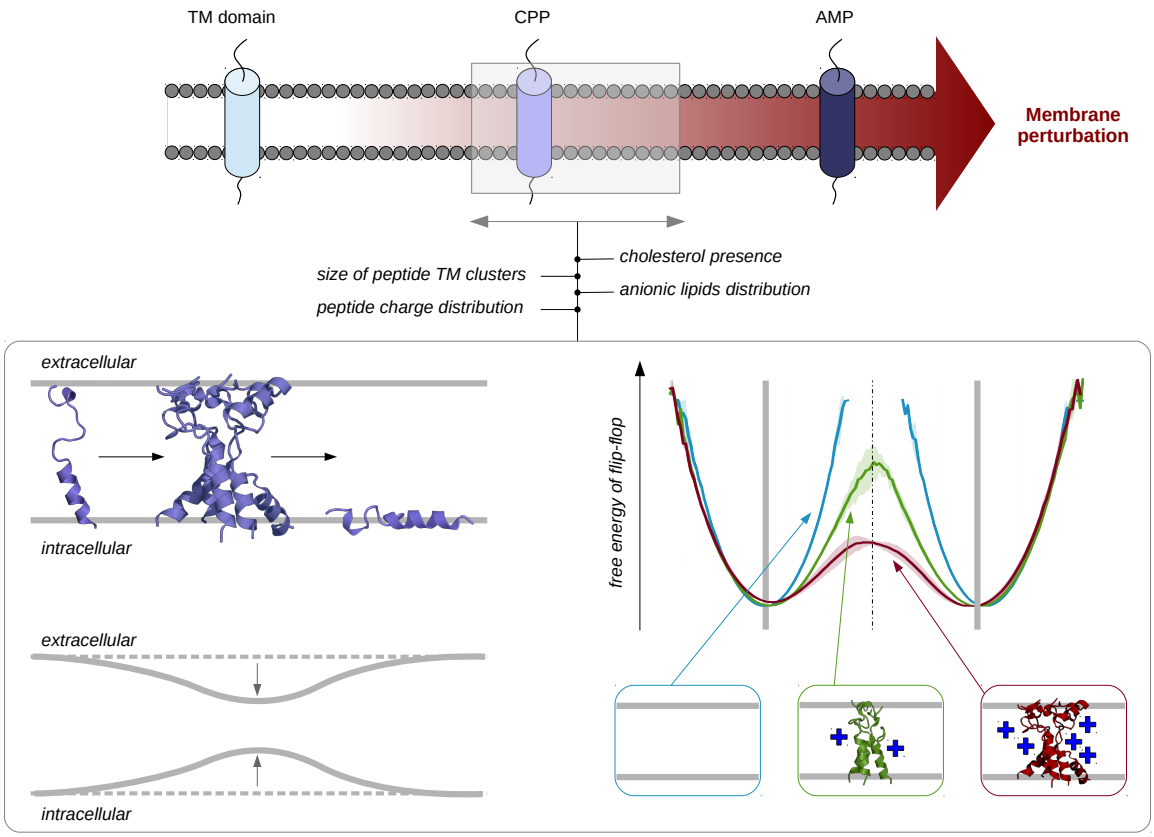

Figure 7.1 Schematic representation of the range of peptide-induced membrane perturbations characterised in this thesis (darker red represents more important perturbations). Penetratin, a non membrane toxic CPP, was observed to reach an interfacial orientation without perturbing the bilayer. Conversely, the translocation of transportan, a more membrane toxic CPP, was shown to depend both on its ability to form transmembrane clusters and on an asymmetric distribution of anionic lipids, with peptides translocating towards the cytoplasmic (anionic) leaflet of the plasma membrane model. Transportan aggregates also induced local membrane destabilisation, such as bilayer thinning and lipid flip-flops. The size of the clusters was an aggravating factor of the extent of these perturbations which appeared to be driven by the ability of peptides to accumulate a positive charge density (blue plus signs) within the membrane interior, as evidenced for instance by the corresponding lowering of the free energy of lipid flip-flops. Membrane perturbations induced by transportan molecules were also compounded by the presence of anionic lipids, suggesting the perturbations mechanisms observed form the basis of antimicrobial activity in presence of symmetric bacterial membranes.

these results, a future series of systematic simulations of different CPPs would then help to understand which peptide characteristics contribute to membrane destabilisation versus translocation.

Finally, in addition to offering new molecular insights into the mechanisms by which membrane active peptides can interact with lipid bilayers, the various methods presented in

this thesis provide a computational framework for further investigations of out-of-equilibrium simulations of peptides or protein behaviour in complex membrane models.

7.2 *In silico* and *in vitro*: bridging the gap

Although the systems studied in this thesis allowed to gain insights in the collective behaviour of transportan peptides and how it could lead to membrane destabilisation, their small size and limited number of peptides does not readily allow comparison with experimental conditions. Here, I present preliminary results illustrating how future research directions based on a large scale approach can build on the work presented previously in order to address these issues and complement the findings obtained.

7.2.1 Large scale CG simulations

The simulation protocol presented in Chapter 5, whereby small systems are duplicated in the x and y directions to create larger ones (see Figure 5.1), was used to create very large systems containing in excess of 50,000 lipids and approximately 500 transportan molecules. Such systems contained more than 3 million particles and simulations had to be executed on dedicated High Performance Computing (HPC) facilities located in France (Curie) and Germany (HERMIT) where up to 8000 cores were used simultaneously. Figure 7.2 illustrates the difference of scale between such systems and those containing 9 transportan molecules.

These large scale CG simulations address several shortcomings of the smaller systems. For instance, as can be seen in Figure 7.2, they allow for greater membrane deformation which may help to assess whether the dynamic properties of CPPs influence, or are influenced by, the local curvature of the membrane as such a mutual dependence has been evidenced for AMPs [532]. Crucially however, they provide significantly increased sampling of the events investigated. In particular, significant features of peptide-peptide and

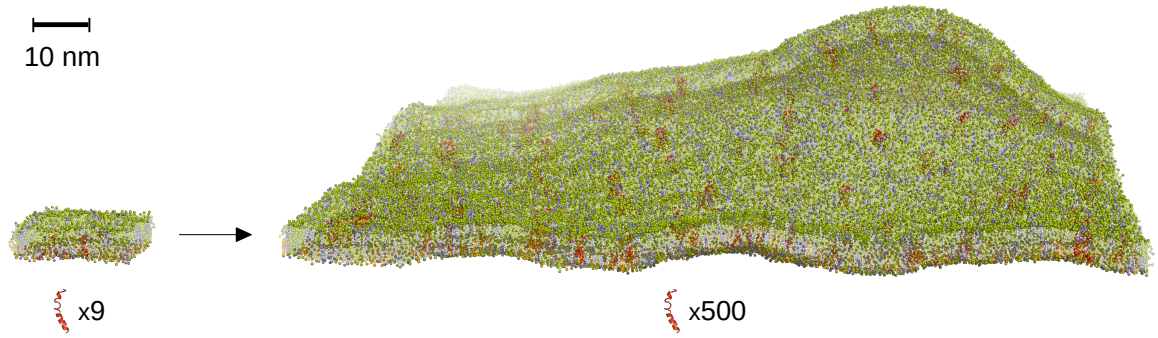

Figure 7.2 Snapshot from a simulation of the AMLarge model containing approximately 54000 lipids and 500 transportan peptides (red). The AM system studied in previous chapters, which contained 9 transportan peptides, is represented to scale for reference. Lipids are represented as spheres and coloured as follows: phosphatidylcholine (POPC) in green, phosphatidylethanolamine (POPE) in purple, phosphatidylserine (POPS) in orange and cholesterol (CHOL) in white. For clarity, phosphate beads are shown as solid spheres while tails particles are transparent.

peptide-lipid interactions can be identified more easily. Correlation between the size of the clusters formed, their structural characteristics and the membrane perturbation they induce can be established with more certainty and investigated further. Similarly, the greater number of flip-flops allows to better characterise these events and to confirm the validity of the mechanism suggested based on the observation of smaller systems. Additionally, the size of the aggregates formed by the peptides is not anymore restricted by the total number of molecules available, thereby providing more data on the stability of these oligomers. Likewise, the large number of peptides present in the system allow to easily detect towards which leaflet they preferentially translocate. Overall, the simulation of a *population* of peptides provides a way to statistically describe the systems simulated and therefore to assess the validity of the hypotheses derived from the analysis of smaller systems. Figure 7.3 illustrates the kind of metrics that can be extracted from the simulation of such large systems. In particular, these results unambiguously demonstrate the preferential translocation of transportan molecules towards the cytosolic leaflet.

In the future, the data obtained from these large scale simulations could be used to fit kinetic models describing the events observed, be it peptide aggregation and translocation

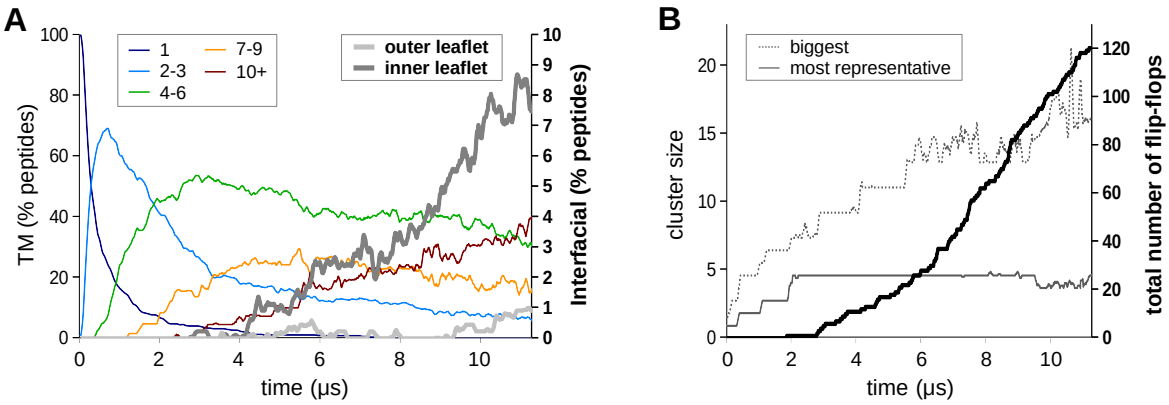

Figure 7.3 Evolution of the distribution of peptides and of the total number of flip-flops observed in the AMLarge system. (A) Evolution of the percentage of peptides represented by different size groups of transmembrane (TM) clusters (left axis) and of the percentage of peptides having reached an interfacial orientation (bold lines, right axis). (B) Evolution of the sizes of the biggest (dotted line) and most representative (solid) TM clusters (left axis) and evolution of the total number of lipids that flip-flopped from the inner to the outer leaflet (bold line, right axis). With the exception of two POPC lipids which flip-flopped from the outer to the inner leaflet (not shown), all flip-flops corresponded to POPS lipids. Cluster sizes were obtained by sampling the trajectory every 8 ns and smoothing the results over 10 consecutive data points, thereby leading to non-integer sizes.

or the rate of flip-flops. Such models could then provide a basis for qualitative, if not quantitative, comparison with experimental observations. Additionally, the dimensions of those large systems, measuring approximately 150 nm in the x and y directions, are within reach of the spatial resolution provided by super-resolution light microscopy [533–535]. It is thus not unreasonable to think that the largest features of such peptide-membrane systems revealed by MD simulations could be directly compared with experimental observations relying on high-end imaging techniques.

7.2.2 Remaining challenges

In spite of the advantages discussed above compared to smaller systems, large scale MD simulations did present several challenges of their own. These highlighted that the ability to extract biologically relevant information from such systems is not solely limited by access to HPC facilities. Some of the issues that should be addressed by future investigations are presented below.

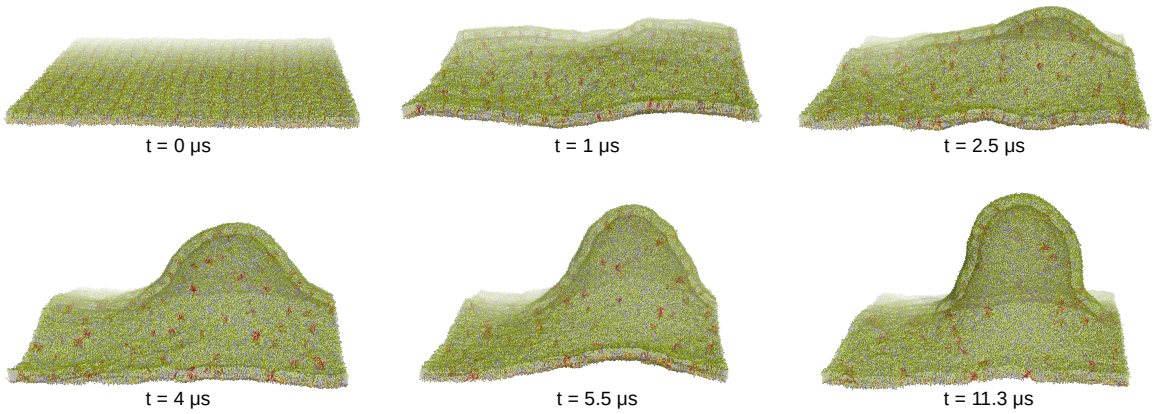

Figure 7.4 Snapshots from a simulation of the AMLarge system. The bilayer built is perfectly planar bilayer (t = 0 µs). As the simulation progresses, the large simulation box allows for membrane undulations. After a few microseconds, a bleb appears that then leads to a diverging tubulation process. Peptides are shown as cartoon in red. Lipids are represented as spheres and coloured as follows: phosphatidylcholine (POPC) in green, phosphatidylethanolamine (POPE) in purple, phosphatidylserine (POPS) in orange and cholesterol (CHOL) in white. For clarity, phosphate beads are shown as solid spheres while tails particles are transparent.

Stability of asymmetric membrane models

As illustrated in Figure 7.4, simulations of a large bilayer with the composition of the AM model revealed significant deformations. In particular, buckling of the membrane occurred over a timescale of a few microseconds, a duration for which similar but medium size systems remained essentially planar. At first, it is tempting to suggest that such deformation is due to the presence of transportan molecules and could not be observed in smaller systems as they contained too few peptides and were more constrained by periodic boundary conditions. Indeed, Huang and co-workers have shown that AMPs caused surface expansion of giant lipid vesicles [415] and, accordingly, the only large scale CG MD study of membrane active peptides available in the literature did report that the presence of surfacic AMP led to membrane buckling [344]. However, control simulations showed that the large AM bilayers consistently led to such deformations regardless of the presence of transportan molecules or of their initial orientation, thereby suggesting these resulted from the intrinsic mechanical properties of the membrane model rather than from its interactions with the peptides.

As a preliminary investigation of the influence of lipid composition on the ability of a bilayer to deform, I performed a series of comparative simulations of symmetric and asymmetric membranes and recorded the extent of their undulations along the z axis. The results are presented in Figure 7.5. As can be seen, striking differences were observed between the membrane models but no clear picture emerged regarding the role played by each lipid species. Notably, an "increase" of the asymmetry in the AM model by replacing POPC lipids present in the inner leaflet by POPE lipids led to a decrease of the extent of the bilayer deformation. Also, it is important to note that in contrast to the simple undulations observed in the other systems simulated, the buckling of the AM bilayer appears to be a diverging process, thus suggesting that this large membrane is mechanically unstable. Extensive theoretical work has been carried out on the characterisation of the elastic properties of membranes and it will be interesting to investigate how such large scale MD simulations relate to it and can provide molecular insights on the influence of lipid composition on the mechanical properties of lipid bilayers [536–540]. Additionally, it may provide a tool to quantify the consequences of the methodological issues associated to building of asymmetric membranes which were discussed in Chapter 3 (see 3.2.4).

Technical issues

The large size of the systems also led to several technical issues which were not encountered, or to a minor extent, with smaller systems. In particular, the extent of the deformation of the membrane and the corresponding deviation from planarity, while an interesting feature of such systems, proved problematic. Indeed, the assumption that the lipid bilayer remains essentially flat throughout the simulation does not hold anymore and, consequently, all analysis methods based on the x, y, z axes of the simulation box fail. For instance, the calculation of the radial density distribution of residues or charges around transportan clusters will necessitate the definition of a local referential based on the local normal to the bilayer.

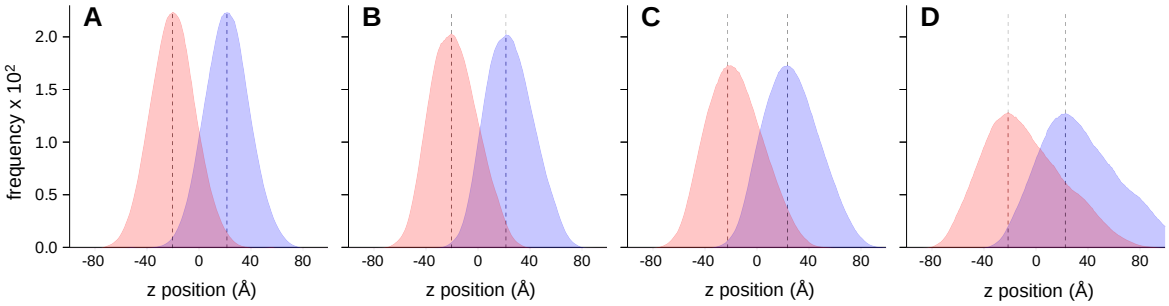

Figure 7.5 Influence of lipid composition on very large bilayers undulations. Average distribution of the z coordinates of phosphate beads in (A) a pure POPC bilayer, (B) an asymmetric bilayer containing POPC in the outer leaflet and POPE in the inner leaflet, (C) a modified version of the AM model where POPC lipids in the inner leaflet have all been replaced by POPE lipids, and (D) the AM model. All systems were pure membranes (no peptides) which contained approximately 50,000 lipids. Distribution profiles were obtained for each leaflet by averaging the z coordinates of phosphate beads over the first microsecond of the simulations, after a 100 ns equilibration period. Outer and inner leaflets are shown in blue and red respectively. The vertical dashed lines indicate the most sampled positions for each leaflet. In (D) the shifting of the distribution of z coordinates towards higher values corresponds to the beginning of the formation of a localised membrane bleb.

Similarly, the quantification of the local membrane curvature, necessary to investigate its possible correlation with the dynamic properties of peptides or simply to compare the respective deformation of different systems, will also require the ability to determine the local normal to the membrane. However, this is not a straightforward task, all the more so in systems where peptides can induce local perturbations of the bilayer. Additionally, besides requiring access to dedicated HPC resources, traditional "big data" issues are associated to simulations of very large systems as they require significant storage capacity as well as analysis tools able to process the amount of data produced. This is compounded by the fact that important deformations of the bilayer can lead to crossing of the periodic boundaries: not only larger box sizes must be used to ensure that the bilayer does not interact with itself, but post-processing of the trajectories obtained may also be required to re-position all non-solvent particles within a unique simulation box. In this regard, future investigations may benefit from approaches relying on an implicit solvent description.

Altogether, these observations illustrate how large scale CG MD may provide a promising approach to compare simulations data to experimental evidence but that it is conditional

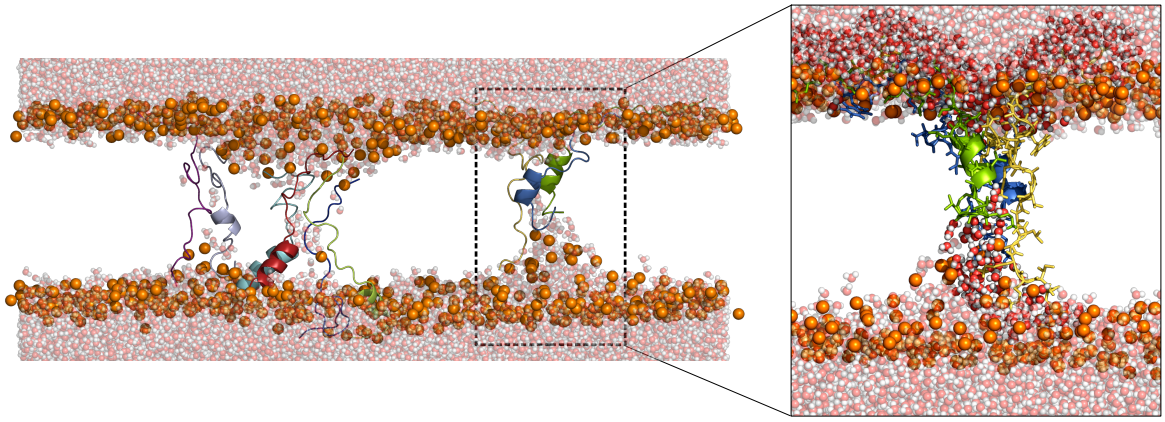

Figure 7.6 Atomistic representation of an AM bilayer containing 9 transportan molecules. This was obtained by converting a CG (MARTINI force field) system, where transportan molecules had already aggregated, back to a united-atom representation (GROMOS53a6 force field) using an in-house fragment-based approach [254]. The resulting atomistic system was then simulated for 200 ns using a 2 fs time step. Peptides are shown as cartoons and the phosphorous atoms of lipids are represented as orange spheres while their other particles are omitted for clarity. Water particles are shown as smaller, transparent, red (oxygen) and white (hydrogen) spheres. The inset corresponds to a zoomed view of the trimer delimited in the full system (rotated by 180°) where transportan molecules are shown as cartoons and sticks and water molecules within 6 Å of them are represented as solid spheres.

on the development of appropriate tools to efficiently analyse and extract relevant information from such systems.

7.3 Towards experimental validation

Thanks to their reduced computational costs, medium size CG MD simulations such as those presented in this thesis, allow the exploration of different membrane models and the systematic investigation of their interactions with various membrane active peptides. With the use of large scale CG MD, the statistical significance of findings derived from the study of such systems can then be assessed and results from the simulations can be more readily compared with experimental observations. Conversely however, because of the reduced resolution of the CG representation structural details possibly providing important information regarding the mechanisms by which peptides molecules interact with each other or neigh-

bouring lipid species are not fully accessible. As illustrated in Figure 7.6, the conversion of a CG system back to atomistic representation presents a convenient way to study in greater details structures detected in CG MD simulations. In particular, the atomistic resolution can help to better characterise flip-flops and/or transient water defects. As a result, such a multiscale approach could allow to identify the key peptide residues involved in such perturbations. Accordingly, substitutions that enhance peptide translocation but hinder membrane destabilisation could be suggested. The properties of these mutants could then be tested *in vitro* hence providing a screening procedure to identify new peptides that promote the desired therapeutic effect *in vivo*.

Appendix A

Lipid structures

This appendix contains the structural formulas of the various lipid species used in the simulations presented in this thesis.

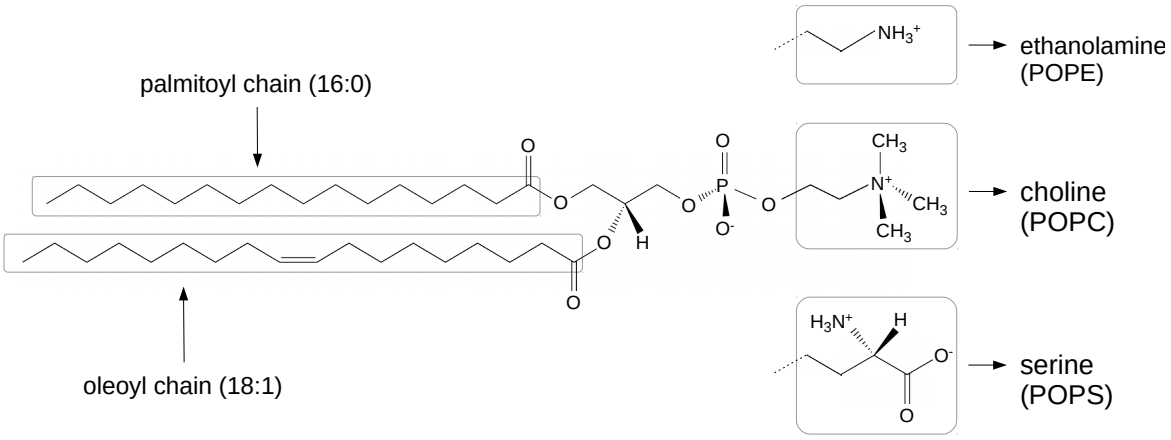

Figure A.1 Chemical structure of the glycerophospholipids used in the asymmetric membrane models. The POPC, POPE and POPS species all possess a palmitoyl and an oleoyl chain while their headgroups are respectively constituted by a phosphatidylcholine, a phosphatidylethanolamine and a phosphatidylserine.

A

- **DPPC** (16:0): 1,2-dipalmitoyl-*sn*-phosphatidylcholine

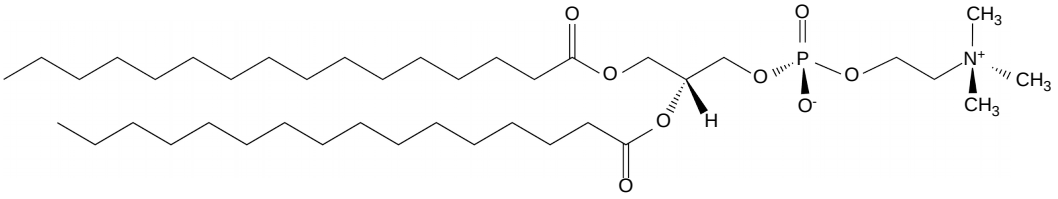

- **DOPC** (18:1): 1,2-dioleoyl-*sn*-phosphatidylcholine

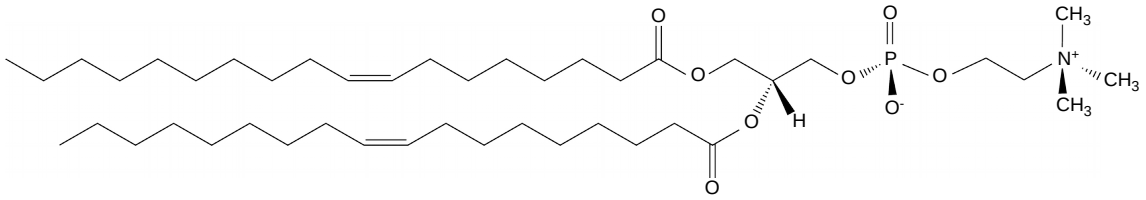

B

- **DHPC** (7:0): 1,2-diheptanoyl-*sn*-phosphatidylcholine

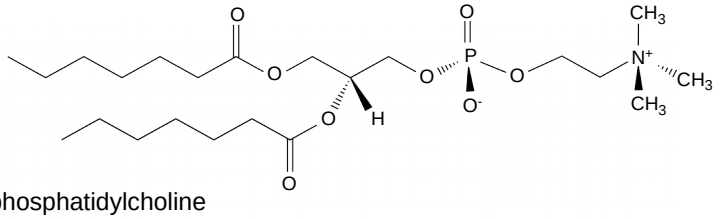

- **DLPC** (12:0): 1,2-dilauroyl-*sn*-phosphatidylcholine

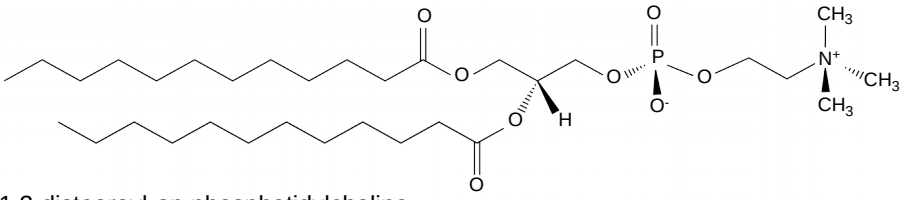

- **DSPC** (18:0): 1,2-distearoyl-*sn*-phosphatidylcholine

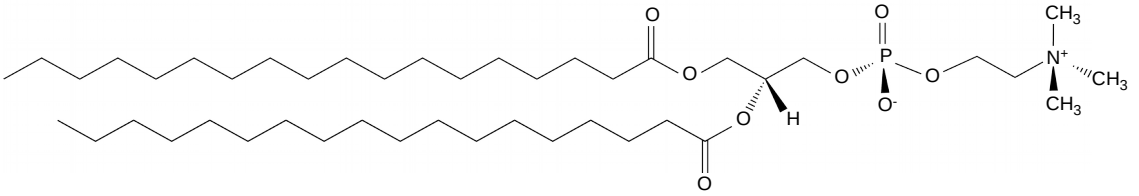

Figure A.2 (A) Chemical structure of a phosphatidylcholine lipid with respectively fully saturated acyl chains (DPPC) and chains containing one unsaturation each (DOPC). (B) Chemical structures of phosphatidylcholine with saturated acyl chains of various lengths.

A • **PPCS** (18:1-16:0): N-palmitoyl-D-*erythro*-sphingosylphosphorylcholine

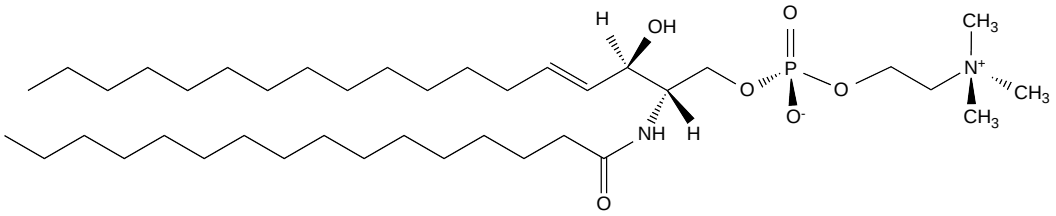

B • **CERA** (18:1-16:0): N-palmitoyl-D-*erythro*-sphingosine

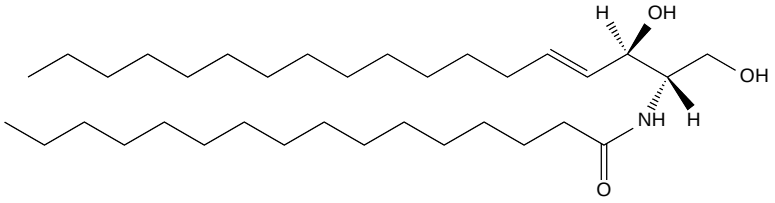

Figure A.3 Chemical structure of the sphingolipids used in the AMv1 model. (A) The sphingomyelin used has an acyl chain of similar length to that of the glycerophospholipids. Sphingomyelins with a longer or shorter acyl chain or possessing a phosphoethanolamine head group instead of a phosphocholine also exist. (B) The chemical structure of the ceramide lipid used is similar to that of sphingomyelin bar the head group.

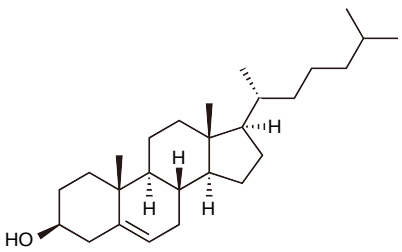

Figure A.4 Chemical structure of cholesterol, the only sterol included in the membrane models.

Bibliography

[1] Alberts, B. et al., *Molecular biology of the cell*, 5th ed., Garland Science, 2007.

[2] Woese, C. R., Kandler, O., and Wheelis, M. L. (1990) Towards a natural system of organisms: proposal for the domains Archaea, Bacteria, and Eucarya, *Proc Natl Acad Sci USA*, 87(12):4576–4579.

[3] Cavicchioli, R. et al. (2003) Pathogenic archaea: do they exist?, *BioEssays*, 25(11):1119–1128.

[4] Taylor, L. H., Latham, S. M., and Woolhouse, M. E. (2001) Risk factors for human disease emergence, *Philos T Roy Soc B*, 356(1411):983–989.

[5] Demchick, P. and Koch, A. L. (1996) The permeability of the wall fabric of Escherichia coli and Bacillus subtilis, *J Bacteriol*, 178(3):768–773.

[6] Grecco, H. E., Schmick, M., and Bastiaens, P. I. H. (2011) Signaling from the living plasma membrane, *Cell*, 144(6):897–909.

[7] Fagerberg, L. et al. (2010) Prediction of the human membrane proteome, *Proteomics*, 10(6):1141–1149.

[8] Berman, H. M., Westbrook, J., and Feng, Z. (2000) The protein data bank, *Nucleic Acids Res*, 28(1):235–242.

[9] Lacapère, J.-J. et al. (2007) Determining membrane protein structures: still a challenge!, *Trends Biochem Sci*, 32(6):259–270.

[10] Bill, R. M. et al. (2011) Overcoming barriers to membrane protein structure determination, *Nat Biotechnol*, 29(4):335–340.

[11] Hediger, M. A. et al. (2004) The ABCs of solute carriers: physiological, pathological and therapeutic implications of human membrane transport proteins, *Pflug Arch Eur J Phy*, 447(5):465–468.

[12] Catterall, A. W. (1995) Structure and function of voltage-gated ion channels, *Annu Rev Biochem*, 64:493–531.

[13] Hucho, F. and Weise, C. (2001) Ligand-Gated Ion Channels, *Angew Chem Int Edit*, 40(17):3100–3116.

[14] Sackin, H. (1995) Mechanosensitive channels, *Annu Rev Physiol*, 57:333–353.

[15] Doherty, G. J. and McMahon, H. T. (2009) Mechanisms of endocytosis, *Annu Rev Biochem*, 78:857–902.

[16] Arnosti, C. (2011) Microbial extracellular enzymes and the marine carbon cycle, *Annu Rev Mar Sci*, 3:401–425.

[17] Kong, F. and Singh, R. P. (2008) Disintegration of solid foods in human stomach, *J Food Sci*, 73(5):67–80.

[18] Conner, S. D. and Schmid, S. L. (2003) Regulated portals of entry into the cell, *Nature*, 422(6927):37–44.

[19] Flannagan, R. S., Jaumouillé, V., and Grinstein, S. (2012) The cell biology of phagocytosis, *Annu Rev Pathol-Mech*, 7:61–98.

[20] Gruenberg, J. and Maxfield, F. R. (1995) Membrane transport in the endocytic pathway, *Curr Opin Cell Biol*, 7(4):552–563.

[21] Steinman, R. M. et al. (1983) Endocytosis and the recycling of plasma membrane, *J Cell Biol*, 96(1):1–27.

[22] Last, N. B., Schlamadinger, D. E., and Miranker, A. D. (2013) A common landscape for membrane-active peptides, *Protein Sci*, 22(7):870–882.

[23] Dubos, R. J. (1939) Studies on a bactericidal agent extracted from a soil bacillus : i. preparation of the agent. its activity in vitro, *J Exp Med*, 70(1):1–10.

[24] Dubos, R. J. (1939) Studies on a bactericidal agent extracted from a soil bacillus : ii. protective effect of the bactericidal agent against experimental pneumococcus infections in mice, *J Exp Med*, 70(1):11–17.

[25] Hotchkiss, R. D. and Dubos, R. J. (1940) Fractionation of the bactericidal agent from cultures of a soil bacillus, *J Biol Chem*, 132(2):791–792.

[26] Steiner, H. et al. (1981) Sequence and specificity of two antibacterial proteins involved in insect immunity, *Nature*, 292(5820):246–248.

[27] Zasloff, M. (1987) Magainins, a class of antimicrobial peptides from Xenopus skin: isolation, characterization of two active forms, and partial cDNA sequence of a precursor, *Proc Natl Acad Sci USA*, 84(15):5449–5453.

[28] Ganz, T., Selsted, M. E., and Lehrer, R. I. (1990) Defensins, *Eur J Haematol*, 44(1):1–8.

[29] Ganz, T. and Lehrer, R. I. (1998) Antimicrobial peptides of vertebrates, *Curr Opin Immunol*, 10(1):41–44.

[30] Hoffmann, J. A. et al. (1999) Phylogenetic perspectives in innate immunity, *Science*, 284(5418):1313–1318.

[31] Zasloff, M. (2002) Antimicrobial peptides of multicellular organisms, *Nature*, 415(6870):389–395.

[32] Zhao, X. et al. (2013) LAMP: a database linking antimicrobial peptides, *PLoS ONE*, 8(6):e66557.

[33] Brogden, K. A. (2005) Antimicrobial peptides: pore formers or metabolic inhibitors in bacteria?, *Nat Rev Microbiol*, 3(3):238–250.

[34] Bahar, A. A. and Ren, D. (2013) Antimicrobial peptides, *Pharmaceuticals*, 6(12):1543–1575.

[35] Wade, D. et al. (1990) All-D amino acid-containing channel-forming antibiotic peptides, *Proc Natl Acad Sci USA*, 87(12):4761–4765.

[36] Bessalle, R. et al. (1990) All-D-magainin: chirality, antimicrobial activity and proteolytic resistance, *FEBS Lett*, 274(1-2):151–155.

[37] Yasin, B. et al. (1996) Protegrins: structural requirements for inactivating elementary bodies of Chlamydia trachomatis, *Infect Immun*, 64(11):4863–4866.

[38] Cho, Y. et al. (1998) Activity of protegrins against yeast-phase candida albicans, *Infect Immun*, 66(6):2486–1575.

[39] Dathe, M. and Wieprecht, T. (1999) Structural features of helical antimicrobial peptides: their potential to modulate activity on model membranes and biological cells, *BBA-Biomembranes*, 1462(1-2):71–87.

[40] Zhang, L., Rozek, A., and Hancock, R. E. (2001) Interaction of cationic antimicrobial peptides with model membranes, *J Biol Chem*, 276(38):35714–35722.

[41] Tamba, Y. and Yamazaki, M. (2005) Single giant unilamellar vesicle method reveals effect of antimicrobial peptide magainin 2 on membrane permeability, *Biochemistry*, 44(48):15823–15833.

[42] Shai, Y. (1999) Mechanism of the binding, insertion and destabilization of phospholipid bilayer membranes by α-helical antimicrobial and cell non-selective membranelytic peptides, *BBA-Biomembranes*, 1462(1-2):55–70.

[43] Matsuzaki, K. (1999) Why and how are peptide-lipid interactions utilized for self-defense? Magainins and tachyplesins as archetypes, *BBA-Biomembranes*, 1462(1-2):1–10.

[44] Yang, L. et al. (2000) Crystallization of antimicrobial pores in membranes: magainin and protegrin, *Biophys J*, 79(4):2002–2009.

[45] He, K. et al. (1996) Neutron scattering in the plane of membranes: structure of alamethicin pores, *Biophys J*, 70(6):2659–2666.

[46] Yang, L. et al. (2001) Barrel-stave model or toroidal model? A case study on melittin pores, *Biophys J*, 81(3):1475–1485.

[47] Axelsen, P. H. (2008) A chaotic pore model of polypeptide antibiotic action, *Biophys J*, 94(5):1549–1550.

[48] Pokorny, A., Birkbeck, T. H., and Almeida, P. F. F. (2002) Mechanism and kinetics of δ-lysin interaction with phospholipid vesicles, *Biochemistry*, 41(36):11044–11056.

[49] Almeida, P. F. F. and Pokorny, A. (2009) Mechanisms of antimicrobial, cytolytic, and cell-penetrating peptides: from kinetics to thermodynamics, *Biochemistry*, 48(34):8083–8093.

[50] Hawkey, P. M. (1998) The origins and molecular basis of antibiotic resistance, *BMJ*, 317(7159):657–660.

[51] Davies, J. and Davies, D. (2010) Origins and evolution of antibiotic resistance, *Microbiol Mol Biol R*, 74(3):417–433.

[52] Fisher, J. F., Meroueh, S. O., and Mobashery, S. (2005) Bacterial resistance to β-lactam antibiotics: compelling opportunism, compelling opportunity, *Chem Rev*, 105(2):395–424.

[53] Hancock, R. E. W. and Sahl, H.-G. (2006) Antimicrobial and host-defense peptides as new anti-infective therapeutic strategies, *Nat Biotechnol*, 24(12):1551–1557.

[54] Wimley, W. C. and Hristova, K. (2011) Antimicrobial peptides: successes, challenges and unanswered questions, *J Membrane Biol*, 239(1-2):27–34.

[55] Green, M. and Loewenstein, P. M. (1988) Autonomous functional domains of chemically synthesized human immunodeficiency virus tat trans-activator protein, *Cell*, 55(6):1179–1188.

[56] Frankel, A. D. and Pabo, C. O. (1988) Cellular uptake of the tat protein from human immunodeficiency virus, *Cell*, 55(6):1189–1193.

[57] Joliot, A. and Pernelle, C. (1991) Antennapedia homeobox peptide regulates neural morphogenesis, *Proc Natl Acad Sci USA*, 88(5):1864–1868.

[58] Derossi, D., Joliot, A. H., and Chassaing, G. (1994) The third helix of the Antennapedia homeodomain translocates through biological membranes, *J Biol Chem*, 269(14):10444–10450.

[59] Vivès, E., Brodin, P., and Lebleu, B. (1997) A truncated HIV-1 tat protein basic domain rapidly translocates through the plasma membrane and accumulates in the cell nucleus, *J Biol Chem*, 272(25):16010–16017.

[60] Fawell, S. et al. (1994) Tat-mediated delivery of heterologous proteins into cells, *Proc Natl Acad Sci USA*, 91(2):664–893.

[61] Prochiantz, A. (1996) Getting hydrophilic compounds into cells: lessons from homeopeptides, *Curr Opin Neurobiol*, 6(5):629–634.

[62] Derossi, D., Chassaing, G., and Prochiantz, A. (1998) Trojan peptides: the penetratin system for intracellular delivery, *Trends Cell Biol*, 8(2):84–87.

[63] Pooga, M. et al. (1998) Cell penetration by transportan, *FASEB J*, 12(1):67–77.

[64] Morris, M. C. et al. (1997) A new peptide vector for efficient delivery of oligonucleotides into mammalian cells, *Nucleic Acids Res*, 25(14):2730–2736.

[65] Schwarze, S. R. et al. (1999) In vivo protein transduction: delivery of a biologically active protein into the mouse, *Science*, 285(5433):1569–1572.

[66] Schwarze, S. R., Hruska, K. A., and Dowdy, S. F. (2000) Protein transduction: unrestricted delivery into all cells?, *Trends Cell Biol*, 10(7):290–295.

[67] Lindgren, M. et al. (2000) Cell-penetrating peptides, *Trends Pharmacol Sci*, 21(3):99–103.

[68] Deshayes, S. et al. (2005) Cell-penetrating peptides: tools for intracellular delivery of therapeutics, *Cell Mol Life Sci*, 62(16):1839–1849.

[69] Mae, M. and Langel, Ü. (2006) Cell-penetrating peptides as vectors for peptide, protein and oligonucleotide delivery, *Curr Opin Pharmacol*, 6(5):509–514.

[70] Morris, M. C. et al. (2008) Cell-penetrating peptides: from molecular mechanisms to therapeutics, *Biol Cell*, 100(4):201–217.

[71] Sebbage, V. (2009) Cell-penetrating peptides and their therapeutic applications, *Bioscience Horizons*, 2(1):64–72.

[72] Chugh, A., Eudes, F., and Shim, Y.-S. (2010) Cell-penetrating peptides: nanocarrier for macromolecule delivery in living cells, *IUBMB Life*, 62(3):183–193.

[73] Margus, H., Padari, K., and Pooga, M. (2012) Cell-penetrating peptides as versatile vehicles for oligonucleotide delivery, *Mol Ther*, 20(3):525–533.

[74] Copolovici, D. M. et al. (2014) Cell-penetrating peptides: design, synthesis, and applications, *ACS Nano*, 8(3):1972–1994.

[75] Torchilin, V. P. (2006) Recent approaches to intracellular delivery of drugs and DNA and organelle targeting, *Annu Rev Biomed Eng*, 8:343–375.

[76] Rawat, A. et al. (2007) Targeted intracellular delivery of therapeutics: an overview, *Pharmazie*, 62(9):643–658.

[77] Mitragotri, S., Burke, P. A., and Langer, R. (2014) Overcoming the challenges in administering biopharmaceuticals: formulation and delivery strategies, *Nat Rev Drug Discov*, 13(9):655–672.

[78] Lipinski, C. A. et al. (2001) Experimental and computational approaches to estimate solubility and permeability in drug discovery and development settings, *Adv Drug Deliver Rev*, 46(1-3):3–26.

[79] Shete, H. K. and Prabhu, R. H. (2014) Endosomal escape: a bottleneck in intracellular delivery, *J Nanosci NAanotechno*, 14(1):460–474.

[80] Chen, Y. and Liu, L. (2012) Modern methods for delivery of drugs across the blood–brain barrier, *Adv Drug Deliver Rev*, 64(7):640–665.

[81] Figueiredo, I. R. de et al. (2014) Cell-penetrating peptides: a tool for effective delivery in gene-targeted therapies, *IUBMB Life*, 66(3):182–194.

[82] Gautam, A. et al. (2012) CPPsite: a curated database of cell penetrating peptides, *Database*, 2012:bas015.

[83] Jones, A. T. and Sayers, E. J. (2012) Cell entry of cell penetrating peptides: tales of tails wagging dogs, *J Control Release*, 161(2):582–591.

[84] Langel, Ü., *Handbook of cell-penetrating peptides*, 2nd ed., CRC Press, 2010.

[85] Marks, J. R. et al. (2011) Spontaneous membrane-translocating peptides by orthogonal high-throughput screening, *J Am Chem Soc*, 133(23):8995–9004.

[86] Futaki, S. et al. (2001) Arginine-rich peptides. An abundant source of membrane-permeable peptides having potential as carriers for intracellular protein delivery, *J Biol Chem*, 276(8):5836–5840.

[87] Oehlke, J. et al. (1998) Cellular uptake of an α-helical amphipathic model peptide with the potential to deliver polar compounds into the cell interior non-endocytically, *BBA-Biomembranes*, 1414(1-2):127–139.

[88] Hessa, T. et al. (2005) Recognition of transmembrane helices by the endoplasmic reticulum translocon, *Nature*, 433(7024):377–381.

[89] Lindgren, M. and Langel, Ü., Classes and prediction of cell-penetrating peptides, in: *Cell-penetrating peptides*, Humana Press, 2011.

[90] Milletti, F. (2012) Cell-penetrating peptides: classes, origin, and current landscape, *Drug Discov Today*, 17(15-16):850–860.

[91] Ziegler, A. (2008) Thermodynamic studies and binding mechanisms of cell-penetrating peptides with lipids and glycosaminoglycans, *Adv Drug Deliver Rev*, 60(4-5):580–597.

[92] Fischer, R. et al. (2005) Break on through to the other side—biophysics and cell biology shed light on cell-penetrating peptides, *ChemBioChem*, 6(12):2126–2142.

[93] Zorko, M. and Langel, Ü. (2005) Cell-penetrating peptides: mechanism and kinetics of cargo delivery, *Adv Drug Deliver Rev*, 57(4):529–545.

[94] Duchardt, F. et al. (2007) A comprehensive model for the cellular uptake of cationic cell-penetrating peptides, *Traffic*, 8(7):848–866.

[95] Jiao, C.-Y. et al. (2009) Translocation and endocytosis for cell-penetrating peptide internalization, *J Biol Chem*, 284(49):33957–33965.

[96] Heitz, F., Morris, M. C., and Divita, G. (2009) Twenty years of cell-penetrating peptides: from molecular mechanisms to therapeutics, *Brit J Pharmacol*, 157(2):195–206.

[97] Trabulo, S. et al. (2010) Cell-penetrating peptides—mechanisms of cellular uptake and generation of delivery systems, *Pharmaceuticals*, 3(4):961–993.

[98] Alves, I. D. et al. (2010) Cell biology meets biophysics to unveil the different mechanisms of penetratin internalization in cells, *BBA-Biomembranes*, 1798(12):2231–2239.

[99] Alves, I. D. et al., Membrane crossover by cell-penetrating peptides: kinetics and mechanisms—from model to cell membrane perturbation by permeant peptides, in: *Intracellular delivery*, ed. by Prokop, A., Springer, 2011.

[100] Madani, F. et al. (2011) Mechanisms of cellular uptake of cell-penetrating peptides, *J Biophys*, 2011:414729.

[101] Alves, I. et al. (2012) Is there anybody in there? On the mechanisms of wall crossing of cell penetrating peptides, *Curr Protein Pept Sc*, 13(7):658–671.

[102] Bechara, C. and Sagan, S. (2013) Cell-penetrating peptides: 20 years later, where do we stand?, *FEBS Lett*, 587(12):1693–1702.

[103] Brock, R. (2014) The uptake of arginine-rich cell-penetrating peptides: putting the puzzle together, *Bioconjugate Chem*, 25(5):863–868.

[104] Derossi, D. et al. (1996) Cell internalization of the third helix of the Antennapedia homeodomain is receptor-independent, *J Biol Chem*, 271(30):18188–18193.

[105] Prochiantz, A. (2000) Messenger proteins: homeoproteins, tat and others, *Curr Opin Cell Biol*, 12(4):400–406.

[106] Lundberg, M. and Johansson, M. (2002) Positively charged DNA-binding proteins cause apparent cell membrane translocation, *Biochem Bioph Res Co*, 291(2):367–371.

[107] Richard, J. P. et al. (2003) Cell-penetrating peptides. A reevaluation of the mechanism of cellular uptake, *J Biol Chem*, 278(1):585–590.

[108] Vendeville, A. (2004) HIV-1 tat enters T cells using coated pits before translocating from acidified endosomes and eliciting biological responses, *Mol Biol Cell*, 15(5):2347–2360.

[109] Wadia, J. S., Stan, R. V., and Dowdy, S. F. (2004) Transducible tat-HA fusogenic peptide enhances escape of tat-fusion proteins after lipid raft macropinocytosis, *Nat Med*, 10(3):310–315.

[110] Fuchs, S. M. and Raines, R. T. (2004) Pathway for polyarginine entry into mammalian cells, *Biochemistry*, 43(9):2438–2444.

[111] Kaplan, I. M., Wadia, J. S., and Dowdy, S. F. (2005) Cationic TAT peptide transduction domain enters cells by macropinocytosis, *J Control Release*, 102(1):247–253.

[112] Mishra, A. et al. (2011) Translocation of HIV TAT peptide and analogues induced by multiplexed membrane and cytoskeletal interactions, *Proc Natl Acad Sci USA*, 108(41):16883–16888.

[113] Rydström, A. et al. (2011) Direct translocation as major cellular uptake for CADY self-assembling peptide-based nanoparticles, *PLoS ONE*, 6(10):e25924.

[114] Ma, Y. et al. (2012) Direct cytosolic delivery of cargoes in vivo by a chimera consisting of D- and L-arginine residues, *J Control Release*, 162(2):286–294.

[115] Hirose, H. et al. (2012) Transient focal membrane deformation induced by arginine-rich peptides leads to their direct penetration into cells, *Mol Ther*, 20(5):984–993.

[116] Maniti, O. et al. (2012) Metabolic energy-independent mechanism of internalization for the cell penetrating peptide penetratin, *Int. J. Biochem. Cell Biol.* 44(6):869–875.

[117] Thorén, P. E. G. et al. (2000) The Antennapedia peptide penetratin translocates across lipid bilayers – the first direct observation, *FEBS Lett*, 482(3):265–268.

[118] Persson, D. et al. (2004) Vesicle size-dependent translocation of penetratin analogs across lipid membranes, *BBA-Biomembranes*, 1665(1-2):142–155.

[119] Deshayes, S. et al. (2006) Interactions of amphipathic CPPs with model membranes, *BBA-Biomembranes*, 1758(3):328–335.

[120] Yandek, L. E. et al. (2007) Mechanism of the cell-penetrating peptide transportan 10 permeation of lipid bilayers, *Biophys J*, 92(7):2434–2444.

[121] Madani, F., Perálvarez-Marín, A., and Gräslund, A. (2010) Liposome model systems to study the endosomal escape of cell-penetrating peptides: transport across phospholipid membranes induced by a proton gradient, *J Drug Deliv*, 2011:897592.

[122] Di Pisa, M., Chassaing, G., and Swiecicki, J. M. (2014) Translocation mechanism(s) of cell-penetrating peptides: biophysical studies using artificial membrane bilayers, *Biochemistry*, just accepted.

[123] Nekhotiaeva, N. et al. (2004) Cell entry and antimicrobial properties of eukaryotic cell-penetrating peptides, *FASEB J*, 18(2):394–396.

[124] Geueke, B. et al. (2005) Bacterial cell penetration by beta3-oligohomoarginines: indications for passive transfer through the lipid bilayer, *ChemBioChem*, 6(6):982–985.

[125] Fretz, M. M. et al. (2007) Temperature-, concentration- and cholesterol-dependent translocation of L- and D-octa-arginine across the plasma and nuclear membrane of CD34+ leukaemia cells, *Biochemical J*, 403(2):335–342.

[126] Maiolo, J. R., Ferrer, M., and Ottinger, E. A. (2005) Effects of cargo molecules on the cellular uptake of arginine-rich cell-penetrating peptides, *BBA-Biomembranes*, 1712(2):161–172.

[127] Tünnemann, G. et al. (2006) Cargo-dependent mode of uptake and bioavailability of tat-containing proteins and peptides in living cells, *FASEB J*, 20(11):1775–1784.

[128] El-Andaloussi, S. et al. (2007) Cargo-dependent cytotoxicity and delivery efficacy of cell-penetrating peptides: a comparative study, *Biochemical J*, 407(2):285–292.

[129] Fischer, R. et al. (2002) A quantitative validation of fluorophore-labelled cell-permeable peptide conjugates: fluorophore and cargo dependence of import, *BBA-Biomembranes*, 1564(2):365–374.

[130] Szeto, H. H. et al. (2004) Fluorescent dyes alter intracellular targeting and function of cell-penetrating tetrapeptides, *FASEB J*, 19(1):118–120.

[131] Henriques, S. T., Costa, J., and Castanho, M. (2005) Re-evaluating the role of strongly charged sequences in amphipathic cell-penetrating peptides: a fluorescence study using pep-1, *FEBS Lett*, 579(20):4498–4502.

[132] Dupont, E., Prochiantz, A., and Joliot, A. (2007) Identification of a signal peptide for unconventional secretion, *J Biol Chem*, 282(12):8994–9000.

[133] Ter-Avetisyan, G., Tunnemann, G., and Nowak, D. (2009) Cell entry of arginine-rich peptides is independent of endocytosis, *J Biol Chem*, 284(6):3370–3378.

[134] Säälik, P. et al. (2011) Penetration without cells: membrane translocation of cell-penetrating peptides in the model giant plasma membrane vesicles, *J Control Release*, 153(2):117–125.

[135] Berlose, J. P. et al. (1996) Conformational and associative behaviours of the third helix of antennapedia homeodomain in membrane-mimetic environments, *Eur J Biochem*, 242(2):372–386.

[136] Alves, I. D. et al. (2008) Membrane interaction and perturbation mechanisms induced by two cationic cell penetrating peptides with distinct charge distribution, *BBA-Biomembranes*, 1780(7-8):948–959.

[137] Lamazière, A. et al. (2007) Non-metabolic membrane tubulation and permeability induced by bioactive peptides, *PLoS ONE*, 2(2):e201.

[138] Lundberg, P. and Langel, Ü. (2003) A brief introduction to cell-penetrating peptides, *J Mol Recognit*, 16(5):227–233.

[139] Wu, R. P. et al. (2007) Cell-penetrating peptides as transporters for morpholino oligomers: effects of amino acid composition on intracellular delivery and cytotoxicity, *Nucleic Acids Res*, 35(15):5182–5191.

[140] Cardozo, A. K. et al. (2007) Cell permeable peptides induce dose and length dependent cytotoxic effects, *BBA-Biomembranes*, 1768(9):2222–2234.

[141] Tunnemann, G. and Ter-Avetisyan, G. (2008) Live-cell analysis of cell penetration ability and toxicity of oligo-arginines, *J Pept Sci*, 14(4):469–476.

[142] Sugita, T. et al. (2008) Comparative study on transduction and toxicity of protein transduction domains, *Brit J Pharmacol*, 153(6):1143–1152.

[143] Saar, K. et al. (2005) Cell-penetrating peptides: a comparative membrane toxicity study, *Anal Biochem*, 345(1):55–65.

[144] Palm-Apergi, C. et al. (2009) The membrane repair response masks membrane disturbances caused by cell-penetrating peptide uptake, *FASEB J*, 23(1):214–223.

[145] Salomone, F. et al. (2012) A novel chimeric cell-penetrating peptide with membrane-disruptive properties for efficient endosomal escape, *J Control Release*, 163(3):293–303.

[146] Bárány-Wallje, E. et al. (2007) Differential membrane perturbation caused by the cell penetrating peptide Tp10 depending on attached cargo, *FEBS Lett*, 581(13):2389–2393.

[147] Deshayes, S. et al. (2006) Formation of transmembrane ionic channels of primary amphipathic cell-penetrating peptides. Consequences on the mechanism of cell penetration, *BBA-Biomembranes*, 1758(11):1846–1851.

[148] Pokorny, A. and Almeida, P. F. F. (2004) Kinetics of dye efflux and lipid flip-flop induced by δ-lysin in phosphatidylcholine vesicles and the mechanism of graded release by amphipathic, α-helical peptides, *Biochemistry*, 43(27):8846–8857.

[149] Henriques, S., Melo, M., and Castanho, M. (2006) Cell-penetrating peptides and antimicrobial peptides: how different are they?, *Biochem J*, 339(1):1–7.

[150] Splith, K. and Neundorf, I. (2011) Antimicrobial peptides with cell-penetrating peptide properties and vice versa, *Eur Biophys J*, 40(4):387–397.

[151] Drin, G. et al. (2001) Translocation of the pAntp peptide and its amphipathic analogue AP-2AL, *Biochemistry*, 40(6):1824–1834.

[152] Hancock, R. and Rozek, A. (2002) Role of membranes in the activities of antimicrobial cationic peptides, *FEMS Microbiol Lett*, 206(2):143–149.

[153] Huang, Y. et al. (2013) Curb challenges of the "Trojan Horse" approach: smart strategies in achieving effective yet safe cell-penetrating peptide-based drug delivery, *Adv Drug Deliver Rev*, 65(10):1299–1315.

[154] Lee, S. H., Castagner, B., and Leroux, J.-C. (2013) Is there a future for cell-penetrating peptides in oligonucleotide delivery?, *Eur J Pharm Biopharm*, 85(1):5–11.

[155] Wooley, J. C. and Lin, H. S., Computational modeling and simulation as enablers for biological discovery, in: *Catalyzing inquiry at the interface of computing and biology*, ed. by Wooley, J. C. and Lin, H. S., National Academies Press (US), 2005.

[156] Ziegler, A. et al. (2005) The cationic cell-penetrating peptide CPP(tat) derived from the HIV-1 protein tat is rapidly transported into living fibroblasts: optical, biophysical, and metabolic evidence, *Biochemistry*, 44(1):138–148.

[157] Holm, T., Andaloussi, S. E., and Langel, Ü., Comparison of CPP uptake methods, in: *Cell-Penetrating Peptides*, Humana Press, 2011.

[158] Burlina, F. et al. (2005) Quantification of the cellular uptake of cell-penetrating peptides by MALDI-TOF mass spectrometry, *Angew Chem Int Edit*, 44(27):4244–4247.

[159] Burlina, F. et al. (2006) A direct approach to quantification of the cellular uptake of cell-penetrating peptides using MALDI-TOF mass spectrometry, *Nat Protoc*, 1(1):200–205.

[160] Palm-Apergi, C. and Hällbrink, M., Calcium and membrane repair, in: *Cell-penetrating peptides*, Humana Press, 2011.

[161] Lin, J. et al. (2012) Interactions of membrane active peptides with planar supported bilayers: an impedance spectroscopy study, *Langmuir*, 28(14):6088–6096.

[162] Coskun, Ü. and Simons, K. (2011) Cell membranes: the lipid perspective, *Structure*, 19(11):1543–1548.

[163] Lee, A. G. (2011) Biological membranes: the importance of molecular detail, *Trends Biochem Sci*, 36(9):493–500.

[164] Rabinovich, A. L. and Lyubartsev, A. P. (2013) Computer simulation of lipid membranes: methodology and achievements, *Polym Sci Ser C+*, 55(1):162–180.

[165] Marrink, S. J., Vries, A. H. de, and Tieleman, P. D. (2009) Lipids on the move: simulations of membrane pores, domains, stalks and curves, *BBA-Biomembranes*, 1788(1):49–168.

[166] Latorraca, N. R. et al. (2014) Continuum approaches to understanding ion and peptide interactions with the membrane, *J Membrane Biol*, 247(5):395–408.

[167] Sodt, A. J. and Pastor, R. W. (2014) Molecular modeling of lipid membrane curvature induction by a peptide: more than simply shape, *Biophys J*, 106(9):1958–1969.

[168] Vanni, S. et al. (2014) A sub-nanometre view of how membrane curvature and composition modulate lipid packing and protein recruitment, *Nat Commun*, 5:4916.

[169] Kopeć, W., Telenius, J., and Khandelia, H. (2013) Molecular dynamics simulations of the interactions of medicinal plant extracts and drugs with lipid bilayer membranes, *FEBS Journal*, 280(12):2785–2805.

[170] Lensink, M. F., Christiaens, B., and Vandekerckhove, J. (2005) Penetratin-membrane association: W48/R52/W56 shield the peptide from the aqueous phase, *Biophys J*, 88(2):939–952.

[171] Polyansky, A. A. et al. (2009) Adaptation of a membrane-active peptide to heterogeneous environment. i. structural plasticity of the peptide, *J Phys Chem B*, 113(4):1107–1119.

[172] Polyansky, A. A. et al. (2009) Adaptation of a membrane-active peptide to heterogeneous environment. ii. the role of mosaic nature of the membrane surface, *J Phys Chem B*, 113(4):1120–1126.

[173] Pourmousa, M. and Karttunen, M. (2013) Early stages of interactions of cell-penetrating peptide penetratin with a DPPC bilayer, *Chem Phys Lipids*, 169:85–94.

[174] Dunkin, C. M. et al. (2011) Molecular dynamics studies of transportan 10 (tp10) interacting with a POPC lipid bilayer, *J Phys Chem B*, 115(5):1188–1198.

[175] Pourmousa, M. et al. (2013) Molecular dynamic studies of transportan interacting with a DPPC lipid bilayer, *J Phys Chem B*, 117(1):230–241.

[176] Song, J. et al. (2011) Cellular uptake of transportan 10 and its analogs in live cells: selectivity and structure–activity relationship studies, *Peptides*, 32(9):1934–1941.

[177] Leontiadou, H., Mark, A. E., and Marrink, S. J. (2006) Antimicrobial peptides in action, *J Am Chem Soc*, 128(37):12156–12161.

[178] Sengupta, D. et al. (2008) Toroidal pores formed by antimicrobial peptides show significant disorder, *BBA-Biomembranes*, 1778(10):2308–2317.

[179] Herce, H. D. and Garcia, A. E. (2007) Molecular dynamics simulations suggest a mechanism for translocation of the HIV-1 tat peptide across lipid membranes, *Proc Natl Acad Sci USA*, 104(52):20805–20810.

[180] Herce, H. D. et al. (2009) Arginine-rich peptides destabilize the plasma membrane, consistent with a pore formation translocation mechanism of cell-penetrating peptides, *Biophys J*, 97(7):1917–1925.

[181] Papo, N. and Shai, Y. (2003) Can we predict biological activity of antimicrobial peptides from their interactions with model phospholipid membranes?, *Peptides*, 24(11):1693–1703.

[182] Bond, P. J. and Khalid, S. (2010) Antimicrobial and cell-penetrating peptides: structure, assembly and mechanisms of membrane lysis via atomistic and coarse-grained molecular dynamic simulations, *Protein Peptide Lett*, 17(11):1313–1327.

[183] Santo, K. P. and Berkowitz, M. L. (2012) Difference between magainin-2 and melittin assemblies in phosphatidylcholine bilayers: results from coarse-grained simulations, *J Phys Chem B*, 116(9):3021–3030.

[184] Dror, R. O. et al. (2012) Biomolecular Simulation: A Computational Microscope for Molecular Biology, *Annu Rev Bioph Biom*, 41(1):429–452.

[185] Amaral, C. et al. (2012) Exploring conformational states of the bacterial voltage-gated sodium channel NavAb via molecular dynamics simulations., *Proc Natl Acad Sci USA*, 109(52):21336–21341.

[186] Bernardi, R. C., Melo, M. C. R., and Schulten, K. (2014) Enhanced sampling techniques in molecular dynamics simulations of biological systems, *BBA-Gen Subjects*.

[187] Shaw, D. E. et al. (2008) Anton, a special-purpose machine for molecular dynamics simulation, *Communications of the ACM*, 51(7):91–97.

[188] Shaw, D. E. et al., Anton 2: raising the bar for performance and programmability in a special-purpose molecular dynamics supercomputer, in: *SC14: International Conference for High Performance Computing, Networking, Storage and Analysis*, IEEE Press, 2014:pp. 41–53.

[189] Piana, S., Lindorff-Larsen, K., and Shaw, D. E. (2011) How Robust Are Protein Folding Simulations with Respect to Force Field Parameterization?, *Biophys J*, 100(9):L47–L49.

[190] Lindorff-Larsen, K. et al. (2012) Systematic validation of protein force fields against experimental data, 7(2):e32131.

[191] Piana, S., Klepeis, J. L., and Shaw, D. E. (2014) Assessing the accuracy of physical models used in protein-folding simulations: quantitative evidence from long molecular dynamics simulations, *Curr Opin Struc Biol*, 24:98–105.

[192] Alder, B. J. and Wainwright, T. E. (1957) Phase transition for a hard sphere system, *J Chem Phys*, 27(5):1208–1209.

[193] Alder, B. J. and Wainwright, T. E. (1959) Studies in molecular dynamics. i. general method, *J Chem Phys*, 31(2):459–466.

[194] Karplus, M. and McCammon, J. A. (2002) Molecular dynamics simulations of biomolecules, *Nat Struct Mol Biol*, 9(9):646–652.

[195] Zhou, H.-X. (2014) Theoretical frameworks for multiscale modeling and simulation, 25:67–76.

[196] Leach, A., *Molecular modelling: principles and applications*, 2nd ed., Prentice Hall, 2001.

[197] Frenkel, D. and Smit, B., *Understanding molecular Simulation: from Algorithms to applications*, 2nd ed., Academic press, 2002.

[198] Kamerlin, S. C. L. et al. (2011) Coarse-grained (multiscale) simulations in studies of biophysical and chemical systems, *Annu Rev Phys Chem*, 62:41–64.

[199] Levitt, M. (2001) The birth of computational structural biology, *Nat Struct Mol Biol*, 8(5):392–393.

[200] McCAmmon, J. A., Gelin, B. R., and Karplus, M. (1977) Dynamics of folded proteins, *Nature*, 267(5612):585–590.

[201] Spoel, D. van der et al. (2005) GROMACS: fast, flexible, and free, *J Comput Chem*, 26(16):1701–1718.

[202] Hess, B., Kutzner, C., and Van Der Spoel, D. (2008) GROMACS 4: Algorithms for highly efficient, load-balanced, and scalable molecular simulation, *J Chem Theory Comput*, 4(3):435–447.

[203] Spoel, D. van der et al., *Gromacs User Manual version 4.5.6*, 2010.

[204] Verlet, L. (1967) Computer "experiments" on classical fluids. i. thermodynamical properties of lennard-jones molecules, *Phys Rev*, 159(1):98–103.

[205] Hockney, R. W. and Eastwood, J. W., *Computer simulation using particles*, McGraw-Hill, 1981.

[206] Nosé, S., *A molecular dynamics method for simulations in the canonical ensemble*, 1984.

[207] Hoover, W. (1985) Canonical dynamics: equilibrium phase-space distributions, *Phys. Rev. A*, 31(3):1695–1697.

[208] Parrinello, M. and Rahman, A. (1981) Polymorphic transitions in single crystals: a new molecular dynamics method, *J Appl Phys*, 52(12):7182–7190.

[209] Martyna, G. J., Tobias, D. J., and Klein, M. L. (1994) Constant pressure molecular dynamics algorithms, *J Chem Phys*, 101(5):4177–4189.

[210] Hünenberger, P. H., Thermostat algorithms for molecular dynamics simulations, in: *Advanced Computer Simulation*, Springer Berlin Heidelberg, 2005.

[211] Berendsen, H. and Postma, J. (1984) Molecular dynamics with coupling to an external bath, *J Chem Phys*, 81(8):3684–3690.

[212] Andersen, H. C. (1980) Molecular dynamics simulations at constant pressure and/or temperature, *J Chem Phys*, 72(4):2384–2393.

[213] Hess, B. et al. (1997) LINCS: a linear constraint solver for molecular simulations, *J Comput Chem*, 18(12):1463–1472.

[214] Jensen, M. Ø. et al. (2010) Principles of conduction and hydrophobic gating in K+ channels., *Proc Natl Acad Sci USA*, 107(13):5833–5838.

[215] Jensen, M. Ø. et al. (2012) Mechanism of voltage gating in potassium channels., *Science*, 336(6078):229–233.

[216] Jensen, M. Ø. et al., *Atomic-level simulation of current-voltage relationships in single-file ion channels.* 2013.

[217] Ostmeyer, J. et al. (2013) Recovery from slow inactivation in K+ channels is controlled by water molecules, *Nature*, 501(7465):121–124.

[218] Schreiber, H. and Steinhauser, O. (1992) Cutoff size does strongly influence molecular dynamics results on solvated polypeptides, *Biochemistry*, 31(25):5856–5860.

[219] Feller, S. E. et al. (1996) Effect of electrostatic force truncation on interfacial and transport properties of water, *J Phys Chem*, 100(42):17011–17020.

[220] Sagui, C. and Darden, T. A. (2003) Molecular dynamics simulations of biomolecules: long-range electrostatic effects, *Annu Rev Bioph Biom*, 28:155–179.

[221] Darden, T., York, D., and Pedersen, L. (1993) Particle mesh Ewald: an Nlog(N) method for Ewald sums in large systems, *J Chem Phys*, 98(12):10089–10092.

[222] Ewald, P. P. (1921) Die berechnung optischer und elektrostatischer gitterpotentiale, *Annalen der Physik*, 369(3):253–287.

[223] Kittel, C., *Introduction to solide state physics*, 8th ed., John Wiley & Sons, 2004.

[224] Toukmaji, A. Y. and Board, J. A. (1996) Ewald summation techniques in perspective: a survey, *Comput Phys Commun*, 95(2-3):73–92.

[225] Muller, M., Katsov, K., and Schick, M. (2006) Biological and synthetic membranes: what can be learned from a coarse-grained description?, *Phys Rep*, 434(5-6):113–176.

[226] Berendsen, H. J. C., *Simulating the physical world: hierarchical modeling from quantum mechanics to fluid dynamics*, Cambridge University Press, 2007.

[227] Lindahl, E. and Sansom, M. S. P. (2008) Membrane proteins: molecular dynamics simulations, *Curr Opin Struc Biol*, 18(4):425–431.

[228] Köpfer, D. A. et al. (2014) Ion permeation in K^+ channels occurs by direct Coulomb knock-on, *Science*, 346(6207):352–355.

[229] Klauda, J. B. et al. (2010) Update of the CHARMM all-atom additive force field for lipids: validation on six lipid types, *J Phys Chem B*, 114(23):7830–7843.

[230] Kaminski, G. A. et al. (2001) Evaluation and reparametrization of the OPLS-AA force field for proteins via comparison with accurate quantum chemical calculations on peptides, *J Phys Chem B*, 105(28):6474–6487.

[231] Pérez, A. et al. (2007) Refinement of the AMBER force field for nucleic acids: improving the description of α/γ conformers, *Biophys J*, 92(11):3817–3829.

[232] Vorobyov, I., Li, L., and Allen, T. W. (2008) Assessing atomistic and coarse-grained force fields for protein-lipid interactions: the formidable challenge of an ionizable side chain in a membrane., *J Phys Chem B*, 112(32):9588–9602.

[233] Oostenbrink, C. et al. (2004) A biomolecular force field based on the free enthalpy of hydration and solvation: the GROMOS force-field parameter sets 53a5 and 53a6, *J Comput Chem*, 25(13):1656–1676.

[234] Shelley, J. C., Shelley, M. Y., and Reeder, R. C. (2001) A coarse grain model for phospholipid simulations, *J Phys Chem B*, 105(19):4464–4470.

[235] Stevens, M. J. (2004) Coarse-grained simulations of lipid bilayers, *J Chem Phys*, 121(23):11942–11948.

[236] Nielsen, S. O., Lopez, C. F., and Srinivas, G. (2004) Coarse grain models and the computer simulation of soft materials, *J Phys-Condens Mat*, 16(15):481–512.

[237] Marrink, S. J., Vries, A. H. de, and Mark, A. E. (2004) Coarse grained model for semiquantitative lipid simulations, 108(2):750–760.

[238] Izvekov, S. and Voth, G. A. (2005) A multiscale coarse-graining method for biomolecular systems, *J Phys Chem B*, 109(7):2469–2473.

[239] Fritz, D. et al. (2011) Multiscale modeling of soft matter: scaling of dynamics, *Phys Chem Chem Phys*, 13(22):10412–10420.

[240] Marrink, S. J. et al. (2007) The MARTINI force field: coarse grained model for biomolecular simulations., *J Phys Chem B*, 111(27):7812–7824.

[241] Ramadurai, S. et al. (2010) Influence of Hydrophobic Mismatch and Amino Acid Composition on the Lateral Diffusion of Transmembrane Peptides, *Biophys J*, 99(5):1447–1454.

[242] Marrink, S. J. and Tieleman, P. D. (2013) Perspective on the MARTINI model, *Chem Soc Rev*, 42(16):6801–6822.

[243] Hakobyan, D. and Heuer, A. (2013) Phase Separation in a Lipid/Cholesterol System: Comparison of Coarse-Grained and United-Atom Simulations, *J Phys Chem B*, 117(14):3841–3851.

[244] Javanainen, M. et al. (2013) Anomalous and normal diffusion of proteins and lipids in crowded lipid membranes, *Faraday Discuss*, 161:397–417.

[245] Milovanovic, D. et al. (2015) Hydrophobic mismatch sorts SNARE proteins into distinct membrane domains, *Nat Commun*, 6:5984.

[246] Cooke, I., Kremer, K., and Deserno, M. (2005) Tunable generic model for fluid bilayer membranes, *Phys Rev E*, 72(1):011506.

[247] Srivastava, A. and Voth, G. A. (2012) Hybrid approach for highly coarse-grained lipid bilayer models, *J Chem Theory Comput*, 9(1):750–765.

[248] Grime, J. M. A. and Voth, G. A. (2013) Highly scalable and memory efficient ultra-coarse-grained molecular dynamics simulations, *J Chem Theory Comput*, 10(1):423–431.

[249] Shi, Q., Izvekov, S., and Voth, G. A. (2006) Mixed atomistic and coarse-grained molecular dynamics: simulation of a membrane-bound ion channel, *J Phys Chem B*, 110(31):15045–15048.

[250] Rzepiela, A. J. et al. (2011) Hybrid simulations: combining atomistic and coarse-grained force fields using virtual sites, *Phys Chem Chem Phys*, 13(22):10437–10448.

[251] Zavadlav, J. et al. (2014) Adaptive resolution simulation of MARTINI solvents, *J Chem Theory Comput*, 10(6):2591–2598.

[252] Wassenaar, T. A. et al. (2013) Mixing MARTINI: electrostatic coupling in hybrid atomistic–coarse-grained biomolecular simulations, *J Phys Chem B*, 117(13):3516–3530.

[253] Rzepiela, A. J. et al. (2010) Reconstruction of atomistic details from coarse-grained structures, *J Comput Chem*, 31(6):1333–1343.

[254] Stansfeld, P. J. and Sansom, M. S. P. (2011) From coarse grained to atomistic: a serial multiscale approach to membrane protein simulations, *J Chem Theory Comput*, 7(4):1157–1166.

[255] Wassenaar, T. A. et al. (2014) Going backward: a flexible geometric approach to reverse transformation from coarse grained to atomistic models, *J Chem Theory Comput*, 10(2):676–690.

[256] Arkhipov, A., Yin, Y., and Schulten, K. (2008) Four-scale description of membrane sculpting by BAR domains, *Biophys J*, 95(6):2806–2821.

[257] Monticelli, L., Kandasamy, S. K., and Periole, X. (2008) The MARTINI coarse-grained force field: extension to proteins, *J Chem Theory Comput*, 4(5):819–834.

[258] MacCallum, J. L., Bennett, W. F. D., and Tieleman, P. D. (2008) Distribution of Amino Acids in a Lipid Bilayer from Computer Simulations, *Biophys J*, 94(9):3393–3404.

[259] Singh, G. and Tieleman, P. D. (2011) Using the Wimley–White Hydrophobicity Scale as a Direct Quantitative Test of Force Fields: The MARTINI Coarse-Grained Model, *J Chem Theory Comput*, 7(7):2316–2324.

[260] Monticelli, L., Tieleman, P. D., and Fuchs, P. F. J. (2010) Interpretation of 2H-NMR Experiments on the Orientation of the Transmembrane Helix WALP23 by Computer Simulations, *Biophys J*, 99(5):1455–1464.

[261] Sengupta, D. and Marrink, S. J. (2010) Lipid-mediated interactions tune the association of glycophorin A helix and its disruptive mutants in membranes, *Phys Chem Chem Phys*, 12(40):12987–12996.

[262] López, C. A. et al. (2009) MARTINI coarse-grained force field: extension to carbohydrates, *J Chem Theory Comput*, 5(12):3195–3210.

[263] López, C. A. et al. (2013) MARTINI force field parameters for glycolipids, *J Chem Theory Comput*, 9(3):1694–1708.

[264] Rossi, G. et al. (2011) Coarse-graining polymers with the MARTINI force-field: polystyrene as a benchmark case, *Soft Matter*, 7(2):698–708.

[265] Milani, A. et al. (2011) Coarse-Grained Simulations of Model Polymer Nanofibres, *Macromol Theor Simul*, 20(5):305–319.

[266] Wallace, J. E. and Sansom, M. S. P. (2007) Carbon Nanotube/Detergent Interactions via Coarse-Grained Molecular Dynamics, *Nano Lett.* 7(7):1923–1928.

[267] Wong-ekkabut, J. et al. (2008) Computer simulation study of fullerene translocation through lipid membranes, *Nature Nanotechnology*, 3(6):363–368.

[268] Khalid, S. et al. (2008) DNA and lipid bilayers: self-assembly and insertion, *J R Soc Interface*, 5(Suppl 3):241–250.

[269] Corsi, J. et al. (2010) DNA Lipoplexes: Formation of the Inverse Hexagonal Phase Observed by Coarse-Grained Molecular Dynamics Simulation, *Langmuir*, 26(14):12119–12125.

[270] Periole, X. et al. (2009) Combining an elastic network with a coarse-grained molecular force field: structure, dynamics, and intermolecular recognition, *J Chem Theory Comput*, 5(9):2531–2543.

[271] Yesylevskyy, S. O. et al. (2010) Polarizable water model for the coarse-grained MARTINI force field., *PLoS Comput Biol*, 6(6):e1000810.

[272] Bond, P. J. et al. (2007) Coarse-grained molecular dynamics simulations of membrane proteins and peptides., *J. Struct. Biol.* 157(3):593–605.

[273] Jong, D. H. de, Singh, G., and Bennett, W. F. D. (2013) Improved parameters for the MARTINI coarse-grained protein force field, *J Chem Theory Comput*, 9(1):687–697.

[274] Arnarez, C. et al. (2014) Dry MARTINI, a coarse-grained force field for lipid membrane simulations with implicit solvent, *J Chem Theory Comput*, just accepted.

[275] Humphrey, W., Dalke, A., and Schulten, K. (1996) VMD: Visual molecular dynamics, *J Mol Graph Model*, 14(1):33–38.

[276] Schrödinger, LLC (2010) The PyMOL molecular graphics system, version 1.4.

[277] Michaud-Agrawal, N. et al. (2011) MDAnalysis: a toolkit for the analysis of molecular dynamics simulations, *J Comput Chem*, 32(10):2319–2327.

[278] Oliphant, T. E. (2007) Python for scientific computing, *Comput Sci Eng*, 9(3):10–20.

[279] Walt, S. van der, Colbert, S. C., and Varoquaux, G. (2011) The numpy array: a structure for efficient numerical computation, *Comput Sci Eng*, 13(2):22–30.

[280] Singer, S. J. and Nicolson, G. L. (1972) The fluid mosaic model of the structure of cell membranes, *Science*, 175(4023):720–731.

[281] Edidin, M. (2003) Lipids on the frontier: a century of cell-membrane bilayers, 4(5):414–418.

[282] Lee, A. G. (2004) How lipids affect the activities of integral membrane proteins, *BBA-Biomembranes*, 1666(1-2):62–87.

[283] Pieztsch, J. (2004) Mind the membrane, *Nat Hor Symp*.

[284] Niggli, V. (2005) Regulation of protein activities by phosphoinositide phosphates, *Annu Rev Cell Dev Biol*, 21:57–79.

[285] Meer, G. van, Voelker, D. R., and Feigenson, G. W. (2008) Membrane lipids: where they are and how they behave, *Nat Rev Mol Cell Biol*, 9(2):112–124.

[286] Shevchenko, A. and Simons, K. (2010) Lipidomics: coming to grips with lipid diversity, *Nat Rev Mol Cell Biol*, 11(8):593–598.

[287] Nicolson, G. L. (2014) The fluid—mosaic model of membrane structure: still relevant to understanding the structure, function and dynamics of biological membranes after more than 40 years, *BBA-Biomembranes*, 1838(6):1451–1466.

[288] Glukhov, E. et al. (2005) Basis for selectivity of cationic antimicrobial peptides for bacterial versus mammalian membranes, *J Biol Chem*, 280(40):33960–33967.

[289] Epand, R. F. et al. (2006) Role of membrane lipids in the mechanism of bacterial species selective toxicity by two α/β-antimicrobial peptides, *BBA-Biomembranes*, 1758(9):1343–1350.

[290] Brender, J. R., McHenry, A. J., and Ramamoorthy, A. (2012) Does cholesterol play a role in the bacterial selectivity of antimicrobial peptides?, *Front Immunol*:195.

[291] Pomorski, T. et al. (2001) Lipid distribution and transport across cellular membranes, *Semin Cell Dev Biol*, 12(2):139–148.

[292] Bretscher, M. S. (1972) Asymmetrical lipid bilayer structure for biological membranes, *Nature*, 236(61):11–12.

[293] Devaux, P. F. (1992) Protein involvement in transmembrane lipid asymmetry, *Annu Rev Bioph Biom*, 21:417–439.

[294] Boon, J. M. and Smith, B. D. (2002) Chemical control of phospholipid distribution across bilayer membranes, *Med Res Rev*, 22(3):251–281.

[295] McConnell, H. M. and Kornberg, R. D. (1971) Inside-outside transitions of phospholipids in vesicle membranes, *Biochemistry*, 10(7):1111–1120.

[296] Zachowski, A. (1993) Phospholipids in animal eukaryotic membranes: transverse asymmetry and movement, *Biochemical J*, 294(1):1–14.

[297] Meer, G. van (2005) Cellular lipidomics, *EMBO J*, 24(18):3159–3165.

[298] Contreras, F. X. et al. (2010) Transbilayer (flip-flop) lipid motion and lipid scrambling in membranes, *FEBS Lett*, 584(9):1779–1786.

[299] Devaux, P. F. (1991) Static and dynamic lipid asymmetry in cell membranes, *Biochemistry*, 30(5):1163–1173.

[300] Daleke, D. L. (2003) Regulation of transbilayer plasma membrane phospholipid asymmetry, *J Lipid Res*, 44(2):233–242.

[301] Pomorski, T. et al. (2004) Tracking down lipid flippases and their biological functions, *J Cell Sci*, 117(6):805–813.

[302] Daleke, D. L. (2008) Regulation of phospholipid asymmetry in the erythrocyte membrane, *Curr Opin Hematol*, 15(3):191–195.

[303] Tanaka, Y. and Schroit, A. J. (1983) Insertion of fluorescent phosphatidylserine into the plasma membrane of red blood cells. Recognition by autologous macrophages, *J Biol Chem*, 258(18):11335–11343.

[304] Fadok, V. A. et al. (1992) Exposure of phosphatidylserine on the surface of apoptotic lymphocytes triggers specific recognition and removal by macrophages, *J Immunol*, 148(7):2207–2216.

[305] Schlegel, R. A. and Williamson, P. (2001) Phosphatidylserine, a death knell, *Cell Death Differ*, 8(6):551–563.

[306] Wali, R. K. et al. (1988) Alterations in organization of phospholipids in erythrocytes as factor in adherence to endothelial cells in diabetes mellitus, *Diabetes*, 37(1):104–111.

[307] Wilson, M. J., Richter-Lowney, K., and Daleke, D. L. (1993) Hyperglycemia induces a loss of phospholipid asymmetry in human erythrocytes, *Biochemistry*, 32(42):11302–11310.

[308] Zwaal, R. F. A. and Schroit, A. J. (1997) Pathophysiologic implications of membrane phospholipid asymmetry in blood cells, *Blood*, 89(4):1121–1132.

[309] Hamilton, J. A. (2003) Fast flip-flop of cholesterol and fatty acids in membranes: implications for membrane transport proteins, *Curr Opin Lipidol*, 14(3):263–271.

[310] Mouritsen, O. G. and Zuckermann, M. J. (2004) What's so special about cholesterol?, *Lipids*, 39(11):1101–1113.

[311] Devaux, P. F. and Morris, R. (2004) Transmembrane asymmetry and lateral domains in biological membranes, *Traffic*, 5(4):241–246.

[312] Meer, G. van and Kroon, A. I. P. M. de (2011) Lipid map of the mammalian cell, *J Cell Sci*, 124(1):5–8.

[313] Epand, R. F. et al. (2010) Depolarization, bacterial membrane composition, and the antimicrobial action of ceragenins, *Antimicrob Agents Ch*, 54(9):3708–3713.

[314] Silhavy, T. J., Kahne, D., and Walker, S. (2010) The bacterial cell envelope, *Cold Spring Harb Perspect Biol*, 2:a000414.

[315] Matsuzaki, K. et al. (1995) Molecular basis for membrane selectivity of an antimicrobial peptide, magainin 2, *Biochemistry*, 34(10):3423–3429.

[316] Verly, R. M. et al. (2008) Effect of cholesterol on the interaction of the amphibian antimicrobial peptide DD K with liposomes, *Peptides*, 29(1):15–24.

[317] Henriksen, J. et al. (2006) Universal behavior of membranes with sterols, *Biophys J*, 90(5):1639–1649.

[318] Genova, J., Bivas, I., and Marinov, R. (2014) Cholesterol influence on the bending elasticity of lipid membranes, *Colloid Surface A*, 460:79–82.

[319] Hoskin, D. W. and Ramamoorthy, A. (2008) Studies on anticancer activities of antimicrobial peptides, *BBA-Biomembranes*, 1778(2):357–375.

[320] Thennarasu, S. et al. (2010) Limiting an antimicrobial peptide to the lipid-water interface enhances its bacterial membrane selectivity: a case study of MSI-367, *Biochemistry*, 49(50):10595–10605.

[321] Epand, R. F. et al. (2010) Probing the "charge cluster mechanism" in amphipathic helical cationic antimicrobial peptides, *Biochemistry*, 49(19):4076–4084.

[322] Binder, H. and Lindblom, G. (2003) Charge-dependent translocation of the trojan peptide penetratin across lipid membranes, *Biophys J*, 85(2):982–995.

[323] Cahill, K. (2010) Molecular electroporation and the transduction of oligoarginines, *Phys Biol*, 7(1):016001.

[324] Cahill, K. (2010) Cell-penetrating peptides, electroporation and drug delivery, *Systems Biol*, 4(6):367–378.

[325] Fraser, J. A. and Huang, C. L. H. (2007) Quantitative techniques for steady-state calculation and dynamic integrated modelling of membrane potential and intracellular ion concentrations, *Prog Biophys Mol Bio*, 94(3):336–372.

[326] Poignard, C. et al. (2011) Ion fluxes, transmembrane potential, and osmotic stabilization: a new dynamic electrophysiological model for eukaryotic cells, *Eur Biophys J*, 40(3):235–246.

[327] Hille, B., *Ion channels of excitable membranes*, 3rd ed., Sinauer Associates, 2001.

[328] Terrone, D. et al. (2003) Penetratin and related cell-penetrating cationic peptides can translocate across lipid bilayers in the presence of a transbilayer potential, *Biochemistry*, 42(47):13787–13799.

[329] Henriques, S. T. and Castanho, M. A. R. B. (2004) Consequences of nonlytic membrane perturbation to the translocation of the cell penetrating peptide pep-1 in lipidic vesicles, *Biochemistry*, 43(30):9716–9724.

[330] Jonathan B Rothbard et al. (2004) Role of membrane potential and hydrogen bonding in the mechanism of translocation of guanidinium-rich peptides into cells, *J Am Chem Soc*, 126(31):9506–9507.

[331] Henriques, S. T., Costa, J., and Miguel A R B Castanho (2005) Translocation of β-galactosidase mediated by the cell-penetrating peptide pep-1 into lipid vesicles and human hela cells is driven by membrane electrostatic potential, *Biochemistry*, 44(30):10189–10198.

[332] Magzoub, M., Pramanik, A., and Gräslund, A. (2005) Modeling the endosomal escape of cell-penetrating peptides: transmembrane pH gradient driven translocation across phospholipid bilayers, *Biochemistry*, 44(45):14890–14897.

[333] Fenz, S. F. and Sengupta, K. (2012) Giant vesicles as cell models, *Integr Biol*, 4(9):982–995.

[334] Pautot, S., Frisken, B. J., and Weitz, D. A. (2003) Engineering asymmetric vesicles, *Proc Natl Acad Sci USA*, 100(19):10718–10721.

[335] Alves, I. D. et al. (2009) The interaction of cell-penetrating peptides with lipid model systems and subsequent lipid reorganization: thermodynamic and structural characterization, *J Pept Sci*, 15(3):200–209.

[336] Walrant, A. et al. (2013) Direct translocation of cell-penetrating peptides in liposomes: a combined mass spectrometry quantification and fluorescence detection study, *Anal Biochem*, 438(1):1–10.

[337] Son, M. and London, E. (2013) The dependence of lipid asymmetry upon phosphatidylcholine acyl chain structure, *J Lipid Res*, 54(1):223–231.

[338] Son, M. and London, E. (2013) The dependence of lipid asymmetry upon polar headgroup structure, *J Lipid Res*, 54(12):3385–3393.

[339] Cheng, H.-T., Megha, and London, E. (2009) Preparation and properties of asymmetric vesicles that mimic cell membranes: effect upon lipid raft formation and transmembrane helix orientation, *J Biol Chem*, 284(10):6079–6092.

[340] Chiantia, S. et al. (2011) Asymmetric GUVs prepared by MβCD-mediated lipid exchange: an FCS study, *Biophys J*, 100(1):1–3.

[341] Cheng, H.-T. and London, E. (2011) Preparation and properties of asymmetric large unilamellar vesicles: interleaflet coupling in asymmetric vesicles is dependent on temperature but not curvature, *Biophys J*, 100(11):2671–2678.

[342] Richmond, D. L. et al. (2011) Forming giant vesicles with controlled membrane composition, asymmetry, and contents, *Proc Natl Acad Sci USA*, 108(23):9431–9436.

[343] Matosevic, S. and Paegel, B. M. (2013) Layer-by-layer cell membrane assembly, *Nature Chem*, 5(11):958–963.

[344] Woo, H.-J. and Wallqvist, A. (2011) Spontaneous buckling of lipid bilayer and vesicle budding induced by antimicrobial peptide magainin 2: a coarse-grained simulation study, *J Phys Chem B*, 115(25):8122–8129.

[345] Wang, Y. et al. (2012) Comparative molecular dynamics simulations of the antimicrobial peptide CM15 in model lipid bilayers, *BBA-Biomembranes*, 1818(5):1402–1409.

[346] Santo, K. P., Irudayam, S. J., and Berkowitz, M. L. (2013) Melittin creates transient pores in a lipid bilayer: results from computer simulations, *J Phys Chem B*, 117(17):5031–5042.

[347] Li, Z., Ding, H., and Ma, Y. (2012) Translocation of polyarginines and conjugated nanoparticles across asymmetric membranes, *Soft Matter*, 9(4):1281–1286.

[348] Gurtovenko, A. A. and Vattulainen, I. (2007) Lipid transmembrane asymmetry and intrinsic membrane potential: two sides of the same coin, *J Am Chem Soc*, 129(17):5358–5359.

[349] Gurtovenko, A. A. and Vattulainen, I. (2008) Membrane potential and electrostatics of phospholipid bilayers with asymmetric transmembrane distribution of anionic lipids, *J Phys Chem B*, 112(15):4629–4634.

[350] Vácha, R., Berkowitz, M. L., and Jungwirth, P. (2009) Molecular model of a cell plasma membrane with an asymmetric multicomponent composition: water permeation and ion effects, *Biophys J*, 96(11):4493–4501.

[351] Gurtovenko, A. A. and Vattulainen, I. (2009) Calculation of the electrostatic potential of lipid bilayers from molecular dynamics simulations: methodological issues, *J Chem Phys*, 130(21):215107.

[352] Maftouni, N. et al. (2013) A molecular dynamics simulation study of nanomechanical properties of asymmetric lipid bilayer, *J Membrane Biol*, 246(1):67–73.

[353] Perlmutter, J. D. and Sachs, J. N. (2011) Interleaflet interaction and asymmetry in phase separated lipid bilayers: molecular dynamics simulations, *J Am Chem Soc*, 133(17):6563–6577.

[354] Yesylevskyy, S. O. and Demchenko, A. P. (2012) How cholesterol is distributed between monolayers in asymmetric lipid membranes, *Eur Biophys J*, 41(12):1043–1054.

[355] Yesylevskyy, S. O. et al. (2013) Cholesterol induces uneven curvature of asymmetric lipid bilayers, *Scientific World Journal*, 2013:965230.

[356] Ingólfsson, H. I. et al. (2014) Lipid organization of the plasma membrane, *J Am Chem Soc*, 136(41):14554–14559.

[357] Bennett, W. F. D. and Tieleman, P. D. (2013) Computer simulations of lipid membrane domains, *BBA-Biomembranes*, 1828(8):1765–1776.

[358] Brown, R. E. (1998) Sphingolipid organization in biomembranes: what physical studies of model membranes reveal, *J Cell Sci*, 111(1):1–9.

[359] Slotte, J. P. (1999) Sphingomyelin–cholesterol interactions in biological and model membranes, *Chem Phys Lipids*, 102(1-2):13–27.

[360] Brown, D. A. and London, E. (2000) Structure and function of sphingolipid- and cholesterol-rich membrane rafts, *J Biol Chem*, 275(23):17221–17224.

[361] Simons, K. and Sampaio, J. L. (2011) Membrane organization and lipid rafts., *Cold Spring Harb Perspect Biol*, 3(10):a004697–a004697.

[362] Tanaka, K.-I. and Ohnishi, S.-I. (1976) Heterogeneity in the fluidity of intact erythrocyte membrane and its homogenization upon hemolysis, *BBA-Biomembranes*, 426(2):218–231.

[363] Morrot, G. et al. (1986) Asymmetric lateral mobility of phospholipids in the human erythrocyte membrane, *Proc Natl Acad Sci USA*, 83(18):6863–6867.

[364] Morrot, G. et al. (1989) Aminophospholipid translocase of human erythrocytes: phospholipid substrate specificity and effect of cholesterol, *Biochemistry*, 28(8):3456–3462.

[365] Cribier, S. et al. (1990) Lateral diffusion of erythrocyte phospholipids in model membranes comparison between inner and outer leaflet components, *Eur Biophys J*, 18(1):33–41.

[366] Whitfield, J. (2004) The need for fat, *Nat Hor Symp*.

[367] Cremesti, A. E., Goñi, F. M., and Kolesnick, R. (2002) Role of sphingomyelinase and ceramide in modulating rafts: do biophysical properties determine biologic outcome?, *FEBS Lett*, 531(1):47–53.

[368] Megha and London, E. (2004) Ceramide selectively displaces cholesterol from ordered lipid domains (rafts), *J Biol Chem*, 279(11):9997–10004.

[369] Draeger, A. and Babiychuk, E. B., Ceramide in plasma membrane repair, in: *Sphingolipids in disease*, ed. by Gulbins, E. and Petrache, I., Springer Vienna, 2013.

[370] Verdurmen, W. P. R. et al. (2010) Cationic cell-penetrating peptides induce ceramide formation via acid sphingomyelinase: implications for uptake, *J Control Release*, 147(2):171–179.

[371] Bhide, S. Y., Zhang, Z., and Berkowitz, M. L. (2007) Molecular dynamics simulations of SOPS and sphingomyelin bilayers containing cholesterol, *Biophys J*, 92(4):1284–1295.

[372] Pronk, S. et al. (2013) GROMACS 4.5: a high-throughput and highly parallel open source molecular simulation toolkit, *Bioinformatics*, 29(7):845–854.

[373] Parton, D. L., Akhmatskaya, E. V., and Sansom, M. S. P. (2012) Multiscale simulations of the antimicrobial peptide maculatin 1.1: water permeation through disordered aggregates, *J Phys Chem B*, 116(29):8485–8493.

[374] Yesylevskyy, S., Marrink, S. J., and Mark, A. E. (2009) Alternative mechanisms for the interaction of the cell-penetrating peptides penetratin and the tat peptide with lipid bilayers, *Biophys J*, 97(1):40–49.

[375] Pilar Veiga, M. et al. (2001) Interaction of cholesterol with sphingomyelin in mixed membranes containing phosphatidylcholine, studied by spin-label ESR and IR spectroscopies. A possible stabilization of gel-phase sphingolipid domains by cholesterol, *Biochemistry*, 40(8):2614–2622.

[376] Sonnino, S. and Prinetti, A. (2012) Membrane domains and the lipid raft concept, *Curr Med Chem*, 20(1):4–21.

[377] Sankaram, M. B. and Thompson, T. E. (1990) Interaction of cholesterol with various glycerophospholipids and sphingomyelin, *Biochemistry*, 29(47):10670–10675.

[378] Bittman, R. et al. (1994) Interaction of cholesterol with sphingomyelin in monolayers and vesicles, *Biochemistry*, 33(39):11776–11781.

[379] Berkowitz, M. L. (2009) Detailed molecular dynamics simulations of model biological membranes containing cholesterol, *BBA-Biomembranes*, 1788(1):86–96.

[380] Risselada, H. J. and Marrink, S. J. (2008) The molecular face of lipid rafts in model membranes, *Proc Natl Acad Sci USA*, 105(45):17367–17372.

[381] Baoukina, S., Mendez-Villuendas, E., and Tieleman, P. D. (2012) Molecular view of phase coexistence in lipid monolayers, *J Am Chem Soc*, 134(42):17543–17553.

[382] Baoukina, S. et al. (2013) Computer simulations of the phase separation in model membranes, *Faraday Discuss*, 161:63–75.

[383] Needham, D. and Nunn, R. S. (1990) Elastic deformation and failure of lipid bilayer membranes containing cholesterol, *Biophys J*, 58(4):997–1009.

[384] López-Montero, I., Vélez, M., and Devaux, P. F. (2007) Surface tension induced by sphingomyelin to ceramide conversion in lipid membranes, *BBA-Biomembranes*, 1768(3):553–561.

[385] Schroeder, F. et al. (1991) Transmembrane distribution of sterol in the human erythrocyte, *BBA-Biomembranes*, 1066(2):183–192.

[386] Müller, P. and Herrmann, A. (2002) Rapid transbilayer movement of spin-labeled steroids in human erythrocytes and in liposomes, *Biophys J*, 82(3):1418–1428.

[387] Bruckner, R. J. et al. (2009) Flip-flop-induced relaxation of bending energy: implications for membrane remodeling, *Biophys J*, 97(12):3113–3122.

[388] Steck, T. L., Ye, J., and Lange, Y. (2002) Probing red cell membrane cholesterol movement with cyclodextrin, *Biophys J*, 83(4):2118–2125.

[389] Leventis, R. and Silvius, J. R. (2001) Use of cyclodextrins to monitor transbilayer movement and differential lipid affinities of cholesterol, *Biophys J*, 81(4):2257–2267.

[390] Garg, S. et al. (2011) Noninvasive neutron scattering measurements reveal slower cholesterol transport in model lipid membranes, *Biophys J*, 101(2):370–377.

[391] Steck, T. L. and Lange, Y. (2012) How slow is the transbilayer diffusion (flip-flop) of cholesterol?, *Biophys J*, 102(4):945–946.

[392] Garg, S. et al. (2012) Response to "How slow is the transbilayer diffusion (flip-flop) of cholesterol?", *Biophys J*, 102(4):947–949.

[393] Marrink, S. J. et al. (2007) Cholesterol shows preference for the interior of polyunsaturated lipid membranes, *J Am Chem Soc*, 130(1):10–11.

[394] Bennett, W. F. D. et al. (2009) Molecular view of cholesterol flip-flop and chemical potential in different membrane environments, *J Am Chem Soc*, 131(35):12714–12720.

[395] Ogushi, F. et al. (2012) Rapid flip-flop motions of diacylglycerol and ceramide in phospholipid bilayers, *Chem Phys Lett*, 522:96–102.

[396] Jo, S. et al. (2010) Cholesterol flip-flop: insights from free energy simulation studies, *J Phys Chem B*, 114(42):13342–13348.

[397] Bennett, W. F. D. and Tieleman, P. D. (2012) Molecular simulation of rapid translocation of cholesterol, diacylglycerol, and ceramide in model raft and nonraft membranes, *J Lipid Res*, 53(3):421–429.

[398] Choubey, A. et al. (2013) Cholesterol translocation in a phospholipid membrane, *Biophys J*, 104(11):2429–2436.

[399] Parisio, G., Sperotto, M. M., and Ferrarini, A. (2012) Flip-flop of steroids in phospholipid bilayers: effects of the chemical structure on transbilayer diffusion, *J Am Chem Soc*, 134(29):12198–12208.

[400] Bennett, W. F. D. and Tieleman, P. D. (2011) Water defect and pore formation in atomistic and coarse-grained lipid membranes: pushing the limits of coarse graining, *J Chem Theory Comput*, 7(9):2981–2988.

[401] Bai, J. and Richard E Pagano (1997) Measurement of spontaneous transfer and transbilayer movement of BODIPY-labeled lipids in lipid vesicles, *Biochemistry*, 36(29):8840–8848.

[402] Harroun, T. A., Katsaras, J., and Wassall, S. R. (2006) Cholesterol hydroxyl group is found to reside in the center of a polyunsaturated lipid membrane, *Biochemistry*, 45(4):1227–1233.

[403] Koldsø, H. et al. (2014) Lipid clustering correlates with membrane curvature as revealed by molecular simulations of complex lipid bilayers, *PLoS Comput Biol*, 10(10):e1003911.

[404] Jo, S. et al. (2009) CHARMM-GUI membrane builder for mixed bilayers and its application to yeast membranes, *Biophys J*, 97(1):50–58.

[405] Ghahremanpour, M. M. et al. (2014) MemBuilder: a web-based graphical interface to build heterogeneously mixed membrane bilayers for the GROMACS biomolecular simulation program, *Bioinformatics*, 30(3):439–441.

[406] Kumar, S. et al. (1992) The weighted histogram analysis method for free-energy calculations on biomolecules. i. the method, *J Comput Chem*, 13(8):1011–1021.

[407] Ferguson, A. L. et al. (2011) Nonlinear dimensionality reduction in molecular simulation: the diffusion map approach, *Chem Phys Lett*, 509(1-3):1–11.

[408] Neale, C. et al. (2011) Statistical convergence of equilibrium properties in simulations of molecular solutes embedded in lipid bilayers, *J Chem Theory Comput*, 7(12):4175–4188.

[409] Romo, T. D. and Grossfield, A. (2014) How fast is your camera? Timescales for molecular motion and their role in restraining molecular dynamics, *Biophys J*, 106(12):2549–2551.

[410] Rappolt, M. et al. (2003) Mechanism of the lamellar/inverse hexagonal phase transition examined by high resolution X-ray diffraction, *Biophys J*, 84(5):3111–3122.

[411] Kučerka, N., Tristram-Nagle, S., and Nagle, J. F. (2006) Structure of fully hydrated fluid phase lipid bilayers with monounsaturated chains, *J Membrane Biol*, 208(3):193–202.

[412] Farge, E. and Devaux, P. F. (1992) Shape changes of giant liposomes induced by an asymmetric transmembrane distribution of phospholipids, *Biophys J*, 61(2):347–357.

[413] Berndl, K. et al. (1990) Shape transformations of giant vesicles: extreme sensitivity to bilayer asymmetry, *Europhysics Letters*, 13(7):659–664.

[414] Heerklotz, H. (2001) Membrane stress and permeabilization induced by asymmetric incorporation of compounds, *Biophys J*, 81(1):184–195.

[415] Lee, M.-T. et al. (2008) Mechanism and kinetics of pore formation in membranes by water-soluble amphipathic peptides, *Proc Natl Acad Sci USA*, 105(13):5087–5092.

[416] Esteban-Martín, S. et al. (2009) Stability of asymmetric lipid bilayers assessed by molecular dynamics simulations, *J Am Chem Soc*, 131(42):15194–15202.

[417] Aksimentiev, A. and Schulten, K. (2005) Imaging α-hemolysin with molecular dynamics: ionic conductance, osmotic permeability, and the electrostatic potential map, *Biophys J*, 88(6):3745–3761.

[418] Wang, L. (2012) Measurements and implications of the membrane dipole potential, *Annu Rev Biochem*, 81:615–635.

[419] Jogini, V. and Roux, B. (2007) Dynamics of the Kv1.2 voltage-gated K+ channel in a membrane environment, *Biophys J*, 93(9):3070–3082.

[420] Khandelia, H. and Kaznessis, Y. N. (2005) Molecular dynamics simulations of helical antimicrobial peptides in SDS micelles: what do point mutations achieve?, *Peptides*, 26(11):2037–2049.

[421] Bond, P. J. et al. (2008) Coarse-grained simulations of the membrane-active antimicrobial peptide maculatin 1.1, *Biophys J*, 95(8):3802–3815.

[422] Rzepiela, A. J. et al. (2010) Membrane poration by antimicrobial peptides combining atomistic and coarse-grained descriptions, *Faraday Discuss*, 144:431–443.

[423] Holm, T. et al. (2011) Retro-inversion of certain cell-penetrating peptides causes severe cellular toxicity, *BBA-Biomembranes*, 1808(6):1544–1551.

[424] Magzoub, M., Eriksson, L., and Gräslund, A. (2002) Conformational states of the cell-penetrating peptide penetratin when interacting with phospholipid vesicles: effects of surface charge and peptide concentration, *BBA-Biomembranes*, 1563(1-2):53–63.

[425] Lindberg, M. et al. (2001) Secondary structure and position of the cell-penetrating peptide transportan in SDS micelles as determined by NMR, *Biochemistry*, 40(10):3141–3149.

[426] Bárány-Wallje, E. et al. (2004) NMR solution structure and position of transportan in neutral phospholipid bicelles., *FEBS Lett*, 567(2-3):265–269.

[427] Ye, J. et al. (2010) Determination of penetratin secondary structure in live cells with Raman microscopy, *J Am Chem Soc*, 132(3):980–988.

[428] Walrant, A. et al. (2011) Different membrane behaviour and cellular uptake of three basic arginine-rich peptides, *BBA-Biomembranes*, 1808(1):382–393.

[429] Takechi, Y. et al. (2011) Physicochemical mechanism for the enhanced ability of lipid membrane penetration of polyarginine, *Langmuir*, 27(11):7099–7107.

[430] Mäler, L. (2013) Solution NMR studies of cell-penetrating peptides in model membrane systems, *Adv Drug Deliver Rev*, 65(8):1002–1011.

[431] Clayton, A. H. A. et al. (2006) Conformation and orientation of penetratin in phospholipid membranes, *J Pept Sci*, 12(3):233–238.

[432] Su, Y. et al. (2008) Reversible sheet-turn conformational change of a cell-penetrating peptide in lipid bilayers studied by solid-state NMR, *Journal of Molecular Biology*, 381(5):1133–1144.

[433] Wender, P. A. and Mitchell, D. J. (2000) The design, synthesis, and evaluation of molecules that enable or enhance cellular uptake: peptoid molecular transporters, *Proc Natl Acad Sci USA*, 97(24):13003–13008.

[434] Christiaens, B., Grooten, J., and Reusens, M. (2004) Membrane interaction and cellular internalization of penetratin peptides, *Eur J Biochem*, 271(6):1187–1197.

[435] Caesar, C. E. B. et al. (2006) Membrane interactions of cell-penetrating peptides probed by tryptophan fluorescence and dichroism techniques: correlations of structure to cellular uptake, *Biochemistry*, 45(24):7682–7692.

[436] Lins, L. et al. (2008) Relationships between the orientation and the structural properties of peptides and their membrane interactions, *BBA-Biomembranes*, 1778(7-8):1537–1544.

[437] Deshayes, S. et al. (2008) Structural polymorphism of two CPP: an important parameter of activity, *BBA-Biomembranes*, 1778(5):1197–1205.

[438] Eiríksdóttir, E. et al. (2010) Secondary structure of cell-penetrating peptides controls membrane interaction and insertion, *BBA-Biomembranes*, 1798(6):1119–1128.

[439] Huang, K. and García, A. E. (2013) Free energy of translocating an arginine-rich cell-penetrating peptide across a lipid bilayer suggests pore formation, *Biophys J*, 104(2):412–420.

[440] Lindberg, M., Biverståhl, H., and Gräslund, A. (2003) Structure and positioning comparison of two variants of penetratin in two different membrane mimicking systems by NMR, *Eur J Biochem*, 270(14):3055–3063.

[441] Almeida, P. F. F. and Pokorny, A. (2009) Mechanisms of antimicrobial, cytolytic, and cell-penetrating peptides: from kinetics to thermodynamics, *Biochemistry*, 48(34):8083–8093.

[442] Clark, K. S. et al. (2011) What determines the activity of antimicrobial and cytolytic peptides in model membranes, *Biochemistry*, 50(37):7919–7932.

[443] Magzoub, M. et al. (2001) Interaction and structure induction of cell-penetrating peptides in the presence of phospholipid vesicles, *BBA-Biomembranes*, 1512(1):77–89.

[444] Drin, G. et al. (2001) Physico-chemical requirements for cellular uptake of pAntp peptide - Role of lipid-binding affinity, *Eur J Biochem*, 268(5):1304–1314.

[445] Lindberg, M. and Gräslund, A. (2001) The position of the cell penetrating peptide penetratin in SDS micelles determined by NMR, *FEBS Lett*, 497(1):39–44.

[446] Bellet-Amalric, E. et al. (2000) Interaction of the third helix of Antennapedia homeodomain and a phospholipid monolayer, studied by ellipsometry and PM-IRRAS at the air–water interface, *BBA-Biomembranes*, 1467(1):131–143.

[447] Persson, D., Thorén, P. E., and Nordén, B. (2001) Penetratin-induced aggregation and subsequent dissociation of negatively charged phospholipid vesicles, *FEBS Lett*, 505(2):307–312.

[448] Maniti, O. et al. (2010) Distinct behaviour of the homeodomain derived cell penetrating peptide penetratin in interaction with different phospholipids, *PLoS ONE*, 5(12):e15819.

[449] Christiaens, B. et al. (2002) Tryptophan fluorescence study of the interaction of penetratin peptides with model membranes, *Eur J Biochem*, 269(12):2918–2926.

[450] Magzoub, M., Eriksson, L. E. G., and Gräslund, A. (2003) Comparison of the interaction, positioning, structure induction and membrane perturbation of cell-penetrating peptides and non-translocating variants with phospholipid vesicles, *Biophys Chem*, 103(3):271–288.

[451] Thorén, P. et al. (2003) Uptake of analogs of penetratin, tat (48–60) and oligoarginine in live cells, *Biochem Bioph Res Co*, 307(1):100–107.

[452] Dupont, E., Prochiantz, A., and Joliot, A., Penetratin story: an overview, in: *Cell-Penetrating Peptides*, Humana Press, 2011.

[453] Su, Y., Mani, R., and Hong, M. (2008) Asymmetric insertion of membrane proteins in lipid bilayers by solid-state NMR paramagnetic relaxation enhancement: a cell-penetrating peptide example, *J Am Chem Soc*, 130(27):8856–8864.

[454] Letoha, T. et al. (2003) Membrane translocation of penetratin and its derivatives in different cell lines, *J Mol Recognit*, 16(5):272–279.

[455] Björklund, J. et al. (2006) Real-time transmembrane translocation of penetratin driven by light-generated proton pumping, *Biophys J*, 91(4):L29–L31.

[456] Jones, S. W., Christison, R., and Bundell, K. (2005) Characterisation of cell-penetrating peptide-mediated peptide delivery, *Brit J Pharmacol*, 145(8):1093–1102.

[457] Langel, Ü. et al. (1996) A galanin-mastoparan chimeric peptide activates the Na+,K+-ATPase and reverses its inhibition by ouabain, *Regulatory Peptides*, 62(1):47–52.

[458] Bárány-Wallje, E. et al. (2006) Dynamics of transportan in bicelles is surface charge dependent, *J. Biomol. NMR*, 35(2):137–147.

[459] Deshayes, S. et al. (2004) Primary amphipathic cell-penetrating peptides: structural requirements and interactions with model membranes, *Biochemistry*, 43(24):7698–7706.

[460] Soomets, U. et al. (2000) Deletion analogues of transportan, *BBA-Biomembranes*, 1467(1):165–176.

[461] Lindgren, M., Gallet, X., and Soomets, U. (2000) Translocation properties of novel cell penetrating transportan and penetratin analogues, *Bioconjugate Chem*, 11(5):619–626.

[462] Hallbrink, M. et al. (2001) Cargo delivery kinetics of cell-penetrating peptides, *BBA-Biomembranes*, 1515(2):101–109.

[463] Pooga, M. et al. (1998) Cell penetrating PNA constructs regulate galanin receptor levels and modify pain transmission in vivo, *Nat Biotechnol*, 16(9):857–861.

[464] Säälik, P. et al. (2004) Protein cargo delivery properties of cell-penetrating peptides. A comparative study, *Bioconjugate Chem*, 15(6):1246–1253.

[465] Padari, K. et al. (2005) Cell transduction pathways of transportans, *Bioconjugate Chem*, 16(6):1399–1410.

[466] Verdurmen, W. P. R. et al. (2013) Cell surface clustering of heparan sulfate proteoglycans by amphipathic cell-penetrating peptides does not contribute to uptake., *J Control Release*, 170(1):83–91.

[467] Chaloin, L. et al. (1997) Conformations of primary amphipathic carrier peptides in membrane mimicking environments, *Biochemistry*, 36(37):11179–11187.

[468] Fanghänel, S. et al. (2014) Structure analysis and conformational transitions of the cell penetrating peptide transportan 10 in the membrane-bound state, *PLoS ONE*, 9(6):e99653.

[469] Czajlik, A. et al. (2002) Investigation of penetratin peptides. Part 1. The environment dependent conformational properties of penetratin and two of its derivatives, *J Pept Sci*, 8(4):151–171.

[470] Planque, M. R. R. de et al. (2003) Interfacial anchor properties of tryptophan residues in transmembrane peptides can dominate over hydrophobic matching effects in peptide-lipid interactions, *Biochemistry*, 42(18):5341–5348.

[471] Hall, B. A. et al. (2014) Sidekick for membrane simulations: automated ensemble molecular dynamics simulations of transmembrane helices, *J Chem Theory Comput*, 10(5):2165–2175.

[472] Lee, M.-T., Chen, F.-Y., and Huang, H. W. (2004) Energetics of pore formation induced by membrane active peptides, *Biochemistry*, 43(12):3590–3599.

[473] Huang, H. W. (2006) Molecular mechanism of antimicrobial peptides: the origin of cooperativity, *BBA-Biomembranes*, 1758(9):1292–1302.

[474] Kim, C. et al. (2009) Evidence of pores and thinned lipid bilayers induced in oriented lipid membranes interacting with the antimicrobial peptides, magainin-2 and aurein-3.3, *BBA-Biomembranes*, 1788(7):1482–1496.

[475] Nielsen, S. B. and Otzen, D. E. (2010) Impact of the antimicrobial peptide Novicidin on membrane structure and integrity, *J Colloid Interface Sci*, 345(2):248–256.

[476] Bertelsen, K. et al. (2012) Mechanisms of peptide-induced pore formation in lipid bilayers investigated by oriented 31P solid-state NMR spectroscopy, *PLoS ONE*, 7(10):e47745.

[477] Manzini, M. C. et al. (2014) Peptide:lipid ratio and membrane surface charge determine the mechanism of action of the antimicrobial peptide BP100. Conformational and functional studies, *BBA-Biomembranes*, 1838(7):1985–1999.

[478] Baumann, G. and Mueller, P. (1974) A molecular model of membrane excitability, *J Supramol Str*, 2(5-6):538–557.

[479] Lopez, C. F. et al. (2006) Probing membrane insertion activity of antimicrobial polymers via coarse-grain molecular dynamics, *J Chem Theory Comput*, 2(3):649–655.

[480] Chen, X. et al. (2013) Insertion of tat peptide and perturbation of negatively charged model phospholipid bilayer revealed by neutron diffraction, *BBA-Biomembranes*, 1828(8):1982–1988.

[481] Wolf, M. G. et al. (2010) g_membed: efficient insertion of a membrane protein into an equilibrated lipid bilayer with minimal perturbation, *J Comput Chem*, 31(11):2169–2174.

[482] Van Mau, N. et al. (1999) Lipid-induced organization of a primary amphipathic peptide: a coupled AFM-monolayer study, *J Membrane Biol*, 167(3):241–249.

[483] Vié, V. et al. (2000) Detection of peptide-lipid interactions in mixed monolayers, using isotherms, atomic force microscopy, and fourier transform infrared analyses, *Biophys J*, 78(2):846–856.

[484] Plénat, T. et al. (2004) Interaction of primary amphipathic cell-penetrating peptides with phospholipid-supported monolayers, *Langmuir*, 20(21):9255–9261.

[485] Hagberg, A., Swart, P., and Chult, D. S., Exploring network structure, dynamics, and function using NetworkX, in: *Proceedings of the 7th Python in Science Conference SciPy*, ed. by Varoquaux, G., Vaught, T., and Millman, J., 2008.

[486] Ester, M. et al., A density-based algorithm for discovering clusters in large spatial databases with noise, in: *2nd International Conference on Knowledge Discovery and Data Mining*, AAAI Press, 1996.

[487] Wieprecht, T., Beyermann, M., and Seelig, J. (2002) Thermodynamics of the coil–α-helix transition of amphipathic peptides in a membrane environment: the role of vesicle curvature, *Biophys Chem*, 96(2-3):191–201.

[488] Dathe, M. et al. (1996) Peptide helicity and membrane surface charge modulate the balance of electrostatic and hydrophobic interactions with lipid bilayers and biological membranes, *Biochemistry*, 35(38):12612–12622.

[489] Allen, W. J., Lemkul, J. A., and Bevan, D. R. (2009) GridMAT-MD: A grid-based membrane analysis tool for use with molecular dynamics, *J Comput Chem*, 30(12):1952–1958.

[490] Gapsys, V., Groot, B. L. de, and Briones, R. (2013) Computational analysis of local membrane properties, *J Comput Aid Mol Des*, 27(10):845–858.

[491] Nagle, J. F. and Tristram-Nagle, S. (2000) Structure of lipid bilayers, *BBA-Biomembranes*, 1469(3):159–195.

[492] Hunter, J. D. (2007) Matplotlib: A 2D Graphics Environment, *Comput Sci Eng*, 9(3):90–95.

[493] Seelig, J. (1977) Deuterium magnetic resonance: theory and application to lipid membranes, *Q Rev Biophys*, 10(3):353–418.

[494] Schäfer, H., Mädler, B., and Sternin, E. (1998) Determination of orientational order parameters from 2H NMR spectra of magnetically partially oriented lipid bilayers., *Biophys J*, 74(2 Pt 1):1007–1014.

[495] Vermeer, L. S. et al. (2007) Acyl chain order parameter profiles in phospholipid bilayers: computation from molecular dynamics simulations and comparison with 2H NMR experiments, *Eur Biophys J*, 36(8):919–931.

[496] Schäfer, L. V. et al. (2011) Lipid packing drives the segregation of transmembrane helices into disordered lipid domains in model membranes, *Proc Natl Acad Sci USA*, 108(4):1343–1348.

[497] Leekumjorn, S. and Sum, A. K. (2006) Molecular simulation study of structural and dynamic properties of mixed DPPC/DPPE bilayers, *Biophys J*, 90(11):3951–3965.

[498] Toke, O. et al. (2004) Secondary structure and lipid contact of a peptide antibiotic in phospholipid bilayers by REDOR, *Biophys J*, 87(1):662–674.

[499] Tremouilhac, P. et al. (2006) Synergistic transmembrane alignment of the antimicrobial heterodimer PGLa/magainin, *J Biol Chem*, 281(43):32089–32094.

[500] Marquette, A., Mason, A. J., and Bechinger, B. (2008) Aggregation and membrane permeabilizing properties of designed histidine-containing cationic linear peptide antibiotics, *J Pept Sci*, 14(4):488–495.

[501] Qian, S. et al. (2008) Structure of the alamethicin pore reconstructed by X-ray diffraction analysis, *Biophys J*, 94(9):3512–3522.

[502] Lundin, P., EL Andaloussi, S., and Langel, Ü., Toxicity methods for CPPs, in: *Cell-penetrating peptides*, ed. by Langel, Ü., Humana Press, 2011.

[503] Su, C.-J. et al. (2013) Peptide-induced bilayer thinning structure of unilamellar vesicles and the related binding behavior as revealed by X-ray scattering, *BBA-Biomembranes*, 1828(2):528–534.

[504] Chen, F. Y., Lee, M. T., and Huang, H. W. (2003) Evidence for membrane thinning effect as the mechanism for peptide-induced pore formation, *Biophys J*, 84(6):3751–3758.

[505] Salnikov, E. S., Mason, A. J., and Bechinger, B. (2009) Membrane order perturbation in the presence of antimicrobial peptides by 2H solid-state NMR spectroscopy, *Biochimie*, 91(6):734–743.

[506] Irudayam, S. J., Pobandt, T., and Berkowitz, M. L. (2013) Free energy barrier for melittin reorientation from a membrane-bound state to a transmembrane state, *J Phys Chem B*, 117(43):13457–13463.

[507] Breen, D. and Bai, L. (2011) Calculating center of mass in an unbounded 2D environment, *J Graph GPU Game Tools*, 13(4):53–60.

[508] Epand, R. M. et al. (2010) Lipid clustering by three homologous arginine-rich antimicrobial peptides is insensitive to amino acid arrangement and induced secondary structure, *BBA-Biomembranes*, 1798(6):1272–1280.

[509] Epand, R. F. et al. (2010) Amphipathic helical cationic antimicrobial peptides promote rapid formation of crystalline states in the presence of phosphatidylglycerol: lipid clustering in anionic membranes, *Biophys J*, 98(11):2564–2573.

[510] Wadhwani, P. et al. (2012) Membrane-active peptides and the clustering of anionic lipids, *Biophys J*, 103(2):265–274.

[511] Lu, J., Blazyk, J., and Lorigan, G. (2006) Exploring membrane selectivity of the antimicrobial peptide KIGAKI using solid-state NMR spectroscopy, *BBA-Biomembranes*, 1758(9):1303–1313.

[512] Devaux, P. F. (1993) Lipid transmembrane asymmetry and flip-flop in biological-membranes and in lipid bilayers, *Curr Opin Struc Biol*, 3(4):489–494.

[513] Epand, R. F. et al. (2003) Transbilayer lipid diffusion promoted by Bax: implications for apoptosis, *Biochemistry*, 42(49):14576–14582.

[514] Fattal, E. et al. (1994) Pore-forming peptides induce rapid phospholipid flip-flop in membranes, *Biochemistry*, 33(21):6721–6731.

[515] Matsuzaki, K. et al. (1996) An antimicrobial peptide, magainin 2, induced rapid flip-flop of phospholipids coupled with pore formation and peptide translocation, *Biochemistry*, 35(35):11361–11368.

[516] Tieleman, P. D. and Marrink, S. J. (2006) Lipids out of equilibrium: energetics of desorption and pore mediated flip-flop, *J Am Chem Soc*, 128(38):12462–12467.

[517] Hu, Q., Joshi, R., and Schoenbach, K. (2005) Simulations of nanopore formation and phosphatidylserine externalization in lipid membranes subjected to a high-intensity, ultrashort electric pulse, *Phys Rev E*, 72(3):031902.

[518] Vernier, P. T. et al. (2006) Nanopore formation and phosphatidylserine externalization in a phospholipid bilayer at high transmembrane potential, *J Am Chem Soc*, 128(19):6288–6289.

[519] Gurtovenko, A. A. and Ilpo Vattulainen (2007) Molecular mechanism for lipid flip-flops, *J Phys Chem B*, 111(48):13554–13559.

[520] Gurtovenko, A. A., Onike, O. I., and Anwar, J. (2008) Chemically induced phospholipid translocation across biological membranes, *Langmuir*, 24(17):9656–9660.

[521] Bennett, W. F. D., MacCallum, J. L., and Tieleman, P. D. (2009) Thermodynamic analysis of the effect of cholesterol on dipalmitoylphosphatidylcholine lipid membranes, *J Am Chem Soc*, 131(5):1972–1978.

[522] Sapay, N., Bennett, W. F. D., and Tieleman, P. D. (2009) Thermodynamics of flip-flop and desorption for a systematic series of phosphatidylcholine lipids, *Soft Matter*, 5(17):3295–3302.

[523] Sapay, N., Bennett, W. F. D., and Tieleman, P. D. (2010) Molecular simulations of lipid flip-flop in the presence of model transmembrane helices, *Biochemistry*, 49(35):7665–7673.

[524] Kaihara, M. et al. (2013) Control of phospholipid flip-flop by transmembrane peptides, *Chem Phys*, 419:78–83.

[525] Swiecicki, J. M. et al. (2014) The efficacies of cell-penetrating peptides in accumulating in large unilamellar vesicles depend on their ability to form inverted micelles, *ChemBioChem*, 15(6):884–891.

[526] Tieleman, P. D. (2004) The molecular basis of electroporation, *BMC Biochem*, 5(1):10.

[527] Tarek, M. (2005) Membrane electroporation: a molecular dynamics simulation, *Biophys J*, 88(6):4045–4053.

[528] Thøgersen, L. et al. (2008) Peptide aggregation and pore formation in a lipid bilayer: a combined coarse-grained and all atom molecular dynamics study, *Biophys J*, 95(9):4337–4347.

[529] Berger, O., Edholm, O., and Jähnig, F. (1997) Molecular dynamics simulations of a fluid bilayer of dipalmitoylphosphatidylcholine at full hydration, constant pressure, and constant temperature, *Biophys J*, 72(5):2002–2013.

[530] Kol, M. A. et al. (2003) Phospholipid flop induced by transmembrane peptides in model membranes is modulated by lipid composition, *Biochemistry*, 42(1):231–237.

[531] Bennett, W. F. D. and Tieleman, P. D. (2014) The importance of membrane defects - Lessons from simulations, *Accounts Chem Res*, 47(8):2244–2251.

[532] Koller, D. and Lohner, K. (2014) The role of spontaneous lipid curvature in the interaction of interfacially active peptides with membranes, *BBA-Biomembranes*, 1838(9):2250–2259.

[533] Sieber, J. J. et al. (2007) Anatomy and dynamics of a supramolecular membrane protein cluster, *Science*, 317(5841):1072–1076.

[534] Sahl, S. J. et al. (2010) Fast molecular tracking maps nanoscale dynamics of plasma membrane lipids, *Proc Natl Acad Sci USA*, 107(15):6829–6834.

[535] Mueller, V. et al. (2011) STED nanoscopy reveals molecular details of cholesterol- and cytoskeleton-modulated lipid interactions in living cells, *Biophys J*, 101(7):1651–1660.

[536] Lindahl, E. and Edholm, O. (2000) Mesoscopic undulations and thickness fluctuations in lipid bilayers from molecular dynamics simulations, *Biophys J*, 79(1):426–433.

[537] Hu, M., Briguglio, J. J., and Deserno, M. (2012) Determining the gaussian curvature modulus of lipid membranes in simulations, *Biophys J*, 102(6):1403–1410.

[538] Tarazona, P., Chacón, E., and Bresme, F. (2013) Thermal fluctuations and bending rigidity of bilayer membranes, *J Chem Phys*, 139(9):094902.

[539] Campelo, F. et al. (2014) Helfrich model of membrane bending: from Gibbs theory of liquid interfaces to membranes as thick anisotropic elastic layers, *Adv Colloid Interface Sci*, 208:25–33.

[540] Tu, Z. C. and Ou-Yang, Z. C. (2014) Recent theoretical advances in elasticity of membranes following Helfrich's spontaneous curvature model, *Adv Colloid Interface Sci*, 208:66–75.